

MSc Thesis

Data-Driven Improvement of RANS Simulations of
Wind Farms in Stable Atmospheric Boundary Layer
Conditions

B.W.J. van de Krol (4389212)

MSc Thesis

Data-Driven Improvement of RANS Simulations of Wind Farms in Stable Atmospheric Boundary Layer Conditions

by

B.W.J. van de Krol (4389212)

to obtain the degree of Master of Science
at the Delft University of Technology,
to be defended publicly on Tuesday August 2, 2022 at 14:00.

Student number: 4389212
Project duration: March, 2021 – July, 2022
Thesis committee: dr. R.P. Dwight, TU Delft, supervisor
dr.ir. E. van Kampen, TU Delft
dr.ir. A.H. van Zuijlen, TU Delft

An electronic version of this thesis is available at <http://repository.tudelft.nl/>.

Abstract

Offshore wind farms have the potential to deliver a significant part of the future energy demands as a renewable energy source. Currently, simulations used to design, control and plan maintenance of wind farms in industry are based on low-fidelity blade element momentum methods. However, these methods are not very accurate and with the increase in available computational capabilities, it is expected for industry to move towards Navier-Stokes based methods. Research mainly uses LES methods as they resolve the large-scale, often anisotropic, atmospheric turbulence while the effect of the small-scale, often more isotropic, turbulence caused by the blades is modelled. However, these LES methods are too computationally demanding for industry. Therefore, the expectation is that industry will move towards less computationally demanding RANS simulations.

RANS simulations do need to provide a sufficient increase in accuracy to justify the additional computational cost. However, the most used RANS-model in relation to wind farms, $k - \epsilon$, has crippling shortcomings. It over-predicts the eddy viscosity in the near wake, leading to an over-prediction of wake recovery and fails to model the anisotropy of the turbulence quantities. To account for these shortcomings, a recent development is to use data-driven techniques to improve turbulence modelling. In literature many of these machine learning techniques use the generalised Galilean invariant effective viscosity hypothesis in connection to some machine learning technique, such as deep neural networks. Within the faculty of Aerospace Engineering of the TU Delft, the sparse regression of the turbulence stress anisotropy (SpaRTA) method has shown a lot of promise. This method uses temporally averaged fields from LES data together with sparse regression methods to learn corrections for the anisotropy tensor and turbulence production terms. The SpaRTA method has already been successfully applied to several wind turbine configurations in neutral atmospheric conditions. Therefore, this thesis aims to extend the SpaRTA methodology to wind turbines in stably stratified atmospheric boundary layers.

The main way in which the SpaRTA method is extended for stable stratification is to include an additional additive correction term for the turbulent heat flux, which is modelled by the gradient-diffusion hypothesis in the baseline model. This extended SpaRTA method is applied to two cases: a stably stratified parcel of air moving over land based on the GABLS1 inter-comparison study and a case with a turbine placed in similar environmental conditions.

The simulations with implemented correction models show significant improvement over the baseline simulations. For the first case the only improvement is in the computation of the turbulence kinetic energy as the anisotropy correction corrects for the slight over-prediction of the baseline model. In the case with the turbine the anisotropy correction removes turbulence kinetic energy in the near-wake while the turbulence production correction increases the turbulence kinetic energy in the shear-layer between the wake and the outside flow. This correction meant that turbulent mixing was modelled better and the over-prediction of the wake in the velocity field was removed when compared to the baseline simulations.

However, it is concluded that the effects of the additional turbulent heat flux correction can also be incorporated in the turbulence production correction, making the turbulent heat flux correction superfluous. Other ways to improve this methodology are mainly related to the availability of high-quality LES data for different configurations in terms of lay-out and atmospheric boundary layer conditions. Lastly, another factor limiting this methodology for these cases is the ability to properly model the turbulence anisotropy correction.

Preface

This thesis marks the end of my time at the TU Delft. A very formative, educational and fun time. However, it also had its fair share of challenges, especially in the last year and a bit. Covid, having to always work at home, delays in my thesis, it was not always easy. But I made it through.

Therefore, I would like to thank all the people which supported me in my journey to my diploma. In particular my supervisor Dr. Richard Dwight for giving me a lot of freedom, but always being available for discussion and feedback when I needed it. Also, Ir. Julia Steiner for getting me up to speed with the different software needed and thinking along when my simulations would not converge again.

Aside from the scientific support, I also want to thank my family, football team and other friends for generally being there and providing distractions from my thesis when I needed it. Especially, my girlfriend Lara, who always stayed positive, even in the most difficult of times.

Lastly, I want to end with a quote from the late, great Enzo Ferrari:

”Aerodynamics are for people who can’t build engines.”

Well, I can’t build engines. But I hope this thesis does prove I can do aerodynamics!

*B.W.J. van de Krol
Den Haag, July 2022*

Contents

Abstract	iii
List of Figures	ix
List of Tables	xv
Acronyms	xvii
Nomenclature	xix
1 Introduction	1
2 Background of Wind Farm Simulation and Machine Learning	3
2.1 Overview of Computational Fluid Dynamics	3
2.1.1 Governing Equations of CFD	3
2.1.2 Length Scales of Turbulence	4
2.1.3 Large Eddy Simulation	5
2.1.4 Reynolds-Averaged Navier-Stokes	5
2.1.5 Turbulence Modelling	6
2.1.6 Realizability of the Reynolds Stress	8
2.1.7 Invariance of the Navier-Stokes Equations	10
2.2 Wind Farms and the Atmospheric Boundary Layer	12
2.2.1 Atmospheric Boundary Layer Characteristics	12
2.2.2 Monin-Oblukhov Similarity Theory	16
2.2.3 Turbine Modelling	18
2.2.4 Adaptation of Navier-Stokes Equations for non-neutral ABL	19
2.2.5 Overview of approaches in research	20
2.3 Machine Learning in Wind Farm Simulation	23
2.3.1 Machine Learning in Turbulence Modelling	23
2.3.2 Machine Learning in Turbulent Scalar Flux Modelling	24
2.3.3 SpaRTA Method	25
3 Generation of LES Reference Data	31
3.1 Case A: Gabls1	31
3.1.1 Case Definition	31
3.1.2 Simulation Methodology	31
3.1.3 Validation	35
3.1.4 Alignment Turbulent Heat Flux and Temperature Gradient	41
3.2 Case B: Kokee SBL	42
3.2.1 Case Definition	42
3.2.2 Simulation Methodology	43
3.2.3 Validation	45
4 Discovery of Optimal Correction Fields	47
4.1 Discovery Simulation Methodology	47
4.1.1 Governing Equations	47
4.1.2 Numerical Schemes	50
4.1.3 Initial Conditions	50
4.1.4 Boundary Conditions	51
4.1.5 Consistency with LES System	51
4.2 Optimal Correction Fields	52
4.2.1 Case A: GABLS1	52
4.2.2 Case B: Kokee SBL	55

5	Learning of Correction Models	57
5.1	Model Learning Methodology	57
5.2	Feature Selection	58
5.2.1	Creation of Library	58
5.2.2	Reduction of Library Using Mutual Information	60
5.3	Selection of models	64
5.3.1	Case A: GABLS1	64
5.3.2	Case B: Kokee SBL	68
6	Implementation of Learned Correction Terms in Simulations	75
6.1	Simulation Methodology	75
6.1.1	Governing Equations	75
6.1.2	Initial Conditions	75
6.1.3	Boundary Conditions	76
6.1.4	Blending and Ramping of Implementation of Correction Models	76
6.1.5	Limiters	77
6.2	Results Case A: GABLS1 with Implemented Models	77
6.2.1	Influence of the THF Correction	77
6.2.2	Model Selection	79
6.2.3	Comparison to Baseline	80
6.2.4	Model Performance	80
6.3	Results Case B: Kokee SBL with Implemented Models	84
6.3.1	Influence of Nonphysical Turbulence Model Constants	84
6.3.2	Influence of the THF Correction	86
6.3.3	Model Selection	88
6.3.4	Comparison to Baseline	93
6.3.5	Model Performance	96
7	Conclusions and Recommendations	101
7.1	Conclusions	101
7.2	Recommendations for Future Work	103
	Bibliography	105
A	Mutual Information of Features in Library	113
B	Generated Models After Regression	121
C	Additional Results of Case B: Kokee SBL with Implemented Models	129
C.1	Influence of Non-physical Turbulence Model Constants	129
C.2	Influence of the THF Correction	129
C.3	Selection of Models for the Turbulence Anisotropy Correction	132
C.4	Selection of Models for the TKE Production Correction	133
C.5	Selection of Models for the THF Correction	134
C.6	Comparison with Baseline	135
C.7	Model Performance	140

List of Figures

2.1	Barycentric map displaying the limiting states of turbulence (Banerjee et al., 2007).	10
2.2	Wind spectrum at wind farm Brookhaven taken from Burton et al. (2011) based on work from Van der Hoven (1957).	12
2.3	Monin-Oblukhov functions for mean velocity gradient (left) and mean potential temperature gradient (right). Based on the experimental results from Businger et al. (1971) and taken from Wyngaard (2010).	17
3.1	Profiles of the initial conditions according to Beare et al. (2006).	34
3.2	Planar-averaged profiles of the mean resolved potential temperature and mean resolved velocity over the last hour of the GABLS1 simulation.	36
3.3	Planar averaged profiles of the mean resolved momentum fluxes over the last hour of the GABLS1 simulation.	36
3.4	Planar averaged profiles of the mean sub-grid scale turbulence over the last hour of the GABLS1 simulation.	37
3.5	Planar averaged profiles of the mean resolved turbulent temperature fluxes over the last hour of the GABLS1 simulation.	37
3.6	Planar averaged mean resolved velocity profiles for multiple different hours.	38
3.7	Planar averaged mean resolved potential temperature profiles for multiple different hours.	38
3.8	Time series of the wall friction velocity and the wall heat flux, compared against reference data from Beare et al. (2006).	39
3.9	Planar averaged mean resolved temperature flux profiles for multiple different hours.	39
3.10	Planar averaged mean resolved momentum flux profiles for multiple different hours.	40
3.11	Vertical slice of mean resolved vertical velocity for the GABLS1 simulation, showing oscillations.	41
3.12	Planar averaged profile of the mean resolved vertical velocity for the GABLS1 simulation.	41
3.13	Angle between the resolved turbulent heat flux and the mean temperature gradient for the GABLS1 simulation.	42
3.14	Schematic of the precursor-successor approach from Churchfield et al. (2012a).	43
3.15	Schematic representation of the domain for Case B: Kokee SBL, with the blue arrow denoting the inflow direction and the black line denoting the wind turbine.	44
4.1	Planar averaged profiles of anisotropy correction components for Case A: GABLS1.	53
4.2	Planar averaged profile of turbulence kinetic energy production correction for Case A: GABLS1.	53
4.3	Planar averaged profiles of turbulent heat flux components for Case A: GABLS1.	54
4.4	Planar averaged profiles of TKE production terms for Case A: GABLS1.	54
4.5	Contour plot of TKE production due to anisotropy correction field at turbine location $y = y_{hub}$ for Case B: Kokee SBL. The turbine is indicated by a black vertical line (Kokee, 2021).	55
4.6	Contour plot of TKE production correction field at turbine location $y = y_{hub}$ for Case B: Kokee SBL. The turbine is indicated by a black vertical line (Kokee, 2021).	55
4.7	Contour plot of TKE production due to THF correction field at turbine location $y = y_{hub}$ for Case B: Kokee SBL. The turbine is indicated by a black vertical line (Kokee, 2021).	56
4.8	Contour plots of THF correction fields at turbine location $y = y_{hub}$ for Case B: Kokee SBL. The turbine is indicated by a black vertical line (Kokee, 2021).	56
5.1	Mutual information between the second invariant of the anisotropy correction b_{ij}^A and the second invariants of the basis tensors for Case A: GABLS1.	61
5.2	Mutual information between the second invariant of the anisotropy correction b_{ij}^A and the second invariants of the basis tensors for Case B: Kokee SBL.	61

5.3	Mutual information between the TKE production correction and the TKE production of the basis tensors for Case A: GABLS1	62
5.4	Mutual information between the TKE production correction and the TKE production of the basis tensors for Case B: Kokee SBL	63
5.5	Mutual information between the z -component of the THF correction and basis tensors for Case A: GABLS1.	64
5.6	Mutual information between the z -component of the THF correction and basis tensors for Case B: Kokee SBL.	64
5.7	Scatter plot of the mean and max squared error of the anisotropy correction models with less than eleven terms, generated using data from Case A: GABLS1. Selected models are denoted by a black circle.	65
5.8	Prediction of the chosen models for the planar-averaged TKE production due to the anisotropy correction b_{ij}^A for Case A: GABLS1, as well as the spread of the predictions of all generated models included in the scatter plot.	66
5.9	Scatter plot of the mean and max squared error of the TKE production correction models with less than eleven terms, generated using data from Case A: GABLS1. Selected models are denoted by a black circle.	66
5.10	Prediction of the chosen models for the planar-averaged TKE production correction \mathcal{R} for Case A: GABLS1, as well as the spread of the predictions of all generated models included in the scatter plot.	67
5.11	Scatter plot of the mean and max squared error of the THF correction models with less than eleven terms, generated using data from Case A: GABLS1. Selected models are denoted by a black circle.	67
5.12	Prediction of the chosen models for the planar-averaged z -component of the THF correction q_z^A for Case B: Kokee SBL, as well as the spread of the predictions of all generated models included in the scatter plot.	68
5.13	Scatter plot of the mean and max squared error of the anisotropy correction models with less than six terms, generated using data from Case B: Kokee SBL. Selected models are denoted by a black circle.	69
5.14	Prediction of the chosen models for the planar-averaged TKE production due to the anisotropy correction b_{ij}^A for Case B: Kokee SBL, as well as the spread of the predictions of all generated models included in the scatter plot.	70
5.15	Scatter plot of the mean and max squared error of the TKE production correction models with less than six terms, generated using data from Case B: Kokee SBL. Selected models are denoted by a black circle.	71
5.16	Prediction of the chosen models for the planar-averaged TKE production correction \mathcal{R} for Case B: Kokee SBL, as well as the spread of the predictions of all generated models included in the scatter plot.	71
5.17	Scatter plot of the mean and max squared error of the THF correction models with less than six terms, generated using data from Case B: Kokee SBL. Selected models are denoted by a black circle.	72
5.18	Prediction of the chosen models for the planar-averaged z -component of the THF correction q_z^A for Case B: Kokee SBL, as well as the spread of the predictions of all generated models included in the scatter plot.	73
6.1	Comparison of the turbulent heat flux from RANS simulations of Case A: GABLS1 with different versions of the frozen THF correction (q_f^A): full correction (blue), only z -component (orange) and no THF correction (green). All simulations implemented the frozen anisotropy (b_{ij}^A) and TKE production (\mathcal{R}) corrections.	78
6.2	Comparison of RANS simulations of Case A: GABLS1 with different versions of the frozen THF correction (q_f^A): full correction (blue), only z -component (orange) and no THF correction (green). All simulations implemented the frozen anisotropy (b_{ij}^A) and TKE production (\mathcal{R}) corrections.	78
6.3	Comparison of planar-averaged profiles of temperature, velocity and TKE for simulations of Case A: GABLS1 with different complexity models implemented.	79

6.4	Comparison of planar-averaged profiles of temperature, velocity and TKE for simulations of Case A: GABLS1 with modelled, frozen and without any corrections implemented. . . .	80
6.5	Planar-averaged profiles of the modelled turbulence anisotropy correction compared against the optimal, frozen correction term and the predicted correction term for Case A: GABLS1.	81
6.6	Planar-averaged profile of the modelled TKE production correction compared against the optimal, frozen correction term and the predicted correction term for Case A: GABLS1.	82
6.7	Planar-averaged profiles of the modelled THF correction compared against the optimal, frozen correction term and the predicted correction term for Case A: GABLS1.	82
6.8	Planar-averaged profiles of the different TKE production terms in the simulation with implemented models (solid lines) and in the k-corrective frozen RANS simulation (dashed lines) for Case A: GABLS1	83
6.9	Planar-averaged profiles of the temperature, velocity and TKE for Case A: GABLS1 simulations with one correction term modelled, and the others frozen.	84
6.10	Comparison of TKE profiles for baseline RANS simulations of Case B: Kokee SBL with different values for C_μ and $C_{\epsilon 1}$	85
6.11	Comparison of stream-wise velocity profiles for baseline RANS simulations of Case B: Kokee SBL with different values for C_μ and $C_{\epsilon 1}$	86
6.12	Profiles of the z-component of the turbulent heat flux behind the rotor for RANS simulations of Case B: Kokee SBL, with full THF correction implemented (blue), only z-component of THF correction (orange) and without THF correction (green). All simulations implemented the optimal, frozen turbulence anisotropy and TKE production corrections.	87
6.13	Profiles of the temperature behind the rotor for RANS simulations of Case B: Kokee SBL, with full THF correction implemented (blue), only z-component of THF correction (orange) and without THF correction (green). All simulations implemented the optimal, frozen turbulence anisotropy and TKE production corrections.	87
6.14	Profiles of the turbulence kinetic energy behind the rotor for RANS simulations of Case B: Kokee SBL, with full THF correction implemented (blue), only z-component of THF correction (orange) and without THF correction (green). All simulations implemented the optimal, frozen turbulence anisotropy and TKE production corrections.	88
6.15	Profiles of the production of turbulence kinetic energy due to the anisotropy correction b_{ij}^A behind the rotor for RANS simulations of Case B: Kokee SBL. Different simulations implemented different models for the anisotropy correction b_{ij}^A	89
6.16	Profiles of the horizontal velocity behind the rotor for RANS simulations of Case B: Kokee SBL. Different simulations implemented different models for the anisotropy correction b_{ij}^A	90
6.17	Profiles of the production of TKE correction \mathcal{R} behind the rotor for RANS simulations of Case B: Kokee SBL. Different simulations implemented different models for the TKE production correction \mathcal{R}	91
6.18	Profiles of the production of TKE correction behind the rotor for RANS simulations of Case B: Kokee SBL. Different simulations implemented different models for the TKE production correction \mathcal{R}	91
6.19	Profiles of the z-component of the THF correction q_z^A behind the rotor for RANS simulations of Case B: Kokee SBL. Different simulations implemented different models for the THF correction q_j^A	92
6.20	Profiles of the horizontal velocity behind the rotor for RANS simulations of Case B: Kokee SBL. Different simulations implemented different models for the THF correction q_j^A	93
6.21	Comparison of TKE profiles behind the rotor between the LES data, the baseline simulation, the simulation with optimal, frozen corrections and the simulation with implemented models for Case B: Kokee SBL.	94
6.22	Comparison of vertical slices of TKE at the location of the rotor between the LES data, the baseline simulation and the simulation with implemented models for Case B: Kokee SBL. The rotor is represented by the black line and all slices are plotted with the same colour scale for better comparison.	94

6.23	Comparison of stream-wise velocity profiles behind the rotor between the LES data, the baseline simulation, the simulation with optimal, frozen corrections and the simulation with implemented models for Case B: Kokee SBL.	95
6.24	Comparison of horizontal slices of stream-wise velocity at hub-height between the LES data, the baseline simulation and the simulation with implemented models for Case B: Kokee SBL. The rotor is represented by the black line and all slices are plotted with the same colour scale for better comparison.	96
6.25	Comparison of the TKE production due to the turbulence anisotropy correction, b_{ij}^{Δ} , for the optimal, predicted and modelled correction term for Case B: Kokee SBL.	96
6.26	Comparison of the TKE production correction, \mathcal{R} , for the optimal, predicted and modelled correction term for Case B: Kokee SBL.	97
6.27	Comparison of the THF correction, \mathcal{R} , for the optimal, predicted and modelled correction term for Case B: Kokee SBL.	97
6.28	Profiles of different TKE production terms from a RANS simulation with implemented models (solid) and from the LES data (dashed) for Case B: Kokee SBL.	98
6.29	TKE profiles for simulations of Case B: Kokee SBL with different configurations of correction terms modelled, all the other correction terms are kept constant at their optimal, frozen values.	99
A.1	Mutual Information between second invariant of anisotropy correction and invariants for Case A: GABLS1	114
A.2	Mutual Information between second invariant of anisotropy correction and invariants for Case B: Kokee SBL	115
A.3	Mutual Information between TKE production correction and invariants for Case A: GABLS1	116
A.4	Mutual Information between TKE production correction and invariants for Case B: Kokee SBL	117
A.5	Mutual Information between z-component of turbulent heat flux correction and invariants for Case A: GABLS1	118
A.6	Mutual Information between z-component of turbulent heat flux correction and invariants for Case B: Kokee SBL	119
B.1	Terms in the generated correction models for the anisotropy correction b_{ij}^{Δ} for Case A: GABLS1. The colours of the squares indicate the relative size of the coefficients, the blue dots indicate the mean-squared error and the yellow diamonds the maximum squared error.	122
B.2	Terms in the generated correction models for the anisotropy correction b_{ij}^{Δ} for Case B: Kokee SBL. The colours of the squares indicate the relative size of the coefficients, the blue dots indicate the mean-squared error and the yellow diamonds the maximum squared error.	123
B.3	Terms in the generated correction models for the TKE production correction \mathcal{R} for Case A: GABLS1. The colours of the squares indicate the relative size of the coefficients, the blue dots indicate the mean-squared error and the yellow diamonds the maximum squared error.	124
B.4	Terms in the generated correction models for the TKE production correction \mathcal{R} for Case B: Kokee SBL. The colours of the squares indicate the relative size of the coefficients, the blue dots indicate the mean-squared error and the yellow diamonds the maximum squared error.	125
B.5	Terms in the generated correction models for the THF correction q_j^{Δ} for Case A: GABLS1. The colours of the squares indicate the relative size of the coefficients, the blue dots indicate the mean-squared error and the yellow diamonds the maximum squared error.	126
B.6	Terms in the generated correction models for the THF correction q_j^{Δ} for Case B: Kokee SBL. The colours of the squares indicate the relative size of the coefficients, the blue dots indicate the mean-squared error and the yellow diamonds the maximum squared error.	127
C.1	Comparison of temperature profiles for baseline RANS simulations of Case B: Kokee SBL with different values for C_{μ} and $C_{\epsilon 1}$	129

C.2	Profiles of the z-component of the turbulent heat flux behind the rotor for RANS simulations of Case B: Kokee SBL, with full THF correction implemented (blue), only z-component of THF correction (orange) and without THF correction (green). All simulations implemented the optimal, frozen turbulence anisotropy and TKE production corrections.	130
C.3	Profiles of the z-component of the turbulent heat flux behind the rotor for RANS simulations of Case B: Kokee SBL, with full THF correction implemented (blue), only z-component of THF correction (orange) and without THF correction (green). All simulations implemented the optimal, frozen turbulence anisotropy and TKE production corrections.	130
C.4	Profiles of the horizontal velocity behind the rotor for RANS simulations of Case B: Kokee SBL, with full THF correction implemented (blue), only z-component of THF correction (orange) and without THF correction (green). All simulations implemented the optimal, frozen turbulence anisotropy and TKE production corrections.	131
C.5	Profiles of the temperature behind the rotor for RANS simulations of Case B: Kokee SBL. Different simulations implemented different models for the anisotropy correction b_{ij}^{Δ}	132
C.6	Profiles of the turbulence kinetic energy behind the rotor for RANS simulations of Case B: Kokee SBL. Different simulations implemented different models for the anisotropy correction b_{ij}^{Δ}	132
C.7	Profiles of the temperature behind the rotor for RANS simulations of Case B: Kokee SBL. Different simulations implemented different models for the TKE Production correction \mathcal{R}	133
C.8	Profiles of the streamwise velocity behind the rotor for RANS simulations of Case B: Kokee SBL. Different simulations implemented different models for the TKE Production correction \mathcal{R}	133
C.9	Profiles of the x-component of the THF correction q_x^{Δ} behind the rotor for RANS simulations of Case B: Kokee SBL. Different simulations implemented different models for the THF correction q_j^{Δ}	134
C.10	Profiles of the y-component of the THF correction q_y^{Δ} behind the rotor for RANS simulations of Case B: Kokee SBL. Different simulations implemented different models for the THF correction q_j^{Δ}	134
C.11	Profiles of the temperature behind the rotor for RANS simulations of Case B: Kokee SBL. Different simulations implemented different models for the THF correction q_j^{Δ}	135
C.12	Profiles of the TKE behind the rotor for RANS simulations of Case B: Kokee SBL. Different simulations implemented different models for the THF correction q_j^{Δ}	135
C.13	Comparison of horizontal slices of TKE at hub-height between the LES data, the baseline simulation and the simulation with implemented models for Case B: Kokee SBL. The rotor is represented by the black line and all slices are plotted with the same colour scale for better comparison.	136
C.14	Comparison of vertical slices of stream-wise velocity at the location of the rotor between the LES data, the baseline simulation and the simulation with implemented models for Case B: Kokee SBL. The rotor is represented by the black line and all slices are plotted with the same colour scale for better comparison.	136
C.15	Comparison of vertical temperature slices at the location of the rotor between the LES data, the baseline simulation and the simulation with implemented models for Case B: Kokee SBL. The rotor is represented by the black line and all slices are plotted with the same colour scale for better comparison.	137
C.16	Comparison of horizontal temperature slices at hub-height between the LES data, the baseline simulation and the simulation with implemented models for Case B: Kokee SBL. The rotor is represented by the black line and all slices are plotted with the same colour scale for better comparison.	137
C.17	Breakdown of TKE production in the simulation with implemented models for Case B: Kokee SBL. Colour scales are scaled for better comparison.	138
C.18	Breakdown of TKE production in the simulation with implemented models for Case B: Kokee SBL. Colour scales are not scaled	138

C.19 Comparison of temperature profiles behind the rotor between the LES data, the baseline simulation, the simulation with optimal, frozen corrections and the simulation with implemented models for Case B: Kokee SBL.	139
C.20 Temperature profiles for simulations of Case B: Kokee SBL with different configurations of correction terms modelled, all the other correction terms are kept constant at their optimal, frozen values.	140
C.21 Stream-wise velocity profiles for simulations of Case B: Kokee SBL with different configurations of correction terms modelled, all the other correction terms are kept constant at their optimal, frozen values.	140

List of Tables

2.1	Set of tensors on which the invariants used in the regression of the correction terms are based.	27
2.2	Invariant bases, number of symmetric and anti-symmetric tensors for each invariant are indicated by n_s and n_a , respectively. The invariant bases are the trace of the tensors listed. The asterisk on a invariant bases indicates that also the cyclic permutation of the anti-symmetric tensors are included (Steiner et al., 2022).	27
2.3	Physics interpreted flow features. For each feature the physical description is denoted including the raw feature with its normalisation. The features that are not Galilean invariant are marked with a †(Steiner et al., 2022).	28
3.1	General parameters used in simulating the GABLS1 case described in Beare et al. (2006).	31
3.2	Finite volume discretization schemes used in LES solver.	33
3.3	Blending parameters used for blending discretization schemes of the convection terms.	33
3.4	Boundary conditions for the LES simulation of Case A: GABLS1.	34
3.5	General parameters used in simulating the wind turbine in SBL case by Kokee (2021).	43
3.6	Finite volume discretization schemes used in LES solver by Kokee (2021).	44
3.7	Boundary conditions for the LES simulation of the successor simulation of case B: Kokee SBL.	45
3.8	Time-averaged parameters for the turbine in the Kokee SBL simulation from Kokee (2021).	45
3.9	Time-averaged results for the LES of Case B: Kokee SBL (Kokee, 2021).	45
4.1	Coefficients and constants used in the turbulence model from Koblitz (2013).	48
4.2	Coefficients and constants used in the baseline turbulence model used by Kokee (2021) for Case B: Kokee SBL.	49
4.3	Finite volume discretization schemes used in the k-corrective frozen simulations.	50
4.4	Boundary conditions for the k-corrective frozen RANS simulations.	51
4.5	Coefficients used to match LES and RANS wall friction and reference values from literature.	52
5.1	Set of tensors on which the invariants used in the regression of the correction terms are based.	59
5.2	Invariant bases. The number of symmetric and anti-symmetric tensors for each invariant are indicated by n_s and n_a , respectively. The invariant bases are the trace of the tensors listed. The asterisk on a invariant bases indicates that also the cyclic permutation of the anti-symmetric tensors are included (Steiner et al., 2022).	59
5.3	Physics interpreted flow features. For each feature the physical description is denoted including the raw feature with its normalisation. The features that are not Galilean invariant are marked with a †(Steiner et al., 2022).	60
5.4	Selected basis tensors, invariants and physical features for forming library used to regress models for anisotropy correction.	62
5.5	Selected basis tensors, invariants and physical features for forming library used to regress models for TKE production correction	63
5.6	Selected basis tensors, invariants and physical features for forming library used to regress models for the THF correction	64
6.1	Boundary conditions for the RANS simulations with implemented models.	76

Acronyms

ABL	Atmospheric Boundary Layer
BEM	Blade Element Momentum Theory
CFD	Computational Fluid Dynamics
DNS	Direct Numerical Simulation
GDH	Gradient-Diffusion Hypothesis
LES	Large Eddy Simulation
MOST	Monin-Obukhov Similarity Theory
PDE	Partial Differential Equation
SGS	Subgrid-scale
SpaRTA	Sparse Regression of Turbulence stress Anisotropy
THF	Turbulent Heat Flux
TKE	Turbulence Kinetic Energy
RANS	Reynolds-Averaged Navier-Stokes
URANS	Unsteady Reynolds-Averaged Navier-Stokes

Nomenclature

Latin Symbols

A_{cell}	Surface area of mesh cell	m^2
\mathbf{A}_k, A_{ij}^k	Non-dimensionalized cross-product of identity matrix and TKE gradient	-
\mathbf{A}_p, A_{ij}^p	Non-dimensionalized cross-product of identity matrix and pressure gradient	-
a_{ij}	Anisotropic part of the Reynolds stress tensor	$kg\ m^{-1}\ s^2$
B	Source/sink term of buoyant production of turbulence	$m^2\ s^{-3}$
b_{ij}	Non-dimensionalized anisotropic part of the Reynolds stress tensor	-
b_{ij}^Δ	Correction of the turbulence anisotropy	-
C_d	2D drag coefficient	-
C_l	2D lift coefficient	-
C_R	Rotta constant	-
C_T	Rotor thrust coefficient	-
c	Rotor chord length	m
D_{ij}^t	Anisotropic turbulent diffusivity tensor	$m^2\ s^{-1}$
E	Total energy	$kg\ m^2\ s^{-2}$
\mathbf{e}_D	Unit vector in direction of drag	-
\mathbf{e}_L	Unit vector in direction of lift	-
F_β	Blending function	-
F_{cell}	Actuator forcing in mesh cell	$kg\ m\ s^{-2}$
\mathbf{f}	Body force term	$kg\ s^{-2}$
f_i	Body forces in direction i	$kg\ m\ s^{-2}$
g	Gravitational acceleration	$m\ s^{-2}$
$g^{(n)}$	Coefficient functions	-
\mathbb{I}	Identity matrix	-
k	Turbulence kinetic energy	$m^2\ s^{-2}$
L	Characteristic length scale	m
L_b	Buoyancy length scale	m
l_m	Local mixing length	m
L_O	Obukhov length scale	m
L_{Oz}	Ozmidov length scale	m
maxse	Max squared error	-
MI	Mutual Information	-
mse	Mean squared error	-
N	Brunt-Väisälä frequency	s^{-1}
N	Number of samples	-
N_L	Number of grid points in one dimension	-
N_T	Number of time steps	-
n_x	Number of samples in x within maximum normal distance to nearest neighbour	-
\mathcal{P}_k	Production term of TKE	$m^2\ s^{-3}$
Pr	Prandtl number	-
Pr_t	Turbulent Prandtl number	-
p	Pressure	$kg\ m^{-1}\ s^{-2}$
p_{rgh}	Pressure without hydrostatic pressure	$kg\ m^{-1}\ s^{-2}$
p_X	Marginal probability density function of random variable X	-
$p_{X,Y}$	Joint probability density function of random variables X and Y	-
P	Earth's rotational period	s
q_j	Turbulent heat flux	$K\ m\ s^{-1}$

q_j^Δ	Turbulent heat flux correction	K m s^{-1}
q_j^{SGS}	Sub-grid scale heat-flux	K m s^{-1}
q_w	Kinematic surface heat flux	K m s^{-1}
\mathcal{R}	Correction of TKE production	$\text{m}^2 \text{s}^{-3}$
Re	Reynolds number	-
R_{ij}	Reynolds stress tensor	$\text{kg m}^{-1} \text{s}^2$
Ri_f	Flux Richardson number	-
Ri_g	Gradient Richardson number	-
\mathbf{S}, S_{ij}	Mean strain rate tensor	s^{-1}
S_i^m	Momentum source term	m s^{-2}
T	Characteristic timescale	s
$T_{ij}^{(n)}$	Tensor basis function	s^{-1}
t	Time	s
U	Characteristic velocity scale	m s^{-1}
u_i	Velocity in direction i	m s^{-1}
u_K	Kolmogorov velocity scale	m s^{-1}
u_*	Friction velocity	m s^{-1}
V_{ij}	Matrix of which the columns are the eigenvectors of a tensor	-
V_{rel}	Relative velocity	m s^{-1}
\mathbf{x}	Location vector	m
x_i	Cartesian coordinate	m
z_0	Roughness length	m

Greek Symbols

α	Thermal diffusivity	$\text{m}^2 \text{s}^{-1}$
α	Blending parameter	-
α_t	Turbulent thermal diffusivity	$\text{m}^2 \text{s}^{-1}$
γ_i	Eigenvalues of the anisotropy tensor	-
Δ_i	Grid resolution in direction i	m
δ_{ij}	Kronecker delta	-
ϵ	Dissipation rate	$\text{m}^2 \text{s}^{-3}$
η_K	Kolmogorov length scale	m
θ	Potential temperature	K
$\hat{\theta}_w$	Surface Heating Rate	K h^{-1}
κ	Von Kármán constant	-
Λ	Local Obukhov length scale	m
λ_i	Invariants	-
ν	Kinematic Viscosity	$\text{m}^2 \text{s}^{-1}$
ν_T	Eddy Viscosity	$\text{m}^2 \text{s}^{-1}$
Π	Second invariant of second order tensor	-
ρ	Density	kg m^{-3}
ρ_m	Mixing parameter	-
σ	Local shear parameter	-
τ_{ij}	Stress tensor	$\text{kg m}^{-1} \text{s}^{-2}$
τ_{ij}^{SGS}	Sub-grid scale stress tensor	$\text{m}^2 \text{s}^{-2}$
τ_K	Kolmogorov time scale	s
Φ_{ij}	Diagonal matrix with eigenvalues on diagonal	-
ϕ	Latitude	°
ϕ_i	Eigenvalues of the Reynolds stress	-
ψ	Digamma function	-
Ω_E	Earth's angular velocity	rad s^{-1}
$\mathbf{\Omega}, \Omega_{ij}$	Mean rotation rate tensor	s^{-1}

Introduction

Much of current research endeavours are part of the push for a more sustainable future in an attempt to limit global warming. Potentially, a significant part of the energy demands in the future could be fulfilled by wind energy. As space becomes more and more scarce, this wind energy demand is increasingly being met by offshore wind farms. In 2019 a record share of 10 % of newly installed wind capacity is accounted for by offshore wind farms (GWEC, 2019). Moreover, the Dutch government envisions a growth of offshore wind energy capacity towards 11.5 GW by 2030 (Wiebes, 2018).

In order to support this development, it is paramount that accurate simulation tools are available to industry. These simulation tools help make more informed design choices with respect to maximising yield of wind farms, optimum control strategies and making lifetime and maintenance predictions based on loading simulation. Currently, industry is mostly reliant on low-fidelity blade element momentum methods. These are the preferred methods of use as they give somewhat accurate results at very low computational cost. However, the shortcomings of these methods become increasingly apparent, especially in situations where wake-interaction is important such as wind farms. Wake losses in wind farms can be as high as 10 % to 20 % according to Barthelmie et al. (2007). Combined with the rapid growth in computational ability, it is expected that industry will move towards more computationally intensive Navier-Stokes methods, provided that the increase in accuracy is worth it.

The most used Navier-Stokes based method for wind farm simulation is LES, where the largest scales of the turbulence are resolved and the effect of the smaller, more isotropic scales are modelled. However, the computational demands for this method are relatively high, so it is more probable that industry will move towards less computationally intensive RANS methods where the Navier-Stokes equations are averaged and all scales of turbulence are modelled.

RANS simulations do need to provide a sufficient increase in accuracy to justify the additional computational cost. However, Réthoré (2009) showed that the most used RANS-model in relation to wind farms, $k - \epsilon$, has crippling shortcomings. It over-predicts the eddy viscosity in the near wake, leading to an over-prediction of wake recovery and fails to model the anisotropy of the turbulence quantities. The increasing computational capabilities and availability of high-fidelity data also supports another development. Recently a lot of effort is put in using data-driven machine learning methods to improve turbulence models. Notably, Ling et al. (2016a) used a deep neural network to develop new models for the anisotropy field of the turbulent stress. Within the Aerospace Engineering faculty of the TU Delft Schmelzer et al. (2020) introduced the SpaRTA framework, which uses k-corrective frozen-RANS simulation to extract the optimal correction fields. Then, sparse symbolic regression is applied in order to train simple, easy to interpret, algebraic models for two turbulence model correction terms: a correction term of the turbulence anisotropy and a correction term of the TKE production. This framework was applied to moderate Reynolds number wind turbine flows in neutral conditions by Steiner et al. (2020). It was further improved upon by expanding the library of features in Steiner et al. (2022) and Steiner et al. (2021) introduced a classifier which differentiated between the wake and the outside flow.

The obvious next step in the development of the SpaRTA methodology is to expand it to non-neutral conditions. Therefore, the main research objective of this thesis is:

To reduce the $k - \epsilon$ turbulence model and gradient-diffusion hypothesis scalar-flux model uncertainties in stably-stratified wind turbine wake applications by extending the SpaRTA methodology to include the effects of stratification and applying it to stably-stratified cases.

In order to achieve the main objective, several sub-objectives are formulated:

- SO1.** Generate or obtain ground-truth LES reference data from the open-source SOWFA-6 toolbox for OpenFOAM.
- SO2.** Determine optimal turbulence model form corrections by extending the k-corrective frozen-RANS approach to include a correction for the gradient-diffusion hypothesis model for the turbulent heat flux.
- SO3.** Train simple algebraic models for the respective correction terms using the sparse regression techniques from SpaRTA.
- SO4.** Implement the trained correction models in OpenFOAM to assess performance compared to the baseline $k - \epsilon$ model.

These objectives have to be fulfilled in order to answer the main research question of this thesis:

To what extent can the SpaRTA methodology extended to include stratification effects improve RANS simulations of wind farms in stable atmospheric boundary layer conditions?

To provide an answer for the main research question, it is supported by the following sub-questions (SQ):

- SQ1.** How does the extension of the SpaRTA methodology to also include a model form correction of the turbulent heat flux influence the corrected simulations?
- SQ2.** How do the original model form corrections of the SpaRTA methodology influence the performance of the corrected simulations?
- SQ3.** What is the best selection criterion for selecting correction models after regression: mean squared error, max squared error or complexity?
- SQ4.** What are the main factors holding back the performance of the corrected simulations of the extended SpaRTA methodology?

This thesis starts answering the research questions by supplying a solid theoretical foundation of the work undertaken in [Chapter 2](#). After the fundamentals and state-of-the-art of current wind-farm simulation and data-driven improvement methods of turbulence modelling are described, the ground-truth data of the two cases used in this thesis are detailed in [Chapter 3](#). Then, [Chapter 4](#) describes the computation of the optimal correction fields for the SpaRTA methodology extended to include stable stratification and applied to the two reference cases. These optimal correction fields are then used to train correction models in [Chapter 5](#). [Chapter 6](#) implements these trained models in RANS simulations and compares them to baseline simulations in order to assess the performance. Lastly, a reflection on the research questions and their answers, as well as recommendations for future work is given in [Chapter 7](#).

2

Background of Wind Farm Simulation and Machine Learning

This chapter describes the fundamentals on which the work in this report is based. Started is with the basics of Computational Fluid Dynamics (CFD), after which atmospheric boundary layers (ABLs), wind farms and their influence on CFD are detailed. Lastly, machine learning in wind farm simulation is investigated.

2.1. Overview of Computational Fluid Dynamics

In order to describe how machine learning can be used to improve simulations of wind farms, first the basics of aerodynamic simulation have to be covered. Therefore, this section gives an overview of the fundamentals of CFD.

2.1.1. Governing Equations of CFD

Turbulent fluid flow is chaotic in nature and characterised by a large range of scales, from tiny to very large scales. The physics of a Newtonian fluid in a Cartesian coordinate system are captured in a system of equations which consists of conservation of mass ((2.1)), conservation of momentum in three directions ((2.2)) and conservation of energy ((2.3)). In these equations ρ is the density, u_i is the velocity in direction i , p is the pressure, τ_{ij} is the stress tensor, f_i are body forces, E is the total energy and q_i denotes the heat conduction.

$$\frac{\partial \rho}{\partial t} + \frac{\partial(\rho u_i)}{\partial x_i} = 0 \quad (2.1)$$

$$\frac{\partial(\rho u_j)}{\partial t} + \frac{\partial(\rho u_i u_j)}{\partial x_i} = -\frac{\partial p}{\partial x_j} + \frac{\partial \tau_{ij}}{\partial x_i} + \rho f_j \quad (2.2)$$

$$\frac{\partial(\rho E)}{\partial t} + \frac{\partial(u_i \rho E)}{\partial x_i} = -\frac{\partial u_i p}{\partial x_i} + \frac{\partial u_i \tau_{ij}}{\partial x_i} - \frac{\partial q_i}{\partial x_i} + u_i \rho f_i \quad (2.3)$$

The above equations are often simplified by assuming incompressible flow and no body forces. This means that energy conservation follows from momentum conservation and is no longer needed. Also, the continuity and momentum equations are simplified as displayed in (2.4) and (2.5). In these simplified equations ν is the kinematic viscosity. These equations are often referred to as the Navier-Stokes equations.

$$\frac{\partial u_i}{\partial x_i} = 0 \quad (2.4)$$

$$\frac{\partial u_i}{\partial t} + \frac{\partial u_i u_j}{\partial x_j} = -\frac{1}{\rho} \frac{\partial p}{\partial x_i} + \nu \frac{\partial^2 u_i}{\partial x_j^2} \quad (2.5)$$

Aside from these equations, conservation can also be applied for a passive scalar, θ , as displayed in (2.6) with no sources or sinks and α the diffusivity (Pope, 2000).

$$\frac{\partial \theta}{\partial t} + \frac{\partial (u_i \theta)}{\partial x_i} = \frac{\partial}{\partial x_j} \left(\alpha \frac{\partial \theta}{\partial x_j} \right) \quad (2.6)$$

In the context of wind farm simulation this passive scalar is usually the potential temperature. However, the passive scalar can also be a mass density of a non-reacting trace constituent in a fluid for example (Wyngaard, 2010).

2.1.2. Length Scales of Turbulence

The Navier-Stokes equations can theoretically be discretised and all turbulence scales can be resolved, this is called a Direct Numerical Simulation (DNS). However, in order to do so, the mesh has to be fine enough to be able to simulate all the turbulent scales. The Reynolds number is used to characterise a flow and is defined as the ratio between inertial and viscous forces. It is computed by using (2.7) where L and U are a flow characteristic length and velocity scale respectively.

$$\text{Re} = \frac{LU}{\nu} \quad (2.7)$$

Turbulence consists of eddies. The largest eddies have characteristic length, velocity and time scales comparable to the characteristic scales of the flow itself. These largest eddies break down into smaller eddies through the energy cascade. These smaller eddies also break down into smaller eddies, until the eddies become so small that the turbulence kinetic energy dissipates due to molecular viscosity. These smallest scales are called the Kolmogorov scales. The Kolmogorov scales of length, velocity and time are related to the kinematic viscosity and the dissipation rate by (2.8), (2.9) and (2.10) respectively. These expressions are based on dimensional arguments (Pope, 2000).

$$\eta_K = \left(\frac{\nu^3}{\epsilon} \right)^{1/4} \quad (2.8)$$

$$u_K = (\nu \epsilon)^{1/4} \quad (2.9)$$

$$\tau_K = \sqrt{\frac{\nu}{\epsilon}} \quad (2.10)$$

When it is assumed that the dissipation rate is equal to the production rate, the dissipation rate is related to the characteristic length and velocity scales by (2.11).

$$\epsilon \sim \frac{U^3}{L} \quad (2.11)$$

Then it can be derived that the total number of grid points in one direction needed to capture all the turbulent length scales, from the largest to the very smallest relates to the Reynolds number through (2.12).

$$N_L \sim \frac{L}{\eta_K} \sim \text{Re}^{3/4} \quad (2.12)$$

The same is done for the number of timesteps needed in (2.13).

$$N_T \sim \frac{T}{\tau_K} \sim \text{Re}^{1/2} \quad (2.13)$$

This means the total amount of computations needed (grid points in three dimensions times the amount of time steps) scales with $\text{Re}^{11/4}$. Seeing that simulations of wind farms often cover circumstances with Reynolds numbers above 10^8 , it is clear that DNS is not feasible for industrial applications. Broadly speaking, two different ways to solve this problem are used: Large eddy simulation (LES) and Reynolds-averaged Navier-Stokes (RANS). These two methods are discussed in more detail in the next two sections.

2.1.3. Large Eddy Simulation

The kinetic energy of the turbulence is divided over a large range of length scales. LES is based on the assumption that the smaller scales of the turbulence have a more universal nature. Whereas the large scales are more heavily influenced by the boundary conditions and are thus more case dependent. Therefore, in LES, the larger scales of the velocity field are resolved directly while the effect of the smaller eddies is modelled. This is done by applying a spatial filter operation over the parameter fields, which splits up the variables in a resolvable and subgrid-scale part. This decomposition for the velocity is given in (2.14).

$$u_i(\mathbf{x}, t) = \tilde{u}_i(\mathbf{x}) + u_i''(\mathbf{x}, t) \quad (2.14)$$

After the filter is applied to the Navier-Stokes equations displayed in (2.4) to (2.6), the LES equations are obtained. These filtered Navier-Stokes equations for continuity, momentum and a passive scalar are displayed in (2.15), (2.16) and (2.17) respectively.

$$\frac{\partial \tilde{u}_i}{\partial x_i} = 0 \quad (2.15)$$

$$\frac{\partial \tilde{u}_i}{\partial t} + \frac{\partial \tilde{u}_i \tilde{u}_j}{\partial x_j} = -\frac{1}{\rho} \frac{\partial \tilde{p}}{\partial x_i} + \frac{\partial}{\partial x_j} \left(\nu \left(\frac{\partial \tilde{u}_i}{\partial x_j} + \frac{\partial \tilde{u}_j}{\partial x_i} \right) \right) - \frac{\partial \tau_{ij}^{SGS}}{\partial x_j} \quad (2.16)$$

$$\frac{\partial \tilde{\theta}}{\partial t} + \frac{\partial \tilde{u}_j \tilde{\theta}}{\partial x_j} = \alpha \frac{\partial^2 \tilde{\theta}}{\partial x_j \partial x_j} - \frac{\partial q_j^{SGS}}{\partial x_j} \quad (2.17)$$

In (2.16), τ_{ij}^{SGS} represents the sub-grid scale stress tensor and is equal to $\overline{u_i u_j} - \tilde{u}_i \tilde{u}_j$. This term requires a closure model to model the influence of the "sub-grid scale" eddies on the resolved larger scales. The Smagorinsky model is a common model used to do this and links the sub-grid scale stress tensor to a sub-grid scale viscosity. The same approach is taken by the one equation eddy viscosity model which differs in the fact that a transport equation is solved for the sub-grid scale TKE Pope (2000).

In the passive scalar equation ((2.17)) closure is needed for the sub-grid scale scalar flux $q_j^{SGS} = \overline{u_j \theta}$. This is usually accomplished using the gradient-diffusion hypothesis, which will be described in more detail in Subsection 2.2.3.

2.1.4. Reynolds-Averaged Navier-Stokes

RANS attempts to ease the computational requirements demanded by DNS and LES by solving for the mean flow quantities. This is done by splitting the quantities into a mean ($\bar{\cdot}$) and a fluctuating (\cdot') part. This decomposition for the velocity is given in (2.18). The approach is the same for the other parameters.

$$u_i(\mathbf{x}, t) = \bar{u}_i(\mathbf{x}) + u_i'(\mathbf{x}, t) \quad (2.18)$$

The mean is obtained by taking the temporal average in (2.19).

$$\bar{u}_i = \frac{1}{T} \int_0^T u_i(\mathbf{x}, t) dt \quad (2.19)$$

The Reynolds-averaged Navier-Stokes equations are obtained by substituting the decomposed velocity and pressure in the conservation equations and applying Reynolds averaging. Some important features of this Reynolds averaging operator are that the mean of a fluctuating component is 0, the mean of two fluctuating components multiplied is nonzero and the mean of the mean is just the mean itself. The resulting incompressible Reynolds Averaged conservation equations for mass and momentum are displayed in (2.20) and (2.21).

$$\frac{\partial \bar{u}_i}{\partial x_i} = 0 \quad (2.20)$$

$$\frac{\partial \bar{u}_i}{\partial t} + \frac{\partial \bar{u}_i \bar{u}_j}{\partial x_j} = -\frac{1}{\rho} \frac{\partial \bar{p}}{\partial x_i} + \frac{\partial}{\partial x_j} \left(\nu \left(\frac{\partial \bar{u}_i}{\partial x_j} + \frac{\partial \bar{u}_j}{\partial x_i} \right) \right) - \frac{\partial \overline{u_i' u_j'}}{\partial x_j} \quad (2.21)$$

When comparing the Reynolds-averaged equations to the original equations it is visible that the averaging operation introduced a new term: the Reynolds flux or Reynolds stress $R_{ij} = \overline{u'_i u'_j}$. This Reynolds stress represents the momentum transfer through turbulent fluctuations and is often decomposed in an isotropic and anisotropic part as displayed in (2.22). Where k is the turbulence kinetic energy which is defined as $k \equiv \frac{1}{2} \overline{u'_i u'_i}$ and δ_{ij} is the Kronecker delta.

$$R_{ij} = \frac{2}{3} k \delta_{ij} + a_{ij} \quad (2.22)$$

The anisotropic part of the Reynolds stress is non-dimensionalised as displayed in (2.23) to obtain b_{ij} which is referred to as the anisotropy tensor (Pope, 2000).

$$b_{ij} = \frac{R_{ij}}{2k} - \frac{1}{3} \delta_{ij} = \frac{a_{ij}}{2k} \quad (2.23)$$

The modelling of the Reynolds stress is a topic of much research. Generally the models can be divided in a few different categories which are detailed in Subsection 2.1.5. Aside from the Navier-stokes equations, Reynolds averaging is also applied to the passive scalar transport equation. This yields the equation displayed in (2.24) (Wyngaard, 2010).

$$\frac{\partial \bar{\theta}}{\partial t} + \frac{\partial \overline{u_i \theta}}{\partial x_i} = \alpha \frac{\partial^2 \bar{\theta}}{\partial x_i \partial x_i} - \frac{\partial \overline{u'_i \theta'}}{\partial x_i} \quad (2.24)$$

Again, a new term is introduced due to the Reynolds averaging operation: $\overline{u'_i \theta'}$. This term is called the turbulence scalar flux and has to be modelled, like the Reynolds stress.

2.1.5. Turbulence Modelling

As mentioned in Subsection 2.1.4, when considering the Reynolds-averaged Navier-Stokes equations and the corresponding scalar transport equation, there are two parameters which have to be modelled: the Reynolds stress and the turbulence scalar flux.

2.1.5.1. Reynolds Stress Modelling

There are two main ways in which the turbulence is modelled in RANS: eddy viscosity methods and Reynolds stress methods. These are both covered in this section.

Eddy Viscosity Models

The approach, which is applied the most, relies on the Boussinesq hypothesis as introduced in Boussinesq (1877). This Boussinesq hypothesis relates the Reynolds stress tensor to the product of the mean strain-rate tensor and an "eddy" viscosity, analogously to laminar flow, as displayed in (2.25) (Wilcox, 2006). The latter term in this equation is absorbed into the pressure term.

$$\overline{u'_i u'_j} = -\nu_T \left(\frac{\partial \overline{u_i}}{\partial x_j} + \frac{\partial \overline{u_j}}{\partial x_i} \right) + \frac{2}{3} k \delta_{ij} \quad (2.25)$$

This leads to a modified version of the RANS-equations as displayed in (2.26).

$$\frac{\partial \overline{u_i}}{\partial t} + \overline{u_j} \frac{\partial \overline{u_i u_j}}{\partial x_j} = -\frac{\partial}{\partial x_i} \left(\bar{p} + \frac{2}{3} k \right) + \frac{\partial}{\partial x_j} \left((\nu + \nu_T) \left(\frac{\partial \overline{u_i}}{\partial x_j} + \frac{\partial \overline{u_j}}{\partial x_i} \right) \right) \quad (2.26)$$

Modelling the effect of turbulence as added viscosity is very useful as an engineering method, seeing that the computational cost only weakly depends on the Reynolds number (Sanderse et al., 2011). However, eddies are not molecules, which means that the physical basis for this assumption is weak. Furthermore, the eddy viscosity is a field quantity and not a property of the fluid and DNS simulations performed by Schmitt (2007) do not show a clear correlation between the Reynolds stress and the mean strain-rate. This means that in many situations the Boussinesq hypothesis is not valid. Especially in flows with sudden changes in mean strain-rate, flows over curved surfaces, flows in ducts with secondary motions, flows in rotating fluids and three-dimensional flows (Wilcox, 2006). Nonetheless, the Boussinesq hypothesis is the basis of the most widely used turbulence models in industry.

The eddy viscosity models can be further divided by the way in which the eddy viscosity is computed. Usually, the models are split based on the number of additional partial differential equations (PDEs) that need to be solved.

Algebraic models The simplest models are algebraic models or zero-equation models. In these models the eddy viscosity is computed based on a characteristic length scale called the mixing length. This is somewhat like the mean free path between molecules in a gas (Wilcox, 2006). Two well known models of this type are the Cebeci-Smith model (Smith and Cebeci, 1967) and the Baldwin-Lomax model (Baldwin and Lomax, 1978). The advantages of these models are the simplicity and ease of implementation. However, these models are very simplified and work well only for the flows for which they have been calibrated according to Wilcox (2006).

One-equation models In order to improve the prediction of turbulent flows Prandtl postulated that the eddy viscosity depends on the turbulence kinetic energy and a length scale (Prandtl and Wieghardt, 1945). This meant a model which solved an additional transport equation for the turbulence kinetic energy. However, the need for a specific length scale for each flow case makes the advantage of this model over algebraic models rather small (Wilcox, 2006). Even so, models based on a postulated equation for the eddy viscosity do not have this problem. Well-known examples of this methodology are the Baldwin-Barth model (Baldwin and Barth, 1991) and the Spalart-Allmaras model (Spalart and Allmaras, 1992). The advantages of these models are the low computational cost and high numerical stability due to only solving one additional PDE (Wilcox, 2006).

Two-equation models The two-equation models are amongst the models which are most widely used. These models generally solve an equation for the turbulence kinetic energy, k and a second quantity, for example the specific turbulence dissipation rate ω or the turbulence dissipation rate ϵ . These quantities are then used to compute the eddy viscosity according to (2.27).

$$v_T = C_\mu \frac{k^2}{\epsilon} \text{ or } v_T = \frac{k}{\omega} \quad (2.27)$$

A widely used model is the $k - \epsilon$ model introduced by Jones and Launder (1972) where an equilibrium of turbulence production and dissipation is assumed. The advantages of this model are the low computational cost, due to only solving two additional transport equations, and the good results for external flows. However, the model struggles with flows with strong pressure gradients, stream line curvature and separation (Wilcox, 2006). This model is the best model for simulating the atmospheric boundary layer according to Sanderse et al. (2011), amongst others. The equations for k and ϵ are displayed in (2.28) and (2.29), where $C_{\epsilon 1}$ and $C_{\epsilon 2}$ are coefficients.

$$\frac{\partial k}{\partial t} + \underbrace{\overline{u_j} \frac{\partial k}{\partial x_j}}_{\text{Advection}} = \underbrace{\tau_{ij} \frac{\partial \overline{u_i}}{\partial x_j}}_{\text{Production}} + \underbrace{\frac{\partial}{\partial x_j} \left(\left(\frac{1}{\text{Re}} + \frac{v_T}{\text{Pr}_k} \right) \frac{\partial k}{\partial x_j} \right)}_{\text{Diffusion}} - \underbrace{\epsilon}_{\text{Dissipation}} \quad (2.28)$$

$$\frac{\partial \epsilon}{\partial t} + \underbrace{\overline{u_j} \frac{\partial \epsilon}{\partial x_j}}_{\text{Advection}} = \underbrace{C_{\epsilon 1} \frac{\epsilon}{k} \tau_{ij} \frac{\partial \overline{u_i}}{\partial x_j}}_{\text{Production}} + \underbrace{\frac{\partial}{\partial x_j} \left(\left(\frac{1}{\text{Re}} + \frac{v_T}{\text{Pr}_\epsilon} \right) \frac{\partial \epsilon}{\partial x_j} \right)}_{\text{Diffusion}} - \underbrace{C_{\epsilon 2} \frac{\epsilon}{k} \epsilon}_{\text{Dissipation}} \quad (2.29)$$

The $k - \omega$ model by Wilcox (1988) is also used a lot. This model solves additional transport equations for the turbulence kinetic energy and the specific dissipation rate. When comparing it to the $k - \epsilon$ model, it gives better results for boundary layer flows and for flows with pressure gradients and separation (Wilcox, 2006). The equations for k and ω are displayed in (2.30) and (2.31), where α and β are coefficients.

$$\frac{\partial k}{\partial t} + \underbrace{\overline{u_j} \frac{\partial k}{\partial x_j}}_{\text{Advection}} = \underbrace{\tau_{ij} \frac{\partial \overline{u_i}}{\partial x_j}}_{\text{Production}} + \underbrace{\frac{\partial}{\partial x_j} \left(\left(\frac{1}{\text{Re}} + \frac{v_T}{\text{Pr}_k} \right) \frac{\partial k}{\partial x_j} \right)}_{\text{Diffusion}} - \underbrace{C_D k \omega}_{\text{Dissipation}} \quad (2.30)$$

$$\frac{\partial \omega}{\partial t} + \underbrace{\overline{u_j} \frac{\partial \omega}{\partial x_j}}_{\text{Advection}} = \underbrace{\alpha \frac{\omega}{k} \tau_{ij} \frac{\partial \overline{u_i}}{\partial x_j}}_{\text{Production}} + \underbrace{\frac{\partial}{\partial x_j} \left(\left(\frac{1}{\text{Re}} + \frac{v_T}{\text{Pr}_\epsilon} \right) \frac{\partial \omega}{\partial x_j} \right)}_{\text{Diffusion}} - \underbrace{\beta \omega^2}_{\text{Dissipation}} \quad (2.31)$$

A blend of the $k - \epsilon$ and the $k - \omega$ models leads to the SST model (Menter, 1993) which is better for simulating regions close to wind turbine blades according to Sanderse et al. (2011).

Reynolds Stress Models

Even though the Boussinesq hypothesis has garnered widespread use, it does have some serious shortcomings as previously discussed. Another fundamentally different approach to modelling the Reynolds stress is the Reynolds stress model introduced by [Launder et al. \(1975\)](#). This approach starts from the exact Reynolds stress transport equations and directly solves model transport equations for the different components. This makes it suitable to simulate anisotropic flow, as opposed to the two-equation models. However, a major drawback is the fact that six additional PDEs have to be solved leading to a large increase in computational cost. Furthermore, the Reynolds stress models can suffer from numerical instability ([Sanderse et al., 2011](#)).

2.1.5.2. Turbulence Scalar Flux Modelling

In order to close the scalar transport equation, the turbulence scalar flux is modelled.

Gradient-Diffusion Models

The most commonly used model is similar to the eddy viscosity model and based on the gradient-diffusion hypothesis as displayed in (2.32) ([Combest et al., 2011](#)).

$$\overline{u_i' \theta'} = -\alpha_t \frac{\partial \bar{\theta}}{\partial x_i} \quad (2.32)$$

The turbulent diffusivity α_t is usually computed by dividing the eddy viscosity from the eddy viscosity model with a turbulent Prandtl or Schmidt number, which is defined as a global flow-specific value. The benefit of this model is its simplicity and low computational overhead. However, it is known that the model is inaccurate in flows where the scalar flux is not aligned with the mean scalar gradient, so in flows with high anisotropy ([Combest et al., 2011](#)).

Algebraic Models

A slightly more complex model was introduced by [Batchelor \(1949\)](#) which replaced the turbulent diffusivity in (2.32) with an anisotropic turbulent diffusivity tensor D_{ij}^t . This method is also called generalised gradient-diffusion hypothesis. Different models introduced by [Daly and Harlow \(1970\)](#) and [Fox \(2003\)](#) use slightly different expressions to determine the turbulent diffusivity tensor. However, what they have in common is that in both models the turbulent diffusivity tensor is directly proportional to the Reynolds stresses. These models overcome the issue with gradient diffusion hypothesis of misalignment between the scalar flux and mean scalar gradient ([Combest et al., 2011](#)). [Abe and Suga \(2001\)](#) introduced the even more complex higher order generalised gradient-diffusion hypothesis. However, research by [Ling et al. \(2016b\)](#) showed that the increase in accuracy of all these models are not significant enough to justify the additional cost.

Scalar-flux Models

The last class of turbulence scalar flux closure models are similar to the Reynolds stress models in the sense that they solve the transport equation of the turbulence scalar flux ([Younis et al., 2005](#)). Models differ in the way the different terms of the transport equation are treated. Methods based on the turbulence scalar flux transport equation are amongst the most detailed for scalar-flux transport. However, the cost of this is a higher computational overhead when compared to the gradient-diffusion hypothesis and algebraic models ([Combest et al., 2011](#)).

2.1.6. Realizability of the Reynolds Stress

As discussed in [Subsection 2.1.5](#) many turbulence models in use today make use of the eddy viscosity assumption, which basically assumes a linear relationship between the anisotropy tensor a_{ij} and the mean strain rate tensor S_{ij} . This does introduce a modelling error, which is why many data-driven approaches aim at finding better ways to model this anisotropy tensor. This is discussed further in [Section 2.3](#). In this section several characteristics of the Reynolds stress tensor and the anisotropy tensor are discussed. Furthermore, this discussion leads to the introduction of the barycentric map which can be used to plot all realizable turbulence states.

2.1.6.1. Realizability Constraints

The discussion starts with looking at the realizability constraints of the Reynolds stress. Any square matrix \mathbf{A} is considered positive semi-definite if (2.33) is satisfied for every nonzero column-vector \mathbf{x} with real numbers.

$$\mathbf{x}^T \mathbf{A} \mathbf{x} \geq 0 \quad (2.33)$$

The Reynolds stress is constructed by Reynolds-averaging the outer product of the velocity fluctuations, displayed in (2.34).

$$u'_i u'_j = \mathbf{u}' \otimes \mathbf{u}' = \begin{bmatrix} u'_1 \\ u'_2 \\ u'_3 \end{bmatrix} \begin{bmatrix} u'_1 & u'_2 & u'_3 \end{bmatrix} = \begin{bmatrix} u'_1 u'_1 & u'_1 u'_2 & u'_1 u'_3 \\ u'_2 u'_1 & u'_2 u'_2 & u'_2 u'_3 \\ u'_3 u'_1 & u'_3 u'_2 & u'_3 u'_3 \end{bmatrix} = u'_i u'_j \quad (2.34)$$

This means that the Reynolds stress is basically the Reynolds-averaged multiplication of the velocity fluctuation vector with its transpose. When this expression is substituted for \mathbf{A} in (2.33) it is shown that the Reynolds stress tensor is positive semi-definite. This is displayed in (2.35).

$$\mathbf{x}^T \mathbf{u}' \mathbf{u}'^T \mathbf{x} = (\mathbf{x}^T \mathbf{u}')^2 \geq 0 \quad (2.35)$$

When Reynolds averaging is applied, positive semi-definiteness is still guaranteed due to the fact that all samples satisfy this condition. Aside from this, the fact that the Reynolds stress tensor is symmetric ensures diagonalizability. Both these properties ensure that the eigenvalues are non-negative (Banerjee et al., 2007). This, together with the Cauchy-Schwartz inequality, leads to the physical realizability constraints the individual components of the Reynolds stress tensor have to satisfy. These constraints are displayed in (2.36) where with Greek indices summation is not implied (Schumann, 1977).

$$\overline{u'_\mu u'_\mu} \geq 0, \quad \overline{u'_\mu u'_\mu} + \overline{u'_\nu u'_\nu} \geq 2 \left| \overline{u'_\mu u'_\nu} \right|, \quad \det(\overline{u'_i u'_j}) \geq 0, \quad \mu, \nu = \{1, 2, 3\} \quad (2.36)$$

The minimum value for the diagonal components of the Reynolds stress is zero, due to the non-negativeness condition in (2.36). Furthermore, from the definition of the turbulence kinetic energy in (2.37) it can be concluded that the maximum value of a single diagonal component of the Reynolds stress is $2k$.

$$k = \frac{\overline{u'_i u'_i}}{2} \quad (2.37)$$

In (2.38) eigenvalue decomposition is applied to the expression for the Reynolds stress. The columns of V_{ij} are the eigenvectors of the Reynolds stress tensor and the diagonal components of Φ_{ij} are the eigenvalues, γ_i of the Reynolds stress tensor.

$$R_{ij} = 2k \left(\frac{\delta_{ij}}{3} + b_{ij} \right) = 2k \left(\frac{\delta_{ij}}{3} + V_{ik} \Phi_{kl} V_{jl} \right) \quad (2.38)$$

From (2.38) the amplitude (TKE), orientation (eigenvectors) and shape (eigenvalues) of the Reynolds stress can be determined. The eigenvectors define the so-called principal coordinate system in which the Reynolds stress is a diagonal tensor with the eigenvalues on the diagonal. From the bounds on the diagonal components of the Reynolds stress it can be concluded that the minimum and maximum value of the eigenvalues are 0 and $2k$ respectively. The eigenvalues of the anisotropy tensor, γ_i , are related to the eigenvalues of the Reynolds stress tensor, ϕ_i , as displayed in (2.39). This means that the eigenvalues of the anisotropy tensor are bounded by $-1/3 \leq \gamma_i \leq 2/3$.

$$\gamma_i = \frac{\phi_i}{2k} - \frac{1}{3} \quad (2.39)$$

From (2.23) for the anisotropy tensor and the realizability conditions of (2.36), it can also be derived that the off-diagonal components of the anisotropy tensor are bounded by $-1/2 \leq b_{\mu\nu} \leq 1/2$ (Banerjee et al., 2007).

2.1.6.2. Barycentric Map

The topic of representation of the Reynolds stress tensor, and specifically the anisotropy tensor, has been the topic of multiple research projects. Lumley (1979) introduced the three independent invariants of the anisotropy tensor, which are displayed in (2.40).

$$I = b_{ii}, \quad II = b_{ij}b_{ji}, \quad III = b_{ij}b_{in}b_{jn} \quad (2.40)$$

Lumley and Newman (1977) used this to represent the realizable states of the turbulence on the II-III map. They all fall within a triangular shape. Lumley (1979) also introduced a triangular mapping based on the eigenvalues of the anisotropy tensor.

Banerjee et al. (2007) expanded this to form the barycentric map. This map is based on the fact that the anisotropy has three limiting states. These are: the one-component turbulence corresponding to one non-zero eigenvalue of the anisotropy tensor, two-component turbulence corresponding to two non-zero eigenvalues and three-component turbulence with three non-zero eigenvalues. Banerjee et al. (2007) expresses the anisotropy tensor in a convex combination of its three limiting states in (2.41).

$$b_{ij} = C_{1c}b_{1c} + C_{2c}b_{2c} + C_{3c}b_{3c} \quad (2.41)$$

The components in (2.41) are computed using eigenvalues γ_1 to γ_3 in decreasing value as displayed in (2.42).

$$C_{1c} = \gamma_1 - \gamma_2, \quad C_{2c} = 2(\gamma_2 - \gamma_3), \quad C_{3c} = 3\gamma_3 + 1 \quad (2.42)$$

These components are mapped to the two-coordinate triangular barycentric map using (2.43) and (2.44), where x_{1c} and y_{1c} correspond to the coordinates of the corner belonging to one-component turbulence.

$$x_{new} = C_{1c}x_{1c} + C_{2c}x_{2c} + C_{3c}x_{3c} \quad (2.43)$$

$$y_{new} = C_{1c}y_{1c} + C_{2c}y_{2c} + C_{3c}y_{3c} \quad (2.44)$$

The barycentric map with the limiting states of the turbulence is displayed in Figure 2.1.

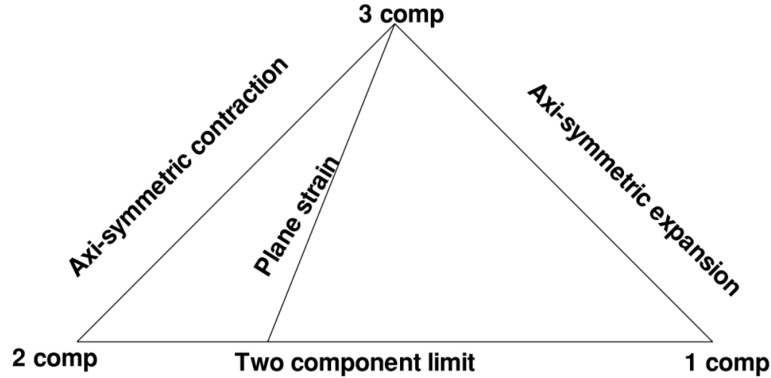


Figure 2.1: Barycentric map displaying the limiting states of turbulence (Banerjee et al., 2007).

Seeing that the three components of the mapping procedure add up to 1, the anisotropy tensor can also be mapped to the RGB-space. This enables the use of colours to display properties of the anisotropy tensor field (Emory and Iaccarino, 2014).

2.1.7. Invariance of the Navier-Stokes Equations

As is discussed in Section 2.3, a lot of data-driven approaches to turbulence modelling focus on generating new models for the anisotropy tensor of the Reynolds stress. An important consideration which needs to be kept in mind when generating these models is that invariance of the Navier-Stokes equations needs to be retained, as is shown by Ling et al. (2016c). Therefore, a (short) discussion of

invariance properties is given and a more general effective-viscosity approach which was introduced by Pope (1975) is discussed.

The Navier-Stokes equations in their general form are Galilean invariant. This means that the equations of motion are equal in any inertial frame. Rotation or translation of the reference frame should not have an influence. For the Navier-Stokes equations this means that when the reference frame is transformed using a rotation or reflection matrix, any vector or tensor is transformed equally to the reference frame. This is also true for the anisotropy tensor b_{ij} . According to Ling et al. (2016a), a scalar function which takes a tensor \mathbf{A} and vector \mathbf{v} as input should satisfy (2.45) when transformed by rotation matrix \mathbf{Q} .

$$f(\mathbf{A}, \mathbf{v}) = f(\mathbf{QAQ}^T, \mathbf{Qv}) \quad (2.45)$$

For a function which computes a tensor, (2.46) should be satisfied (Speziale et al., 1991).

$$\mathbf{Q}f(\mathbf{A}, \mathbf{v})\mathbf{Q}^T = f(\mathbf{QAQ}^T, \mathbf{Qv}) \quad (2.46)$$

(2.46) can be guaranteed for b_{ij} by using invariant input features to derive an integrity basis (Ling et al., 2016a). Pope (1975) derived such an integrity basis to formulate a more general effective-viscosity approach. This approach is based on the assumption that all Reynolds stresses are uniquely related to the non-dimensionalised rates of strain and rotation and local scalars: $b_{ij} = f(S_{ij}, \Omega_{ij})$. The non-dimensionalised rates of strain and rotation are computed according to (2.47) and (2.48).

$$S_{ij} = \frac{1}{2} \frac{k}{\epsilon} \left(\frac{\partial \bar{u}_i}{\partial x_j} + \frac{\partial \bar{u}_j}{\partial x_i} \right) \quad (2.47)$$

$$\Omega_{ij} = \frac{1}{2} \frac{k}{\epsilon} \left(\frac{\partial \bar{u}_i}{\partial x_j} - \frac{\partial \bar{u}_j}{\partial x_i} \right) \quad (2.48)$$

From the Cayley-Hamilton theorem it can be concluded that there is a limited number of linearly independent tensors which can be formed from S_{ij} and Ω_{ij} . Based on this theorem Pope (1975) derives 10 linearly independent basis tensors $T_{ij}^{(n)}$ and five tensor invariants λ_i . These can be used to compute b_{ij} as displayed in (2.49).

$$b_{ij} = \sum_{n=1}^{10} T_{ij}^{(n)}(S_{ij}, \Omega_{ij}) g^{(n)}(\lambda_1, \lambda_2, \lambda_3, \lambda_4, \lambda_5) \quad (2.49)$$

The tensor basis functions are displayed in (2.50).

$$\begin{aligned} T_{ij}^{(1)} &= S_{ij}, \quad T_{ij}^{(2)} = S_{ik}\Omega_{kj} - \Omega_{ik}S_{kj}, \quad T_{ij}^{(3)} = S_{ik}S_{kj} - \frac{1}{3}\delta_{ij}S_{mn}S_{nm}, \\ T_{ij}^{(4)} &= \Omega_{ik}\Omega_{kj} - \frac{1}{3}\delta_{ij}\Omega_{mn}\Omega_{nm}, \quad T_{ij}^{(5)} = \Omega_{ik}S_{kl}S_{lj} - S_{ik}S_{kl}\Omega_{lj}, \\ T_{ij}^{(6)} &= \Omega_{ik}\Omega_{kl}S_{lj} + S_{ik}\Omega_{kl}\Omega_{lj} - \frac{2}{3}\delta_{ij}S_{mn}\Omega_{no}\Omega_{om}, \quad T_{ij}^{(7)} = \Omega_{ik}S_{kl}\Omega_{lm}\Omega_{mj} - \Omega_{ik}\Omega_{kl}S_{lm}\Omega_{mj}, \\ T_{ij}^{(8)} &= S_{ik}\Omega_{kl}S_{lm}S_{mj} - S_{ik}S_{kl}\Omega_{lm}S_{mj}, \\ T_{ij}^{(9)} &= \Omega_{ik}\Omega_{kl}S_{lm}S_{mj} + S_{ik}S_{kl}\Omega_{lm}\Omega_{mj} - \frac{2}{3}\delta_{ij}S_{no}S_{op}\Omega_{pq}\Omega_{qn}, \\ T_{ij}^{(10)} &= \Omega_{ik}S_{kl}S_{lm}\Omega_{mn}\Omega_{nj} - \Omega_{ik}\Omega_{kl}S_{lm}S_{mn}\Omega_{nj}, \end{aligned} \quad (2.50)$$

Moreover, the invariants are given in (2.51).

$$\lambda_1 = S_{ij}S_{ji}, \quad \lambda_2 = \Omega_{ij}\Omega_{ji}, \quad \lambda_3 = S_{ij}S_{jk}S_{ki}, \quad \lambda_4 = \Omega_{ij}\Omega_{jk}S_{ki}, \quad \lambda_5 = \Omega_{ij}\Omega_{jk}S_{kl}S_{li} \quad (2.51)$$

2.2. Wind Farms and the Atmospheric Boundary Layer

This section is focused on characterising the ABL, its different states and the mutual influence between the ABL and wind farms. Furthermore, an overview is given of the ways these characteristics influence simulations of the ABL and wind farms. This is done with the aim of determining a baseline RANS approach to simulating wind farms.

2.2.1. Atmospheric Boundary Layer Characteristics

The airflow over the Earth is usually split into two parts. The top part of the flow in the free atmosphere is called the geostrophic wind. The geostrophic wind is mostly free from surface influences and is driven by a balance of large-scale pressure differences and the Coriolis force due to the rotation of the Earth. The bottom part of the flow is called the atmospheric boundary layer and its properties are governed by the strength of the geostrophic wind, surface roughness, Coriolis effects and thermal influences (Burton et al., 2011). The ABL is generally continuously turbulent, as opposed to the geostrophic wind. Between these two regions is a thin, sharp inversion layer called the capping inversion (Wyngaard, 2010). This capping inversion has a strong increase in potential temperature, limits penetration of turbulent gusts from the ABL into the free atmosphere and controls the height of the ABL (Allaerts, 2016). The focus of this section is to describe several properties of the ABL which need to be considered when simulating wind farms in ABL flow.

2.2.1.1. Scales

An example of the spectrum of wind motions is given in Figure 2.2.

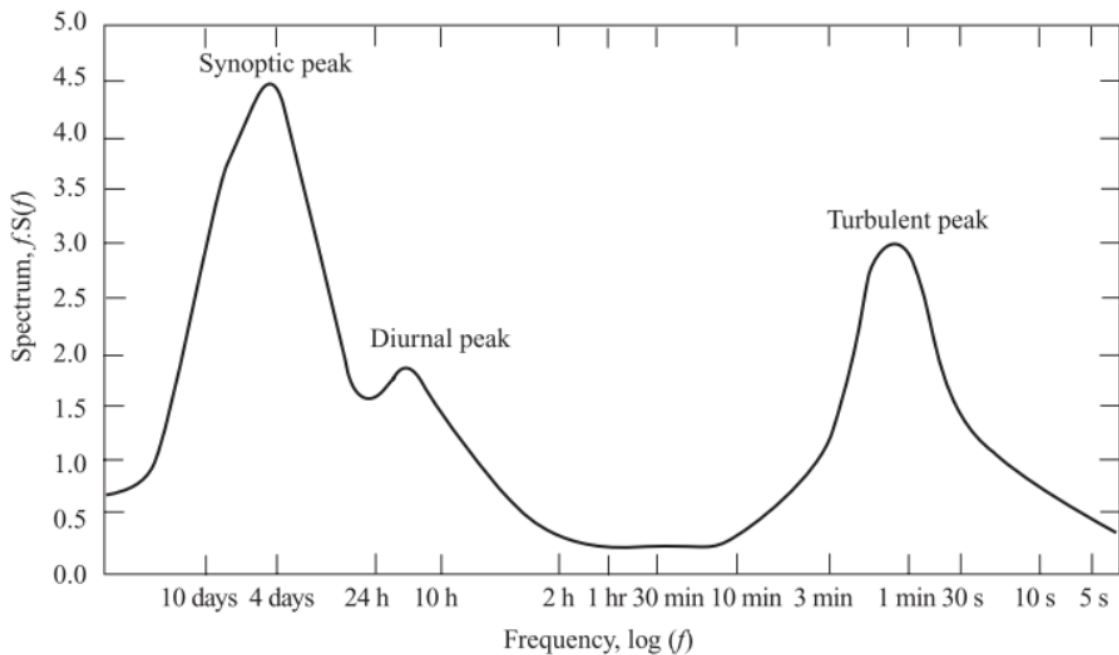


Figure 2.2: Wind spectrum at wind farm Brookhaven taken from Burton et al. (2011) based on work from Van der Hoven (1957).

As can be seen in Figure 2.2 there are three discernible peaks in the spectrum of wind motions at one location: the synoptic variations due to passing weather systems, diurnal variations due to the difference between day and night and turbulence variations which are of a much shorter timescale (Burton et al., 2011). These turbulent variations are the main focus of the simulations of wind farms as they have a large effect on power production and fatigue of wind turbines (Wyngaard, 2010).

According to Burton et al. (2011) turbulence in the ABL is created in two ways: due to friction and due to thermal effects. These two production mechanisms are also largely interconnected. For a wind farm in the ABL there is a large variety of turbulent length scales according to Réthoré (2009). The largest scales are constituted by the atmospheric turbulence scale, created by wind shear, friction with the ground and thermal effects. Then, there are the smaller turbulent scales which are created in the

shear layer between the low-velocity flow in the wake of a wind turbine and the faster free stream. Lastly, the smallest scales of turbulence are the turbulence length scale of the blade-induced vortex structures. Capturing this large range of scales for a wind farm is not feasible. Therefore, simulations often focus on either the near wake, where blade induced turbulence is dominant, or the far wake, where shear induced turbulence is dominant (Vermeer et al., 2003). This is further investigated when discussing the treatment of turbines in simulations in Subsection 2.2.3.

2.2.1.2. Thermal Stability of the Atmospheric Boundary Layer

During a diurnal cycle, the properties of the ABL at a particular location vary a lot. This is largely due to the influence of thermal stability. During the day, the Sun warms the surface and heat is transferred from the ground to the air above. During the night, the opposite is true and heat is transferred from the air to the ground as the Earth cools due to emitted radiation. This means a rough division of three boundary layer states can be made: neutral, stable and unstable (also called convective) (Burton et al., 2011). These different states have vastly different properties which directly affect mechanical turbulence in the turbine wake regions, and strongly determine the ambient turbulence intensity (Allaerts, 2016).

Neutral Boundary Layer

The first ABL state which is discussed is the neutral state. This state is reached when there is no heat flux at the surface, which means the potential temperature is constant with height. Adiabatic cooling of air as it rises, is in thermal equilibrium with its surroundings. This results in the absence of buoyancy forces, making simulating these conditions easier than when thermal effects need to be included (Allaerts, 2016; Burton et al., 2011). Therefore, the neutral atmospheric boundary layer has received significant attention in research, an overview of which is given in Hess and Garratt (2002a,b). Even though it has received a lot of attention, true neutral conditions are almost never found in practise (Wyngaard, 2010).

Unstable Boundary Layer

The unstable boundary layer usually occurs during the day when there is a positive heat flux from the Earth to the air. This means that parcels of warm air near the surface start to rise. As the parcel rises it expands and cools adiabatically. When this cooling is not sufficient to achieve thermal equilibrium with its surroundings, it continues to rise. This leads to large convection cells, hence the fact that the unstable ABL is also called the convective boundary layer. This whole process leads to a lot of vertical mixing, transfer of momentum and large-scale turbulent eddies. Therefore, the unstable boundary layer is characterised by high levels of turbulence and, consequently, a thick boundary layer (Allaerts, 2016; Burton et al., 2011; Wyngaard, 2010).

Stable Boundary Layer

The stable boundary layer occurs most often during the night when there is a negative heat flux at the surface. Other circumstances where this state can occur are when the ABL encounters a cooler surface downwind and when the ABL is entraining higher potential temperature air from the capping inversion. In a stable boundary layer the buoyancy forces which enhance turbulence in the convective boundary layer, actually suppress vertical motions. The turbulence is now dominated by friction with the ground or wind turbines (Burton et al., 2011). When the stability is very high, it can even lead to the complete shutdown of the turbulent energy cascade. The thermal stability selectively dampens the largest eddies, while the smallest scales viscously dissipate turbulence kinetic energy. In extreme conditions this can lead to a laminar boundary layer with intermittent turbulence (Allaerts, 2016). Furthermore, the limiting of the vertical length scales makes the turbulence highly anisotropic. Also, smaller spatial turbulence scales and low diffusion make the stable boundary layer much more sensitive to terrain related inhomogeneities (Wyngaard, 2010). This boundary layer is also characterised by a low height and large wind veer (Allaerts, 2016).

2.2.1.3. Relevant Flow Phenomena

Aside from the thermal stability, there are a few other phenomena which influence the airflow at a wind farm.

Wind Turbine wakes

Wind turbine wakes are regions characterised by decreased velocity and increased turbulence. The magnitude of the velocity deficit is related to the thrust coefficient of the turbine. The wind speed gradient between the velocity deficit in the wake and the free stream results in shear-generated turbulence. Additionally, the turbine itself generates turbulence through tip vortices shed by the blades and general disturbances caused by the nacelle, blades and tower (Burton et al., 2011).

In a wind farm, the turbulence intensity increases with each turbine the flow passes and the wake deficit increases in magnitude. However, after only a small number of turbines this effect is not visible anymore. This is due to the fact that the increased turbulence causes better mixing and faster restoration of the wake (Witha et al., 2014).

The thermal stability of the boundary layer also has a large effect on the wakes of wind turbines. This is mainly due to the dependence of ambient turbulence levels on thermal stability. More turbulence means better mixing and faster restoration of the wake. Dörenkämper et al. (2015) reported wake effects which were twice as strong in a stably stratified boundary layer as in an unstable boundary layer. This also means that the influence of turbines on each other is much larger in stable boundary layers. For example, Wharton and Lundquist (2012) reported 15% difference in individual wind turbine performance between different stability classes for equal hub height wind speed and research by Hansen et al. (2012) found approximately the same results for the Horn Rev wind farm.

Low-level Turbulent Jets

Low-level turbulent jets are a thin stream of fast moving air close to the ground, whose velocity can even surpass the geostrophic wind. These jets frequently develop in stable boundary layers and are an elevated source of turbulence. There are many possible causes for these low-level jets and they develop through inertial oscillations. These can be triggered by the collapse of daytime turbulence due to surface cooling, when the flow becomes decoupled from the surface (Allaerts, 2016). The low-level turbulent jets can be eliminated by wind turbines of a wind farm due to energy extraction and enhanced mixing of momentum according to LES simulations performed by Lu and Porté-Agel (2011).

Waves

According to Sun et al. (2015), there are two types of waves which occur in the atmosphere. Firstly, there are vorticity waves which are caused by vortex sheets and rolls due to shear instability. Examples are Kelvin-Helmholtz billows. Low-level turbulent jets can trigger vorticity waves in the stable boundary layer due to the large shear instability.

Buoyancy waves constitute the other type of waves and are forced by displacement of streamlines. Internal gravity waves are an example of this type of waves which can be triggered in a stably stratified boundary layer. Propagating gravity waves can redistribute large amounts of energy and momentum over large distances and break down into turbulence (Sun et al., 2015). These waves are propagated upwards and advected downstream by the mean background flow. At large heights, the non-linear effects cause the waves to break down, resulting in clear air turbulence. Gravity waves can be triggered by streamline displacement due to wind farms. However, the impact of these waves is probably small when compared to mountain induced gravity waves (Allaerts, 2016).

Internal boundary layers

A fully developed boundary layer that encounters a discontinuity, for example a heat flux or wind farm, does not adjust immediately at all heights. The portion of the boundary layer that is influenced by the discontinuity increases with downstream distance. This portion is called the internal boundary layer and is defined as the portion where the velocity and the turbulent stress are significantly affected by the change in inflow conditions. The adjustment of the ABL to the increase of drag due to wind turbines shows similarities to the effects of surface roughness (Allaerts, 2016). Namely, the presence of a wind farm causes increased boundary layer height, reduced surface flux, reduced wind speed and enhanced turbulence (Lu and Porté-Agel, 2015).

Wake Meandering

Wake meandering is a phenomenon which occurs in all boundary layer states. It basically, constitutes the unsteady movement with low frequencies of entire turbine wakes under the influence of large scale atmospheric turbulence eddies (Wyngaard, 2010). When the frequency of the wake meandering

matches the torsional natural frequency of the wind turbines, actual damage might occur (Lu and Porté-Agel, 2011). It is found in research by, amongst others, Abkar and Porté-Agel (2015) and Machefaux et al. (2016) that increasing instability leads to larger magnitude wake meandering. This can be explained by the fact that the more unstable the boundary layer is, the more energy is in the large scale atmospheric turbulence.

2.2.1.4. Characterizing Length Scales and Non-Dimensional Parameters

In this section the characterization of the flow of a wind farm in the ABL is finished by discussing several parameters which are used in literature to characterise it.

Brunt-Väisälä Frequency

Traditionally, the different thermal states of the ABL were classified purely based on the heat flux at the Earth's surface. However, in the 1970s that classification was not sufficient anymore and the expression for the Brunt-Väisälä frequency, displayed in (2.52), was introduced (Allaerts, 2016).

$$N = \sqrt{\frac{g}{\theta_0} \frac{\partial \theta}{\partial z}} \quad (2.52)$$

When a parcel of air is vertically displaced, it will start to oscillate at the Brunt-Väisälä frequency, making it characteristic for the free-atmosphere stratification. It is also a scaling parameter in expressions for the ABL height.

Ozmidov Length Scale

The Ozmidov length scale is used to characterise stratified turbulence and its expression is given in (2.53), where ϵ is the dissipation rate and N is the Brunt-Väisälä frequency (Lumley, 1964; Ozmidov, 1965).

$$L_{Oz} = 2\pi \sqrt{\frac{\epsilon}{N^3}} \quad (2.53)$$

The smallest eddies for which the influence of buoyancy is important are of the Ozmidov scale. This means that in ABL flow, the Ozmidov scale divides the turbulence in two parts. Turbulence of larger length scale which is anisotropic and turbulence of smaller length scale which displays more isotropic properties (Khani and Waite, 2014). When performing LES, the Ozmidov scale could be used as cut-off scale.

Buoyancy Length Scale

The buoyancy length scale corresponds to the thickness of shear layers in stratified turbulence and is given by (2.54), where N is the Brunt-Väisälä frequency (Lindborg, 2006; Waite and Bartello, 2004).

$$L_b = \frac{2\pi u_{rms}}{N} \quad (2.54)$$

Research from Waite and Bartello (2004), Lindborg (2006), Brethouwer et al. (2007) and Khani and Waite (2014) has shown that to capture the stratified turbulent energy cascade, the buoyancy length scale has to be resolved in a LES simulation.

Obukhov Length

Presently, the stability of the ABL is usually based on the stability parameter z/L_O with L_O the Obukhov length. This length scale is based on the Monin-Obukhov Similarity Theory (MOST) which is discussed in Subsection 2.2.2. The Obukhov length corresponds to the height above the surface above which buoyancy effects become important (Wyngaard, 2010). Loosely, this means the height at which buoyancy production of TKE equals shear-induced TKE (Thé and Yu, 2017). The expression of the Obukhov length is given in (2.55), where θ is the potential temperature, u_* is the friction velocity, κ is the von Kármán constant and q_w is the surface heat flux.

$$L_O = -\frac{\overline{\theta_0} u_*^3}{\kappa g q_w} \quad (2.55)$$

Also, a local version of the Obukhov length scale is given in (2.56), where the surface heat flux is replaced by the local vertical heat flux $\overline{w'\theta'}$.

$$\Lambda = -\frac{\overline{\theta_0} u_*^3}{\kappa g \overline{w'\theta'}} \quad (2.56)$$

The Obukhov length is negative for unstable boundary layers, positive for stable boundary layers and approaches infinity for neutral boundary layers (Wyngaard, 2010). Peña et al. (2010) went even further and classified seven stability regimes based on the Obukhov length scale, from very stable to very unstable.

Richardson numbers

In stably stratified turbulence, the strength of the stability is given by the flux Richardson number Ri_f . As can be seen in the expression displayed in (2.57), the flux Richardson number gives the relative importance of buoyant destruction in the TKE budget (Wyngaard, 2010).

$$Ri_f = \frac{\text{buoyant destruction rate}}{\text{shear production rate}} = \frac{\frac{g}{\theta_0} \overline{w'\theta'}}{u'_i u'_j \frac{\partial \theta}{\partial x_j}} \quad (2.57)$$

The flux Richardson number indicates the strength of the stability. However, when the stability becomes very strong, the ABL is forced to a laminar state, for which the flux Richardson number cannot be computed (Allaerts, 2016). Therefore, the gradient Richardson number Ri_g is defined in (2.58).

$$Ri_g = \frac{\frac{g}{\theta_0} \frac{\partial \theta}{\partial z}}{\left(\frac{\partial \bar{u}}{\partial z}\right)^2 + \left(\frac{\partial \bar{v}}{\partial z}\right)^2} \quad (2.58)$$

The gradient Richardson number is the ratio of buoyancy forces to inertial forces (Wyngaard, 2010). Traditionally, it was accepted that turbulence would decay when the gradient Richardson number exceeded a value of around 0.20-0.25 (Wyngaard, 2010). However, more recent research by Zilitinkevich et al. (2013) has shown that the velocity shear maintains turbulence, even for very high gradient Richardson numbers, sparking a debate on the existence of a critical Richardson number.

Rossby number

The last non-dimensional number is used to characterise the influence of external parameters on the ABL and is called the Rossby number. It is defined as displayed in (2.59), where G is the geostrophic wind, f_c the Coriolis parameter and z_0 the surface roughness (Peña et al., 2010). The Coriolis parameter is defined as $f_c = 2\Omega \sin \lambda$ where Ω is the angular velocity of the Earth and λ is the latitude.

$$Ro = \frac{G}{f_c z_0} \quad (2.59)$$

The Rossby number is included in multiple models for the length scale of the wind profile and characterises the relative importance of inertial forces with respect to the Coriolis force due to the planetary rotation. Length scale models by Lettau (1962), Blackadar (1962), Gryning et al. (2007) and Peña et al. (2010) include the influence of the Rossby number.

2.2.2. Monin-Obukhov Similarity Theory

MOST is based on the paper by Obukhov (1946) and later Monin and Obukhov (1954). A history and discussion of its evolution is given in Foken (2006). MOST is used in a lot of simplified models for ABLs. Also, it is used in a lot of simulation approaches, either to define inflow conditions or as a wall-treatment model. Aside from that, it was one of the most important developments in understanding the structure and properties of the atmospheric surface layer. Therefore, an overview of Monin-Obukhov Similarity Theory is given, based on the discussion given by Wyngaard (2010).

MOST is based on dimensional analysis and the Buckingham Pi theorem. This theorem states that when you know the $m - 1$ governing parameters of a dependant variable, and n is the number

of dimensions, then $m - n$ independent dimensionless quantities can be formed. The dimensionless quantities can be arbitrarily chosen. Furthermore, the dependent variable can be taken as a function of these $m - n$ dimensionless quantities.

In MOST five parameters are considered to govern the quasi-steady turbulence structure above a flat, horizontally homogeneous land surface. These parameters are: the length scale of the turbulence L , the velocity scale of the turbulence U , the mean temperature flux at the surface q_w , the mean surface flux of a conserved scalar C_0 and the buoyancy parameter g/θ_0 . In MOST the turbulence length scale is taken as the distance z from the surface and the turbulence velocity scale is taken as the friction velocity u_* . It is assumed that the outer part of the boundary layer does not exert a significant influence on the surface layer.

Among the parameters which are not considered to govern the turbulence structure in the surface layer are the boundary-layer depth, as it was wrongly assumed that it does not directly influence surface layer turbulence, and the mean velocity, to maintain Galilean invariance. Furthermore, the Coriolis parameter was excluded as its influence is very small compared to the turbulent inertia: the Rossby number is high. The molecular diffusivities are neglected because of high Reynolds number and the roughness length, z_0 is excluded, constituting an assumption of $z \gg z_0$.

The five chosen parameters mean that $m = 6$ with $n = 4$ dimensions: length, time, temperature and c . This means that 2 independent dimensionless quantities can be formed. MOST takes one as the dependent variable (velocity, temperature or C) non-dimensionalised with z , the other is taken as z/L_0 with L_0 the Obukhov length as given by (2.55).

MOST implies that the gradients of the mean wind speed, mean potential temperature and concentration are given by (2.60), (2.61) and (2.62).

$$\frac{\kappa z}{u_*} \frac{\partial \bar{u}}{\partial z} = \phi_m \left(\frac{z}{L_0} \right) \quad (2.60)$$

$$-\frac{\kappa z u_*}{q_w} \frac{\partial \bar{\theta}}{\partial z} = \phi_h \left(\frac{z}{L_0} \right) \quad (2.61)$$

$$-\frac{\kappa z u_*}{C_0} \frac{\partial \bar{C}}{\partial z} = \phi_c \left(\frac{z}{L_0} \right) \quad (2.62)$$

Functions ϕ_m , ϕ_h and ϕ_c are the same in all locally, quasi-steady surface layers. Examples of these functions taken from experimental results are displayed in Figure 2.3.

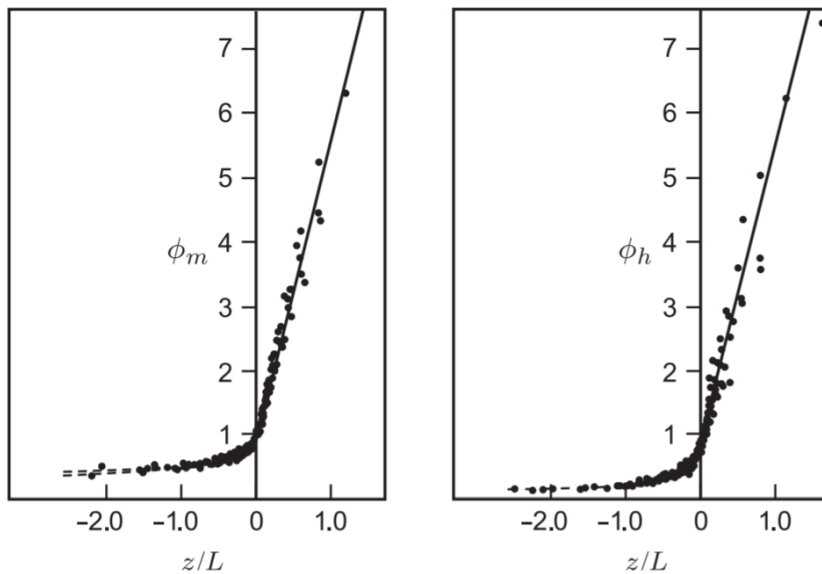


Figure 2.3: Monin-Obukhov functions for mean velocity gradient (left) and mean potential temperature gradient (right). Based on the experimental results from [Businger et al. \(1971\)](#) and taken from [Wyngaard \(2010\)](#).

According to [Wyngaard \(2010\)](#), the MOST functions for quasi-steady stable atmospheric conditions were determined based on experimental results to be given by (2.63). However, many other expressions do exist in literature.

$$\phi_m = 1.0 + 4.8 \frac{z}{L_0}, \quad \phi_h = 1.0 + 7.8 \frac{z}{L_0} \quad (2.63)$$

The same equations for quasi-steady unstable atmospheric conditions are displayed in (2.64).

$$\phi_m = \left(1 - 19.3 \frac{z}{L_0}\right)^{-1/4}, \quad \phi_h = \left(1 - 12 \frac{z}{L_0}\right)^{-1/2} \quad (2.64)$$

The functions given in (2.63) together with the expressions in (2.60) and (2.61) can be combined to give expressions for the velocity and potential temperature in the surface layer close to the wall displayed in (2.65).

$$\bar{u}(z) = \frac{u_*}{\kappa} \left(\ln \frac{z}{z_0} + 4.8 \frac{z}{L_0} \right), \quad \bar{\theta}(z) = \bar{\theta}(z_r) - \frac{q_w}{\kappa u_*} \left(\ln \frac{z}{z_r} + 7.8 \frac{z}{L_0} \right) \quad (2.65)$$

In (2.65), z_0 is the surface roughness and z_r is the reference height for the reference temperature. Similar expressions are generated for unstable atmospheric conditions, however these tend to be more complex. The expressions in (2.65) are used in wall functions of LES and RANS simulations to compute the velocity and potential temperature in the wall cells.

2.2.3. Turbine Modelling

In order to be able to simulate the flow field in a wind farm, the wind turbines have to be included. Generally, the methods to include these turbines can be divided into two approaches: direct modelling in which the blades are discretised on a computational mesh and the generalised actuator disk approach ([Sanderse et al., 2011](#)).

2.2.3.1. Direct Modelling

The most straightforward approach is to include the blades in the computational grid and directly model the flow around the blades. This method is also the most accurate. However, this accuracy does come at a cost: simulating the boundary layer on the blades including transition, separation and stall is computationally very expensive. Especially, when this has to be done for multiple wind turbines in a wind farm. Furthermore, capturing compressibility effects at the blade tips requires the use of the compressible Navier-Stokes equations while the wakes are approximately incompressible, further driving up the computational costs. Therefore, direct modelling is mainly used in research on single turbine wakes, or research in which near-wake effects are important ([Sanderse et al., 2011](#)). Examples of research which used this method is research done by [Sørensen and Hansen \(1998\)](#), [Duque et al. \(1999\)](#) and [Xu and Sankar \(2000\)](#).

2.2.3.2. Generalised Actuator Disk Approach

Direct modelling is too computationally demanding for industry to simulate the flow for a whole wind farm. Therefore, other, less demanding approaches are used. These approaches are based on generalised actuator disk theory. In this approach, the rotor is represented by an actuator disk, line or surface. Because of this, the boundary layers on the blades do not have to be computed, alleviating the computational demands. The actuator disk acts as a body force on the flow, so as a momentum sink, leading to a discontinuity in pressure. The way in which the force term is included in the equations depends on whether a disk, line or surface discretization is used. When a method based on this approach is used, one should also include sources of turbulence to account for the creation of mechanical turbulence by the blades ([Sanderse et al., 2011](#)).

Actuator Disk

The basic form of the actuator disk methodology distributes the load exerted by the rotor uniformly over the actuator disk. This is displayed in (2.66) where C_T is the turbine thrust coefficient, V_{rel} is the local velocity at the actuator disk and A is the surface area.

$$\rho \mathbf{f} = \frac{1}{2} C_T \rho V_{rel}^2 A \quad (2.66)$$

An adaptation of this approach to include a non-uniform force distribution is displayed in (2.67) where c is the local chord length of the rotor, C_l and C_d are the sectional lift and drag coefficient and \mathbf{e}_L and \mathbf{e}_D are unit vectors in the lift and drag direction.

$$\rho \mathbf{f}_{2D} = \frac{1}{2} C_T \rho V_{rel}^2 c (C_l \mathbf{e}_L + C_d \mathbf{e}_D) \quad (2.67)$$

This approach is similar to Blade Element Momentum Theory (BEM). However, the difference is in the fact that the local velocity is taken from the flow field and not from an iterative procedure based on global momentum balance as in BEM. This method gives a relatively accurate representation of turbulent mixing in the far wake (further than three diameters) according to [Allaerts \(2016\)](#). However, due to the simplifications made, inaccuracy is introduced in the near wake.

The largest source of inaccuracy introduced by the actuator disk approach is its reliance on the sectional airfoil data. This data is often not complete due to the different conditions a turbine in a wind farm encounters. A turbine in the wake of another turbine encounters different levels of turbulence which can trigger very different stall regimes, significantly altering the lift and drag. Even though the inflow angle might be the same. Furthermore, the fact that present day wind turbines make use of different stall regimes makes it very difficult for the sectional data to accurately represent reality ([Vermeer et al., 2003](#)).

Another problem with the actuator disk methodology is the fact that discontinuities introduced in the pressure field can cause numerical oscillations. This is often solved by distributing the forces over multiple cells using a Gaussian distribution ([Réthoré, 2009](#)).

Lastly, the actuator disk approach neglects induced tangential velocities by the rotor. Even though, the rotation of the turbine causes significant rotation in the wake. This was solved in research by [Porté-Agel et al. \(2010\)](#) and [Wu and Porté-Agel \(2011\)](#) which included rotation in the actuator disk methodology. They also showed that the inclusion of non-uniformity and rotation significantly improved the prediction of the mean velocity profile and turbulence intensity with respect to a uniformly loaded disk.

Actuator Line

An extension of the actuator disk methodology is the actuator line approach introduced by [Sørensen and Shen \(2002\)](#). In this approach, the line forces are not averaged over the disk but dependent on time, making it unsuitable for steady RANS simulation. The advantage of this approach is also the fact that it is able to compute distinct tip vortices. A drawback of this method is its reliance on 2D airfoil data, just as with the actuator disk approach. When this data is used, it should be corrected for Coriolis, centrifugal and tip effects according to [Sanderse et al. \(2011\)](#). Aside from the introduction by [Sørensen and Hansen \(1998\)](#), examples of research employing the actuator line method are research by [Mikkelsen \(2003\)](#) and [Howard and Pereira \(2006\)](#).

Actuator Surface

The actuator line method was extended to an actuator surface method by [Shen et al. \(2009\)](#). This method represents the blade as a planar surface. As with the surface line method, its dependence on time makes it unsuitable for RANS simulation. The fact that the forces are distributed over a surface, more accurate airfoil data is needed. Instead of just the lift and drag coefficient, also the pressure and skin-friction distributions over the surface is needed ([Sanderse et al., 2011](#)).

2.2.4. Adaptation of Navier-Stokes Equations for non-neutral ABL

As discussed in [Subsection 2.2.1](#), the flow in the ABL has some very specific characteristics. These characteristics can influence the governing equations in a myriad of ways. A lot of research has been done about how the different phenomena can be included in these equations. Even the same phenomena are included in many different ways in different pieces of research.

2.2.4.1. Buoyancy Treatment

As discussed in [Subsection 2.2.1](#) the ABL can be classified in a number of different states according to thermal stability. While a lot of research has been done into the simulation of neutral boundary layers where buoyancy effects are absent (for example [Réthoré \(2009\)](#)), more and more research is done which includes the effects of thermal stability. In order to do this, generally the Boussinesq approximation ([Spiegel and Veronis, 1960](#)) is applied together with an additional transport equation for the potential temperature.

This Boussinesq approximation should not be confused with the Boussinesq hypothesis used in turbulence modelling and its main assumption is that the adiabatic base state is independent of height. This means that the base state is characterised by constant density ρ_0 , temperature T_0 and potential temperature θ_0 . Furthermore, an important part of the Boussinesq approximation is the fact that all density variations are neglected, except when they are multiplied with the gravitational acceleration in the buoyancy term. This reduces the continuity equation to a requirement of non-divergent flow. Another consequence is the linearization of the equation of state to [\(2.68\)](#) ([Allaerts, 2016](#)).

$$\frac{\rho'}{\rho_0} = -\frac{T'}{T_0} = -\frac{\theta'}{\theta_0} \quad (2.68)$$

[\(2.68\)](#) couples ρ' and θ' and, therefore, the buoyancy term in the momentum equation and the transport equation for the potential temperature. This transport equation in a RANS simulation framework means that not only the turbulence flux, but also the turbulent scalar flux has to be modelled. The ways in which these two terms are modelled are discussed in [Subsection 2.1.5](#).

Aside from that, a source/sink term of the form displayed in [\(2.69\)](#) is added to the k - and ϵ -equations. This is done to account for buoyant production and destruction of turbulence, in accordance to [Koblitz \(2013\)](#).

$$B = -\mu_t g_i \frac{\partial \rho}{\partial x_i} \quad (2.69)$$

The term in [\(2.69\)](#) is positive in unstable conditions and negative in stable conditions.

2.2.4.2. Coriolis force

The Coriolis force is a force exerted on the flow due to the rotation of the Earth. The magnitude of the force is determined by the Coriolis parameter which is computed according to [\(2.70\)](#), where Ω^E is the rotational velocity of the Earth and ϕ is the latitude.

$$f_c = 2\Omega^E \sin \phi \quad (2.70)$$

The balance of the Coriolis force with the large scale pressure gradients determines the geostrophic wind. However, for the scale of wind turbine simulations it used to be assumed that the Coriolis force was of negligible impact. But the fact that wind turbines, and wind farms, become larger and larger means that the Coriolis force becomes increasingly relevant in simulations. Research by [Porté-Agel et al. \(2010\)](#) shows that for large wind turbines and wind farms the inclusion of the Coriolis force does have an effect on the results. Furthermore, [van der Laan et al. \(2015a\)](#) showed that the wake of a wind farm is significantly deflected due to the Coriolis effect. This drives more and more research to include the Coriolis force in the simulations. For example, [Allaerts \(2016\)](#) investigated, amongst other things, the effect of the Coriolis force on wind farm flow and [Koblitz \(2013\)](#) included the Coriolis force in his RANS model for non-neutral ABL.

2.2.5. Overview of approaches in research

This section gives an overview of the simulation approaches used in research for wind farms in different conditions of the atmospheric boundary layers. The discussion is split in two: LES approaches and RANS approaches.

2.2.5.1. LES

According to [Vermeer et al. \(2003\)](#), the turbulence in the wake of a wind turbine in an ABL is generally more isotropic than the outside flow. This makes LES a particularly suitable approach as the larger

scales in the outside flow, where most anisotropy is, are resolved. While the smaller scales of turbulence in the wake, which are more isotropic, are modelled. However, the major downside of this is the large increase in computational demands when compared to RANS simulation. [Troldborg et al. \(2007\)](#) used an actuator line approach together with LES to investigate the wake of wind turbines in turbulent inflow. Turbulence was introduced by using time-varying body forces upstream of the wind turbine. It confirmed the assumption that the turbulence inside the far wake tends to be more isotropic than the outside flow. Furthermore, it confirmed that the main factor governing large scale motion of the wake (wake meandering) are the large coherent structures of atmospheric turbulence.

[Porté-Agel et al. \(2010\)](#) introduced a framework for using LES to simulate wind farms in ABL flow. This framework parameterises both SGS stress and SGS heat flux using the tuning-free scale-dependent Lagrangian models introduced by [Stoll and Porté-Agel \(2006\)](#). These models optimise the model coefficients locally based on the dynamics of the resolved scales. The framework, in combination with actuator line and actuator disk models, yielded good results when compared with wind-tunnel measurements. [Lu and Porté-Agel \(2011\)](#) used the framework in combination with the actuator line model to investigate a large wind farm in a stably-stratified ABL. Notable findings included the elimination of the low-level jet due to energy extraction by the wind turbines and enhanced momentum mixing, non-axisymmetric wakes due to the Coriolis effect, non-uniform incoming turbulence and blade rotations. Also, the height of the stable boundary layer was increased. The framework is also used to investigate the impact of wind farms on a convective ABL by [Lu and Porté-Agel \(2015\)](#). Results showed a modification of the stability of the ABL in the presence of a wind farm. Furthermore, the presence of a wind farm increases turbulence, reduces wind speed and increases the height of the ABL. Lastly, the framework was improved upon with a new SGS model by [Lu and Porté-Agel \(2013\)](#). This model computes the structure of the SGS flux based on the normalised gradient vector. This improved model showed good correspondence with reference results.

An LES study based on the framework from [Porté-Agel et al. \(2010\)](#), combined with an actuator disk model with rotation, was performed by [Abkar and Porté-Agel \(2015\)](#). This study found that stability has a significant influence on the spatial distribution of the mean velocity deficit, turbulence intensity and turbulent momentum fluxes. Furthermore, this method was used to simulate a whole diurnal cycle by [Abkar et al. \(2016\)](#). It showed that ABL flow is almost never steady in nature, making it difficult for RANS to simulate it properly.

[Witha et al. \(2014\)](#) used LES with an actuator disk model to investigate wind farms in different thermal stratification regimes and discovered that the turbulence intensity increases with each turbine the flow passes. However, after a number of wind turbines the wake deficit does not increase anymore. [Dörenkämper et al. \(2015\)](#) used the standard SGS flux closure by [Deardorff \(1980\)](#) in combination with an actuator disk with rotation to investigate the impact of stable ABL on wind turbine wakes. He found that wake effects in the stably stratified ABL were up to twice as strong as in an unstable ABL. This leads to a difference of up to 20 % in power output. Furthermore, it was shown that turbines tend to reduce stability of the ABL. The rotors enhance mixing, neutralizing a stable ABL.

[Johnstone and Coleman \(2012\)](#) investigated the interaction between a large wind farm and the fully developed ABL with Coriolis effects. A DNS with artificially low Reynolds number was applied and it showed that the work by the driving pressure gradient can vary in two ways to balance the sum of turbulent energy dissipation and farm energy extraction. The boundary layer can become thicker or the wind can rotate towards the pressure gradient.

Lastly, [Allaerts \(2016\)](#) performed LES simulations of wind farms in conventionally neutral and stable ABLs. This work focused on the influence of atmospheric stability, inversion layers and the Coriolis effects. The characteristic length scales in stable boundary layers are smaller than for neutral or unstable ABLs, which makes the SGS-model more important. [Allaerts \(2016\)](#) used only eddy viscosity models that did not require additional filtering operations. A TKE model by [Deardorff \(1980\)](#) and a stability dependent Smagorinsky model by [Stevens et al. \(2000\)](#) were used together with a non-rotating actuator disk method. Both SGS-models yielded results which corresponded well with reference results.

2.2.5.2. RANS

According to [Vermeer et al. \(2003\)](#) the $k - \epsilon$ turbulence model is best suited for wind farm simulations where far wake phenomena are more important and $k - \omega$ SST is better for near wake simulations. However, research by [Réthoré \(2009\)](#) shows that the $k - \epsilon$ model does have a lot of shortcomings when simulating wind farms in atmospheric boundary layers. According to [Réthoré \(2009\)](#) it is difficult

for RANS to model the complex interaction between different turbulence scales as all scales are mixed together. However, the $k - \epsilon$ model together with the actuator disk model does give the fastest results. The standard $k - \epsilon$ model largely overpredicts wake recovery compared to measurements. Furthermore, it fails to model the anisotropy of turbulence quantities. Réthoré (2009) gives two main reasons for this: the eddy viscosity assumption is not valid in the near wake region and the effect of the turbine on the turbulence mean quantities is not considered in the transport equations of the turbulence model.

In an attempt to overcome these shortcomings, the $k - \epsilon - f_p$ model was introduced by van der Laan et al. (2015b). This model was based on previous research on non-linear eddy viscosity models by van der Laan et al. (2013). This research found that non-linear eddy viscosity models were superior in the simulation of wind turbine wakes compared to linear eddy viscosity models. However, they were also much more numerically unstable. It was concluded that the performance increase could mainly be attributed to the flow dependence of the C_μ coefficient in the computation of the turbulent eddy viscosity for the non-linear eddy viscosity models. Therefore, a linear eddy viscosity model with a flow-dependant C_μ was created in the $k - \epsilon - f_p$ model (van der Laan et al., 2015b). This model multiplied the original C_μ coefficient with a flow dependant factor f_p . This factor is computed according to (2.71), where f_0 is computed by (2.72) and C_R is the Rotta constant which is calibrated against LES results to be 4.5

$$f_p \left(\frac{\sigma}{\bar{\sigma}} \right) = \frac{2f_0}{1 + \sqrt{1 + 4f_0(f_0 - 1) \left(\frac{\sigma}{\bar{\sigma}} \right)^2}} \quad (2.71)$$

$$f_0 = \frac{C_R}{C_R - 1} \quad (2.72)$$

In (2.71) σ is the local shear parameter computed according to (2.73). This parameter is used to determine how far the flow deviates from the log-law regime of a simple shear flow. In regions with a high shear parameter, f_p is smaller than 1 and the eddy viscosity is decreased. This results in a lower prediction of wake recovery.

$$\sigma = \frac{k}{\epsilon} \sqrt{\left(\frac{\partial \bar{u}_i}{\partial x_j} \right)^2} \quad (2.73)$$

This model is shown to yield more accurate predictions for the velocity deficit over the standard $k - \epsilon$ model in van der Laan et al. (2015b). van der Laan et al. (2015c) showed that the model also is more accurate for double wind turbine set-up and van der Laan et al. (2015d) tested the model for three different wind farm set-ups. The model shows better results for wind farms, especially for the near wake. This yields better power predictions for the first downstream wind turbines. However, the difference between the standard $k - \epsilon$ and $k - \epsilon - f_p$ models becomes smaller for wind turbines further downstream. Furthermore, the difference in predictions becomes smaller for increasing wind farm size and wind turbine spacing. Moreover, when the wind direction is not aligned with the wind turbines, the difference between the two models becomes negligible. This can be attributed to the fact that the $k - \epsilon - f_p$ is still a linear eddy viscosity model and has trouble modelling anisotropic flows.

When including thermal stratification in the simulation, buoyancy forces are introduced which have a significant impact on the turbulence characteristics. This means that the standard $k - \epsilon$ or $k - \epsilon - f_p$ model are not sufficient to simulate non-neutral ABLs. Aside from including the buoyancy forces in the momentum equation, the adaptation is usually done by introducing additional source and sink terms in the transport equations for the TKE and ϵ . Rodi (1987) proposed a buoyancy extended $k - \epsilon$ model. Duynderke (1988) proposed to modify the model constants to be able to simulate neutral and stable boundary layers. This method is shown to be inadequate in maintaining turbulence profiles and inconsistent with the transport equations in stable conditions by Huser et al. (1997). This was due to the missing buoyancy source terms in the transport equation for TKE according to Vendel et al. (2010). Wyngaard (1975) and Brost and Wyngaard (1978) used a constant surface cooling rate in order to obtain quasi-steady conditions. According to Sogachev et al. (2012), the lack of a consistent formulation of the length scale determining equation for ϵ has limited the practical use of these closures.

MOST is often used to validate ABL models. However, it has multiple shortcomings. MOST is only valid in the surface layer and it has underlying assumptions of homogeneity and stationarity which only appear in idealised cases. Therefore, Sogachev et al. (2012) concluded that MOST is not applicable for

significant amounts of the day due to the unsteady nature of the ABL. This also led to the formulation of a consistent closure model for $k - \epsilon$ model, that includes buoyancy and vegetation effects, which does not rely on MOST in [Sogachev et al. \(2012\)](#). This closure model is not limited to homogeneous surfaces and steady state ABL conditions. [Koblitz \(2013\)](#) used the closure model from [Sogachev et al. \(2012\)](#) to simulate non-neutral ABLs. It was concluded that the vertical structure of the ABL highly depends on surface conditions which continuously change in time, leading to the use of unsteady RANS (URANS) in the simulations.

[Rodrigo et al. \(2008\)](#) also modified the $k - \epsilon$ model in order to account for thermal stratification and be in equilibrium with MOST. Even though the shortcomings of MOST are pointed out. [Cabezón et al. \(2011\)](#) compared four different closure models to simulate a wind turbine in ABL flow. The standard $k - \epsilon$ model by [Jones and Launder \(1972\)](#), the standard $k - \epsilon$ model with a correction in the ϵ equation proposed by [El Kasmí and Masson \(2008\)](#), the realizable $k - \epsilon$ model which formulates a new turbulent viscosity, includes a new transport equation for the dissipation rate and is proposed in [Shih et al. \(1995\)](#). The last model considered is the Reynolds Stress Model by [Gibson and Launder \(1978\)](#). [Cabezón et al. \(2011\)](#) concluded that the standard $k - \epsilon$ model leads to underestimations of the wind speed deficit in the stable ABL. The Reynolds Stress Model gave better results when compared to LES data, at the cost of higher computational demands.

2.3. Machine Learning in Wind Farm Simulation

Machine learning is a term used to describe a wide range of data-driven techniques within the broader field of artificial intelligence. A short discussion is given based on [Duraismy et al. \(2019\)](#). For a more complete discussion of the various machine learning techniques, [Shalev-Shwartz and Ben-David \(2014\)](#) can be referred to.

Usually machine learning methods are categorised in two categories: unsupervised and supervised learning.

In unsupervised learning there are no specific targets to predict. Instead, the goal is to discover patterns and reduce complexity. Examples of unsupervised learning techniques are clustering, which is grouping data points based on similarity, and dimension reduction, which is identifying the dependent variables that describe the data.

Supervised learning, on the other hand, constructs a mapping of the inputs to the outputs. When the output is categorical, the technique is referred to as classification. If the output is continuous, the technique is referred to as regression. Examples of supervised learning techniques are random forests, support vector machines and neural networks.

This section mainly focuses on the machine learning techniques used in turbulence and turbulent scalar flux modelling. Special attention is given to the SpaRTA method as it will be used in improving RANS simulation for wind farms in stable atmospheric boundary layers.

2.3.1. Machine Learning in Turbulence Modelling

[Duraismy et al. \(2019\)](#) gives an overview of the different ways data is being used in turbulence modelling. To do that four levels of simplifications related to RANS closure are identified.

- **L1:** uncertainties introduced by ensemble averaging that are fundamentally irrecoverable.
- **L2:** uncertainties in the functional and operational representation of the Reynolds stress.
- **L3:** uncertainties in the functional forms within a model.
- **L4:** uncertainties in the coefficients within a model.

A lot of work is done in quantifying the uncertainties introduced in the different levels. For example, [Oliver and Moser \(2011\)](#) and [Cheung et al. \(2011\)](#) used DNS data from plane channel flow, in combination with Bayesian inference, to compute posterior probability distributions of model parameters used in several different turbulence models. This quantifies L4-uncertainties and more research is done to do this. However, focus is on approaches which aim to improve the accuracy of the predictions of RANS simulations.

[Tracey et al. \(2013\)](#) used machine learning to reconstruct discrepancies in the anisotropy tensor. Starting from the eigenvalue decomposition as discussed in [Subsection 2.1.6](#), perturbations to the

eigenvalues were derived at every spatial location using a DNS data set. These perturbations were mapped into a feature space containing functions of relevant quantities, such as mean velocity gradients and turbulence quantities. This mapping was done via Gaussian process regression based on DNS data. The resulting discrepancy was relatively accurate. This was a starting point of a lot of research that combines turbulence modelling, statistical inference, uncertainty quantification and learning strategies, according to [Duraismy et al. \(2019\)](#).

[Wang et al. \(2017\)](#) and [Wu et al. \(2018\)](#) improved this perturbation strategy in order to predict discrepancies in the magnitude, anisotropy and orientation of the Reynolds stress tensor. These strategies were applied to separated flows over periodic hills and secondary flows in a square duct, significantly improving predictions of the Reynolds stress anisotropy and mean velocities.

As discussed in [Subsection 2.1.7](#) it is important to ensure Galilean invariance of learned Reynolds stress models. [Tracey et al. \(2013\)](#), [Wang et al. \(2017\)](#) and [Wu et al. \(2018\)](#) used tensor invariants based on the eigenvalue decomposition of the Reynolds stress, while [Wu et al. \(2019\)](#) considered using Euler angles and unit quaternions for representation of the orientation of the Reynolds stress. [Pope \(1975\)](#) already introduced a formulation of a more generalised expansion of the Reynolds stress tensor. This expansion is based on five invariants and ten linearly independent basis tensors. Based on the generalised expansion by [Pope \(1975\)](#), [Ling et al. \(2016c\)](#) proposed a neural network architecture with embedded invariance properties to learn the coefficients, $g^{(n)}$, of the Reynolds stress expansion. This architecture had a good predictive capability, but lacked an explicit expression for the resulting model. [Weatheritt and Sandberg \(2016, 2017\)](#) used symbolic regression and gene expression programming to learn expressions for the coefficient functions $g^{(n)}$ in the context of algebraic Reynolds stress models. These approaches yielded explicit models that are suitable for implementation. The models were learned based on DNS data of flow over a backwards facing step at a low Reynolds number and used to predict flow at a high Reynolds number, which yielded reasonably good results. However, the results still showed a high level of uncertainty when applying the models to flow over periodic hills. Lastly, [Tracey et al. \(2015\)](#) did a proof of concept study to learn known turbulence modelling terms from data using neural networks demonstrating the viability of using machine learning methods in a hybrid PDE/neural networks setting.

2.3.2. Machine Learning in Turbulent Scalar Flux Modelling

The methods described in the previous section are also being used in order to create new, more accurate models for the turbulent scalar flux. As described in [Subsection 2.1.5](#) the prevalent methods in the field are currently based on the gradient-diffusion hypothesis. However, the gradient-diffusion hypothesis has significant shortcomings, leading to the introduction of machine learning in turbulent scalar flux modelling.

[Milani et al. \(2018\)](#) tries to improve turbulent scalar flux predictions by using a random forest algorithm to infer an improved turbulent diffusivity field, purely based on local flow quantities which are computed in $k - \epsilon$ RANS simulations. These features are the mean velocity gradient, mean scalar gradient, distance to the nearest wall and the eddy viscosity. They are non-dimensionalised in order to maintain dimensional consistency. To maintain Galilean invariance invariant tensor basis functions are created from the features. The random forest method is trained using data from a skewed jet in crossflow and a wall mounted cube in crossflow and trained using data from an inclined jet in crossflow. The results showed significant quantitative and qualitative improvements over the baseline RANS case, where the turbulent diffusivity is computed using a constant turbulent Prandtl number. Especially, temperature predictions at the wall were improved. This model is further analysed in [Milani et al. \(2019\)](#) where a slight adjustment is made to the numerical scheme for solving the scalar equation, leading to improved results. Also, the model is tested for an inclined jet in favourable pressure gradient crossflow. In order to gain a more physical understanding of the created model, an investigation to the importance of the different features is performed. The most important features are the Reynolds number based on wall-distance and the turbulent viscosity ratio, even though roughly 55 % of the results are determined by features based on the velocity gradient and mean scalar gradient. Lastly, the ability of this random forest model to generalise beyond the training data is investigated in [Milani et al. \(2020b\)](#). Again small adjustments with respect to the model from [Milani et al. \(2018\)](#) are made. In [Milani et al. \(2020b\)](#) LES-based mean quantities are used as input in stead of RANS quantities. Furthermore, the turbulent diffusivity extracted from LES computations and used in training are extracted in a different way, mitigating the underestimation of turbulent diffusion. The results show improvement of mean temperature

results. In order to improve the results even further, machine learning should be used in conjunction with a more advanced, anisotropic model for the turbulent heat flux.

[Sandberg et al. \(2018\)](#) employed gene expression programming to symbolically regress nonlinear explicit algebraic stress models and heat flux closures. The Reynolds stress closure was based on [Pope \(1975\)](#) and the heat flux closure was very similar to [Milani et al. \(2018\)](#). The heat flux closure approach was still based on the gradient-diffusion hypothesis or generalised gradient hypothesis. The gene expression programming is used to develop models for the turbulent diffusivity based on eight tensor basis functions based on the non-dimensionalised temperature gradient, strain rate and rotation rate tensors. Furthermore, the model coefficients are functions of four independent invariants. This approach is applied to a fundamental trailing edge slot and results show significant improvement over the baseline RANS case.

[Weatheritt et al. \(2019\)](#) used the gene expression programming framework introduced by [Sandberg et al. \(2018\)](#) to develop scalar-flux models via symbolic regressions. The aim was to develop a more general scalar-flux closure as opposed to [Sandberg et al. \(2018\)](#) and [Milani et al. \(2018\)](#), which still relied on the gradient-diffusion hypothesis. This was done similarly to the approach of [Pope \(1975\)](#) for the Reynolds stress. [Younis et al. \(2005\)](#) identified ten basis functions and five invariants based on the non-dimensionalised Reynolds stress, strain rate and rotation rate tensors and the non-dimensionalised temperature gradient. In order to simplify the resulting model, [Weatheritt et al. \(2019\)](#) only used three tensor basis functions which were chosen based on alignment and regression power arguments. The resulting model was applied to jets in crossflow showing promising results.

[Sotgiu et al. \(2018\)](#) also created a turbulent heat flux prediction framework based on tensor representation theory from [Younis et al. \(2005\)](#). This Galilean invariant tensor representation allows the model to simulate anisotropic thermal diffusivities, as opposed to the gradient-diffusion hypothesis. However, only a few of the terms proposed in [Younis et al. \(2005\)](#) are kept, as more terms leads to irregular coefficient curves. [Sotgiu et al. \(2018\)](#) used a neural network in order to define the model coefficients as functions of invariants of the non-dimensional shear rate and Reynolds stress. The method is validated for a Poiseuille flow at different Reynolds numbers and showed improved results. This neural network framework is also shown to work for creating models for the Reynolds stress in [Sotgiu et al. \(2019\)](#).

[Milani et al. \(2020a\)](#) modified the machine learning approach from [Ling et al. \(2016a\)](#) for scalar flux closure. This constitutes a deep neural network with embedded coordinate frame invariance. As in [Milani et al. \(2018\)](#) the model is dependant on the non-dimensionalised symmetric and anti-symmetric parts of the mean velocity flux, the non-dimensionalised mean scalar gradient, turbulent viscosity ratio and Reynolds number based on wall distance. However, [Milani et al. \(2020a\)](#) identified 15 invariants and six tensor basis functions based on [Zheng \(1994\)](#). The final model takes the form of the gradient-diffusion hypothesis with a turbulent diffusivity tensor in stead of a turbulent diffusivity scalar. The model is validated with good results for inclined jets in crossflow for multiple blowing ratios.

Lastly, [Kim and Lee \(2020\)](#) applied a convolutional neural network to predict the wall-normal heat flux at the wall based only on nonlinear combinations of the wall shear stress in stream-wise and span-wise direction and the pressure fluctuations at the wall. This was done on the notion that the prediction of the turbulent heat transfer in RANS (and LES) is much less accurate than the prediction of skin friction. The results were more accurate when compared to the baseline RANS case and to simple linear and multiple linear regression.

In the future, the machine learning approaches can be improved from a better understanding where uncertainties and errors come from. This is why this field also receives significant attention. For example, [Hao and Gorlé \(2020\)](#) investigated the effects of pressure scrambling on the quantification of turbulent scalar flux model uncertainties.

2.3.3. SpaRTA Method

The SpaRTA method is introduced in [Schmelzer et al. \(2020\)](#) and aims to improve RANS simulation by learning correction terms for the turbulence anisotropy and TKE production. [Schmelzer et al. \(2020\)](#) tested the method for periodic hills, a converging-diverging channel and a curved backwards facing step. For these fundamental flows the models yielded systematic improvements over the baseline. Even models trained for one flow performed well for flows outside training range but with similar features. [Steiner et al. \(2020\)](#) applied the method to wind farms in neutral conditions. The results were encouraging, but improvement is still needed. Especially, the learned corrections for the anisotropy

tensors showed issues. [Steiner et al. \(2022\)](#) improved on this by expanding the library of features and introducing a supplemental scalar correction term for the TKE production correction. Within the learned models cancellation between different terms of complex models was observed due to the fact that the dataset requires large corrections in the wake and small corrections in the outside flow. Therefore [Steiner et al. \(2021\)](#) introduced a classifier which differentiates between the wake and outside flow. The current report is meant as a first step in expanding the SpaRTA methodology to wind farms in stable atmospheric boundary conditions, as such the classifier is considered too advanced and the focus of the following sections is on the methodology as described in [Steiner et al. \(2022\)](#).

2.3.3.1. Derivation of Optimal Correction Terms

The first step in the SpaRTA methodology is finding the optimal way to correct the RANS equations such that they match the time-averaged LES results in terms of mean velocity and turbulence intensity. To do that, the turbulence equations of the RANS simulation are solved with frozen time-averaged LES fields for velocity, \bar{u}^{LES} , turbulence kinetic energy, \bar{k}^{LES} , and Reynolds stresses, $\bar{\tau}_{ij}^{LES}$. Two correction terms are added to the transport equations: a correction of the anisotropy tensor, b_{ij}^Δ , and a correction of the turbulence kinetic energy production, \mathcal{R} . The correction term for the TKE is included in the transport equations as displayed in (2.74) and (2.75), where all frozen time-averaged quantities extracted from the LES data are denoted with a $\hat{\cdot}$ and $\sigma_k, C_{\epsilon 1}, C_{\epsilon 2}$ and σ_ϵ are coefficients. This method is called the k-corrective frozen approach.

$$\frac{D\hat{k}}{Dt} = \hat{\mathcal{P}}_k + \mathcal{R} - \epsilon + \frac{\partial}{\partial x_j} [(v + \sigma_k v_t)\hat{k}] \quad (2.74)$$

$$\frac{D\epsilon}{Dt} = [C_{\epsilon 1}(\hat{\mathcal{P}}_k + \mathcal{R}) - C_{\epsilon 2}\epsilon] \frac{\epsilon}{\hat{k}} + \frac{\partial}{\partial x_j} [(v + \sigma_\epsilon v_t)\epsilon] \quad (2.75)$$

The production term in (2.74) and (2.75) is computed according to (2.76) where the correction for the anisotropy tensor is included according to (2.77).

$$\hat{\mathcal{P}}_k = 2\hat{k}\hat{b}_{ij} \frac{\partial \hat{u}_i}{\partial x_j} \quad (2.76)$$

$$\hat{b}_{ij} = -\frac{v_t}{\hat{k}} \hat{S}_{ij} + b_{ij}^\Delta \quad (2.77)$$

The optimal values of the correction terms are computed by iteratively solving (2.74) and (2.75).

2.3.3.2. Feature Selection

In order to make a library of candidate functions, the generalised eddy viscosity formulation by [Pope \(1975\)](#), which is explained in [Subsection 2.1.7](#), is used. This means that the anisotropic part of the Reynolds stress tensor is modelled as displayed in (2.78).

$$b_{ij}^\Delta = \sum_{n=1}^{10} T_{ij}^{(n)}(S_{ij}, \Omega_{ij}) g_n^{b_{ij}^\Delta}(\boldsymbol{\lambda}, \mathbf{q}) = C^{b_{ij}^\Delta} \boldsymbol{\Theta}^{b_{ij}^\Delta} \quad (2.78)$$

In (2.78) the tensors and invariance are based on the strain rate and rotation rate tensors. A similar expression is also formulated for the production correction term in (2.79). However, (2.79) also contains a more general scalar correction, made dimensionally sound through multiplication with ϵ . This is done to capture errors in the production term itself, as well as the other model-form errors. An example of the latter is the omission of the effect of the rotor forcing on the turbulence.

$$\mathcal{R} = 2k \sum_{n=1}^{10} T_{ij}^{(n)} g_n^{\mathcal{R}}(\boldsymbol{\lambda}, \mathbf{q}) \frac{\partial \bar{u}_i}{\partial x_j} + \epsilon \cdot g_\epsilon^{\mathcal{R}}(\boldsymbol{\lambda}, \mathbf{q}) = C^{\mathcal{R}} \boldsymbol{\Theta}^{\mathcal{R}} \quad (2.79)$$

Generally, the SpaRTA methodology uses only the first four tensor basis functions of the eddy viscosity formulation from [Pope \(1975\)](#) displayed in (2.80). This is done as the first four tensors are considered sufficient in capturing the main flow correction phenomena.

$$\begin{aligned}
T_{ij}^{(1)} &= S_{ij} \\
T_{ij}^{(2)} &= S_{ik}\Omega_{kj} - \Omega_{ik}S_{kj} \\
T_{ij}^{(3)} &= S_{ik}\Omega_{kj} - \frac{1}{3}\delta_{ij}S_{mn}S_{nm} \\
T_{ij}^{(4)} &= \Omega_{ik}\Omega_{kj} - \frac{1}{3}\delta_{ij}\Omega_{mn}\Omega_{nm}
\end{aligned} \tag{2.80}$$

Aside from the changed model formulation for the TKE production correction, [Steiner et al. \(2022\)](#) also significantly increased the library of features with respect to the original formulation from [Pope \(1975\)](#). The invariants are now taken of the set $\{S_{ij}, \Omega_{ij}, A_{ij}^p, A_{ij}^k\}$, the definitions of which are given in [Table 2.1](#).

Table 2.1: Set of tensors on which the invariants used in the regression of the correction terms are based.

Tensor ID	Definition	Normalisation
S_{ij}	$\frac{1}{2}\left(\frac{\partial \bar{u}_i}{\partial x_j} + \frac{\partial \bar{u}_j}{\partial x_i}\right)$	$\frac{\epsilon}{k}$
Ω_{ij}	$\frac{1}{2}\left(\frac{\partial \bar{u}_i}{\partial x_j} - \frac{\partial \bar{u}_j}{\partial x_i}\right)$	$\frac{\epsilon}{k}$
A_{ij}^k	$-\mathbb{I} \times \nabla k$	$\frac{\epsilon}{\sqrt{k}}$
A_{ij}^p	$-\mathbb{I} \times \nabla p$	$\rho_0 \ u \nabla u\ $

Increasing the tensor set makes the pressure and turbulence kinetic energy gradients available to the models. This is done because [Kaandorp and Dwight \(2020\)](#) proved that invariants of S_{ij} and Ω_{ij} are insufficient to represent the required correction b_{ij}^A . The set of resulting invariants are displayed in [Table 2.2](#).

Table 2.2: Invariant bases, number of symmetric and anti-symmetric tensors for each invariant are indicated by n_s and n_a , respectively. The invariant bases are the trace of the tensors listed. The asterisk on a invariant bases indicates that also the cyclic permutation of the anti-symmetric tensors are included ([Steiner et al., 2022](#)).

(n_s, n_a)	Feature Index	Invariant bases
(1,0)	1-2	$\mathbf{S}^2, \mathbf{S}^3$
(0,1)	3-5	$\Omega^2, \mathbf{A}_p^2, \mathbf{A}_k^2$
(1,1)	6-14	$\Omega^2 \mathbf{S}, \Omega^2 \mathbf{S}^2, \Omega^2 \mathbf{S} \Omega \mathbf{S}^2$ $\mathbf{A}_p^2 \mathbf{S}, \mathbf{A}_p^2 \mathbf{S}^2, \mathbf{A}_p^2 \mathbf{S} \mathbf{A}_p \mathbf{S}^2$ $\mathbf{A}_k^2 \mathbf{S}, \mathbf{A}_k^2 \mathbf{S}^2, \mathbf{A}_k^2 \mathbf{S} \mathbf{A}_k \mathbf{S}^2$
(0,2)	15-17	$\Omega \mathbf{A}_p, \mathbf{A}_p \mathbf{A}_k, \Omega \mathbf{A}_k$
(1,2)	18-41	$\Omega \mathbf{A}_p \mathbf{S}, \Omega \mathbf{A}_p \mathbf{S}^2, \Omega^2 \mathbf{A}_p \mathbf{S}^*, \Omega^2 \mathbf{A}_p \mathbf{S}^{2*}, \Omega^2 \mathbf{S} \mathbf{A}_p \mathbf{S}^{2*}$ $\Omega \mathbf{A}_k \mathbf{S}, \Omega \mathbf{A}_k \mathbf{S}^2, \Omega^2 \mathbf{A}_k \mathbf{S}^*, \Omega^2 \mathbf{A}_k \mathbf{S}^{2*}, \Omega^2 \mathbf{S} \mathbf{A}_k \mathbf{S}^{2*}$ $\mathbf{A}_p \mathbf{A}_k \mathbf{S}, \mathbf{A}_p \mathbf{A}_k \mathbf{S}^2, \mathbf{A}_p^2 \mathbf{A}_k \mathbf{S}^*, \mathbf{A}_p^2 \mathbf{S} \mathbf{A}_k \mathbf{S}^{2*}$
(0,3)	42	$\Omega \mathbf{A}_p \mathbf{A}_k$
(1,3)	43-47	$\Omega \mathbf{A}_p \mathbf{A}_k \mathbf{S}, \Omega \mathbf{A}_k \mathbf{A}_p \mathbf{S}, \Omega \mathbf{A}_p \mathbf{A}_k \mathbf{S}^2, \Omega \mathbf{A}_k \mathbf{A}_p \mathbf{S}^2, \Omega \mathbf{A}_p \mathbf{S} \mathbf{A}_k \mathbf{S}^2$

Complementary to the invariants displayed in [Table 2.2](#), [Steiner et al. \(2022\)](#) also uses a set of additional physics based invariants. These physical features are displayed in [Table 2.3](#)

Table 2.3: Physics interpreted flow features. For each feature the physical description is denoted including the raw feature with its normalisation. The features that are not Galilean invariant are marked with a †(Steiner et al., 2022).

ID	Description	Raw Feature	Normalisation
q_Q	Ratio excess rotation rate to strain rate (Q criterion)	$\frac{1}{2}(\ \boldsymbol{\Omega}\ ^2 - \ \mathbf{S}\ ^2)$	$\ \mathbf{S}\ ^2$
q_{TI}^\dagger	Turbulence Intensity	k	$\frac{1}{2}\overline{u_i u_i}$
q_{ReD}	Wall distance based Reynolds number	$\frac{\sqrt{k}d}{50\nu}$	-
$q_{\partial p \partial s}^\dagger$	Pressure gradient along streamline	$\frac{\partial P}{u_k \partial x_k}$	$\sqrt{\frac{\partial P}{\partial x_j} \frac{\partial P}{\partial x_j} \overline{u_i u_i}}$
q_T	Ratio of mean turbulent to mean strain time scale	$\frac{k}{\epsilon}$	$\frac{1}{\ \mathbf{S}\ }$
q_ν	Viscosity ratio	ν_t	100ν
q_\perp^\dagger	Non-orthogonality velocity and its gradient	$\left \overline{u_i u_j} \frac{\partial \overline{u_i}}{\partial x_j} \right $	$\sqrt{\overline{u_i u_i} \overline{u_i} \frac{\partial \overline{u_i}}{\partial x_j} \overline{u_k} \frac{\partial \overline{u_k}}{\partial x_j}}$
q_{C_k/P_k}^\dagger	Ratio convection to Boussinesq production of TKE	$\overline{u_i} \frac{dk}{dx_i}$	$\left \overline{u_j' u_k' S_{jk}} \right $
q_τ	Ratio total to normal Boussinesq Reynolds stresses	$\ \overline{u_i' u_j'}_{BS}\ $	k
q_γ	Shear parameter	$\left\ \frac{\partial \overline{u_i}}{\partial x_j} \right\ $	$\frac{\epsilon}{k}$
q_F^\dagger	Actuator forcing	$\ F_{cell}\ $	$\frac{1}{2}\rho_0 A_{cell} \ \overline{u}\ $

In order to compute the library of model features, all the invariants and physical features in Table 2.2 and Table 2.3 are recombined with each other up to a maximum of three features. After which, exponentiation is applied by -1 , $-\frac{1}{2}$, $\frac{1}{2}$ and 2 . These are then multiplied with the four basis tensors displayed in (2.80) to achieve the final feature set. This feature set is vastly bigger than the feature set from Pope (1975), together with the generally large data vectors in CFD simulation, means that a preliminary step has to be taken to reduce the feature library. This is done using two methods: mutual information and cliqueing.

Mutual Information

The first method to reduce the library is by estimating the mutual information between the invariants, features and the targets. This determines whether a feature is relevant for inclusion in the regression. Mutual information is used for this as it gives an estimation of the amount of information (in bits) is obtained about the output, given an observation of the input. This means that the method does not rely on any a priori assumptions about the models, contrary to correlation coefficients, which relies on the linearity assumption. For continuous random variables X and Y , the mutual information between them is defined as (2.81) (Ver Steeg and Galstyan, 2013).

$$MI(X; Y) = \int_y \int_x p_{X,Y}(x, y) \log \frac{p_{X,Y}(x, y)}{p_X(x)p_Y(y)} dx dy \quad (2.81)$$

In (2.81) $p_{X,Y}$ is the joint probability density function and p_X and p_Y are the marginal probability functions of random variables X and Y . In practise, these underlying probability density functions are unknown and have to be estimated. Generally this is done in either of two ways: through kernel density estimators (Moon et al., 1995) or through k-nearest neighbour distances (Walters-Williams and Li, 2009). According to Goderie (2020), k-nearest neighbour is the most suitable for the current application as it has a lower computational cost, gives more accurate estimates of the mutual information, with less variation and the setting of its parameter is more straightforward than for the kernel density estimators. The k-nearest neighbours method estimates the mutual information between two random variables through (2.82) (Ver Steeg, 2000).

$$MI(X; Y) = \psi(k) + \psi(N) - \frac{1}{N} \sum_{i=1}^N (\psi(n_x(i) + 1) + \psi(n_y(i) + 1)) \quad (2.82)$$

In (2.82), ψ is the digamma function, N is the number of samples and n_x and n_y are the number of points in x and y within the maximum normal distance to the k th nearest neighbour. This method assumes that the probability density function is constant within the maximum normal distance to the k th nearest neighbour.

Cliqueing

Mutual information is used to eliminate irrelevant invariants and physical features before they are combined with each other. However, after the combination another technique is used: cliqueing. This technique is applied as there is inherently a lot of multi-collinearity within the library. Therefore, the correlation coefficient is computed between all combined features. Cliques of multiple features are formed when the correlation coefficients between them are all above 0.99. From these cliques the algebraically simplest features are kept and the rest discarded from the library. This can be done as the data is insufficient to distinguish between them anyway. Furthermore, a linear measure of correlation can be used in this case, as the combined features are linearly combined in (2.78).

2.3.3.3. Regression of Correction Terms

Then, elastic net regression is applied to identify the important terms, as displayed in (2.83).

$$\Theta = \min_{\hat{\Theta}} \left[\left\| C\hat{\Theta} - b_{ij}^A \right\|_2^2 + \alpha \rho_m \|\hat{\Theta}\|_1 + 0.5\alpha(1 - \rho_m) \|\hat{\Theta}\|_2^2 \right] \quad (2.83)$$

Elastic net regression is a mixture of Lasso regression and Ridge regression. Lasso regression promotes sparsity by allowing only a few nonzero coefficients and shrinking the rest to zero. This creates simpler models. Ridge regression enforces relatively small coefficients. Small coefficients lead to models with better convergence properties when implemented in CFD simulations. In (2.83) α is the regularisation weight and ρ_m is the mixing parameter. A larger value of α will lead to a model with less terms. The best values of ρ_m and α are not known a priori. Therefore, the elastic net regression is performed using multiple different combinations of the two values, each yielding a model.

Once a model is found from the elastic net, the unnecessary entries in the libraries are removed and the model coefficients are calibrated using Ridge regression as displayed in (2.84). λ_R is a regularization parameter which ensures the magnitude of the coefficients are not too far apart.

$$\Theta = \min_{\hat{\Theta}} \left[\left\| C\hat{\Theta} - b_{ij}^A \right\|_2^2 + \lambda_R \|\hat{\Theta}\|_2^2 \right] \quad (2.84)$$

The Ridge regression yields models for all values of λ_R for all input model structures. Then, a few models are hand-picked and tested against high-fidelity data.

2.3.3.4. Implementation in Simulation

When implementing the models trained in the previous section into CFD simulations, Steiner et al. (2021) and Steiner et al. (2022) showed there were two steps which had to be taken specific for this methodology.

Blending

The first thing which is implemented is the blending of the correction terms close to the top and bottom of the domain to zero. This is done in order to avoid interaction between the correction terms and the boundary conditions, specifically the wall model. Steiner et al. (2022) used a simplified version of the blending function from Menter (1994), which is displayed in (2.85).

$$F_{\beta}(z) = \begin{cases} \tanh \left[\left(\frac{z}{z_{low,\beta}} \right)^{\alpha} \right] & \text{for } z \leq z_{mid} \\ \tanh \left[\left(\frac{z_{max}-z}{z_{max}-z_{up,\beta}} \right)^{\alpha} \right] & \text{for } z > z_{mid} \end{cases} \quad (2.85)$$

The blending parameter, α , in (2.85) is chosen to be 4 and the lower and upper bounds for the blending was chosen for the correction to be zero in the first cell centre.

Limiters

In [Steiner et al. \(2021\)](#) numerical instabilities related to the correction terms are observed. The model for the anisotropy correction sometimes diverges in the near-wake and the model for the TKE production correction sometimes diverges at the rotor disk. [Steiner et al. \(2021\)](#) surmises there are two factors contributing to these instabilities. Firstly, the corrections remove energy almost everywhere in the flow domain as the baseline $k-\epsilon$ model tends to overpredict the TKE. Secondly, most models of [Steiner et al. \(2021\)](#) depend on products of the shear strain invariant, $\text{tr}(S_{ij}^2)$, normalised shear stress tensor, S_{ij} , and the velocity gradient. This means that when locally one component of the velocity gradient becomes too large, the effect can be amplified by the model, which means that more energy is removed and velocity gradients are increased further. In order to break the positive feedback loop without influencing the results too much, two limiters for the correction terms are introduced:

- **Eddy viscosity limiter:** the linear components of the anisotropy correction models are limited based on [van der Laan et al. \(2013\)](#):

$$b_{ij,lin}^A = \min\left(0.8 \frac{\epsilon}{k^2} \nu_t, b_{ij,lin}^A\right) \quad (2.86)$$

- **Form error limiter:** This limiter is active in areas where actuator forcing is applied, so very close to the actuator disk. It is formulated as displayed in (2.87).

$$\mathcal{R} = \text{sgn}(\mathcal{R}) \cdot \min\left(0.5 \mathcal{P}_k^{Boussinesq}, |\mathcal{R}|\right) \quad (2.87)$$

3

Generation of LES Reference Data

In order to be able to expand the SpaRTA methodology to stable atmospheric boundary layers, first high fidelity data for stable environments needs to be available. Two cases are chosen for this: an LES based on the GABLS1 inter-comparison study described in [Beare et al. \(2006\)](#) and an LES of a turbine in a stably stratified ABL data obtained from [Kokee \(2021\)](#).

3.1. Case A: Gabls1

The GABLS1 inter comparison study is a cooperative project between different universities and research institutes, all simulating a quasi-equilibrium moderately stable case based on arctic observations ([Beare et al., 2006](#)). They all performed LES simulations based on the same set of instructions, which were originally adapted from [Kosović and Curry \(2000\)](#). This case is chosen to be simulated as a large amount of validation data is available.

3.1.1. Case Definition

The case is a simple simulation of a cubic domain of air moving over flat terrain where heat is extracted to create the stable stratification. It does not contain any turbines and the general parameters of the simulation are given in [Table 3.1](#).

Table 3.1: General parameters used in simulating the GABLS1 case described in [Beare et al. \(2006\)](#).

Parameter	Description	Value	Unit
$x \times y \times z$	Domain	$400 \times 400 \times 400$	m
$\Delta_x \times \Delta_y \times \Delta_z$	Grid Resolution	$6.25 \times 6.25 \times 6.25$	m
ρ_0	Reference Density	1.3223	kg m^{-3}
θ_0	Reference Potential Temperature	263.5	K
ν	Kinematic Viscosity	1.0E-5	$\text{m}^2 \text{s}^{-1}$
κ	Von Kármán constant	0.4	-
ϕ	Latitude	73.0	°
z_0	Surface Roughness	0.1	m
U_g, V_g	Geostrophic Velocity	8.0, 0.0	m s^{-1}
θ_w	Surface Cooling Rate	0.25	K h^{-1}
S_i^m	Momentum Forcing	(0, 0.00111271, 0)	m s^{-2}
P	Simulation Period	9.0	h

3.1.2. Simulation Methodology

The LES simulations are performed using the SOWFA-6 toolbox ([Lee et al., 2016](#)) for OpenFOAM.

3.1.2.1. Governing Equations

The governing equations for continuity, momentum and potential temperature used in the SOWFA-6 toolbox are displayed in (3.1), (3.2) and (3.3) respectively (Churchfield et al., 2012b).

$$\frac{\partial \tilde{u}_i}{\partial x_i} = 0 \quad (3.1)$$

$$\frac{\partial \tilde{u}_i}{\partial t} + \frac{\partial \tilde{u}_i \tilde{u}_j}{\partial x_j} = -\frac{1}{\rho_0} \frac{\partial \tilde{p}_{rgh}}{\partial x_i} + \frac{\partial}{\partial x_j} \left(\nu \left(\frac{\partial \tilde{u}_i}{\partial x_j} + \frac{\partial \tilde{u}_j}{\partial x_i} \right) - \tau_{ij}^{SGS} - \tau_{ij}^{wall} \right) + \left(\frac{\tilde{\theta} - \theta_0}{\theta_0} \right) g_i - 2\epsilon_{i3k} \Omega_3 \tilde{u}_k + S_i^m + \frac{1}{\rho_0} f_i^T \quad (3.2)$$

$$\frac{\partial \tilde{\theta}}{\partial t} + \frac{\partial \tilde{u}_j \tilde{\theta}}{\partial x_j} = \frac{\partial}{\partial x_j} \left(\frac{\nu}{Pr} \frac{\partial \tilde{\theta}}{\partial x_j} - q_j^{SGS} - q_j^{wall} \right) \quad (3.3)$$

When comparing the SOWFA-6 momentum equation implementation in (3.2) to the general LES momentum (2.16) in Subsection 2.1.3, a couple of things are visible. First of all, the Boussinesq approximation discussed in Subsection 2.2.4 is used. Aside from that, $\frac{1}{\rho_0} \frac{\partial \tilde{p}_{rgh}}{\partial x_i}$ is the pressure gradient as deviation from hydrostatic and horizontal-mean gradient. Furthermore, τ_{ij}^{SGS} is the sub-grid scale stress and the wall stress is enforced by source term τ_{ij}^{wall} . Moreover, $\left(\frac{\tilde{\theta} - \theta_0}{\theta_0} \right) g_i$ is the buoyancy term and S_i^m is the momentum forcing term representing the mean horizontal pressure gradient driving the flow. This momentum forcing is set such that the desired geostrophic velocity is achieved. Ω_3 in the Coriolis force term equals $\frac{2\pi}{P} \sin \phi$ with P Earth's rotational period and ϕ the latitude. Lastly f_i^T are the turbine actuator forces, therefore this term is zero for the GABLS1 case.

In the potential temperature transport equation implementation in (3.3), the thermal diffusivity is replaced by the kinematic viscosity, ν , divided by the Prandtl number. Similar to the wall stress in (3.2), the wall heat flux is implemented as source term q_j^{wall} .

As sub-grid scale model for the turbulent stresses, the SOWFA-6 standard one-equation Deardorff model for planetary boundary layer flows is used (Deardorff, 1980; Moeng, 1984). This model relates the sub-grid scale stresses to the velocity gradients through a sub-grid scale viscosity as displayed in (3.4).

$$\tau_{ij}^{SGS} = -\nu_{SGS} \left(\frac{\partial \tilde{u}_i}{\partial x_j} + \frac{\partial \tilde{u}_j}{\partial x_i} \right) \quad (3.4)$$

Deardorff (1980) models the sub-grid scale viscosity as displayed in (3.5).

$$\nu_{SGS} = l C_k \sqrt{k_{SGS}} \quad (3.5)$$

In (3.5), C_k is a model constant with value 0.0673 for this case and l is a stability dependent length-scale. The value of this length-scale decreases for stably stratified conditions to include the effects of turbulence suppression. Its value is computed according to (3.6).

$$l = \min \left(\Delta, 0.76 \sqrt{k_{SGS}} N^{-1} \right) \quad (3.6)$$

In (3.6) Δ is the local grid resolution, N is the Brunt-Väisälä frequency discussed in Subsection 2.2.1 and k_{SGS} is computed by solving the transport function for the sub-grid scale TKE displayed in (3.7).

$$\frac{\partial k_{SGS}}{\partial t} + \tilde{u}_j \frac{\partial k_{SGS}}{\partial x_j} = \nu_{SGS} S^2 - \frac{\nu_{SGS}}{Pr_{SGS}} N^2 + \frac{\partial}{\partial x_j} \left(2\nu_{SGS} \frac{\partial k_{SGS}}{\partial x_j} \right) - c_\epsilon \frac{k_{SGS}^{3/2}}{l} \quad (3.7)$$

In (3.7) $S = (2S_{ij}S_{ij})^{1/2}$, which is the characteristic filtered rate of strain. c_ϵ is a model coefficient and computed according to $c_\epsilon = 0.19 + 0.74 \frac{l}{\Delta}$. Lastly, the sub-grid scale Prandtl number from (3.7) is computed according to (3.8).

$$Pr_{SGS} = \frac{1}{1 + \frac{2l}{\Delta}} \quad (3.8)$$

(3.8) causes Pr_{SGS} to approach one if the flow is locally stable and $1/3$ if the flow is unstable or neutral (Churchfield et al., 2012b).

The sub-grid scale heat flux is computed according to the gradient-diffusion hypothesis displayed in (3.9).

$$q_j^{SGS} = -\frac{\nu_{SGS}}{Pr_{SGS}} \frac{\partial \tilde{\theta}}{\partial x_j} \quad (3.9)$$

3.1.2.2. Numerical Schemes

In the LES solver, the differential operators in the equations of the previous section are discretized according to the numerical schemes named in Table 3.2. Additionally, the time stepping is constrained for a maximum CFL number of 0.75.

Table 3.2: Finite volume discretization schemes used in LES solver.

Operator	Description	Scheme	Order
$\frac{\partial}{\partial t}$	Time	CrankNicolson 0.7	2nd/1st
∇	Gradient	Gauss linear	2nd
$\nabla \cdot$	Divergence	Gauss linear	2nd
	Convection term	Gauss local blended linear upwind	2nd/1st
∇^2	Laplacian	Gauss linear uncorrected	2nd
∇_{\perp}	Surface normal gradient	Uncorrected	2nd

The schemes set in Table 3.2 are set generally according to the recommendations from Churchfield et al. (2012b). This means that no correction for non-orthogonality is implemented as the mesh is fully orthogonal. However, the CrankNicolson parameter 0.7 is slightly lower than recommended by Churchfield et al. (2012b). This parameter blends the second order accurate CrankNicolson (Crank and Nicolson, 1947) with the first order accurate Euler scheme. A higher value for this parameter means increased accuracy, but lower robustness. In this case, the simulations suffers a lot from non-physical oscillations which are dampened by a lower value for the CrankNicolson parameter. This is also the reason why the convection terms in the velocity and potential temperature equations are discretized by a blend of the second order accurate Gauss linear and first order accurate Upwind schemes. The damping of these oscillations is due to the more diffusive Upwind scheme. To compute the blending parameters for the velocity and potential temperature equation convection terms the parameters in Table 3.3 are used.

Table 3.3: Blending parameters used for blending discretization schemes of the convection terms.

Location	z	F_U	F_{θ}
1	200 m	1.0	1.0
2	300 m	0.5	0.9

Below location 1, the blending parameters are equal to the blending parameters F at location 1. This means that below this location, only the second order accurate Gauss linear scheme is used. Above location 2, the blending factors are equal to the blending factors at location 2. Between the two locations there is a smooth transition between the values. It is chosen to only blend above 200 m as that is approximately the height of the ABL. The turbulence in the ABL needs to be accurately simulated without the added diffusivity of the Upwind scheme.

3.1.2.3. Initial Conditions

The initial conditions of the GABLS1 simulations are set up according to Beare et al. (2006). The initial conditions are only a function of the altitude z and the profiles are displayed in Figure 3.1.

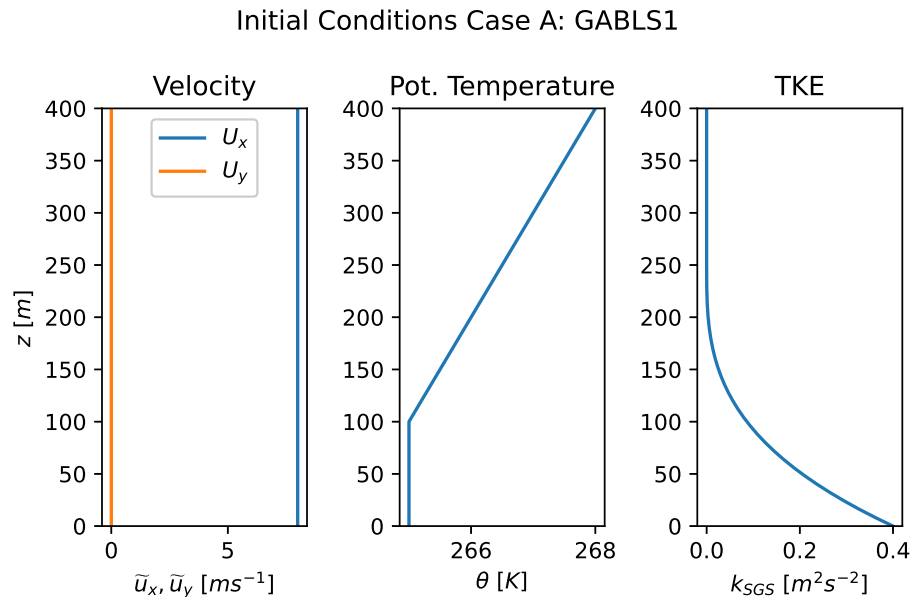


Figure 3.1: Profiles of the initial conditions according to [Beare et al. \(2006\)](#).

As can be seen in [Figure 3.1](#), the velocity is initialised throughout the domain equal to the geostrophic velocity of 8 m s^{-1} in the x-direction. The potential temperature is set as 265 K below an altitude of 100 m above which there is a capping inversion with a strength of 0.01 K m^{-1} . Aside from this, a random potential temperature perturbation of 0.1 K and 0 mean is introduced to stimulate turbulence. The turbulence kinetic energy is computed according to $k_{SGS} = 0.4(1 - z/250)^3$ below an altitude of 250 m . The sub-grid scale viscosity, sub-grid scale thermal diffusivity and pressure without hydro-static pressure are all set to 0 in the beginning after which the simulation is run for nine hours.

3.1.2.4. Boundary Conditions

The boundary conditions of the simulation are largely implemented according to the instructions of [Beare et al. \(2006\)](#). However, where necessary adaptations are made to better suit the SOWFA-6 software. All boundary conditions are displayed in [Table 3.4](#).

Table 3.4: Boundary conditions for the LES simulation of Case A: GABLS1.

BC	Lower	Upper	West	South	East	North
\tilde{u}_i	velocityABLWallFunction	slip	cyclic	cyclic	cyclic	cyclic
\tilde{p}_{rgh}	fixedFluxPressure	fixedFluxPressure	cyclic	cyclic	cyclic	cyclic
$\tilde{\theta}$	zeroGradient	fixedGradient 0.01	cyclic	cyclic	cyclic	cyclic
k_{SGS}	zeroGradient	zeroGradient	cyclic	cyclic	cyclic	cyclic
ν_{SGS}	fixedValue 0	fixedValue 0	cyclic	cyclic	cyclic	cyclic
τ_{ij}^{wall}	SchumannGrotzbach	fixedValue 0	cyclic	cyclic	cyclic	cyclic
q_j^{wall}	SpecifiedSurfaceTemperature	fixedValue 0	cyclic	cyclic	cyclic	cyclic

The velocityABLWallFunction is implemented in stead of the more commonly used no slip wall boundary condition for the velocity as this is recommended by [Churchfield et al. \(2012b\)](#) for SOWFA. This boundary condition sets the parallel velocity at the wall such that the wall-normal velocity gradient at the centre of the first cell from the wall is equal to the wall-normal velocity gradient at the top of the first cell. This is done in order for the SGS model to have a meaningful velocity gradient to use in the production terms. Important to note is that the velocity at the wall is kept parallel to the wall, so there is absolutely no wall-normal flow.

The SchumannGrotzbach boundary condition for the total stress at the boundary uses Monin-Obukhov Similarity Theory according to the Schumann/Grotzbach formulation ([Schumann, 1975](#)). The

only non-zero wall shear stress components are determined according to (3.10), where $\tilde{u}_{\parallel} = \sqrt{\tilde{u}_x^2 + \tilde{u}_y^2}$ is the wall-parallel velocity.

$$\tau_{i3} = -\frac{\tilde{u}_i}{u_{\parallel}} \tau_{wall}, \quad i = 1, 2 \quad (3.10)$$

The total wall shear stress in (3.10) is computed according to the stable version of the rough wall ABL log-law from Monin-Obukhov similarity theory as displayed in (3.11).

$$\tau_{wall} = u_*^2 = \left(\frac{\kappa \tilde{u}_{\parallel}}{\ln \frac{z_1}{z_0} + \beta_M \frac{z_1}{L_O}} \right)^2 \quad (3.11)$$

In (3.11) z_1 is the height of the first cell, z_0 is the surface roughness length scale and κ is the von Kármán constant. The MOST parameter β_M is set to be 4.8 in accordance to Beare et al. (2006). The Obukhov length is computed according to (2.55), which means that it depends on u_* . This causes the computation of the wall shear stress to be an iterative procedure until the values of u_* and L_O are converged.

Furthermore, the SpecifiedSurfaceTemperature boundary condition also uses the stable version of MOST to compute the wall heat flux needed to achieve a certain prescribed wall temperature. Following the instructions from Beare et al. (2006), the wall temperature is initially set to be 265 K, after which it decreases by -0.25 K h^{-1} . The vertical component of the wall heat flux is the only non-zero component and is computed according to (3.12).

$$q_z^{wall} = q_w = \frac{\kappa u_* \Delta \tilde{\theta}}{\ln \frac{z_1}{z_0} + \beta_H \frac{z_1}{L_O}} \quad (3.12)$$

In (3.12) $\Delta \tilde{\theta}$ is the difference between the prescribed surface temperature and the temperature in the first cell above the wall. The Obukhov length L_O also depends on the wall heat flux, as can be seen in (2.55). Therefore, the computation of the wall heat flux is also an iterative process until the values of q_w and L_O are converged. Furthermore, the value of the MOST parameter β_H is set to be 7.8 according to Beare et al. (2006).

3.1.3. Validation

In order for the LES of the GABLS1 case to be validated as ground truth for the SpaRTA methodology, first the time and planar averaged profiles are compared against literature. After that, it is investigated how steady the temporal average is and the influence of nonphysical oscillations is determined.

3.1.3.1. Profiles

The first step in validating the LES of the GABLS1 case, is comparing planar-averaged profiles of some mean parameters over the last hour of the simulation to reference data from Beare et al. (2006). It is important that the temporally averaged data is good, as this data will be used in training RANS models which only solve for time-averaged fields. Even though the stable LES set-up is inherently unsteady, as heat keeps getting removed from the domain, temporal averaging is allowed to be performed as the set-up is in quasi-equilibrium during the last hour of the simulation according to Beare et al. (2006). Quasi-equilibrium is defined by Beare et al. (2006) as when the hour-averaged mean wind velocities reach a quasi-steady state. This is also the reason why the planar averaged profiles can be used.

Figure 3.2 displays the planar averaged profiles of the temporal mean resolved potential temperature and velocity for the last hour of the simulation. The profiles show good agreement to the reference profiles from Beare et al. (2006). The most apparent difference is the fact that the atmospheric boundary layer height is slightly lower when compared to most of the other profiles. This can be ascribed to a relatively low CrankNicolson parameter which causes extra energy dissipation from the atmospheric boundary layer. This lower CrankNicolson parameter is necessitated by the oscillations in the simulation. Furthermore, the profiles are still close enough to the spread of reference profiles to be acceptable.

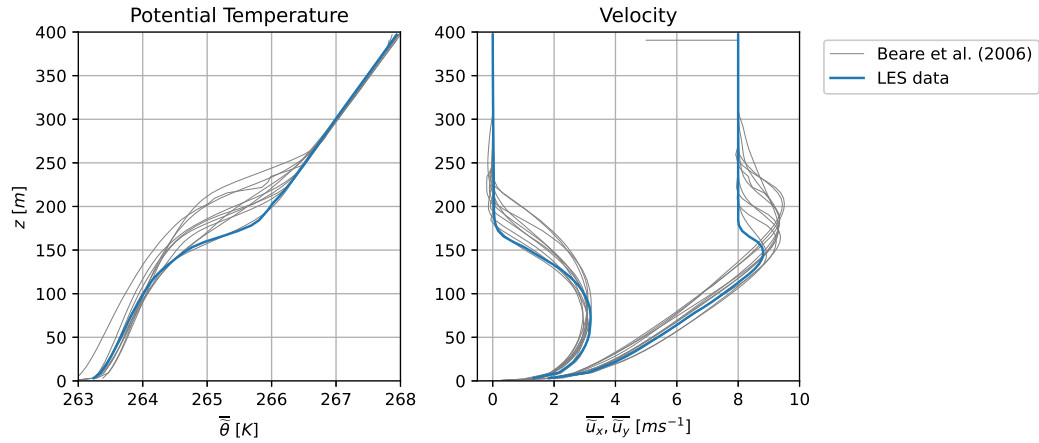


Figure 3.2: Planar-averaged profiles of the mean resolved potential temperature and mean resolved velocity over the last hour of the GABLS1 simulation.

The planar averaged profiles of the temporal averages of the resolved momentum fluxes over the last hour of the GABLS1 simulation are displayed in Figure 3.3. The mean resolved momentum fluxes are computed according to (3.13).

$$\overline{u'_i u'_j} = \frac{1}{N} \sum_{n=0}^N (u_i^n - \overline{u_i})(u_j^n - \overline{u_j}), \quad \text{with } \overline{u_i} = \frac{1}{N} \sum_{n=0}^N u_i^n \quad (3.13)$$

It is essential the data of the momentum fluxes is accurate as this data is used to compute correction terms with which to train new RANS models. When considering Figure 3.3 the profiles show good agreement with the reference data for all components. For each component the profiles are comfortably within the spread, except for $\overline{u'v'}$ for which no reference data is available. It is also visible that the horizontal momentum fluxes $\overline{u'u'}$ and $\overline{v'v'}$ are the dominant turbulence components. This confirms that the vertical turbulent motions are dampened by the stability present in the atmospheric boundary layer.

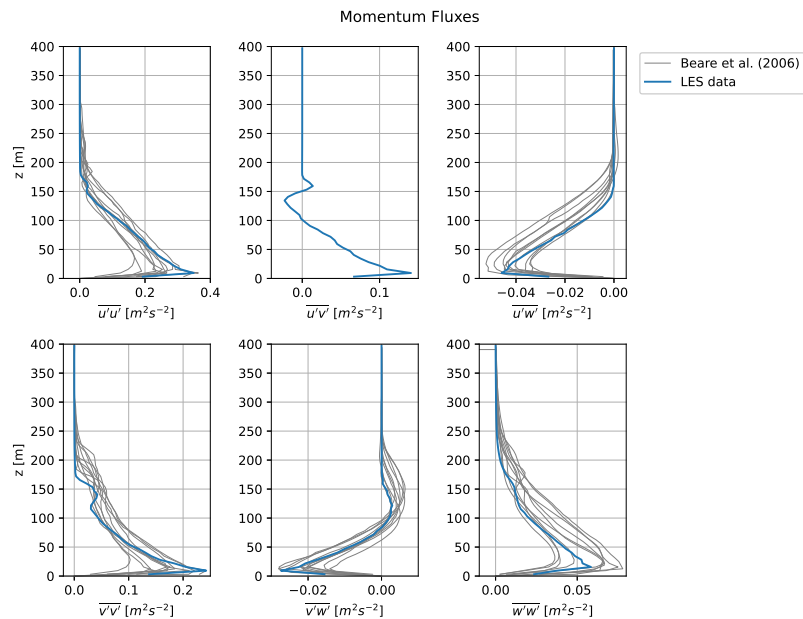


Figure 3.3: Planar averaged profiles of the mean resolved momentum fluxes over the last hour of the GABLS1 simulation.

Not only the resolved turbulence is compared to the reference data, also the sub-grid scale turbulence is compared in Figure 3.4. Figure 3.4 shows all profiles for which reference data was available. Unfortunately, that only includes the sub-grid scale turbulence kinetic energy and the xz and yz components. The profiles again show good agreement with the reference profiles, building confidence in the simulation of the turbulence present for this case.

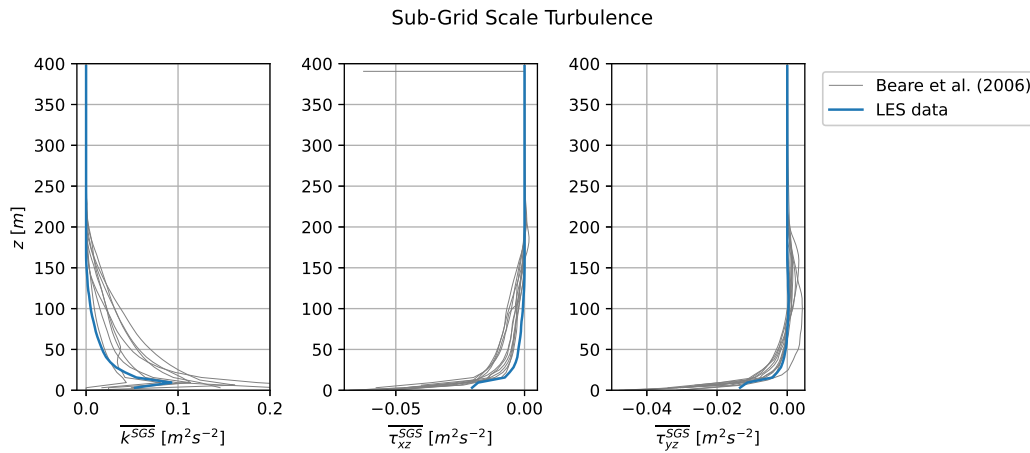


Figure 3.4: Planar averaged profiles of the mean sub-grid scale turbulence over the last hour of the GABL1 simulation.

The last profiles compared to the reference data are that of the resolved temperature fluxes in Figure 3.5. These profiles also show good agreement with the reference data, which is essential as this work aims to extend the SpaRTA methodology towards stable ABLs by improving upon the gradient-diffusion hypothesis. For this to be effective, the temperature flux data needs to be accurate. The z -component of the turbulence heat flux is approximately two times as small as the other components, suggesting that the velocity fluctuations are dominant over the temperature fluctuations in this term.

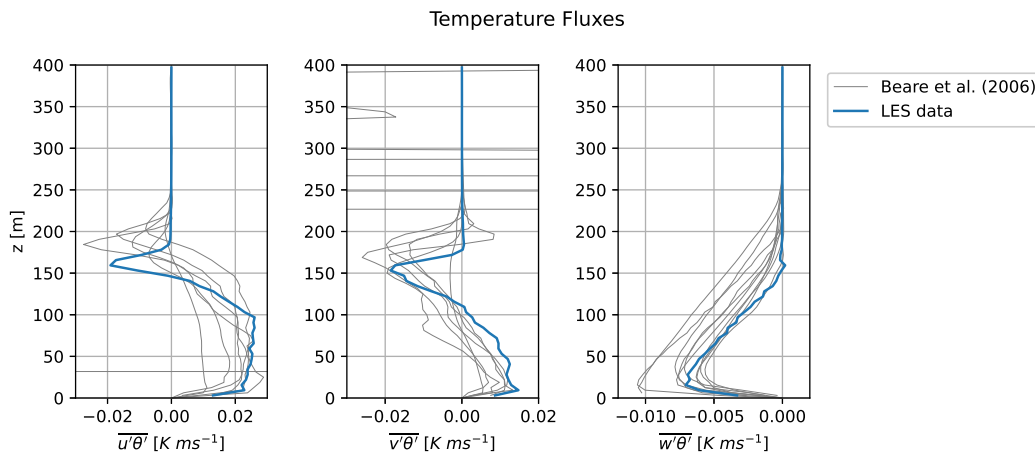


Figure 3.5: Planar averaged profiles of the mean resolved turbulent temperature fluxes over the last hour of the GABL1 simulation.

3.1.3.2. Quasi-Equilibrium

According to Beare et al. (2006) the GABL1 simulation is quasi-steady after 9 h and the temporal average can be taken over the last hour. However, the data will be used for input in a steady state RANS simulation. Therefore, this section investigates how steady the simulation actually is after nine hours.

Beare et al. (2006) defines quasi-equilibrium as when the hour-averaged mean wind reaches a quasi-steady state. When considering the mean velocity profiles taken over multiple different hours

displayed in [Figure 3.6](#), it is visible that the simulation is quite close to quasi-equilibrium. There are some deviations between the hours, especially for the transversal velocity, but for an inherently unsteady simulation the profiles are quite close.

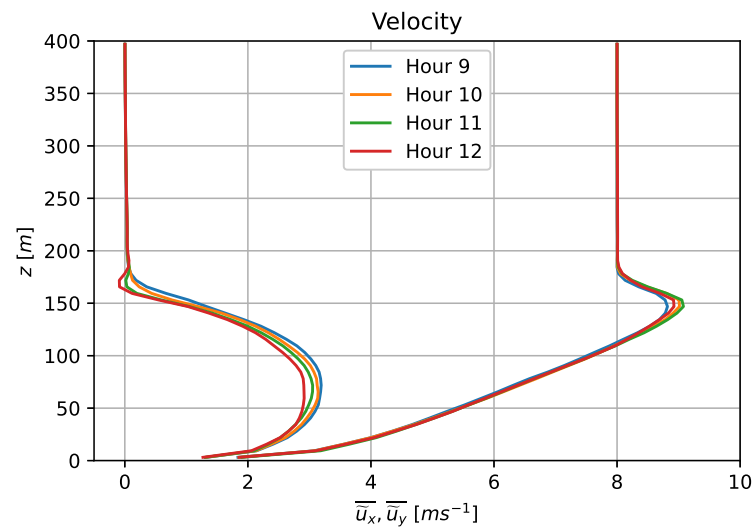


Figure 3.6: Planar averaged mean resolved velocity profiles for multiple different hours.

Doing the same for the resolved potential temperature in [Figure 3.7](#), it is visible that the temperature is far from steady state. However, this is to be expected as the bottom boundary temperature keeps decreasing with time.

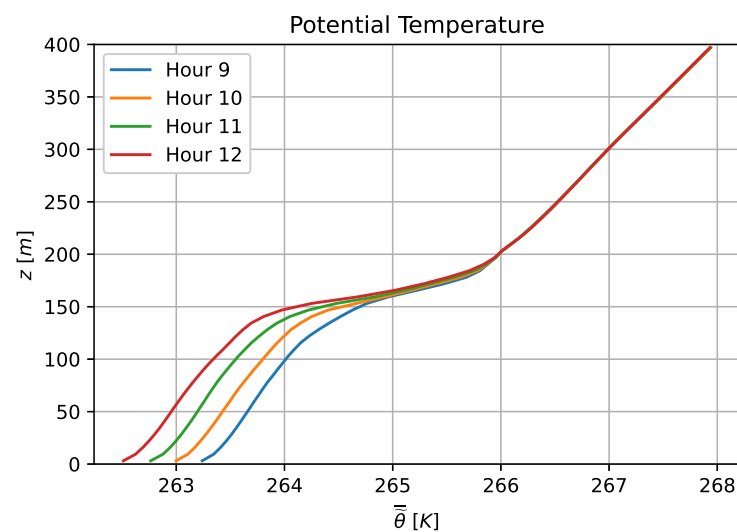


Figure 3.7: Planar averaged mean resolved potential temperature profiles for multiple different hours.

In order to judge the steadiness of the boundary conditions, a measure for the wall friction (u_*) and the wall heat flux q_w are plot over time in [Figure 3.8](#). Both show some large-timescale transient behaviour. This is somewhat more pronounced for the wall heat flux due to the scale, but the friction velocity also shows a large wavelength oscillation. This indicates that the simulation is not fully steady state. However, this is also the case for the reference data from [Beare et al. \(2006\)](#).

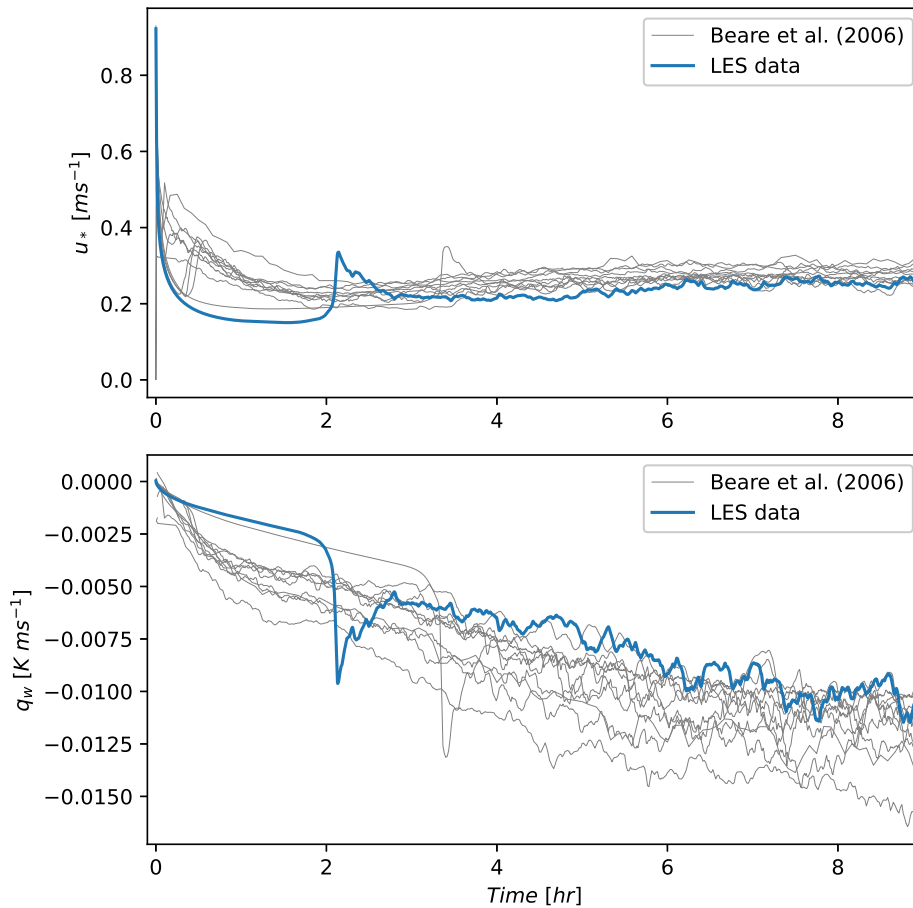


Figure 3.8: Time series of the wall friction velocity and the wall heat flux, compared against reference data from Beare et al. (2006).

The temporal average taken over different hours for the components of temperature fluxes are displayed in Figure 3.9 to judge the unsteadiness of the turbulence. These profiles show quite some unsteady behaviour. This could be explained by the fact that the temperature is unsteady while the velocity has reached quasi-equilibrium.

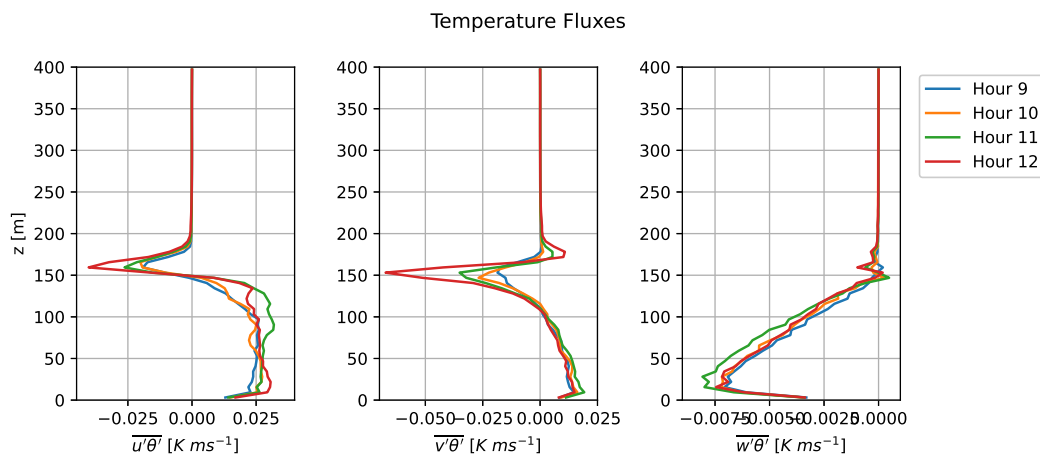


Figure 3.9: Planar averaged mean resolved temperature flux profiles for multiple different hours.

As opposed to the profiles of the temperature fluxes in Figure 3.9, the profiles of the momentum fluxes in Figure 3.10 are quite steady. The most significant transient behaviour is visible for the zz component. This would support the hypothesis that the unsteadiness in the temperature fluxes is caused by unsteadiness in the temperature itself.

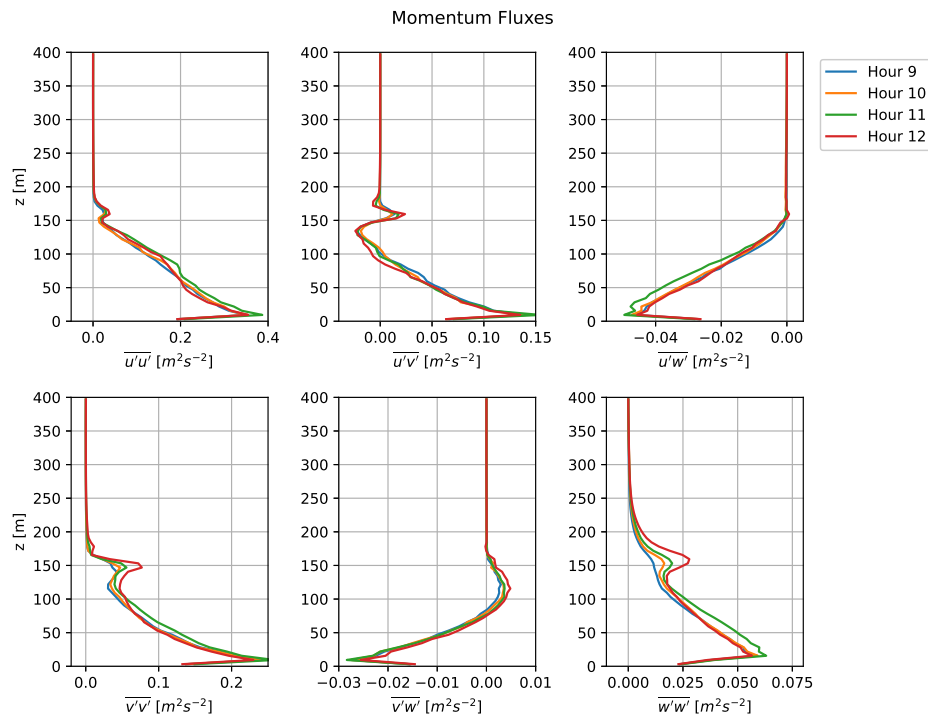


Figure 3.10: Planar averaged mean resolved momentum flux profiles for multiple different hours.

All in all, it can be concluded that quasi-equilibrium has been reached, but that is far from steady state. Especially the temperature and temperature fluxes show some clear unsteadiness. This in itself is not a huge problem when the temporally averaged data is used for steady state RANS simulations. However, it has to be kept in mind that the data is far from true steady state.

3.1.3.3. Oscillations

As described in Subsection 3.1.2, it is attempted to suppress nonphysical oscillations in two ways: blending the CrankNicolson with the more diffusive backwards time discretization scheme and blending the Gauss linear discretization of the convection terms with upwind discretization above the atmospheric boundary layer. However, when considering a slice of the mean resolved velocity in Figure 3.11, it is clear to see that some oscillations are still emanating from the ABL. It is possible that these oscillations are triggered by gravity waves, that is also why Beare et al. (2006) recommended a damping layer. However, seeing that the wavelength of these oscillations is equal to the mesh resolution, it can be concluded that the oscillations are nonphysical. Moreover, the damping layer is doing its job, as the oscillations are clearly dampened out towards the top of the domain. Unfortunately, performing this damping within the ABL itself would significantly deteriorate the results, making it impossible to dampen out all oscillations.

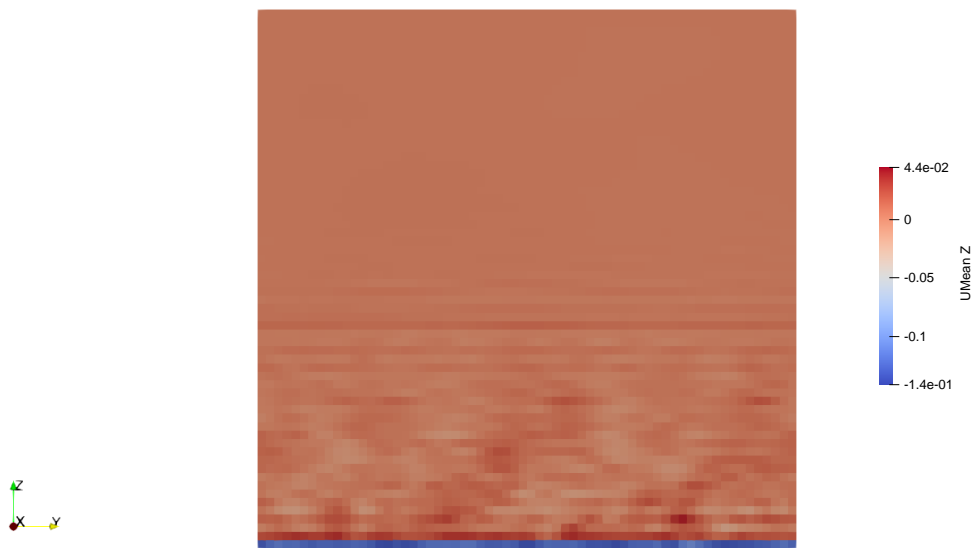


Figure 3.11: Vertical slice of mean resolved vertical velocity for the GABLS1 simulation, showing oscillations.

When taking the planar averaged profile of the mean vertical velocity in [Figure 3.12](#), the oscillations are not as present anymore. There is definitely some noise, but the fact that this noise does not have the wavelength of the grid resolution could mean that the effect of the oscillations is diminished by taking the planar average. Therefore, it is recommended to use planar averaged data whenever possible within the SpARTA methodology as this limits the influence of the nonphysical oscillations on the trained models.

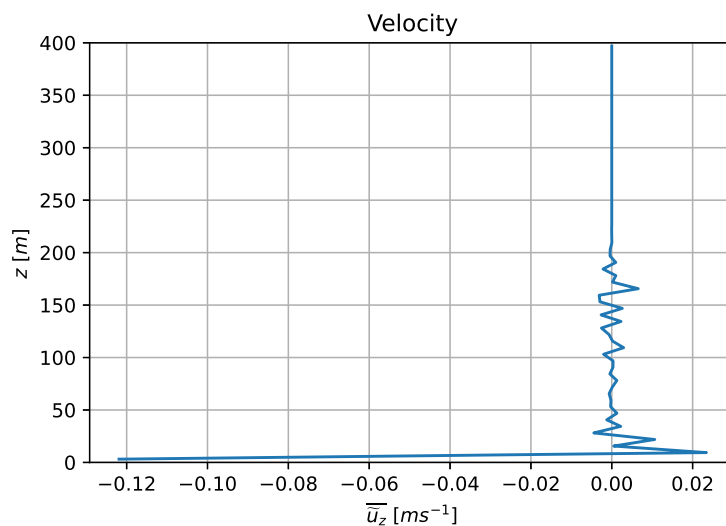


Figure 3.12: Planar averaged profile of the mean resolved vertical velocity for the GABLS1 simulation.

3.1.4. Alignment Turbulent Heat Flux and Temperature Gradient

As is explained in [Subsection 2.1.5](#), the most used method for modelling the turbulent heat flux in RANS simulation is the gradient-diffusion hypothesis. This method assumes that the turbulent heat flux vector is proportional to the temperature gradient. To see how well this hypothesis holds up, the

angle between the resolved turbulent heat flux and mean temperature gradient is computed according to (3.14) and displayed in Figure 3.13.

$$\cos \phi = \frac{\overline{u'_i \theta'} \cdot \frac{\partial \bar{\theta}}{\partial x_i}}{\left| \overline{u'_i \theta'} \right| \left| \frac{\partial \bar{\theta}}{\partial x_i} \right|} \quad (3.14)$$

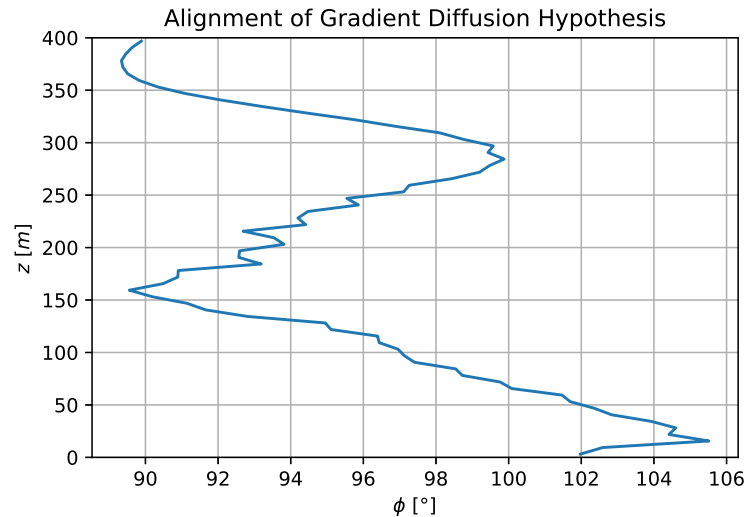


Figure 3.13: Angle between the resolved turbulent heat flux and the mean temperature gradient for the GABLS1 simulation.

Quite surprisingly, Figure 3.13 shows that the gradient-diffusion hypothesis is fundamentally flawed for the GABLS1 case as the mean temperature gradient is approximately perpendicular to the resolved turbulent heat flux throughout the domain. This is due to the fact that the gradient-diffusion hypothesis assumes isotropic turbulence, while in this case the vertical temperature gradient component is dominant, while the vertical temperature fluctuations are apparently not enough to overcome the suppressed vertical turbulent motions due to stability. Consequently, this is a highly anisotropic flow due to the stable stratification and the gradient-diffusion hypothesis breaks down. This is in accordance with observations from [Lobocki \(2013\)](#) and would suggest that not only the magnitude, but also the direction of the gradient-diffusion hypothesis needs to be corrected for when extending the SpARTA methodology towards ABLs in stably stratified regimes. However, it remains to be seen how large the effect of this discrepancy is on the RANS simulation.

3.2. Case B: Kokee SBL

The LES of this case is performed by [Kokee \(2021\)](#) and simulates a wind turbine in a similarly stable ABL as the GABLS1 inter-comparison study. This case is chosen to work with as the data is readily available to the author. As the simulation is not performed by the author, only a brief description of the simulation methodology and results is given for completeness. For a more in depth description, please refer to [Kokee \(2021\)](#).

3.2.1. Case Definition

As stated before, this case is a simulation of one wind turbine in a similar stable ABL to the GABLS1 simulation. Therefore, most general parameters displayed in [Table 3.5](#) are very similar.

Table 3.5: General parameters used in simulating the wind turbine in SBL case by Kokee (2021).

Parameter	Description	Value	Unit
$x \times y \times z$	Domain	$2000 \times 600 \times 600$	m
ρ_0	Reference Density	1.225	kg m^{-3}
θ_0	Reference Potential Temperature	263.5	K
ν	Kinematic Viscosity	1.569E-5	$\text{m}^2 \text{s}^{-1}$
κ	Von Kármán constant	0.4	-
ϕ	Latitude	73.0	°
z_0	Surface Roughness	0.1	m
U_g, V_g	Geostrophic Velocity	9.0, 0.0	m s^{-1}
θ_w	Surface Cooling Rate	0.25	K h^{-1}
S_i^m	Momentum Forcing	(0.00041, 0.00103, 0)	m s^{-2}
P	Simulation Period	10.5	h
D	Rotor Diameter	126.0	m
z_{hub}	Hub Height	87.6	m
x_{rot}, y_{rot}	Rotor location	(250, 300)	m

3.2.2. Simulation Methodology

Just as for the GABLS1 simulation, Kokee (2021) used the SOWFA-6 toolbox for OpenFOAM to perform the simulations. This means that the governing equations for the two cases are the same. In the following sections the focus will be on the differences between the two simulations.

3.2.2.1. Precursor-Successor Approach

This case simulates a wind turbine in a rectangular domain where the air flows from West to East. However, in order for the simulation to have realistic turbulent inflow conditions at the Western boundary, Kokee (2021) first performed a precursor simulation.

This precursor simulation is similar to the GABLS1 simulation, except for the fact that the momentum forcing is used to force the flow to have no lateral component at hub-height. This means a rotation of the precursor simulation with respect to the GABLS1 simulation. After nine hours the flow is considered quasi-stationary and inflow boundary data planes are gathered for another hour and a half. These data planes are then used as inflow conditions for the simulation including wind turbine as displayed in the schematic in Figure 3.14.

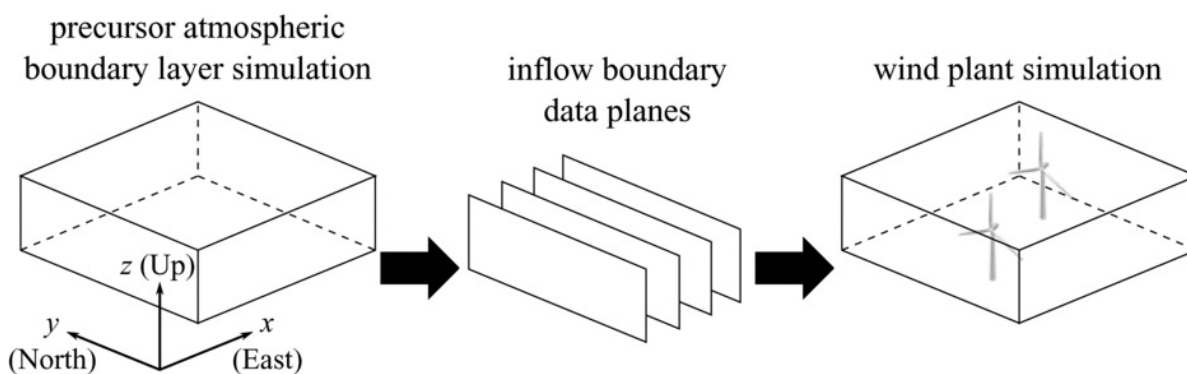


Figure 3.14: Schematic of the precursor-successor approach from Churchfield et al. (2012a).

3.2.2.2. Domain and Mesh

The domain of the Kokee SBL simulation is $2000 \text{ m} \times 600 \text{ m} \times 600 \text{ m}$. This is significantly bigger than the GABLS1 simulation domain as the wake of the turbine needs to be accurately simulated. The stable conditions contribute to a longer wake, increasing the need for a longer simulation domain. Aside from the simulation domain, the mesh resolution is also different. According to Kokee (2021) the turbine needs 25 grid cells per rotor diameter for accurate representation. This means a mesh resolution of

5 m in all directions at the turbine. To achieve this [Kokee \(2021\)](#) used a resolution of 5 m in all directions below a height of 200 m and of 10 m in all directions above 200 m. A horizontal depiction of the domain including the wind turbine is displayed in [Figure 3.15](#).

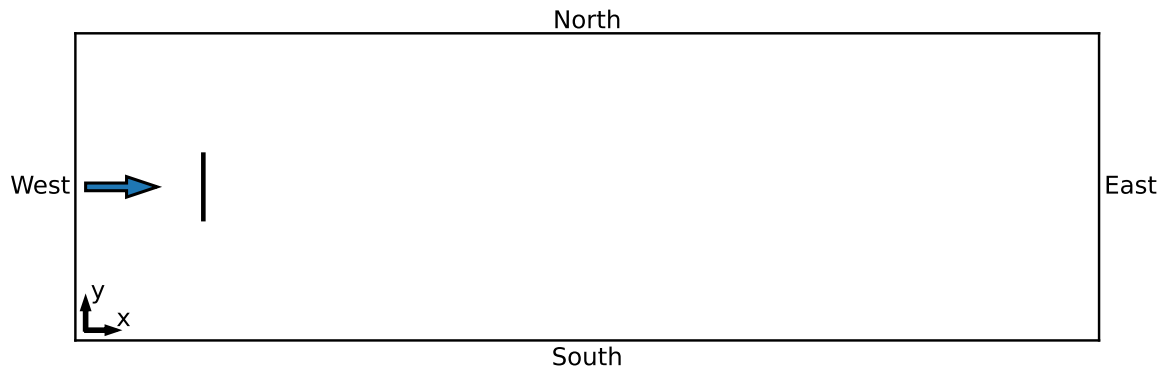


Figure 3.15: Schematic representation of the domain for Case B: Kokee SBL, with the blue arrow denoting the inflow direction and the black line denoting the wind turbine.

3.2.2.3. Numerical Schemes

[Kokee \(2021\)](#) used largely the same numerical schemes as were used for the GABLS1 simulation. The most noticeable difference is a higher CrankNicolson parameter which leads to more accurate profiles, at the cost of less damping of nonphysical oscillations.

Table 3.6: Finite volume discretization schemes used in LES solver by [Kokee \(2021\)](#).

Operator	Description	Scheme	Order
$\frac{\partial}{\partial t}$	Time	CrankNicolson 0.9	2nd/1st
∇	Gradient	Gauss linear	2nd
$\nabla \cdot$	Divergence	Gauss linear	2nd
	Convection term	Gauss local blended linear upwind	2nd/1st
∇^2	Laplacian	Gauss linear corrected	2nd
∇_{\perp}	Surface normal gradient	Corrected	2nd

3.2.2.4. Initial Conditions

For the precursor case, the initial conditions are largely the same as used for the GABLS1 simulation. The main difference is that [Kokee \(2021\)](#) initialises the sub-grid scale turbulence kinetic energy $k_{SGS} = 0.5 \text{ m}^2 \text{ s}^{-2}$ in stead of the function advised by [Beare et al. \(2006\)](#).

The successor case is initialised with the planar averaged profiles of the last time step before collecting inflow data planes of the precursor case. The downside of this is that there is a lack of proper turbulence in the initial conditions. However, this is remedied by the turbulent inflow conditions.

3.2.2.5. Boundary Conditions

The precursor case uses the same boundary conditions as the GABLS1 simulation which are displayed in [Table 3.4](#). The successor simulation uses the boundary conditions as displayed in [Table 3.7](#). The main difference in the boundary conditions between the precursor and successor simulations is the fact that the successor uses prescribed inflow conditions for the resolved velocity and resolved potential temperature in stead of cyclic boundary conditions for the inflow and outflow.

Table 3.7: Boundary conditions for the LES simulation of the successor simulation of case B: Kokee SBL.

BC	Lower	Upper	West
\tilde{u}_i	velocityABLWallFunction	slip	timeVaryingMappedFixedValue
\tilde{p}_{rgh}	fixedFluxPressure	fixedFluxPressure	fixedFluxPressure
$\tilde{\theta}$	zeroGradient	fixedGradient 0.01	timeVaryingMappedFixedValue
k_{SGS}	zeroGradient	zeroGradient	zeroGradient
ν_{SGS}	fixedValue 0	fixedValue 0	zeroGradient
τ_{ij}^{wall}	SchumannGrotzbach	fixedValue 0	fixedValue 0
q_j^{wall}	SpecifiedSurfaceTemperature	fixedValue 0	fixedValue 0
BC	South	East	North
\tilde{u}_i	cyclic	inletOutlet	cyclic
\tilde{p}_{rgh}	cyclic	zeroGradient	cyclic
$\tilde{\theta}$	cyclic	zeroGradient	cyclic
k_{SGS}	cyclic	zeroGradient	cyclic
ν_{SGS}	cyclic	zeroGradient	cyclic
τ_{ij}^{wall}	cyclic	fixedValue 0	cyclic
q_j^{wall}	cyclic	fixedValue 0	cyclic

3.2.2.6. Turbine Representation

For its turbine, Kokee (2021) used the NREL 5 MW reference turbine as described by Jonkman et al. (2009). This turbine has three blades and is representative of current industrial-scale off-shore wind turbines. The Actuator Disk Method as described in Subsection 2.2.3 is used to parameterise this turbine due to the lower computational costs and comparable performance for time-averaged fields with respect to the Actuator Line Method. According to Jonkman et al. (2009), two independent control systems control the wind power production, the generator-torque controller and the collective rotor blade pitch controller. The former controls the rotational velocity of the blades and is most active below the point where power is maximised, the latter is mostly active above that point in order for the power to be limited. This leads to the time-averaged results for the turbine displayed in Table 3.8. The wind turbine operates in the lowly loaded region below its rated point of maximum power.

Table 3.8: Time-averaged parameters for the turbine in the Kokee SBL simulation from Kokee (2021).

Parameter	Description	Value	Unit
Ω	Turbine Rotational Velocity	9.00	rpm
ϕ	Turbine Blade Pitch	0.0	$^\circ$
C_T	Thrust Coefficient	0.80	-
C_P	Power Coefficient	0.56	-

3.2.3. Validation

Table 3.9 shows some general time averaged results for the LES of Case B: Kokee SBL.

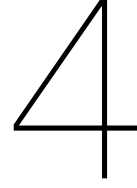
Table 3.9: Time-averaged results for the LES of Case B: Kokee SBL (Kokee, 2021).

Parameter	Description	Value	Unit
U_{hub}	Hub-height Velocity	7.45	m s^{-1}
u_*	Friction Velocity	0.25	m s^{-1}
q_w	Wall Heat Flux	-0.011	K m s^{-1}
L_O	Monin-Obukhov Length	100.0	m

As the validation of this simulation is given in Kokee (2021), only a summary of the most important results is given.

The problems of the LES for the Kokee SBL case are very similar to those for the GABLS1 LES. Most notably, that the boundary conditions and turbulence profiles show some large-period unsteady phenomena. Furthermore, the nonphysical oscillations visible in the GABLS1 simulation are also visible in the LES from [Kokee \(2021\)](#). If anything, they are even more pronounced due to the higher CrankNicolson parameter. Lastly, the misalignment between the resolved turbulence heat flux and resolved temperature gradient is also observed in this simulation.

Aside from these problems, the profiles of the time averaged simulation are validated against profiles from literature and the Rough wall atmospheric log-law. Therefore, it is determined that the quality of the simulation is sufficient to serve as a ground truth for the SpaRTA methodology.



Discovery of Optimal Correction Fields

Using the data from [Chapter 3](#), the next step in the SpaRTA methodology is discovering the optimal correction fields. The discovery is performed for Case A, and for Case B the optimal correction fields are obtained from [Kokee \(2021\)](#).

4.1. Discovery Simulation Methodology

In order to discover the optimal correction fields, a version of the k-corrective frozen RANS method first introduced in [Schmelzer et al. \(2020\)](#) is used. This method is adapted in order to account for the stratification effects.

4.1.1. Governing Equations

The implementation of the k-corrective frozen approach depends on the baseline turbulence models, which are described first. After that, the way in which the correction fields are extracted is described.

4.1.1.1. Baseline Turbulence Model

For Case A: Gabls1 it is chosen to use the two-equation $k - \epsilon$ model from [Koblitz \(2013\)](#) as baseline turbulence model, as it is developed to include stratification effects in ABL flow. [Kokee \(2021\)](#) opted for a slightly more basic turbulence model from [Duykerke \(1988\)](#) and [Wyngaard \(1975\)](#).

Case A: Gabls1

The turbulence model from [Koblitz \(2013\)](#) computes the turbulence viscosity according to (4.1) and uses the transport equations for k and ϵ displayed in (4.2) and (4.3) respectively.

$$\nu_t = C_\mu \frac{k^2}{\epsilon} \quad (4.1)$$

$$\frac{Dk}{Dt} = \mathcal{P}_k - \epsilon + \mathcal{B} + \frac{\partial}{\partial x_j} \left[\left(\nu + \frac{\nu_t}{\sigma_k} \right) \frac{\partial k}{\partial x_j} \right] \quad (4.2)$$

$$\frac{D\epsilon}{Dt} = \frac{\epsilon}{k} \left((C_{\epsilon 1}^* \mathcal{P}_k) - C_{\epsilon 2} \epsilon + C_{\epsilon 3} \mathcal{B} \right) + \frac{\partial}{\partial x_j} \left[\left(\nu + \frac{\nu_t}{\sigma_\epsilon} \right) \frac{\partial \epsilon}{\partial x_j} \right] \quad (4.3)$$

The production term \mathcal{P}_k in (4.2) and (4.3) is computed according to (4.4). Furthermore, \mathcal{B} constitutes the buoyant production or destruction of turbulence kinetic energy and is computed according to (4.5). In stable stratification, such as the GABLS1 case, this term is negative and destroys turbulence kinetic energy.

$$\mathcal{P}_k = 2\nu_t S_{ij} \frac{\partial \bar{u}_i}{\partial x_j} \quad (4.4)$$

$$\mathcal{B} = -\frac{g_j}{\theta_0} \overline{u_j' \theta'} = \frac{g_j}{\theta_0} \frac{\nu_t}{Pr_t} \frac{\partial \bar{\theta}}{\partial x_j} \quad (4.5)$$

Koblitz (2013) altered the coefficients in (4.2) and (4.3) to include the limitation of the maximum size of turbulent eddies by the finite ABL height or the stratification. Therefore, coefficient $C_{\epsilon 1}^*$ is computed according to (4.7), where the local mixing length l_m is computed according to (4.7) and the maximum mixing length l_{max} according to (4.8).

$$C_{\epsilon 1}^* = C_{\epsilon 1} + (C_{\epsilon 2} - C_{\epsilon 1}) \frac{l_m}{l_{max}} \quad (4.6)$$

$$l_m = C_{\mu}^{3/4} \frac{k^{3/2}}{\epsilon} \quad (4.7)$$

$$l_{max} = C_{\lambda} \frac{\int_0^{\infty} z \sqrt{k} dz}{\int_0^{\infty} \sqrt{k} dz} \quad (4.8)$$

Moreover, the coefficient for including the buoyant destruction in the transport equation for the dissipation, $C_{\epsilon 3}$, is computed according to (4.9). In (4.9), α_B is a stability dependent coefficient which depends on the local gradient Richardson number and the local ratio of mixing lengths, as displayed in (4.10).

$$C_{\epsilon 3} = (C_{\epsilon 1} - C_{\epsilon 2}) \alpha_B + 1 \quad (4.9)$$

$$\alpha_B = \begin{cases} 1 - \frac{l_m}{l_{max}}, & \text{Ri} = -\frac{B}{\mathcal{P}_k} > 0 \\ 1 - \left[1 + \frac{C_{\epsilon 2} - 1}{C_{\epsilon 2} - C_{\epsilon 1}} \right] \frac{l_m}{l_{max}}, & \text{Ri} = -\frac{B}{\mathcal{P}_k} < 0 \end{cases} \quad (4.10)$$

Lastly, the turbulent heat flux is computed according to the gradient-diffusion hypothesis displayed in (4.11).

$$\overline{u_j' \theta'} = -\frac{\nu_t}{\text{Pr}_t} \frac{\partial \bar{\theta}}{\partial x_j} \quad (4.11)$$

All coefficients and constants used in the implemented turbulence model from Koblitz (2013) are displayed in Table 4.1. C_{μ} and $C_{\epsilon 1}$ are different from the values recommended by Koblitz (2013) in order to better match the wall shear stress of the LES data. This will be further expanded upon in Subsection 4.1.5. $C_{\epsilon 2}$, σ_k , σ_{ϵ} and C_{λ} are set as recommended by Koblitz (2013) and Pr , ν and θ_0 are set according to the GABLS1 instructions. Lastly, the turbulent Prandtl number Pr_t is set to the standard value of 0.7 (Combest et al., 2011).

Table 4.1: Coefficients and constants used in the turbulence model from Koblitz (2013).

Coefficient	Value	Coefficient	Value
C_{μ}	0.0771	C_{λ}	0.075
$C_{\epsilon 1}$	1.6347	Pr	0.7
$C_{\epsilon 2}$	1.83	Pr_t	0.7
σ_k	2.95	ν	$1.0 \times 10^{-5} \text{ m}^2 \text{ s}^{-1}$
σ_{ϵ}	2.95	θ_0	263.5 K

Case B: Kokee SBL

The baseline turbulence model used by Kokee (2021) is very similar to the model from Koblitz (2013), but has some key differences. The eddy viscosity is also computed using (4.1) and the transport equation for the turbulence kinetic energy is the same as (4.2). However, Kokee (2021) uses a slightly altered version of the transport equation of the dissipation as displayed in (4.12).

$$\frac{D\epsilon}{Dt} = \frac{\epsilon}{k} \left(C_{\epsilon 1} \mathcal{P}_k - C_{\epsilon 2} \epsilon + C_{\epsilon 3} \mathcal{B} + C_{\epsilon 4} \frac{\mathcal{B}^2}{\epsilon} \right) + \frac{\partial}{\partial x_j} \left[\left(\nu + \frac{\nu_t}{\sigma_{\epsilon}} \right) \frac{\partial \epsilon}{\partial x_j} \right] \quad (4.12)$$

In (4.12) the (buoyant) production terms, \mathcal{P}_k and \mathcal{B} , are also computed using (4.4) and (4.5). Contrary to the baseline turbulence model used for Case A, the coefficients of the model used by Kokee (2021) are all constants and no limitation of the size of the turbulent eddies takes place. The values of the different coefficients used in the above equations are given in Table 4.2 for Case B.

Table 4.2: Coefficients and constants used in the baseline turbulence model used by Kokee (2021) for Case B: Kokee SBL.

Coefficient	Value	Coefficient	Value
C_μ	1.17	σ_k	1.0
$C_{\epsilon 1}$	1.81	σ_ϵ	1.3
$C_{\epsilon 2}$	1.92	Pr	0.7
$C_{\epsilon 3}$	0.5	Pr _t	0.85
$C_{\epsilon 4}$	1.0	ν	$1.569 \times 10^{-5} \text{ m}^2 \text{ s}^{-1}$
		θ_0	263.5 K

4.1.1.2. Postulation of Model Form Errors

As the baseline models for the two cases are slightly different, the equations for the postulation of the model form errors are also slightly different. Even though the principle of the k-corrective frozen RANS approach is the same for both cases.

Case A: GABLS1

When the k-corrective frozen approach from the SpaRTA methodology is applied to extract the model form errors from the turbulence model implementation from Koblitz (2013), the transport equations for k and ϵ are displayed in (4.13) and (4.14) (Steiner et al., 2022). In these equations, parameters denoted by a hat ($\hat{\cdot}$) are frozen fields taken from the LES data. The velocity, potential temperature, turbulent kinetic energy and turbulent heat flux are all taken to be the mean fields over the last hour of the LES.

$$\frac{D\hat{k}}{Dt} = \mathcal{P}_k + \mathcal{R} - \epsilon + \mathcal{B} + \frac{\partial}{\partial x_j} \left[\left(\nu + \frac{\nu_t}{\sigma_k} \right) \frac{\partial \hat{k}}{\partial x_j} \right] \quad (4.13)$$

$$\frac{D\epsilon}{Dt} = \frac{\epsilon}{\hat{k}} (C_{\epsilon 1}^* (\mathcal{P}_k + \mathcal{R}) - C_{\epsilon 2} \epsilon + C_{\epsilon 3} \mathcal{B}) + \frac{\partial}{\partial x_j} \left[\left(\nu + \frac{\nu_t}{\sigma_\epsilon} \right) \frac{\partial \epsilon}{\partial x_j} \right] \quad (4.14)$$

The anisotropy correction term, b_{ij}^Δ , is computed according to (4.15) and implemented in the production term as is displayed in (4.16).

$$b_{ij}^\Delta = \frac{\text{dev}(\hat{\tau}_{ij})}{2\hat{k}} + \frac{\nu_t}{\hat{k}} \hat{S}_{ij} \quad (4.15)$$

$$\mathcal{P}_k = \hat{\mathcal{P}}_k^{\text{Bouss}} + \mathcal{P}_k^\Delta = 2\nu_t \hat{S}_{ij} \frac{\partial \hat{u}_i}{\partial x_j} - 2\hat{k} b_{ij}^\Delta \frac{\partial \hat{u}_i}{\partial x_j} \quad (4.16)$$

The above equations are adaptations of the k-corrective frozen method from Steiner et al. (2022). However, in Subsection 3.1.4 it was seen that the gradient-diffusion hypothesis breaks down in the stably stratified flows of the GABLS1 and Kokee SBL cases. Therefore, a new correction term for the turbulent heat flux, q_j^Δ , is introduced in the computation of the turbulent heat flux in (4.17). Chosen is for a full correction and not just a spatial correction of the turbulent diffusivity or turbulent Prandtl number such as in Milani et al. (2018, 2019). A correction of just the turbulent diffusivity or turbulent Prandtl number constitutes a correction of just the magnitude of the turbulent heat flux, even though the misalignment between the temperature gradient and turbulent heat flux causes the gradient-diffusion hypothesis to fundamentally break down in stably stratified flows. Therefore, the directionality needs to be corrected for as well.

To compute the turbulent heat flux correction, q_j^Δ , the turbulent heat flux and temperature fields from the LES and the turbulent viscosity from the turbulence model are used.

$$\hat{q}_j = q_j^{\text{GDH}} + q_j^\Delta = -\frac{\nu_t}{\text{Pr}_t} \frac{\partial \hat{\theta}}{\partial x_j} + q_j^\Delta \quad (4.17)$$

The correction of the turbulent heat flux also means that the term for buoyant production or destruction of TKE in the transport equations is altered as displayed in (4.18).

$$\mathcal{B} = -\frac{g_j}{\theta_0} \hat{q}_j = \frac{g_j}{\theta_0} \left[\frac{\nu_t}{\text{Pr}_t} \frac{\partial \hat{\theta}}{\partial x_j} - q_j^\Delta \right] \quad (4.18)$$

Lastly, the implementation of the new turbulent heat flux correction also leads the transport equation for the potential temperature to change to (4.19). This equation is not solved in order to compute the correction fields, as the temperature field is known from the LES data.

$$\frac{\partial \hat{u}_j \hat{\theta}}{\partial x_j} = \frac{\partial}{\partial x_j} \left[\left(\frac{\nu}{\text{Pr}} + \frac{\nu_t}{\text{Pr}_t} \right) \frac{\partial \hat{\theta}}{\partial x_j} \right] - \frac{\partial q_j^\Delta}{\partial x_j} \quad (4.19)$$

Case B: Kokee SBL

The same principle is used for postulating the model form errors by Kokee (2021). Largely the same equations are used as for Case A, only the equation for the turbulent dissipation in (4.20) is slightly different due to a different transport equation in the baseline turbulence model.

$$\frac{D\epsilon}{Dt} = \frac{\epsilon}{\hat{k}} \left(C_{\epsilon 1} (\mathcal{P}_k + \mathcal{R}) - C_{\epsilon 2} \epsilon + C_{\epsilon 3} \mathcal{B} + C_{\epsilon 4} \frac{\mathcal{B}^2}{\epsilon} \right) + \frac{\partial}{\partial x_j} \left[\left(\nu + \frac{\nu_t}{\sigma_\epsilon} \right) \frac{\partial \epsilon}{\partial x_j} \right] \quad (4.20)$$

4.1.2. Numerical Schemes

The numerical schemes used in discretising the different terms in the governing equations of the two cases are displayed in Table 4.3. Important is to realise that the RANS simulation is a steady-state simulation which solves for mean quantities, rendering discretisation of the time derivative to be superfluous.

Table 4.3: Finite volume discretization schemes used in the k-corrective frozen simulations.

Operator	Description	Parameter	Scheme	Order
$\frac{\partial}{\partial t}$	Time	-	steadyState	-
$\frac{\partial}{\partial x_j}$	Gradient	-	cellLimited Gauss Linear 1.0	2nd
$\nabla \cdot$	Divergence	$\hat{u}_j, \hat{\theta}$	bounded Gauss linearUpwind	2nd
$\nabla \cdot$	Divergence	$\hat{k}, \epsilon, \hat{\tau}_{ij}$	bounded Gauss upwind	1st
$\nabla \cdot$	Divergence	default	Gauss linear	2nd
∇^2	Laplacian	-	Gauss linear corrected	2nd
∇_{\perp}	Surface normal gradient	-	Corrected	2nd

4.1.3. Initial Conditions

In order for the correction fields to be computed, initial conditions for the different parameters have to be given. For both cases, the initial conditions, and thus frozen fields, for the velocity (\hat{u}_j), potential temperature ($\hat{\theta}$) and pressure (\hat{p}_{rgh}) are taken straight from the mean fields over the last hour of the LES. The frozen field of the turbulence kinetic energy (\hat{k}) is also set from the LES data, however it is not as straightforward as for the other frozen fields. Specifically, the total frozen turbulence kinetic energy is computed from the LES fields of both the resolved and the sub-grid scale Reynolds stresses, as displayed in (4.21).

$$\hat{k} = \frac{1}{2} \text{tr} \left(\widehat{u'_i u'_j} \right) + \frac{1}{2} \text{tr} \left(\hat{\tau}_{ij}^{SGS} \right) \quad (4.21)$$

Furthermore, the frozen field for the turbulent heat flux (\hat{q}_j) also needs to be computed from a contribution from the resolved and sub-grid scale turbulent heat fluxes as displayed in (4.22).

$$\hat{q}_j = \overline{u'_j \theta'} + \hat{q}_j^{SGS} \quad (4.22)$$

From the remaining non-frozen parameters, the turbulent viscosity (ν_t) is set initially to $1 \times 10^{-5} \text{ m}^2 \text{ s}^{-1}$ throughout the domain, the dissipation rate (ϵ) initially to $1 \times 10^{-15} \text{ m}^3 \text{ s}^{-2}$ and all the correction terms (b_{ij}^Δ , \mathcal{R} , q_j^Δ) to 0.

4.1.4. Boundary Conditions

Both cases use the same boundary conditions for the k-corrective frozen RANS simulation which are displayed in Table 4.4.

Table 4.4: Boundary conditions for the k-corrective frozen RANS simulations.

BC	Lower	Upper	West
ν_t	nutkStratAtmRoughWallFunction	slip	zeroGradient
k	kqRwallFunction	slip	zeroGradient
ϵ	epsilonWallFunction	slip	zeroGradient
b_{ij}^Δ	calculated	calculated	calculated
\mathcal{R}	calculated	calculated	calculated
q_j^Δ	calculated	calculated	calculated
BC	South	East	North
ν_t	cyclic	zeroGradient	cyclic
k	cyclic	zeroGradient	cyclic
ϵ	cyclic	zeroGradient	cyclic
b_{ij}^Δ	cyclic	calculated	cyclic
\mathcal{R}	cyclic	calculated	cyclic
q_j^Δ	cyclic	calculated	cyclic

Just as for the LES the North and South boundaries are linked through a cyclic boundary condition. However, as opposed to the LES where the wall stress was set through the τ_{ij}^{wall} boundary conditions, for RANS simulations the wall stress is set through the nutkStratAtmRoughWallFunction. This is an adapted version of the generally used nutkAtmRoughWallFunction in order to include the effects of stratification. This is done according to (4.23), where \tilde{u}_\parallel is the wall-parallel velocity in the first cell, z_1 is the location of the first cell above the wall, z_0 is the roughness length scale and L_0 is the Obukhov length scale computed according to (2.55) (Kokee, 2021). Constants κ , z_0 and β_M are set to 0.4, 0.1 m and 4.8 respectively in order to match the LES.

$$\frac{\tau_{wall}}{\rho} = \nu \frac{\partial U}{\partial z} \Big|_{wall} = u_*^2 = u_* \frac{\kappa \tilde{u}_\parallel}{\ln \frac{z_1}{z_0} + \beta_M \frac{z_1}{L_0}} = C_\mu^{1/4} \sqrt{k} \frac{\kappa \tilde{u}_\parallel}{\ln \frac{z_1}{z_0} + \beta_M \frac{z_1}{L_0}} \simeq (\nu + \nu_t) \frac{\tilde{u}_\parallel}{z_1} \quad (4.23)$$

The kqRwallFunction in Table 4.4 is a simple wrapper around a zeroGradient boundary condition for TKE and the epsilonWallFunction uses either the viscous or inertial sublayer assumptions to compute ϵ at the wall.

Similarly, to Steiner et al. (2022) the corrections are blended close to the boundaries to avoid interaction with the wall functions, as described in Subsubsection 2.3.3.4. Case A uses the same blending function as Steiner et al. (2022) displayed in (2.85) to blend b_{ij}^Δ and \mathcal{R} in the lower and upper 15 m of the domain. q_j^Δ is not blended at all in Case A, as this prevents convergence of the simulation. Kokee (2021) opted to set all corrections to zero in the upper 30 m of the domain in Case B.

4.1.5. Consistency with LES System

As discussed in Subsection 4.1.4, the wall friction is implemented differently in the boundary conditions for the LES and the RANS. In order to better match the profiles between the two, the boundary conditions need to be matched according to Steiner et al. (2022). This is done to remove the influence of the mismatch from the correction fields.

The difference in the implementation of the wall friction for the LES and RANS simulations is in how they both compute u_* . The LES implementation uses the MOST log-law as displayed in (4.24).

$$u_*^{LES} \simeq \frac{\kappa \tilde{u}_{||}}{\ln \frac{z_1}{z_0} + \beta_m \frac{z_1}{L_O}} \quad (4.24)$$

Whereas the RANS implementation relates the friction velocity to the turbulence kinetic energy in the first cell above the wall according to (4.25).

$$u_*^{RANS} \simeq \sqrt[4]{C_\mu \sqrt{k_1}} \quad (4.25)$$

In order to match the TKE in the first cell above the wall in the RANS simulation to that of the LES simulation, the C_μ parameter is tuned according to (4.26).

$$C_\mu = \frac{(u_*^{LES})^4}{k_1^2} \quad (4.26)$$

Changing the value of C_μ also influences the value of $C_{\epsilon 1}$ according to the assumption of equilibrium turbulence near a wall displayed in (4.27) (Sørensen, 1995).

$$C_{\epsilon 1} = C_{\epsilon 2} - \frac{\kappa^2}{\sqrt{C_\mu} \sigma_\epsilon} \quad (4.27)$$

The resulting values for the two cases, as well as reference values from literature, are displayed in Table 4.5. The values for Case B: Kokee SBL are computed from the precursor simulation values (Kokee, 2021).

Table 4.5: Coefficients used to match LES and RANS wall friction and reference values from literature.

Flow	C_μ	$C_{\epsilon 1}$
Case A: Gabls1	0.0771	1.6347
Case B: Kokee SBL (Kokee, 2021)	1.17	1.81
Standard (Launder et al., 1975)	0.09	1.42
ABL (Sogachev et al., 2012)	0.03	1.52

In Table 4.5 it is clearly visible that the value for C_μ used by Kokee (2021) in Case B is far removed from the reference values, while Case A is much closer. Upon closer inspection of the data it is discovered that Kokee (2021) used a far too low value for the TKE at the wall to compute C_μ : $0.06 \text{ m}^2 \text{ s}^{-2}$ while the value is actually $0.18 \text{ m}^2 \text{ s}^{-2}$. This leads to a nonphysical value for C_μ which has a large influence in the wall functions as well as in the computation of the eddy viscosity. Unfortunately, this mistake was discovered too late and the data for the optimal correction fields as computed by Kokee (2021) is used moving forward. This also necessitates the use of the nonphysical value for C_μ in all RANS simulations of Case B. Moreover, this means that the optimal correction fields do not only correct model form errors, but also correct for the nonphysical value of C_μ for Case B.

4.2. Optimal Correction Fields

The methodology as described in Section 4.1 leads to correction fields for the three correction terms: b_{ij}^Δ , \mathcal{R} and q_j^Δ . For Case A, the planar averaged profiles of these fields are considered while for the successor simulation of Case B the full fields are reviewed.

4.2.1. Case A: GABLS1

When considering the planar averaged profiles for the anisotropy correction in Figure 4.1 it is clear that for most components the Boussinesq hypothesis vastly underestimates the anisotropy tensor. This leads to the correction to be approximately equal to the LES data of the anisotropy tensor. The only two components where the Boussinesq hypothesis has a significant contribution, xz and yz , the Boussinesq anisotropy tensor overshoots the trends of the LES data. This causes the anisotropy tensor correction for these two components to also be large.

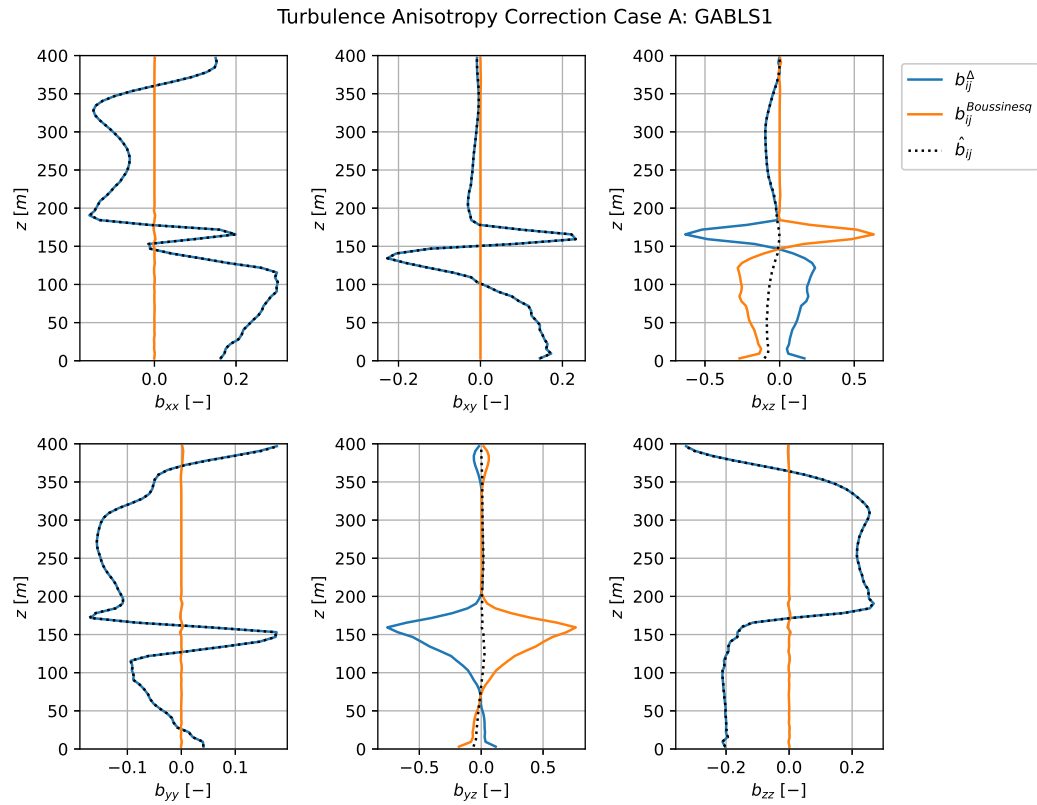


Figure 4.1: Planar averaged profiles of anisotropy correction components for Case A: GABLS1.

The planar averaged profile of the TKE production correction term is displayed in Figure 4.2. It is only active in the ABL, which is below a height of approximately 200 m and increases in magnitude closer to the wall.

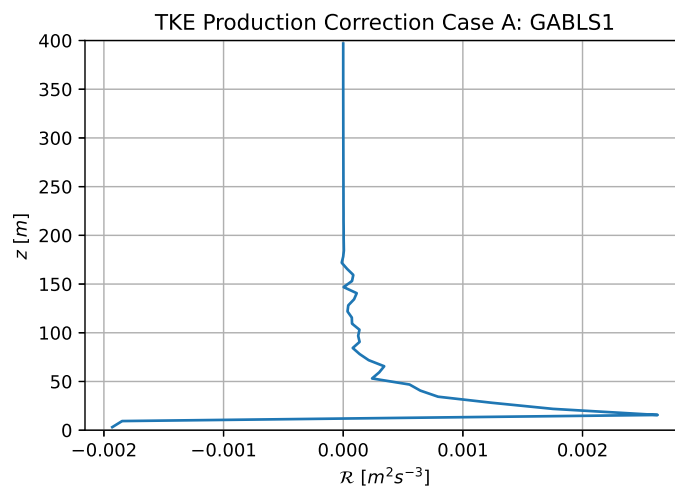


Figure 4.2: Planar averaged profile of turbulence kinetic energy production correction for Case A: GABLS1.

The planar averaged profiles of the last correction term, q_j^A , are displayed in Figure 4.3. It is clear that this term needs to correct for the complete absence of horizontal temperature fluxes in the gradient-diffusion hypothesis due to an absence of horizontal temperature gradients. The contrary is true for the vertical component, here the gradient-diffusion hypothesis overestimates the temperature flux due to

the presence of a large negative vertical temperature gradient. However, the LES data for the vertical temperature flux is smaller, leading to a positive correction of this component.

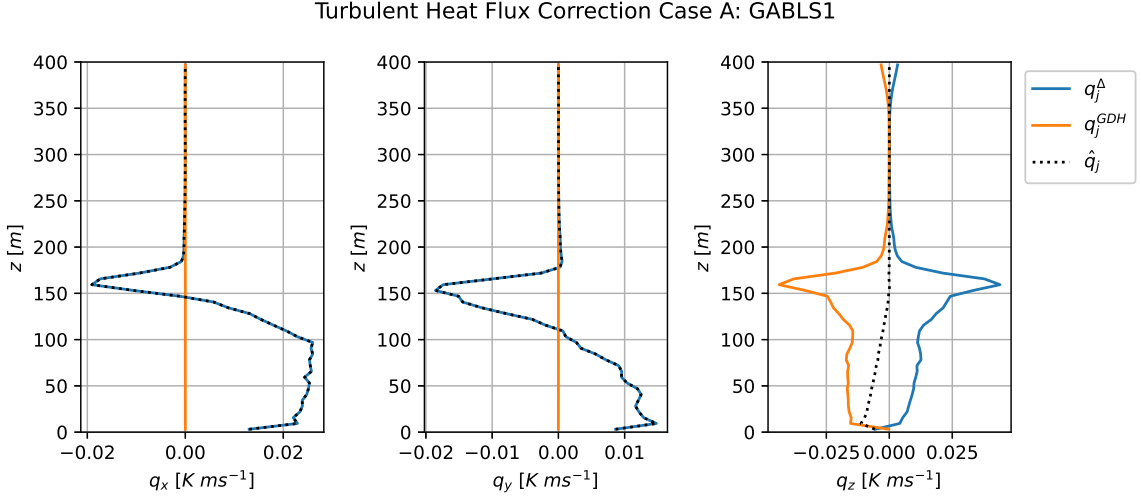


Figure 4.3: Planar averaged profiles of turbulent heat flux components for Case A: GABLS1.

Lastly, Figure 4.4 shows all the different turbulence kinetic energy production terms present in the transport equations for k and ϵ . This is done in order to capture the relative influence of the different correction terms on the simulations. Only the turbulence heat flux correction, q_j^Δ , has an influence not captured in Figure 4.4 as this term is also present in the temperature equation. In Figure 4.4 \mathcal{P}_k^Δ is the production of TKE due to the anisotropy correction, $\mathcal{P}_k^{Boussinesq}$ due to the conventional Boussinesq hypothesis, \mathcal{R}^Δ due to the turbulence kinetic energy production correction, \mathcal{B}^Δ is the buoyant TKE production due to the turbulent heat flux correction and \mathcal{B}^{GDH} is the buoyant TKE production due to the gradient-diffusion hypothesis.

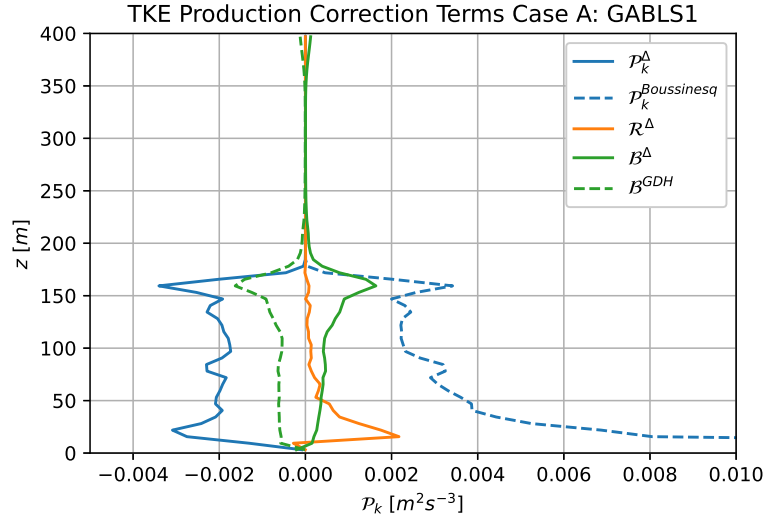


Figure 4.4: Planar averaged profiles of TKE production terms for Case A: GABLS1.

Figure 4.4 shows that the anisotropy generally counteracts the Boussinesq production of TKE. However, close to the wall this effect diminishes as the anisotropy correction is blended while the Boussinesq production only becomes larger. When considering the effect of the transport residual on the TKE correction it is clear that it is blended at the wall and generally adds TKE. Lastly, the turbulent heat flux correction counteracts most of the destruction of TKE due to the gradient-diffusion hypothesis. This

is due to the fact that the vertical component of the turbulent heat flux, which is the only component relevant in the buoyant production of TKE, is much smaller in the LES data than the gradient-diffusion hypothesis predicts.

4.2.2. Case B: Kokee SBL

Figure 4.5 displays a contour plot of the TKE production due to the anisotropy correction at the location of the rotor. This allows for a straightforward analysis of the influence of the anisotropy correction on the simulation. It is visible that the correction is most active in the near wake of the rotor, especially in the shear layer between the turbine wake and the outside flow. This is where the velocity gradients are largest and turbulence anisotropy is highest. Similarly to Case A, the anisotropy correction mainly removes TKE from the flow for Case B.

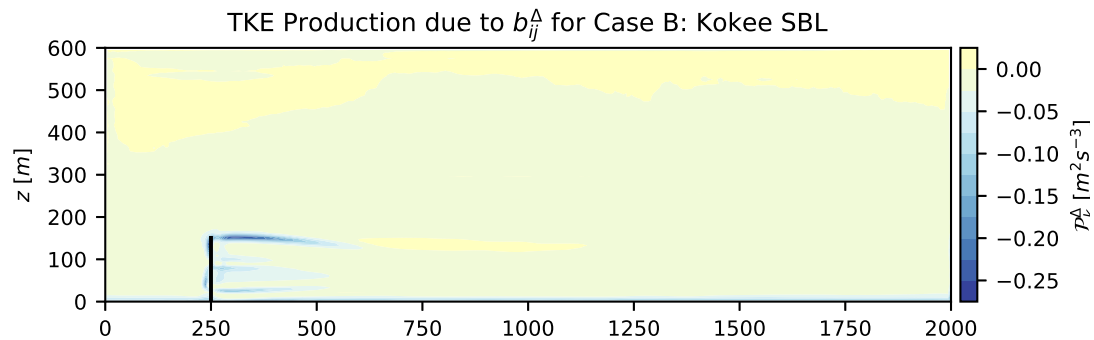


Figure 4.5: Contour plot of TKE production due to anisotropy correction field at turbine location $y = y_{hub}$ for Case B: Kokee SBL. The turbine is indicated by a black vertical line (Kokee, 2021).

Looking at the same contour plot of the TKE production correction in Figure 4.6, some differences are visible with respect to the anisotropy correction. This correction is mostly active in the shear layer of the far wake, which is the location where the wake starts to break down and turbulence is generated by the interaction between the wake and the outside flow. This correction mainly adds TKE to the simulation.

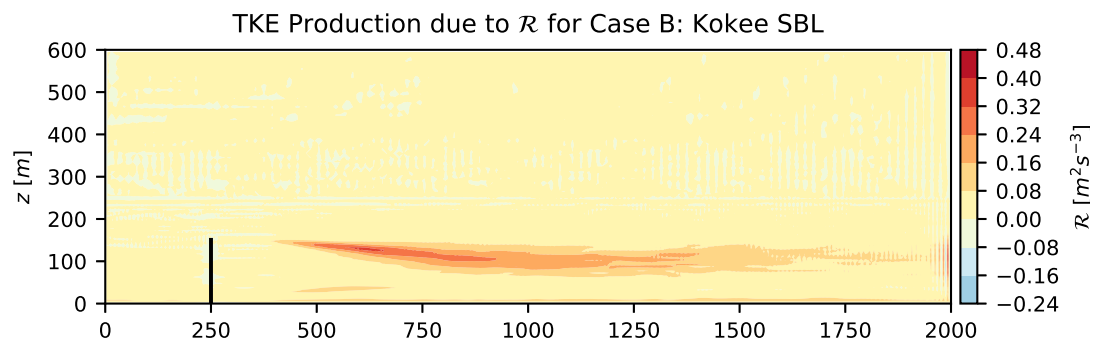


Figure 4.6: Contour plot of TKE production correction field at turbine location $y = y_{hub}$ for Case B: Kokee SBL. The turbine is indicated by a black vertical line (Kokee, 2021).

Lastly, looking at the TKE production due to the THF correction it can be seen that the correction is most active in the capping inversion of the atmospheric boundary layer. The magnitude of this production of TKE is actually not influenced by the wake, except within the wake where the production tends to zero. This would indicate that the gradient-diffusion hypothesis is more accurate within the turbine wake than in the ABL flow. Moreover, when the magnitudes of the TKE production due to the different corrections are compared, it can be concluded that the TKE production due to the THF correction is negligible.

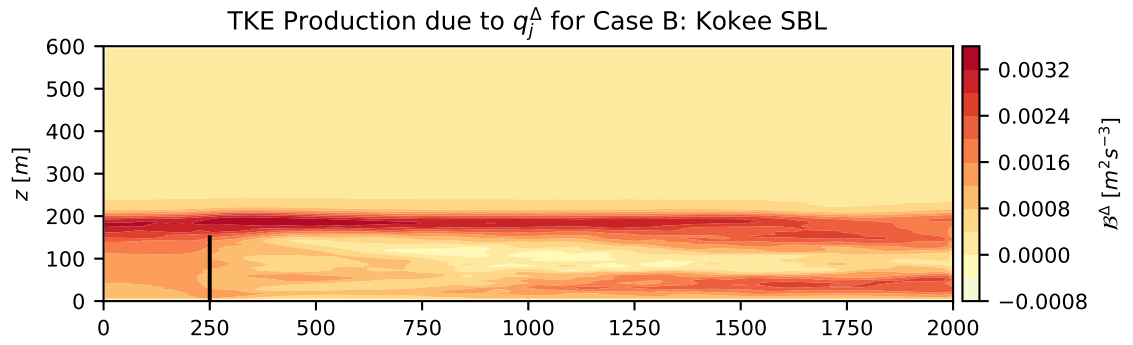


Figure 4.7: Contour plot of TKE production due to THF correction field at turbine location $y = y_{hub}$ for Case B: Kokee SBL. The turbine is indicated by a black vertical line (Kokee, 2021).

However, the THF correction influences the simulation not only due to the TKE production, but also through the temperature equation. Therefore, the different components of the THF correction field are displayed in Figure 4.8. The x -component is negative in the capping inversion and positive in the shear layer while the y -component is negative in both the shear layer and the capping inversion. Lastly, as seen in Figure 4.7, the z -component is mainly active in the capping inversion and ABL flow in stead of the turbine wake.

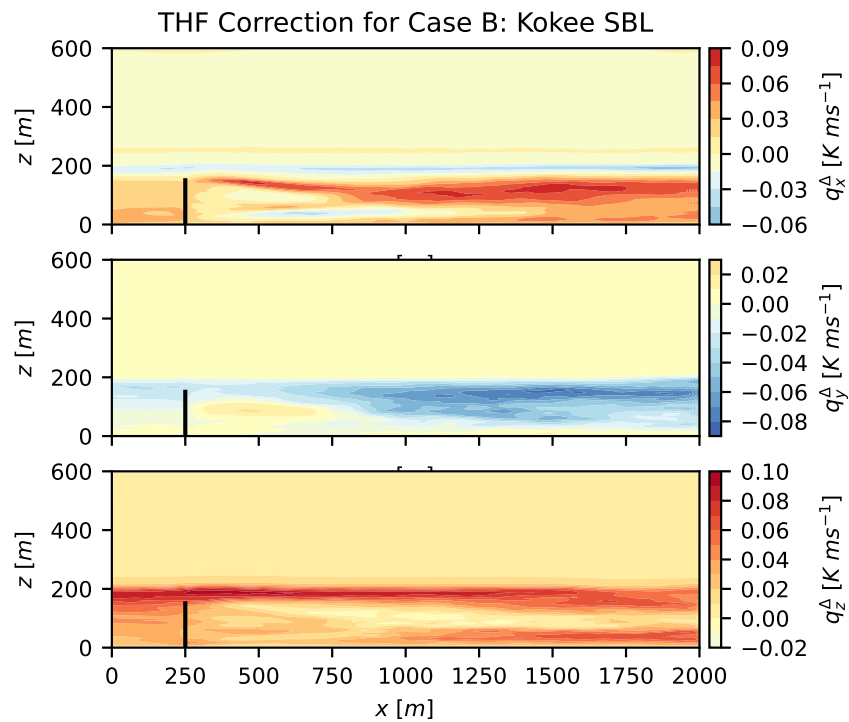


Figure 4.8: Contour plots of THF correction fields at turbine location $y = y_{hub}$ for Case B: Kokee SBL. The turbine is indicated by a black vertical line (Kokee, 2021).

5

Learning of Correction Models

In [Chapter 4](#) the optimal correction fields are generated for Case A and described for Case B. These optimal fields are used to train models to improve the RANS simulations. The optimal fields for Case B are taken from [Kokee \(2021\)](#), but the actual training of the models is performed by the author.

5.1. Model Learning Methodology

As described in [Subsection 2.3.3](#), the SpaRTA methodology uses the generalised eddy viscosity formulation by [Pope \(1975\)](#) to express the anisotropy correction as a function of ten basis tensors, T_{ij}^n , and invariant-based functions as displayed in [\(5.1\)](#) ([Steiner et al., 2022](#)).

$$b_{ij}^{\Delta} = \sum_{n=1}^{10} T_{ij}^{(n)}(S_{ij}, \Omega_{ij}) g_n^{b_{ij}^{\Delta}}(\boldsymbol{\lambda}, \mathbf{q}) = C^{b_{ij}^{\Delta}} \Theta^{b_{ij}^{\Delta}} \quad (5.1)$$

The adapted version in [\(5.2\)](#) is used for the TKE production ([Steiner et al., 2022](#)).

$$\mathcal{R} = 2k \sum_{n=1}^{10} T_{ij}^{(n)} g_n^{\mathcal{R}}(\boldsymbol{\lambda}, \mathbf{q}) \frac{\partial \bar{u}_i}{\partial x_j} + \epsilon \cdot g_{\epsilon}^{\mathcal{R}}(\boldsymbol{\lambda}, \mathbf{q}) = C^{\mathcal{R}} \Theta^{\mathcal{R}} \quad (5.2)$$

And a similar expression for the turbulent heat flux is taken from [Milani et al. \(2020a\)](#) and displayed in [\(5.3\)](#). This expression uses a different set of basis tensors, which are also based on the temperature gradient.

$$q_j^{\Delta} = \nu_t \sum_{n=11}^{16} T_j^{(n)} \left(S_{ij}, \Omega_{ij}, \frac{\partial \theta}{\partial x_j} \right) g_n^{q_j^{\Delta}}(\boldsymbol{\lambda}, \mathbf{q}) = C^{q_j^{\Delta}} \Theta^{q_j^{\Delta}} \quad (5.3)$$

The learning of the invariant-based coefficient functions happens in four steps:

1. Create library of features
2. Reduce library using mutual information and cliquing
3. Model discovery using elastic net regression
4. Model Calibration using Ridge regression

The creation of the library is done by combining all invariants and physical features with each other up to a maximum of two features. As opposed to [Steiner et al. \(2022\)](#), no exponentiation is applied in an attempt to arrive at simpler, robuster models which allow for more physical interpretation. The combined features are then combined with the tensor basis to arrive at the library. For Case A, planar-averaged data is used to alleviate the memory requirements, but for Case B this is not a possibility

and the library needs to be reduced. The first way in which this is done is by selecting the sub-domain displayed in (5.4) to be used for data, in the same way as done in Steiner et al. (2022).

$$\begin{aligned} x_{rot} - D < x < x_{rot} + 20D \\ y_{rot} - 1.5D < y < y_{rot} + 1.5D \\ 0 < z < z_{rot} + 1.5D \end{aligned} \quad (5.4)$$

The sub-domain of (5.4) spans 27 % of the total domain, but due to the mesh refinement in the lower regions, it contains 51 % of the data. Therefore, further reduction of the library is required to alleviate memory issues. Similar to Steiner et al. (2022), mutual information and cliquing are used to achieve this. Mutual information estimates the amount of information which is obtained about the output, given an observation of the input and is described in more detail in Subsection 2.3.3. Cliquing combines features with correlation coefficients above 0.99 in cliques and selects the algebraically simplest feature for representation of the whole clique. Both cases split the data in training data (75 %) to regress the models with and test data (25 %) to compute the mean and max squared error.

All the features in the resulting library are standardised to unit variance without shifting of the mean, as this would introduce a nonphysical constant term in the final model. Furthermore, the components of the target tensors are also standardised to unit variance in order to not let one component of the target tensors dominate the others.

After the final library is computed, elastic net regression is performed according to (5.5).

$$\Theta = \min_{\hat{\Theta}} \left[\left\| C\hat{\Theta} - b_{ij}^A \right\|_2^2 + \alpha \rho_m \|\hat{\Theta}\|_1 + 0.5\alpha(1 - \rho_m) \|\hat{\Theta}\|_2^2 \right] \quad (5.5)$$

In (5.5), 100 values for the regularisation weight α are used uniformly spaced on a log-scale between α_0 and α_{max} . α_0 is defined as $10^{-3}\alpha_{max}$ while α_{max} is computed according to $\alpha_{max} = \max(\mathbf{w}^T \mathbf{x}) / (N\rho_m)$, where \mathbf{w} are the feature coefficients, \mathbf{x} is the library of feature samples and N is the number of samples. α_{max} is chosen in such a way that each regularisation weight α larger than α_{max} leads to all feature coefficients \mathbf{w} set to zero. The values for the mixing parameter ρ_m are taken from (5.6). For each combination of the two parameters a model structure is computed.

$$\rho_m = [0.001, 0.01, 0.1, 0.2, 0.5, 0.7, 0.9, 0.95, 0.99, 0.999, 1.0]^T \quad (5.6)$$

For each model structure the coefficients are calibrated using Ridge regression according to (5.7).

$$\Theta = \min_{\hat{\Theta}} \left[\left\| C\hat{\Theta} - b_{ij}^A \right\|_2^2 + \lambda_R \|\hat{\Theta}\|_2^2 \right] \quad (5.7)$$

Each value for the Ridge parameter λ_R displayed in (5.8), generates a new model. Therefore, this methodology generates 7700 models from which a few are picked for implementation based on criteria such as algebraic complexity, mean-squared error and maximum error. As of yet there is no a priori set of selection criteria to consistently choose the best model.

$$\lambda_R = [0, 1e-5, 0.001, 0.01, 0.1, 0.25, 0.5]^T \quad (5.8)$$

5.2. Feature Selection

As discussed in Section 5.1 the selection of the features consists of two main steps: creation and reduction of the library.

5.2.1. Creation of Library

As displayed in (5.9), the tensor basis for regressing the correction models for the anisotropy and TKE production, b_{ij}^A and \mathcal{R} , are taken from Pope (1975), just as done by Steiner et al. (2022).

$$\begin{aligned}
T_{ij}^{(1)} &= S_{ij}, T_{ij}^{(2)} = S_{ik}\Omega_{kj} - \Omega_{ik}S_{kj}, T_{ij}^{(3)} = S_{ik}S_{kj} - \frac{1}{3}\delta_{ij}S_{mn}S_{nm}, \\
T_{ij}^{(4)} &= \Omega_{ik}\Omega_{kj} - \frac{1}{3}\delta_{ij}\Omega_{mn}\Omega_{nm}, T_{ij}^{(5)} = \Omega_{ik}S_{kl}S_{lj} - S_{ik}S_{kl}\Omega_{lj}, \\
T_{ij}^{(6)} &= \Omega_{ik}\Omega_{kl}S_{lj} + S_{ik}\Omega_{kl}\Omega_{lj} - \frac{2}{3}\delta_{ij}S_{mn}\Omega_{no}\Omega_{om}, T_{ij}^{(7)} = \Omega_{ik}S_{kl}\Omega_{lm}\Omega_{mj} - \Omega_{ik}\Omega_{kl}S_{lm}\Omega_{mj}, \\
T_{ij}^{(8)} &= S_{ik}\Omega_{kl}S_{lm}S_{mj} - S_{ik}S_{kl}\Omega_{lm}S_{mj}, \\
T_{ij}^{(9)} &= \Omega_{ik}\Omega_{kl}S_{lm}S_{mj} + S_{ik}S_{kl}\Omega_{lm}\Omega_{mj} - \frac{2}{3}\delta_{ij}S_{no}S_{op}\Omega_{pq}\Omega_{qn}, \\
T_{ij}^{(10)} &= \Omega_{ik}S_{kl}S_{lm}\Omega_{mn}\Omega_{nj} - \Omega_{ik}\Omega_{kl}S_{lm}S_{mn}\Omega_{nj},
\end{aligned} \tag{5.9}$$

The tensor basis for the turbulent heat flux correction, q_j^A , is displayed in (5.10) according to Milani et al. (2020a).

$$\begin{aligned}
T_j^{(11)} &= \frac{\partial \theta}{\partial x_j}, & T_j^{(12)} &= S_{jk} \frac{\partial \theta}{\partial x_k}, & T_j^{(13)} &= \Omega_{jk} \frac{\partial \theta}{\partial x_k}, \\
T_j^{(14)} &= S_{jk} S_{kl} \frac{\partial \theta}{\partial x_l}, & T_j^{(15)} &= \Omega_{jk} \Omega_{kl} \frac{\partial \theta}{\partial x_l}, & T_j^{(16)} &= (S_{jk} \Omega_{kl} + \Omega_{jk} S_{kl}) \frac{\partial \theta}{\partial x_l}
\end{aligned} \tag{5.10}$$

The same set of invariants and physical features is used for learning the models for all three correction terms. The invariants used in this case are not based on the set $\{S_{ij}, \Omega_{ij}, A_{ij}^p, A_{ij}^k\}$ as in Steiner et al. (2022), but rather the invariants are taken of the set $\{S_{ij}, \Omega_{ij}, A_{ij}^\theta, A_{ij}^k\}$. This allows for the stratification to be included in the correction models. The definitions of the different terms are displayed in Table 5.1

Table 5.1: Set of tensors on which the invariants used in the regression of the correction terms are based.

Tensor ID	Definition	Normalisation
S_{ij}	$\frac{1}{2} \left(\frac{\partial \bar{u}_i}{\partial x_j} + \frac{\partial \bar{u}_j}{\partial x_i} \right)$	$\frac{\epsilon}{k}$
Ω_{ij}	$\frac{1}{2} \left(\frac{\partial \bar{u}_i}{\partial x_j} - \frac{\partial \bar{u}_j}{\partial x_i} \right)$	$\frac{\epsilon}{k}$
A_{ij}^k	$-\mathbb{I} \times \nabla k$	$\frac{\epsilon}{\sqrt{k}}$
A_{ij}^θ	$-\mathbb{I} \times \nabla \theta$	$\theta_0 \frac{\epsilon}{k\sqrt{k}}$

The resulting set of invariants used in creating the library is displayed in Table 5.2.

Table 5.2: Invariant bases. The number of symmetric and anti-symmetric tensors for each invariant are indicated by n_s and n_a , respectively. The invariant bases are the trace of the tensors listed. The asterisk on a invariant bases indicates that also the cyclic permutation of the anti-symmetric tensors are included (Steiner et al., 2022).

(n_s, n_a)	Feature Index	Invariant bases
(1,0)	1-2	$\mathbf{S}^2, \mathbf{S}^3$
(0,1)	3-5	$\mathbf{\Omega}^2, \mathbf{A}_\theta^2, \mathbf{A}_k^2$
(1,1)	6-14	$\mathbf{\Omega}^2 \mathbf{S}, \mathbf{\Omega}^2 \mathbf{S}^2, \mathbf{\Omega}^2 \mathbf{S} \mathbf{\Omega} \mathbf{S}^2$ $\mathbf{A}_\theta^2 \mathbf{S}, \mathbf{A}_\theta^2 \mathbf{S}^2, \mathbf{A}_\theta^2 \mathbf{S} \mathbf{A}_\theta \mathbf{S}^2$ $\mathbf{A}_k^2 \mathbf{S}, \mathbf{A}_k^2 \mathbf{S}^2, \mathbf{A}_k^2 \mathbf{S} \mathbf{A}_k \mathbf{S}^2$
(0,2)	15-17	$\mathbf{\Omega} \mathbf{A}_\theta, \mathbf{A}_\theta \mathbf{A}_k, \mathbf{\Omega} \mathbf{A}_k$
(1,2)	18-41	$\mathbf{\Omega} \mathbf{A}_\theta \mathbf{S}, \mathbf{\Omega} \mathbf{A}_\theta \mathbf{S}^2, \mathbf{\Omega}^2 \mathbf{A}_\theta \mathbf{S}^*, \mathbf{\Omega}^2 \mathbf{A}_\theta \mathbf{S}^{2*}, \mathbf{\Omega}^2 \mathbf{S} \mathbf{A}_\theta \mathbf{S}^{2*}$ $\mathbf{\Omega} \mathbf{A}_k \mathbf{S}, \mathbf{\Omega} \mathbf{A}_k \mathbf{S}^2, \mathbf{\Omega}^2 \mathbf{A}_k \mathbf{S}^*, \mathbf{\Omega}^2 \mathbf{A}_k \mathbf{S}^{2*}, \mathbf{\Omega}^2 \mathbf{S} \mathbf{A}_k \mathbf{S}^{2*}$ $\mathbf{A}_\theta \mathbf{A}_k \mathbf{S}, \mathbf{A}_\theta \mathbf{A}_k \mathbf{S}^2, \mathbf{A}_\theta^2 \mathbf{A}_k \mathbf{S}^*, \mathbf{A}_\theta^2 \mathbf{S} \mathbf{A}_k \mathbf{S}^{2*}$
(0,3)	42	$\mathbf{\Omega} \mathbf{A}_\theta \mathbf{A}_k$
(1,3)	43-47	$\mathbf{\Omega} \mathbf{A}_\theta \mathbf{A}_k \mathbf{S}, \mathbf{\Omega} \mathbf{A}_k \mathbf{A}_\theta \mathbf{S}, \mathbf{\Omega} \mathbf{A}_\theta \mathbf{A}_k \mathbf{S}^2, \mathbf{\Omega} \mathbf{A}_k \mathbf{A}_\theta \mathbf{S}^2, \mathbf{\Omega} \mathbf{A}_\theta \mathbf{S} \mathbf{A}_k \mathbf{S}^2$

Decided is to use the same physics based features as [Steiner et al. \(2022\)](#), with the addition of one feature based on the magnitude of the turbulent heat flux according to the gradient-diffusion hypothesis in order to include a thermal stratification feature. The resulting set of physics informed flow features is displayed in [Table 5.3](#). The actuator forcing feature is only used for Case B as there are no turbines, and thus no actuator forces, in Case A.

Table 5.3: Physics interpreted flow features. For each feature the physical description is denoted including the raw feature with its normalisation. The features that are not Galilean invariant are marked with a †([Steiner et al., 2022](#)).

ID	Description	Raw Feature	Normalisation
q_Q	Ratio excess rotation rate to strain rate (Q criterion)	$\frac{1}{2}(\ \boldsymbol{\Omega}\ ^2 - \ \mathbf{S}\ ^2)$	$\ \mathbf{S}\ ^2$
q_{TI}^\dagger	Turbulence Intensity	k	$\frac{1}{2}\overline{u_i u_i}$
q_{ReD}	Wall distance based Reynolds number	$\frac{\sqrt{k}d}{50\nu}$	-
$q_{\partial p \partial s}^\dagger$	Pressure gradient along streamline	$\frac{\partial P}{u_k \partial x_k}$	$\sqrt{\frac{\partial P}{\partial x_j} \frac{\partial P}{\partial x_j} \overline{u_i u_i}}$
q_T	Ratio of mean turbulent to mean strain time scale	$\frac{k}{\epsilon}$	$\frac{1}{\ \mathbf{S}\ }$
q_ν	Viscosity ratio	ν_t	100ν
q_\perp^\dagger	Non-orthogonality velocity and its gradient	$\left \overline{u_i u_j} \frac{\partial \overline{u_i}}{\partial x_j} \right $	$\sqrt{\overline{u_i u_i} \overline{u_i u_i} \frac{\partial \overline{u_i}}{\partial x_j} \frac{\partial \overline{u_k}}{\partial x_j}}$
q_{C_k/P_k}^\dagger	Ratio convection to Boussinesq production of TKE	$\overline{u_i} \frac{dk}{dx_i}$	$\left \overline{u'_j u'_k} S_{jk} \right $
q_τ	Ratio total to normal Boussinesq Reynolds stresses	$\ \overline{u'_i u'_j}_{BS}\ $	k
q_γ	Shear parameter	$\left\ \frac{\partial \overline{u_i}}{\partial x_j} \right\ $	$\frac{\epsilon}{k}$
q_F^\dagger	Actuator forcing	$\ F_{cell}\ $	$\frac{1}{2}\rho_0 A_{cell} \ \overline{u}\ $
q_{GDH}	Magnitude of THF according to GDH	$\left\ -\frac{\nu_t}{Pr_t} \frac{\partial \overline{\theta}}{\partial x_j} \right\ $	$\theta_0 \sqrt{k}$

5.2.2. Reduction of Library Using Mutual Information

As discussed in [Section 5.1](#), when all the basis tensors, invariants and features from [Subsection 5.2.1](#) are used, the library for Case B exceeds the memory requirements imposed by the available hardware. Therefore, the mutual information between the different correction fields and the basis tensors, invariants and features is computed as described in [Subsubsection 2.3.3.2](#). The features with the highest mutual information with the target correction fields are chosen to form the library with. For consistency, this is also done for Case A, even though the ability to use planar-averaged data for this case drastically reduces the imposed memory requirements.

5.2.2.1. Anisotropy Correction b_{ij}^Δ

The first correction field for which the mutual information analysis is performed is the anisotropy correction b_{ij}^Δ . As the anisotropy correction is a tensor, and the mutual information analysis methodology requires scalar input, the second invariant of b_{ij}^Δ is used similarly to [Steiner et al. \(2022\)](#) and [Goderie \(2020\)](#). This scalar metric of b_{ij}^Δ is chosen as it quantifies the degree of turbulent anisotropy in the flow, making it a convenient scalar target for computing the mutual information according to [Ling and Templeton \(2015\)](#). This metric is computed according to (5.11) where γ_i are the eigenvalues of b_{ij}^Δ with $\gamma_1 \geq \gamma_2 \geq \gamma_3$.

$$\Pi_{b_{ij}^\Delta} = \frac{1}{2} b_{ij}^\Delta b_{ji}^\Delta = \gamma_1^2 + \gamma_1 \gamma_2 + \gamma_2^2 \quad (5.11)$$

(5.11) is also used to compute the second invariant of the different basis tensors to compare them to the anisotropy correction. The results for the mutual information between the anisotropy correction and the basis tensors for Case A and Case B are displayed in Figure 5.1 and Figure 5.2 respectively.

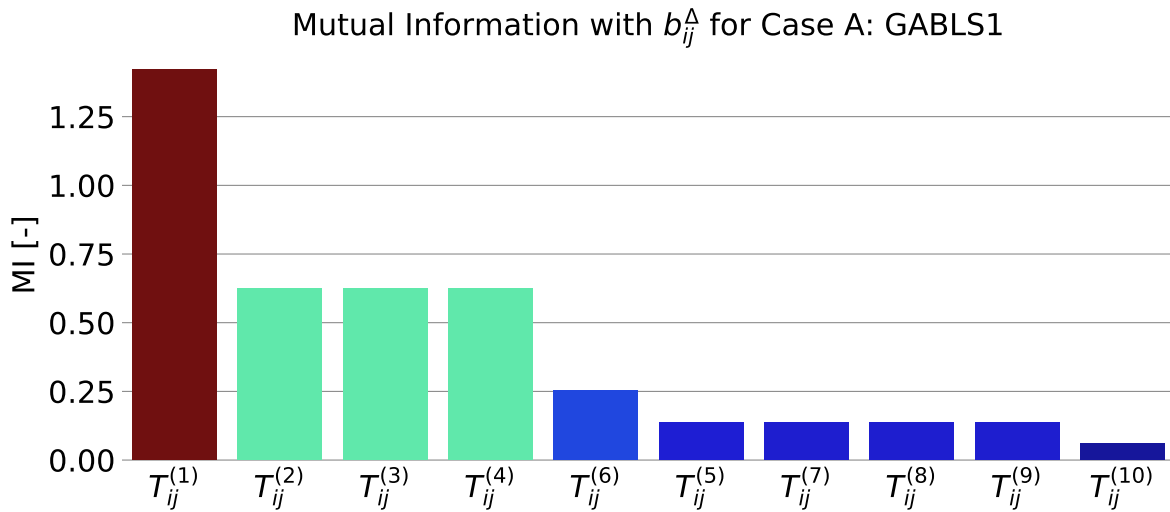


Figure 5.1: Mutual information between the second invariant of the anisotropy correction b_{ij}^{Δ} and the second invariants of the basis tensors for Case A: GABLS1.

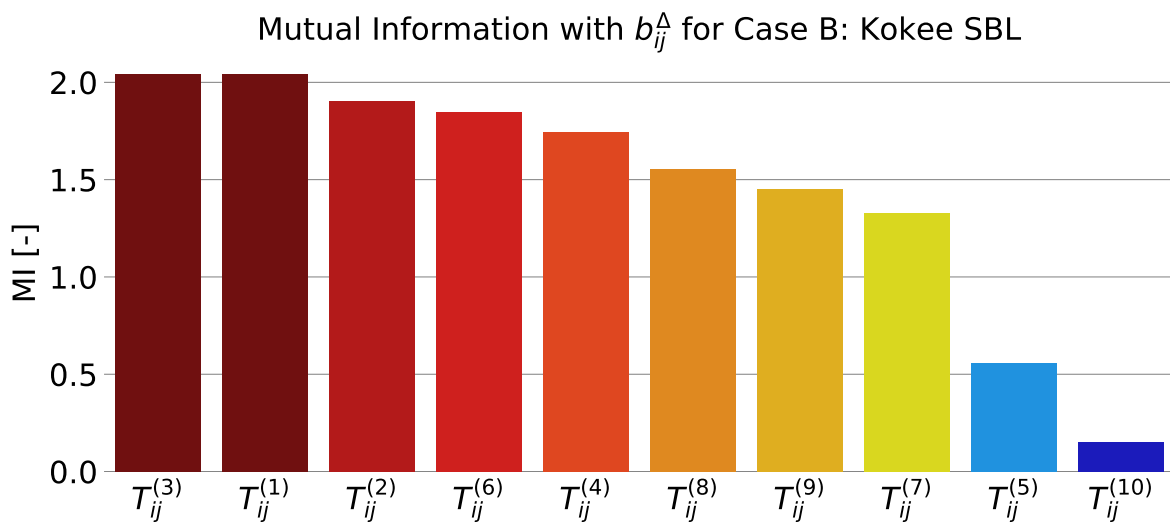


Figure 5.2: Mutual information between the second invariant of the anisotropy correction b_{ij}^{Δ} and the second invariants of the basis tensors for Case B: Kokee SBL.

The figures for the mutual information between the anisotropy correction and the invariants and physics-informed features are included in Appendix A. Based on all these results, chosen is to include the basis tensors and invariants as displayed in Table 5.4 for training the correction models.

Table 5.4: Selected basis tensors, invariants and physical features for forming library used to regress models for anisotropy correction.

Feature Type	Case A: GABLS1	Case B: Kokee SBL
Basis Tensors	$T_{ij}^{(1)}, T_{ij}^{(2)}, T_{ij}^{(3)}, T_{ij}^{(4)}$	$T_{ij}^{(1)}, T_{ij}^{(2)}, T_{ij}^{(3)}, T_{ij}^{(4)}$
Invariants	$\lambda_1, \lambda_3, \lambda_4, \lambda_7, \lambda_{16}$	$\lambda_1, \lambda_3, \lambda_7, \lambda_{10}, \lambda_{11}, \lambda_{21}, \lambda_{22}, \lambda_{25}, \lambda_{33}, \lambda_{35}, \lambda_{40}, \lambda_{43}, \lambda_{44}, \lambda_{45}, \lambda_{46}$
Physical Features	$q_T, q_{ReD}, q_v, q_\tau, q_{TI}$	$q_T, q_{ReD}, q_v, q_{TI}$

Even though they have relatively high mutual information for both cases, physical features q_\perp and q_γ are removed from the regression library as they showed large deviations from the expected values when implemented in the simulations. The same goes for higher order basis tensors (higher than $T_{ij}^{(4)}$) for Case B. When implemented in models, peaks in profiles of these higher order tensors were smoothed a lot when compared to the frozen reference data.

5.2.2.2. TKE Production Correction \mathcal{R}

The TKE production correction field, \mathcal{R} , is already a scalar so the mutual information between this correction field and the invariants can readily be computed. However, to compute the mutual information for the basis tensors, the TKE production of each basis tensor is computed according to (5.12). Therefore it is deemed a suitable metric to compute the mutual information with the target with. ϵ is already a scalar and is therefore unaltered in the computation of the mutual information.

$$\mathcal{P}_k^{T_{ij}^{(n)}} = 2kT_{ij}^{(n)} \frac{\partial \bar{u}_i}{\partial x_j} \quad (5.12)$$

The mutual information between the basis tensors and the TKE production correction for Case A and Case B are displayed in Figure 5.3 and Figure 5.4 respectively. The same figures for the invariants and the physical features are included in Appendix A.

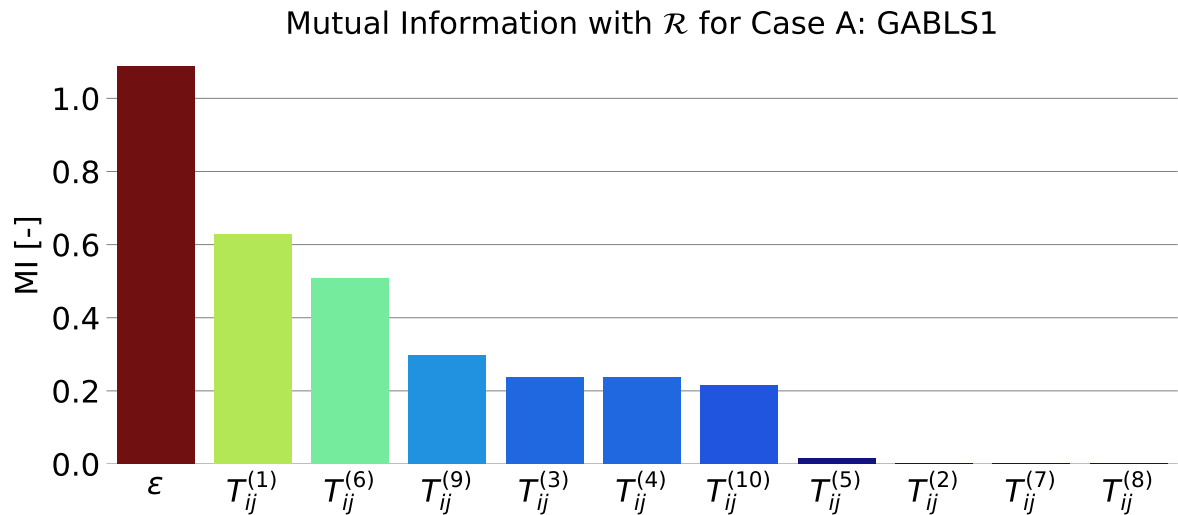


Figure 5.3: Mutual information between the TKE production correction and the TKE production of the basis tensors for Case A: GABLS1

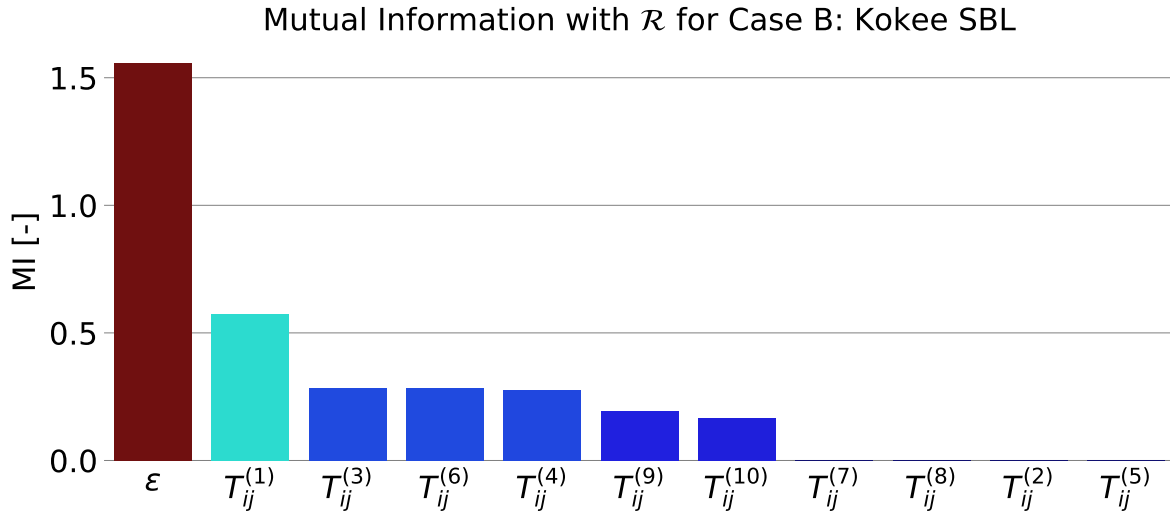


Figure 5.4: Mutual information between the TKE production correction and the TKE production of the basis tensors for Case B: Kokee SBL

Based on the figures in [Figure 5.3](#), [Figure 5.4](#) and [Appendix A](#) the basis tensors, invariants and physical features in [Table 5.5](#) are selected for building the regression library to regress the correction models for the TKE production. Similarly to the anisotropy correction, higher order basis tensors are excluded from the regression for Case B due to inaccuracies when implemented.

Table 5.5: Selected basis tensors, invariants and physical features for forming library used to regress models for TKE production correction

Feature Type	Case A: GABLS1	Case B: Kokee SBL
Basis Tensors	$\epsilon, T_{ij}^{(1)}, T_{ij}^{(3)}, T_{ij}^{(4)}, T_{ij}^{(6)}, T_{ij}^{(9)}, T_{ij}^{(10)}$	$\epsilon, T_{ij}^{(1)}, T_{ij}^{(3)}, T_{ij}^{(4)}$
Invariants	$\lambda_1, \lambda_3, \lambda_4, \lambda_7, \lambda_{16}$	$\lambda_1, \lambda_3, \lambda_7, \lambda_{10}, \lambda_{21}, \lambda_{22}, \lambda_{25}, \lambda_{30}, \lambda_{33}, \lambda_{35}, \lambda_{43}, \lambda_{44}$
Physical Features	$q_T, q_{ReD}, q_v, q_{TI}, q_{GDH}$	$q_T, q_{ReD}, q_v, q_{TI}, q_{GDH}$

5.2.2.3. THF Correction q_f^A

Lastly, the mutual information analysis is performed for the turbulent heat flux correction, q_f^A . Again, this correction is not a scalar, so the mutual information cannot be readily computed. Chosen is to use the z-component of the correction and the basis tensors as this is deemed the most important component. This assertion is made as the z-component of the correction is the only component which also influences the buoyant TKE production and not only the temperature equation. The mutual information between the THF correction and the basis tensors for Case A and Case B are displayed in [Figure 5.5](#) and [Figure 5.6](#) respectively, while the same figures for the invariants and physical features are included in [Appendix A](#).

Based on the figures in [Figure 5.5](#), [Figure 5.6](#) and [Appendix A](#) the basis tensors, invariants and physical features in [Table 5.6](#) are selected for building the library used for regressing the THF correction models.

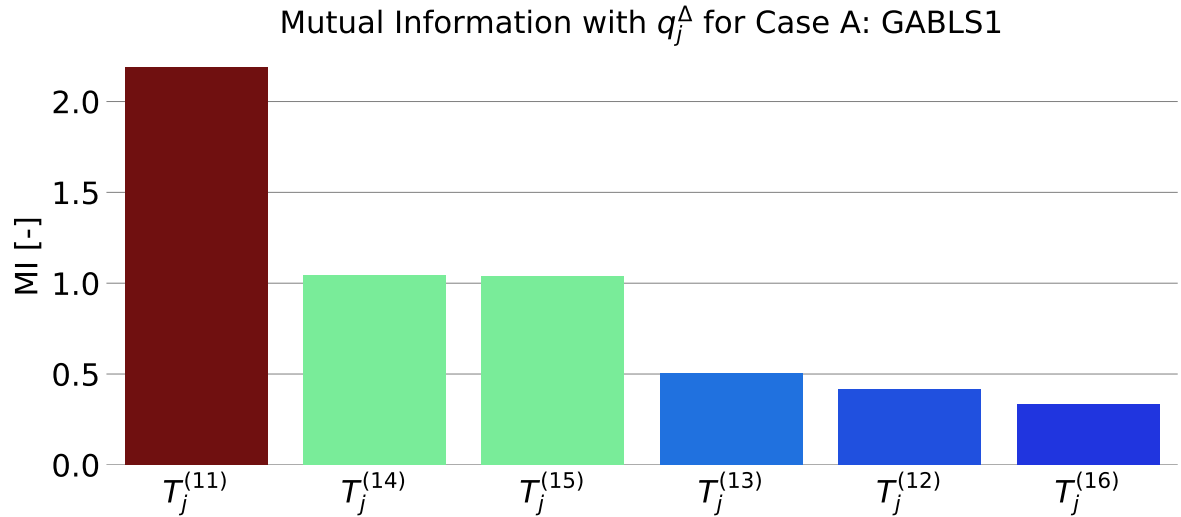


Figure 5.5: Mutual information between the z -component of the THF correction and basis tensors for Case A: GABLS1.

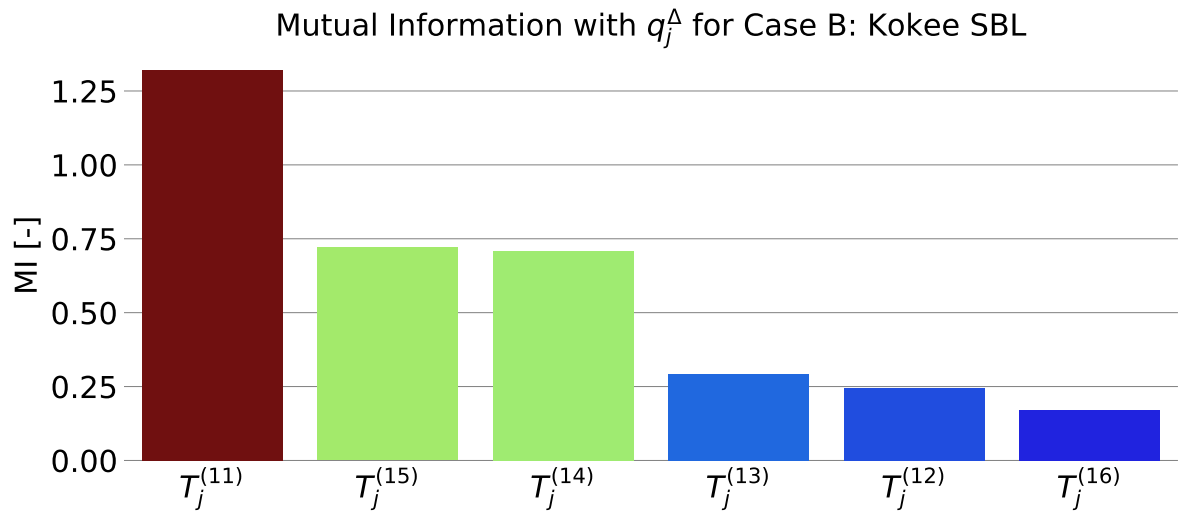


Figure 5.6: Mutual information between the z -component of the THF correction and basis tensors for Case B: Kokee SBL.

Table 5.6: Selected basis tensors, invariants and physical features for forming library used to regress models for the THF correction

Feature Type	Case A: GABLS1	Case B: Kokee SBL
Basis Tensors	$T_j^{(11)}, T_j^{(12)}, T_j^{(13)}, T_j^{(14)}, T_j^{(15)}$	$T_j^{(11)}, T_j^{(12)}, T_j^{(13)}, T_j^{(14)}, T_j^{(15)}$
Invariants	$\lambda_1, \lambda_3, \lambda_4, \lambda_5, \lambda_{16}$	$\lambda_1, \lambda_3, \lambda_4, \lambda_7, \lambda_{10}, \lambda_{11}, \lambda_{16}, \lambda_{21}, \lambda_{25}, \lambda_{35}, \lambda_{43}, \lambda_{44}$
Physical Features	$q_v, q_T, q_{ReD}, q_{GDH}, q_{TI}$	$q_v, q_{ReD}, q_{GDH}, q_{TI}$

5.3. Selection of models

Once the library is complete and the regression is performed, a lot of models are created. From these models a few are selected to be implemented in RANS simulations.

5.3.1. Case A: GABLS1

A few models are selected to be implemented for each of the three correction terms.

5.3.1.1. Anisotropy Correction b_{ij}^A

After the regression is performed according to the description in Section 5.1, the mean squared error and max squared error are computed using the test data. These metrics are displayed for all models with less than eleven terms in Figure 5.7. Chosen is to keep only simpler models as they are more robust and it allows for more physical interpretation of the resulting models. Furthermore, for models with the same features, only the model with the lowest mean squared error is displayed. A figure which displays the terms present in all the models is included in Appendix B.

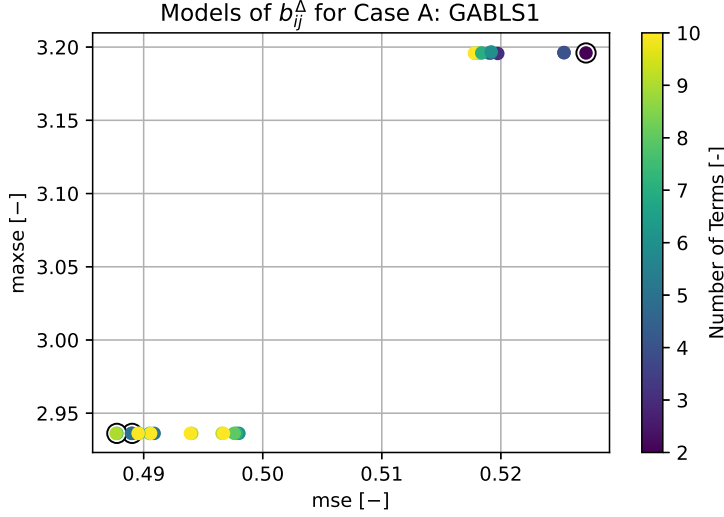


Figure 5.7: Scatter plot of the mean and max squared error of the anisotropy correction models with less than eleven terms, generated using data from Case A: GABLS1. Selected models are denoted by a black circle.

The selected models in Figure 5.7 are selected based on their low mse and maxse. Also, it is chosen to select models with different numbers of terms, namely two, four and seven, to investigate the effect the complexity of the models has on the simulations. The expressions of the chosen models are included in (5.13). The models in (5.13) only include physical features and none of the invariants. Also, the more complex models include all the terms of the simpler models, only adding features and changing the coefficients a bit.

$$\begin{aligned}
 [b_{ij}^A]_9^A &= 0.0707 \cdot T_{ij}^{(1)} + 2.8825 \cdot 10^{-5} \cdot q_{ReD} \cdot q_{Tl} \cdot T_{ij}^{(2)} \\
 [b_{ij}^A]_{16}^A &= 0.0493 \cdot T_{ij}^{(1)} + 2.6595 \cdot 10^{-5} \cdot q_{ReD} \cdot q_{Tl} \cdot T_{ij}^{(2)} + 3.3035 \cdot 10^{-5} \cdot q_{ReD} \cdot q_{Tl} \cdot T_{ij}^{(3)} \\
 &\quad + 0.0018 \cdot q_T \cdot T_{ij}^{(1)} \\
 [b_{ij}^A]_{2164}^A &= 0.1441 \cdot T_{ij}^{(1)} + 2.6590 \cdot 10^{-5} \cdot q_{ReD} \cdot q_{Tl} \cdot T_{ij}^{(2)} + 4.2728 \cdot 10^{-5} \cdot q_{ReD} \cdot q_{Tl} \cdot T_{ij}^{(3)} \\
 &\quad + 0.0017 \cdot q_T \cdot T_{ij}^{(1)} + 2.0034 \cdot 10^{-7} \cdot q_{ReD} \cdot T_{ij}^{(1)} + 9.6907 \cdot 10^{-6} \cdot q_{ReD} \cdot q_{Tl} \cdot T_{ij}^{(4)} \\
 &\quad - 0.0763 \cdot q_\tau \cdot T_{ij}^{(1)}
 \end{aligned} \tag{5.13}$$

The predictions of the planar-averaged TKE production due to the anisotropy correction b_{ij}^A are displayed for the models from (5.13) in Figure 5.8. All predictions are quite close to the target, only the simplest model 9 is slightly further off than the more complicated models 16 and 2164. This also means that the extra terms in model 2164 with respect to model 16 have a negligible effect on the accuracy of the prediction.

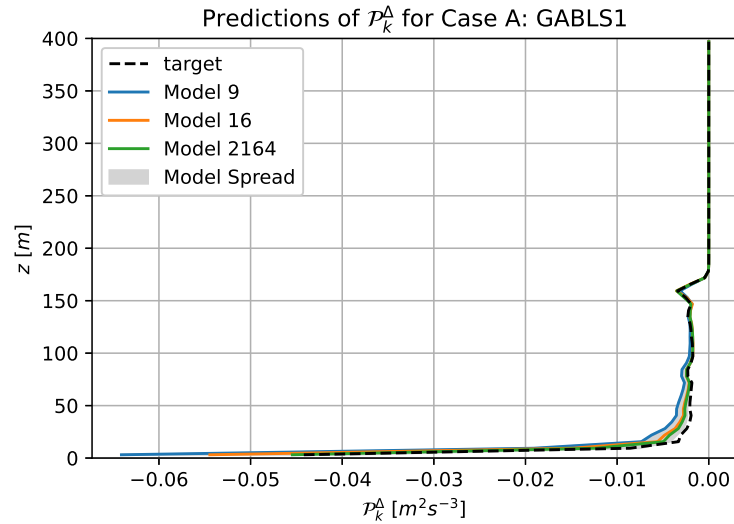


Figure 5.8: Prediction of the chosen models for the planar-averaged TKE production due to the anisotropy correction b_{ij}^A for Case A: GABLS1, as well as the spread of the predictions of all generated models included in the scatter plot.

5.3.1.2. TKE Production Correction \mathcal{R}

The same analysis as for b_{ij}^A is performed for the TKE production correction \mathcal{R} . The mse and maxse of the best simple models generated by the regression are displayed in Figure 5.9. Figure 5.9 shows quite a surprising result, namely that a model of one term performs the best in terms of mse and maxse of all the models with ten terms or less. Therefore, this is the only model that is selected.

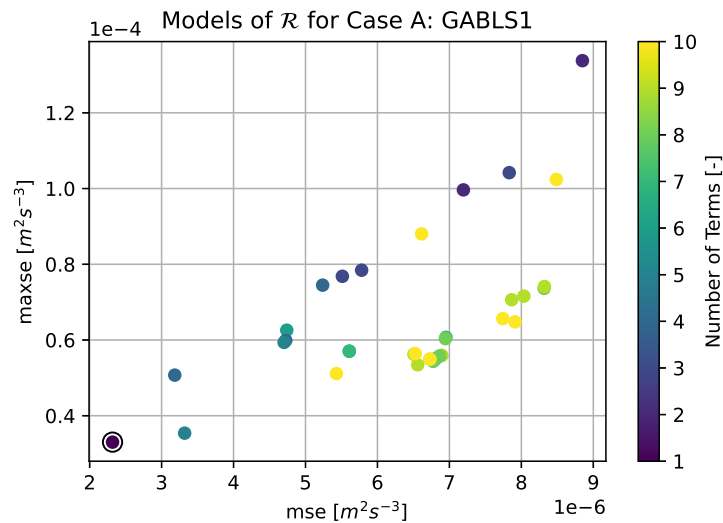


Figure 5.9: Scatter plot of the mean and max squared error of the TKE production correction models with less than eleven terms, generated using data from Case A: GABLS1. Selected models are denoted by a black circle.

The expression of the selected model is displayed in (5.14) and it includes the physical feature based on the magnitude of the turbulent heat flux according to the gradient-diffusion hypothesis and the dissipation rate.

$$[\mathcal{R}]_{1850}^A = 2682.1 \cdot q_{GDH} \cdot \epsilon \tag{5.14}$$

The prediction of the selected model is displayed in Figure 5.10 where it is visible that the selected model performs the best towards the bottom of the domain.

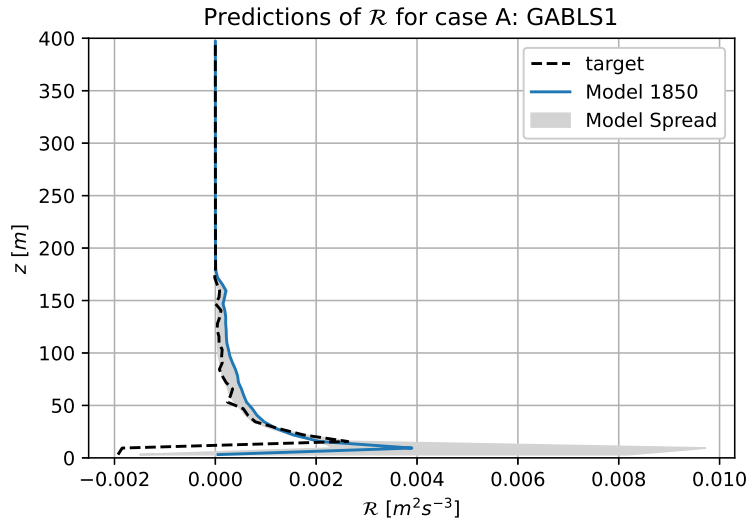


Figure 5.10: Prediction of the chosen models for the planar-averaged TKE production correction \mathcal{R} for Case A: GABLS1, as well as the spread of the predictions of all generated models included in the scatter plot.

5.3.1.3. THF Correction q_f^A

The mse and maxse for the generated models for the THF correction are displayed in Figure 5.11. Again, models are chosen based on these metrics as well as the number of terms in the model.

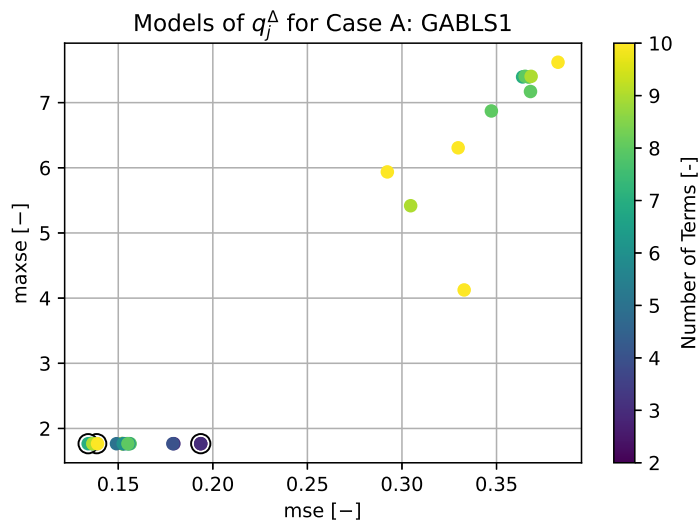


Figure 5.11: Scatter plot of the mean and max squared error of the THF correction models with less than eleven terms, generated using data from Case A: GABLS1. Selected models are denoted by a black circle.

The chosen models have a complexity of two, four and seven and are displayed in (5.15). Just as

with the models for b_{ij}^{Δ} it is visible that more complex models contain the same terms as the simpler models.

$$\begin{aligned}
 [q_j^{\Delta}]_{117}^A &= 2.1332 \cdot 10^{-5} \cdot q_{ReD} \cdot T_j^{(11)} - 0.0018 \cdot q_{ReD} \cdot q_{TI} \cdot T_j^{(13)} \\
 [q_j^{\Delta}]_{119}^A &= 9.4812 \cdot 10^{-6} \cdot q_{ReD} \cdot T_j^{(11)} - 0.0018 \cdot q_{ReD} \cdot q_{TI} \cdot T_j^{(13)} + 0.0516 \cdot q_T \cdot T_j^{(11)} \\
 &\quad + 0.2827 \cdot T_j^{(11)} \\
 [q_j^{\Delta}]_{3401}^A &= 1.0332 \cdot 10^{-5} \cdot q_{ReD} \cdot T_j^{(11)} - 9.5505 \cdot 10^{-4} \cdot q_{ReD} \cdot q_{TI} \cdot T_j^{(13)} + 0.0813 \cdot q_T \cdot T_j^{(11)} \\
 &\quad + 0.3704 \cdot T_j^{(11)} + 9.1374 \cdot 10^{-4} \cdot q_{ReD} \cdot q_{TI} \cdot T_j^{(12)} + 3.6458 \cdot 10^{-11} \cdot q_{ReD}^2 \cdot T_j^{(11)} \\
 &\quad - 5.9425 \cdot 10^{-5} \cdot q_T \cdot q_v \cdot T_j^{(11)}
 \end{aligned} \tag{5.15}$$

The predictions according to the models in (5.15) are displayed in Figure 5.12. It is visible that the simplest model shows quite a large deviation from the target, while the two more complex models match the target quite well. Also, the model with the highest number of terms is not significantly better than the model 119 with four terms.

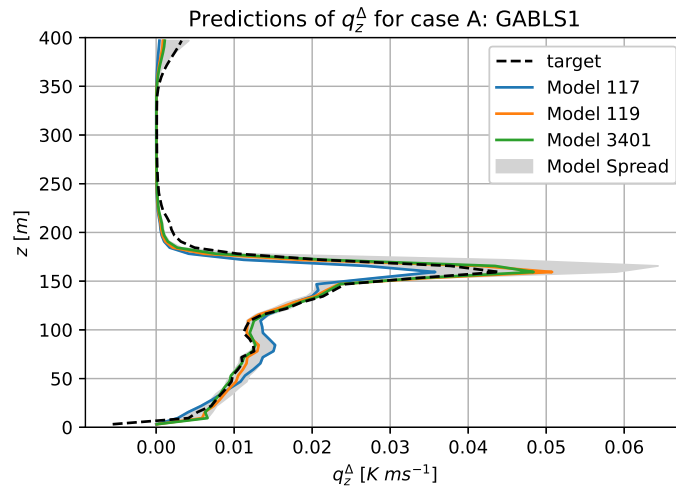


Figure 5.12: Prediction of the chosen models for the planar-averaged z-component of the THF correction q_z^{Δ} for Case B: Kokee SBL, as well as the spread of the predictions of all generated models included in the scatter plot.

5.3.2. Case B: Kokee SBL

The same process of choosing models to implement in RANS simulations is done for the models trained with the data from Case B: Kokee SBL.

5.3.2.1. Turbulence Anisotropy Correction b_{ij}^{Δ}

Just as for Case A, the regression results in a lot of models. The mean squared error and max squared error of the created models with five terms or less are displayed in Figure 5.13, where the black circles denote selected models. The structures of the models displayed in Figure 5.13 are included in Appendix B. As discussed before, chosen is to focus on the simpler models as they are more robust and allow for more physical interpretation while still being able to describe complex phenomena. The models which are chosen in Figure 5.13 are chosen because they have the lowest mean squared error (4167), lowest complexity (4159) or lowest max squared error (4371).

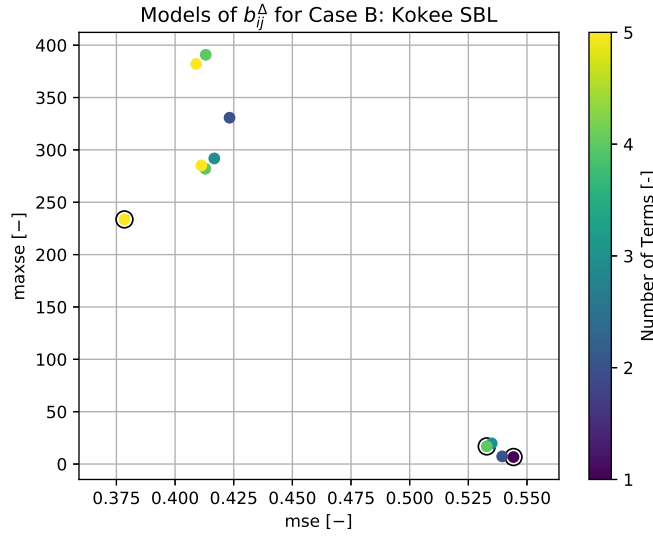


Figure 5.13: Scatter plot of the mean and max squared error of the anisotropy correction models with less than six terms, generated using data from Case B: Kokee SBL. Selected models are denoted by a black circle.

The expressions of the chosen models are included in (5.16). Similarly to Case A, it is visible that only physical features are selected in the model and no invariants. Furthermore, for all selected models, the first basis tensor is the most important.

$$\begin{aligned}
 \left[b_{ij}^{\Delta} \right]_{4167}^B &= 0.9054 \cdot T_{ij}^{(1)} + 0.0910 \cdot q_T \cdot T_{ij}^{(1)} + 0.0559 \cdot T_{ij}^{(2)} - 0.1425 \cdot T_{ij}^{(4)} \\
 &\quad + 2.7725 \cdot 10^{-9} \cdot q_v^2 \cdot T_{ij}^{(2)} \\
 \left[b_{ij}^{\Delta} \right]_{4159}^B &= 1.0534 \cdot T_{ij}^{(1)} \\
 \left[b_{ij}^{\Delta} \right]_{4371}^B &= 1.3048 \cdot T_{ij}^{(1)} + 0.0699 \cdot q_T \cdot T_{ij}^{(1)} - 7.3302 \cdot 10^{-5} \cdot q_v \cdot T_{ij}^{(1)} \\
 &\quad - 2.8620 \cdot 10^{-6} \cdot q_{ReD} \cdot T_{ij}^{(1)}
 \end{aligned} \tag{5.16}$$

The prediction of the chosen models for the TKE production due to the anisotropy correction b_{ij}^{Δ} is included in Figure 5.14, where the models are also compared to the rest of the models included in Figure 5.13. It is visible that the model with the lowest mean squared error (4167) provides the best prediction of the selected polars, while the model with the lowest complexity (4159) is the furthest from the target data.

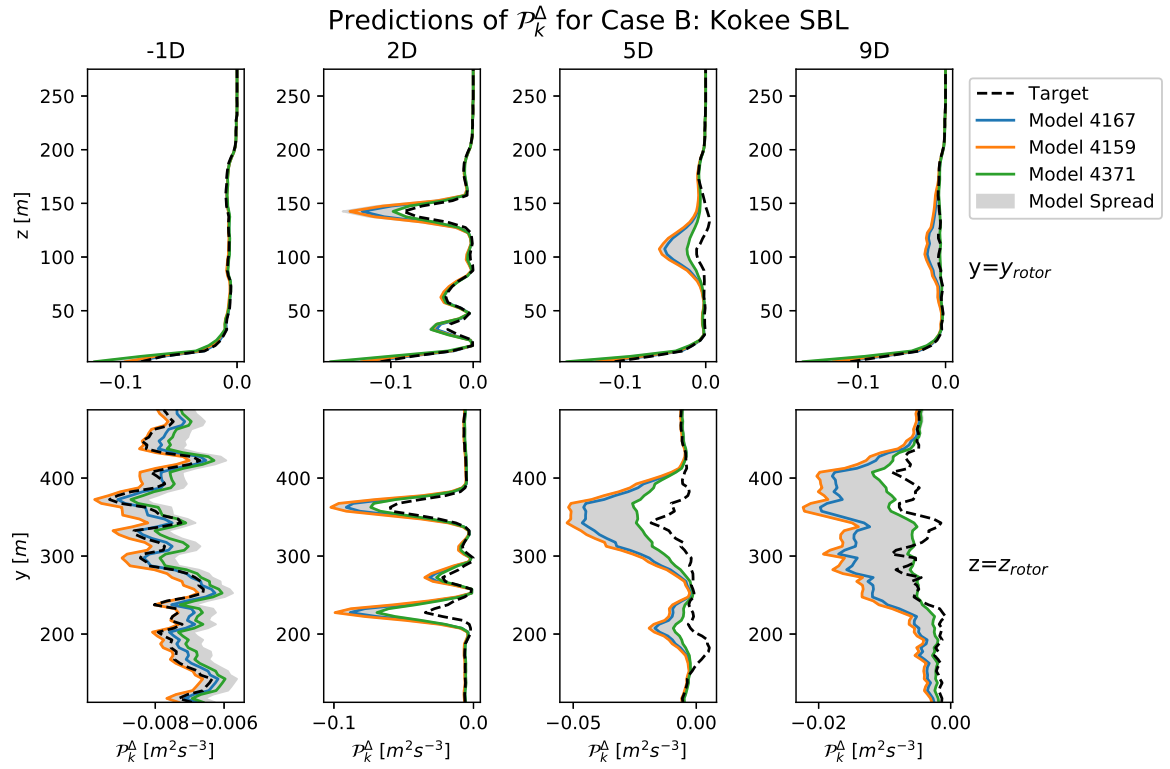


Figure 5.14: Prediction of the chosen models for the planar-averaged TKE production due to the anisotropy correction b_{ij}^A for Case B: Kokee SBL, as well as the spread of the predictions of all generated models included in the scatter plot.

5.3.2.2. TKE Production Correction \mathcal{R}

A similar process is done to select the correction models for the TKE production to implement. Figure 5.15 displays the mean squared error and the max squared error for all generated models with less than six terms and the chosen models are denoted by black circles. The model structures of the models included in Figure 5.15 are included in Appendix B. The chosen models are again based on their low mean squared error (10), max squared error (12) or complexity (7). Furthermore, model 12 is chosen as the model with the lowest maxse proved not robust when implemented in RANS simulations.

The expressions of the chosen models are included in (5.17). Again it is visible that no invariants are used in the chosen models, only physics based features. Furthermore, it is clear that ϵ is the most important basis, as only model $[\mathcal{R}]_{10}^B$ uses a basis tensor in the model. Another noteworthy thing is that all models include a term with only ϵ multiplied with a positive coefficient close to 1. This means that the correction models are effectively removing almost all of the dissipation as computed by the transport equation for ϵ .

$$\begin{aligned}
 [\mathcal{R}]_{10}^B &= 0.9483 \cdot \epsilon + 568.76 \cdot q_{GDH} \cdot q_T \cdot \epsilon + 3.1999 \cdot 10^{-5} \cdot q_T \cdot q_v \cdot \epsilon - 1.0249 \cdot 10^{-5} \cdot q_v \cdot \epsilon \\
 &\quad + 2k \left(-6.2982 \cdot q_{TI} \cdot q_T \cdot T_{ij}^{(1)} \right) \frac{\partial \bar{u}_i}{\partial x_j} \\
 [\mathcal{R}]_{12}^B &= 0.8093 \cdot \epsilon - 72.458 \cdot q_{GDH} \cdot q_T \cdot \epsilon + 5.0962 \cdot 10^{-5} \cdot q_T \cdot q_v \cdot \epsilon + 299.45 \cdot q_{GDH} \cdot \epsilon \\
 [\mathcal{R}]_7^B &= 0.9432 \cdot \epsilon
 \end{aligned} \tag{5.17}$$

Sample profiles of the prediction of the TKE production correction by the chosen models behind the rotor are included in Figure 5.16. In contrast to the predictions for the turbulence anisotropy correction, the predictions in Figure 5.16 show very little difference between the models. Even though there is quite a large difference in model complexity.

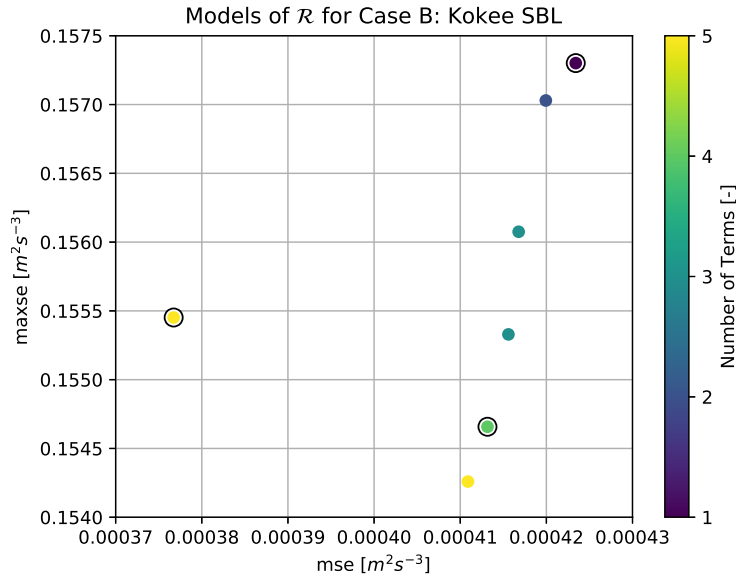


Figure 5.15: Scatter plot of the mean and max squared error of the TKE production correction models with less than six terms, generated using data from Case B: Kokee SBL. Selected models are denoted by a black circle.

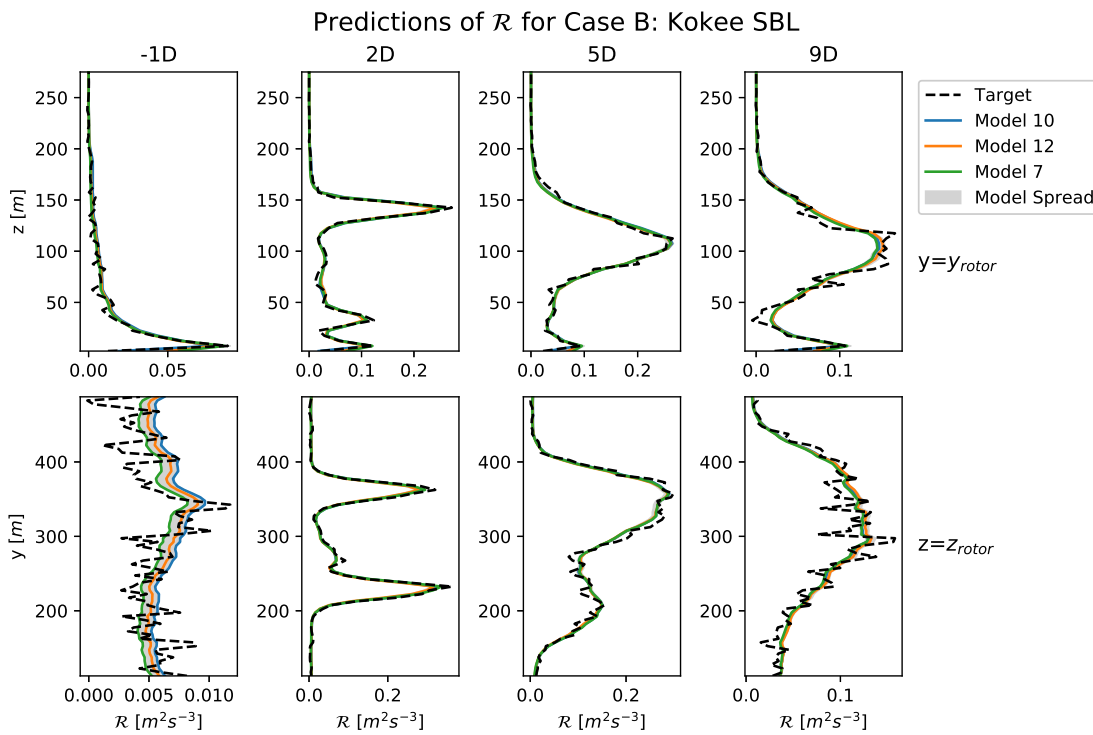


Figure 5.16: Prediction of the chosen models for the planar-averaged TKE production correction \mathcal{R} for Case B: Kokee SBL, as well as the spread of the predictions of all generated models included in the scatter plot.

5.3.2.3. THF Correction q_j^A

Lastly, the selection of turbulence heat flux correction models is done. Figure 5.17 shows the performance of the simplest models in terms of mean squared error and max squared errors. The model structures of the models displayed in Figure 5.17 are included in Appendix B. Figure 5.17 shows that there are only a few unique models with less than six terms. Only two models are selected: the model

with the lowest mean and max squared error (9) and a model with the lowest complexity (7).

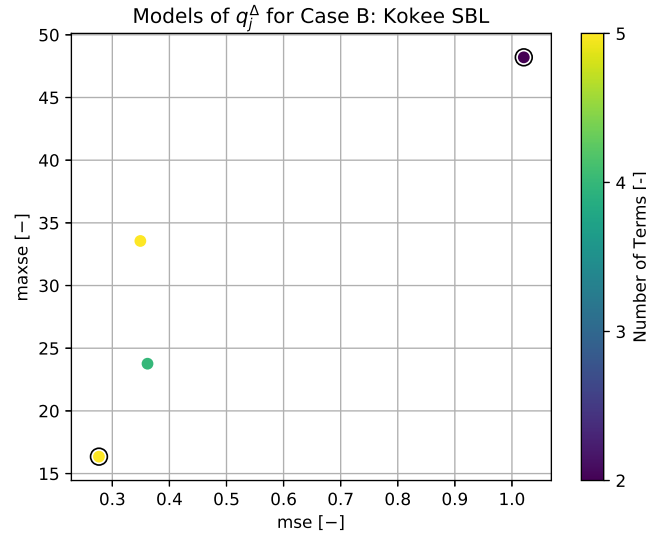


Figure 5.17: Scatter plot of the mean and max squared error of the THF correction models with less than six terms, generated using data from Case B: Kokee SBL. Selected models are denoted by a black circle.

The expressions of the chosen models are included in (5.18). Again, the trend that only physical features are incorporated in models is visible. Furthermore, (5.18) shows that models 9 and 7 are very similar, with model 9 having the same first two terms with only slightly differing coefficients. Lastly it is visible that a correction of the turbulent diffusivity in the gradient-diffusion hypothesis (all terms multiplied with $T_j^{(11)}$) is dominant for both models. Especially for model 7 which only corrects the gradient-diffusion hypothesis based on the magnitude of the turbulent heat flux according to the gradient-diffusion hypothesis.

$$\begin{aligned}
 [q_j^A]_9^B &= 0.3143 \cdot T_j^{(11)} + 792.53 \cdot q_{GDH} \cdot T_j^{(11)} + 1.2815 \cdot 10^{-10} \cdot q_{ReD}^2 \cdot T_j^{(12)} \\
 &\quad - 3.3919 \cdot 10^{-11} \cdot q_{ReD}^2 \cdot T_j^{(13)} - 0.0115 \cdot q_{TI} \cdot q_v \cdot T_j^{(13)} \\
 [q_j^A]_7^B &= 0.3138 \cdot T_j^{(11)} + 796.37 \cdot q_{GDH} \cdot T_j^{(11)}
 \end{aligned} \tag{5.18}$$

The predictions of sample profiles between the rotor of the vertical component of the THF correction term for the chosen models are displayed in Figure 5.18. Some minor differences are visible between the simpler model 7 and the slightly more complex model 9. However, one is not clearly closer to the target data than the other.

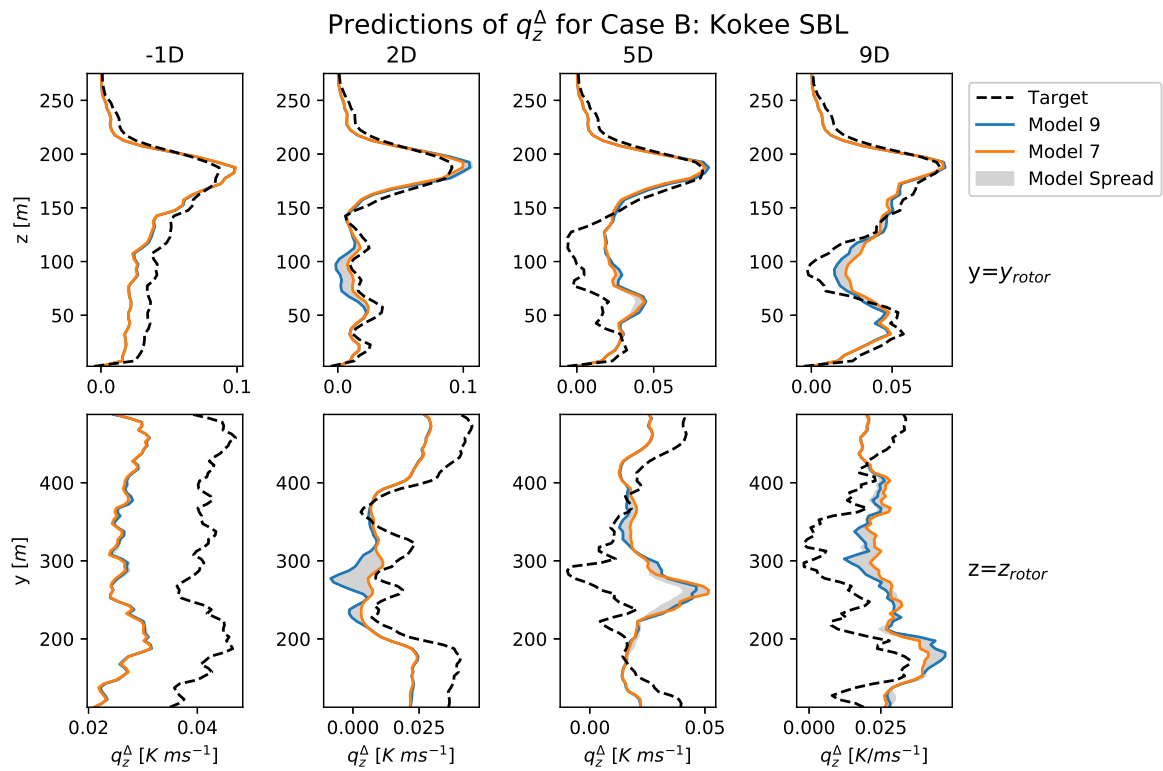


Figure 5.18: Prediction of the chosen models for the planar-averaged z-component of the THF correction q_z^Δ for Case B: Kokee SBL, as well as the spread of the predictions of all generated models included in the scatter plot.

6

Implementation of Learned Correction Terms in Simulations

The correction models have been trained in [Chapter 5](#), therefore the next step is to implement these trained correction models in RANS simulations.

6.1. Simulation Methodology

The methodology for RANS simulations with implemented models is largely the same for the two cases. Just as for the LES, the simulations are performed in OpenFOAM-6 using SOWFA-6, with the addition of the models.

6.1.1. Governing Equations

The governing equations for continuity, momentum and potential temperature are displayed in (6.1), (6.2) and (6.3) respectively ([Churchfield et al., 2012b](#)). These equations are the same for both cases.

$$\frac{\partial \bar{u}_i}{\partial x_i} = 0 \quad (6.1)$$

$$\frac{\partial \bar{u}_i \bar{u}_j}{\partial x_i} = -\frac{1}{\rho_0} \frac{\partial \bar{p}_{rgh}}{\partial x_i} + \frac{\partial}{\partial x_j} \left(\nu \left(\frac{\partial \bar{u}_i}{\partial x_j} + \frac{\partial \bar{u}_j}{\partial x_i} \right) - \overline{u'_i u'_j} \right) + \left(\frac{\bar{\theta} - \theta_0}{\theta_0} \right) g_i - 2\epsilon_{i3k} \Omega_3 \bar{u}_k + S_i^m + \frac{1}{\rho_0} \overline{f_i^T} \quad (6.2)$$

$$\frac{\partial \bar{\theta} \bar{u}_j}{\partial x_j} = \frac{\partial}{\partial x_j} \left(\frac{\nu}{\text{Pr}} \frac{\partial \bar{\theta}}{\partial x_j} - \overline{\theta' u'_j} - \bar{q}_j^{wall} \right) \quad (6.3)$$

The Reynolds stress, $\overline{u'_i u'_j}$, and turbulent heat flux, $\overline{\theta' u'_j}$, are computed according to the turbulence models with implemented correction models described in [Subsubsection 4.1.1.2](#). This means that there is a slight difference in the turbulence models for the two cases in order to keep consistent with the k-corrective frozen approach used to extract the optimal correction terms. The momentum source, S_i^m is taken as the mean value in the LES data for the two cases and the same is done for the wall heat flux \bar{q}_j^{wall} . The turbine forcing $\overline{f_i^T}$ is zero for Case A and for Case B it is computed by the Actuator Disk Model. However, contrary to the LES, the pitch and rpm are kept fixed at the mean LES value in stead of being controlled by a controller. For Case B this means a mean rotational velocity of 9.30 rpm and a mean rotor pitch of 0.0°.

6.1.2. Initial Conditions

The initial conditions for \bar{u}_i , \bar{p}_{rgh} and $\bar{\theta}$ are taken as the mean fields over the last hour of the LES. The initial conditions for k , ϵ and ν_t are taken from the converged k-corrective frozen RANS simulations, just as the initial values of the correction terms b_{ij}^Δ , \mathcal{R} and q_j^Δ . For Case A these fields can straightforwardly

be copied as the RANS simulation is performed on the same domain and mesh as the LES. However, when running the simulation with implemented models for Case B, it is discovered that part of the turbine wake exits the domain through the Southern boundary causing some instabilities with the models. Therefore, the 100 m next to the Northern boundary is moved and attached to the Southern boundary. This could be done as the Northern and Southern boundaries are linked through a cyclic boundary condition.

6.1.3. Boundary Conditions

The boundary conditions used in the RANS simulations with implemented models are the same for both cases and displayed in Table 6.1. The only difference is the value for q_w , which is $0.0101 \text{ K m s}^{-1}$ for Case A and $0.0109 \text{ K m s}^{-1}$ for Case B. The boundary conditions in Table 6.1 are chosen to keep consistent with the k-corrective frozen RANS simulations and the different wall models used are explained in more detail in Subsection 4.1.4. The most significant difference from the k-corrective frozen RANS boundary conditions, is the fact that inflow conditions need to be specified for \bar{u}_i , $\bar{\theta}$, k and ϵ . This is indicated by the mappedFixedValue boundary condition in Table 6.1. These inflow conditions are taken from the inflow plane of the converged k-corrective frozen simulation.

Table 6.1: Boundary conditions for the RANS simulations with implemented models.

BC	Lower	Upper	West
\bar{u}_i	fixedValue 0	slip	mappedFixedValue
\bar{p}_{rgh}	fixedFluxPressure	fixedFluxPressure	fixedFluxPressure
$\bar{\theta}$	zeroGradient	fixedGradient 0.01	mappedFixedValue
\bar{q}_j^{wall}	fixedValue q_w	fixedValue 0	fixedValue 0
ν_t	nutkStratAtmRoughWallFunction	slip	zeroGradient
k	kqRwallFunction	slip	mappedFixedValue
ϵ	epsilonWallFunction	slip	mappedFixedValue
b_{ij}^A	fixedValue 0	fixedValue 0	fixedValue 0
\mathcal{R}	fixedValue 0	fixedValue 0	fixedValue 0
q_j^A	fixedValue 0	fixedValue 0	fixedValue 0
BC	South	East	North
\bar{u}_i	cyclic	inletOutlet	cyclic
\bar{p}_{rgh}	cyclic	zeroGradient	cyclic
$\bar{\theta}$	cyclic	zeroGradient	cyclic
\bar{q}_j^{wall}	cyclic	fixedValue 0	cyclic
ν_t	cyclic	zeroGradient	cyclic
k	cyclic	zeroGradient	cyclic
ϵ	cyclic	zeroGradient	cyclic
b_{ij}^A	cyclic	fixedValue 0	cyclic
\mathcal{R}	cyclic	fixedValue 0	cyclic
q_j^A	cyclic	fixedValue 0	cyclic

6.1.4. Blending and Ramping of Implementation of Correction Models

In order to be consistent with the k-corrective frozen RANS simulations used to extract the optimal correction fields, the simulations with implemented models employ the same blending. For Case A: GABLS1 this means that the blending function from Steiner et al. (2022) and displayed in (2.85) is used to blend the anisotropy correction, b_{ij}^A , and TKE production correction, \mathcal{R} , in the top and bottom 15 m of the domain. For Case B: Kokee SBL this means that these terms are set to zero in the top 30 m of the domain. In both cases the THF correction, q_j^A , is not blended anywhere in the domain.

Aside from blending, ramping of the implementation of the correction models is also used in the implementation of the correction models. This is needed as in the first iterations there are large changes in the different parameters. These large changes can lead to large changes in the correction model values and thus even larger variations in the different parameters. This can snowball and lead to

a diverging simulation. Therefore, Case A waits 10 iterations after which the correction models are ramped to full implementation in another 10 iterations. For the Case B simulations, the solver waits 100 iterations and the ramp-time is another 100 iterations.

6.1.5. Limiters

After implementing the correction models for Case B, the same instabilities as observed in Steiner et al. (2021) and described in Subsubsection 2.3.3.4 are observed. Therefore, it is decided to implement the same limiters for the anisotropy correction, b_{ij}^A , and for the TKE production correction, \mathcal{R} , as in Steiner et al. (2021). These limiters are displayed in (6.4) and (6.5).

- **Eddy viscosity limiter:** the linear components of the anisotropy correction models are limited based on van der Laan et al. (2013):

$$b_{ij,lin}^A = \min\left(0.8 \frac{\epsilon}{k^2} \nu_t, b_{ij,lin}^A\right) \quad (6.4)$$

- **Form error limiter:** This limiter is active in areas where actuator forcing is applied, so very close to the actuator disk:

$$\mathcal{R} = \text{sgn}(\mathcal{R}) \cdot \min\left(0.5 \mathcal{P}_k^{Boussinesq}, |\mathcal{R}|\right) \quad (6.5)$$

However, after these two limiters are implemented, instabilities in the temperature field at the shear layer between the wake and the outside flow are observed. These instabilities are similar to those caused by the anisotropy correction: large gradients in the temperature causes large THF correction terms, causing even larger gradients. Therefore, it is chosen to apply a similar limiter as the eddy viscosity limiter for the THF correction displayed in (6.6).

- **THF limiter:** the "GDH" components of the THF correction models are limited:

$$q_{j,GDH}^A = \min\left(\frac{1}{2Pr_t}, q_{j,GDH}^A\right) \quad (6.6)$$

The limiter displayed in (6.6) limits the part of the THF correction containing basis tensor $T_j^{(11)}$. This is done as this part of the correction is basically a correction of the coefficient in front of the temperature gradient in the gradient-diffusion hypothesis. When this coefficient becomes larger than $\frac{1}{Pr_t}$, the gradient-diffusion hypothesis part of the THF model switches sign. Meaning that there is counter-gradient transport of turbulent heat flux, something which is generally nonphysical. To make the limiter a little more stringent, and avoid getting close to the nonphysical limit, it is chosen to set the limit at $\frac{1}{2Pr_t}$.

Due to the absence of turbines, and hence the absence of wakes, in Case A, the RANS simulations with implemented models for this case are able to being performed without the use of any limiters.

6.2. Results Case A: GABLS1 with Implemented Models

A number of different aspects of simulations for Case A: GABLS1 with implemented models is investigated. Namely, the influence the THF correction has in the simulation, which correction models perform the best, how much the results of the simulation are improved compared to a baseline simulation and how good the different models perform.

6.2.1. Influence of the THF Correction

The first aspect of the simulations which is analysed, is the influence of the new addition to the SpARTA methodology: the THF correction q_j^A . To do this it is not necessary to use results with implemented models, just using the frozen optimal correction fields is enough. Figure 6.1 displays the planar-averaged turbulent heat flux of RANS simulations with implemented frozen, so optimal, corrections for Case A. Furthermore, Figure 6.1 compares three different implementations for the THF correction to judge its influence: full implementation, implementation of only the z-component and no implementation of the THF correction.

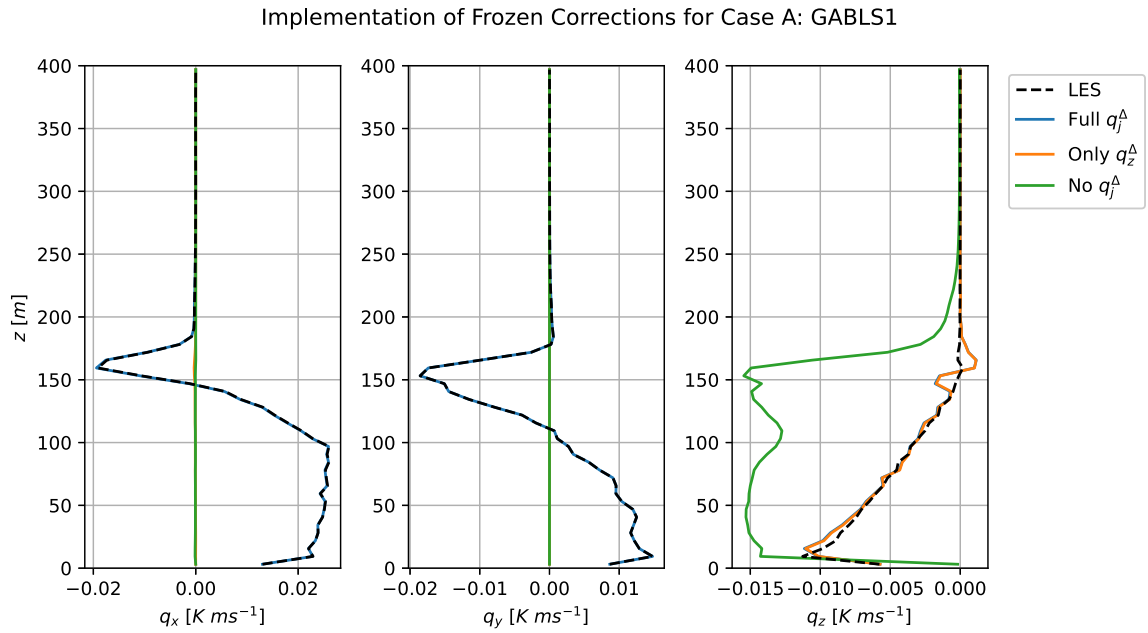


Figure 6.1: Comparison of the turbulent heat flux from RANS simulations of Case A: GABLS1 with different versions of the frozen THF correction (q_j^Δ): full correction (blue), only z-component (orange) and no THF correction (green). All simulations implemented the frozen anisotropy (b_{ij}^Δ) and TKE production (\mathcal{R}) corrections.

When considering the different profiles in Figure 6.1 it is visible that the turbulent heat flux is computed much more accurately when the frozen corrections are implemented, almost exactly matching the target data. This is expected, the real question is how much this improvement of THF computation influences the other parameters in the RANS simulation. Therefore, Figure 6.2 displays the planar-averaged profiles for the temperature, velocity and TKE for the different simulations.

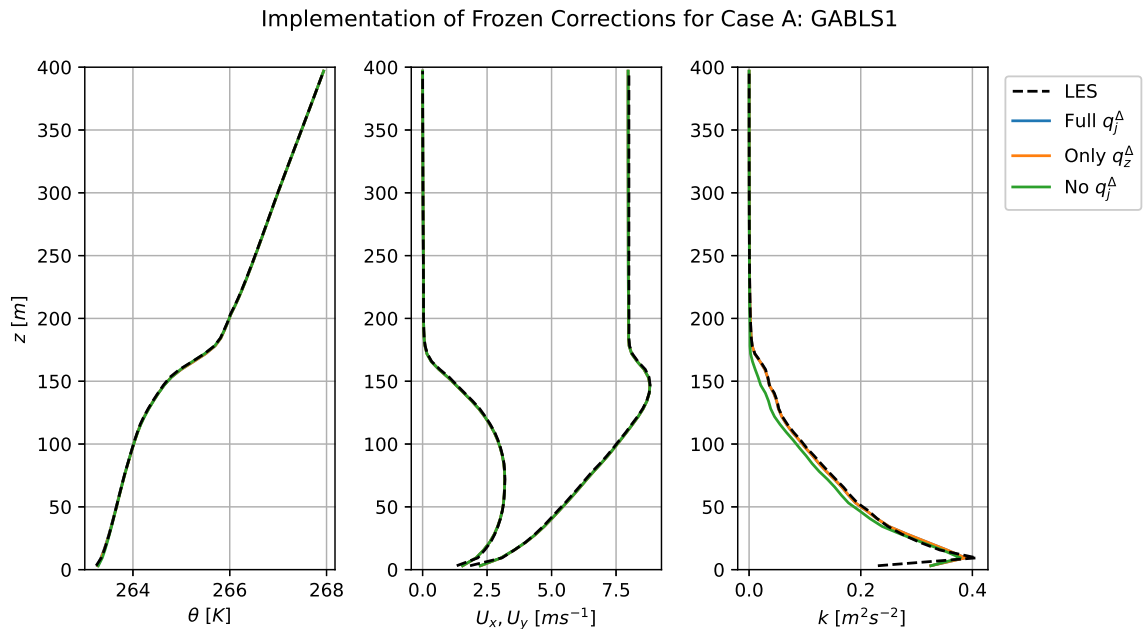


Figure 6.2: Comparison of RANS simulations of Case A: GABLS1 with different versions of the frozen THF correction (q_j^Δ): full correction (blue), only z-component (orange) and no THF correction (green). All simulations implemented the frozen anisotropy (b_{ij}^Δ) and TKE production (\mathcal{R}) corrections.

Looking at Figure 6.2 it is clear that the full implementation matches the LES profiles almost exactly, as was to be expected. The only difference is for the TKE profile at the bottom of the domain where the corrections are blended out to avoid interaction with the wall model. Furthermore, it is clear that the THF correction does not influence the temperature or velocity profiles for Case A. A reason for this could be the fact that these profiles are prescribed at the inflow boundary and the domain is not very long, leaving very little time for these profiles to change.

The fact that all the profiles of the z-component implementation of the THF correction is equal to the profiles for the full implementation, indicate that the main effect of this THF correction in this case is through the buoyant production term in the k - and ϵ -equations as only the z-component is included in this term. The other components are only included in the temperature equation but their effect is apparently negligible.

Looking at the profiles for the TKE, it can be concluded that there is a small influence of the THF correction due to the deviation in the profile for the implementation without THF correction. This deviation was expected, because as seen in Figure 4.4 it was seen that the THF correction introduces additional production of TKE. Without this additional production the amount of TKE in the simulation is lower.

Lastly, seeing that the only effect of the THF correction is through the buoyant production, it can be concluded that it is not necessary to include the THF correction in the SpARTA methodology for this case. The additional production of TKE due to the THF correction would have been absorbed in the TKE production correction. However, it does allow for more detailed analysis of the influence of the corrections on the TKE production.

6.2.2. Model Selection

In Section 5.3 multiple models with differing numbers of terms were selected for implementation, with a lower number of terms generally being associated with a higher mse and maxse. These models are implemented in different simulations to determine the optimal number of terms in the correction models. The simulation with high complexity models implements $[b_{ij}^A]_{2164}^A$ (7 terms), $[\mathcal{R}]_{1850}^A$ (1 term) and $[q_j^A]_{3401}^A$ (7 terms). The simulation with medium complexity models implements $[b_{ij}^A]_{16}^A$ (4 terms), $[\mathcal{R}]_{1850}^A$ (1 term) and $[q_j^A]_{119}^A$ (4 terms). Lastly, the low complexity models implemented are $[b_{ij}^A]_9^A$ (2 terms), $[\mathcal{R}]_{1850}^A$ (1 term) and $[q_j^A]_{117}^A$ (2 terms). It is chosen for all simulations to implement the one-term model for the TKE production correction \mathcal{R} as this model significantly outperformed the other, more complex models in terms of mse and maxse. The resulting planar-averaged profiles for the simulations are displayed in Figure 6.3.

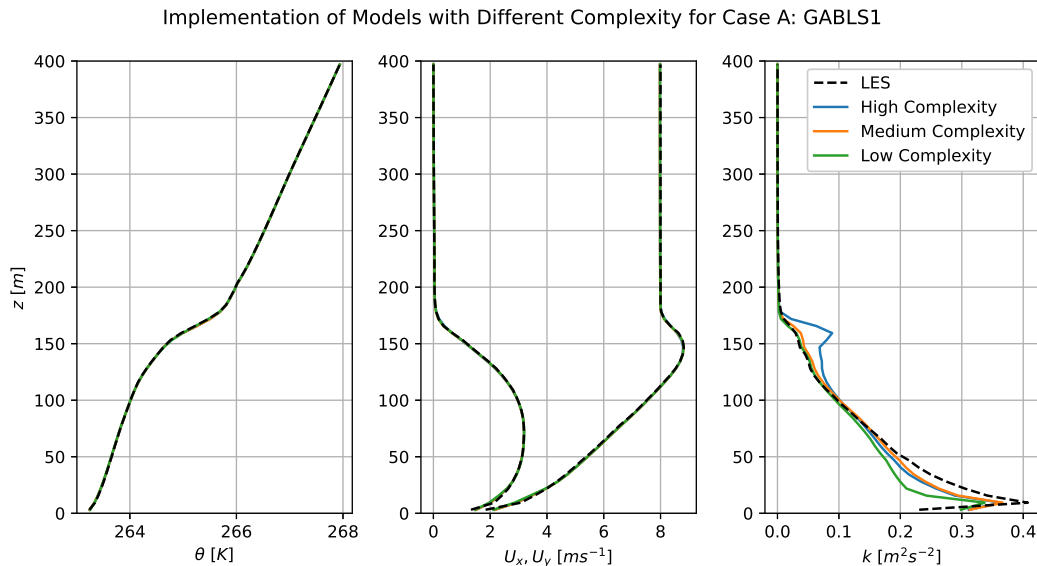


Figure 6.3: Comparison of planar-averaged profiles of temperature, velocity and TKE for simulations of Case A: GABLS1 with different complexity models implemented.

The profiles for the temperature and velocity in Figure 6.3 show no significant deviations from the LES data for all simulations with implemented models. This can be explained by the fact that these are prescribed at the inflow and the case itself is not very complex as there are no turbines. The only parameter for which the profiles in Figure 6.3 for the different simulations show deviations is the TKE. The surprising conclusion is that the simulation with medium complexity models is the closest to the LES data, even though the higher complexity models performed slightly better in terms of mse and maxse. At the top of the ABL even the low complexity models outperform the high complexity models. A possible explanation for this could be that with more complex models, the different terms are more sensitive to changes and start interacting with each other.

6.2.3. Comparison to Baseline

The profiles of the baseline simulation are compared to the simulation with medium complexity models from the previous section in Figure 6.4. This simulation implements models $[b_{ij}^A]_{16}^A$, $[\mathcal{R}]_{1850}^A$ and $[q_j^A]_{119}^A$ and is chosen as it performed the best out of the selected combination of models.

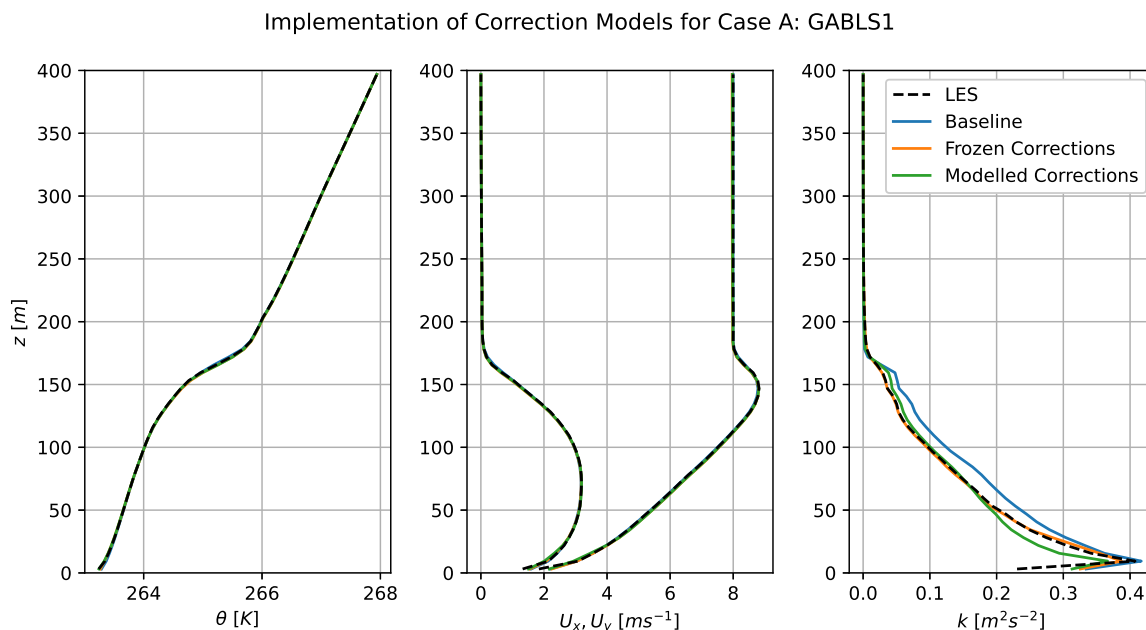


Figure 6.4: Comparison of planar-averaged profiles of temperature, velocity and TKE for simulations of Case A: GABLS1 with modelled, frozen and without any corrections implemented.

In Figure 6.4, the TKE profile is again the only profile which displays deviations from the LES data. For the majority of the profile in the ABL the simulation with modelled corrections shows improvement over the baseline simulation which slightly over-predicts the TKE. Only towards the bottom of the domain, the simulation with modelled corrections slightly under-predicts the TKE while the baseline simulation TKE is closer to the LES reference data. An explanation for this is the fact that for such a simple case the baseline simulation is already quite good.

6.2.4. Model Performance

As seen in the previous section, the simulation with the implemented models deviates slightly from the target simulation with frozen corrections. In order to investigate what causes this deviation, the modelled correction terms are compared to the expected correction terms, the influence of deviations in the correction terms on the TKE production terms is investigated and it is researched what correction terms have the biggest influence on the final results.

6.2.4.1. Errors in Modelled Correction Terms

First, the values of the different correction terms in the simulation with implemented models are compared to their respective optimal, frozen values and their expected values. These expected values are

generated by using the implemented models and the data from the k-corrective frozen RANS simulation. This comparison is displayed for the turbulence anisotropy correction, b_{ij}^{Δ} , in Figure 6.5.

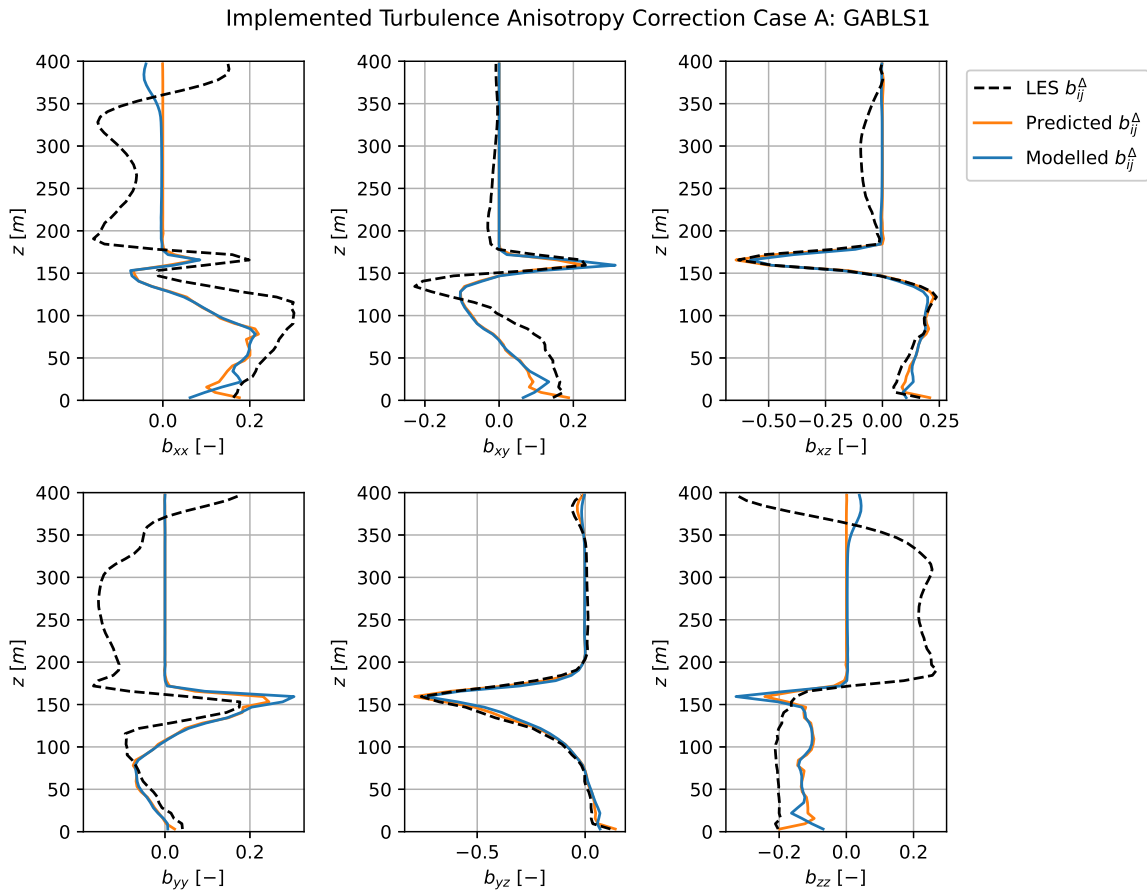


Figure 6.5: Planar-averaged profiles of the modelled turbulence anisotropy correction compared against the optimal, frozen correction term and the predicted correction term for Case A: GABLS1.

When considering Figure 6.5, it is visible that the modelled turbulence anisotropy correction term stays very close to the predicted value throughout the domain. Only towards the bottom of the domain there are some visible deviations due to the blending of the correction terms close to the wall. The fact that the implemented model is so close to the expected value is caused by the fact that the data used to train the models is from from the same case as the models are implemented in. The only cause of deviations are a compound effect between the three different modelled correction terms. This would indicate that the main bottleneck of increasing the accuracy of this method is the ability for models to match the target data of the turbulence anisotropy correction. In Figure 6.5 it is visible that the model matches the relatively largest component of the turbulence anisotropy correction (xz and yz quite well, while the other components show quite a large deviation. The same analysis for the TKE production correction term, \mathcal{R} , is displayed in Figure 6.6.

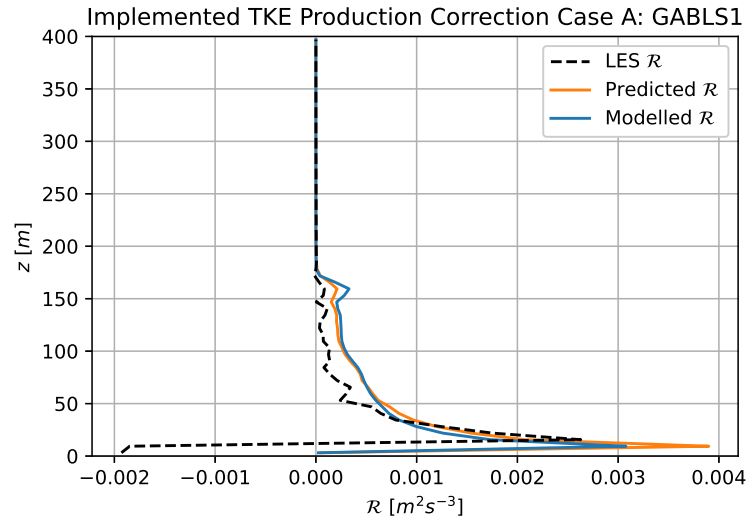


Figure 6.6: Planar-averaged profile of the modelled TKE production correction compared against the optimal, frozen correction term and the predicted correction term for Case A: GABLS1.

The modelled TKE production term is generally almost equal to the predicted value, just as for the turbulence anisotropy correction. This means that in this case the compound effect of the correction terms on each other is quite small. However, there is a slight overestimation of the modelled TKE production correction term in the ABL when compared to the target value. Lastly, the modelled components of the turbulent heat flux correction are compared against their expected and target values in Figure 6.7.

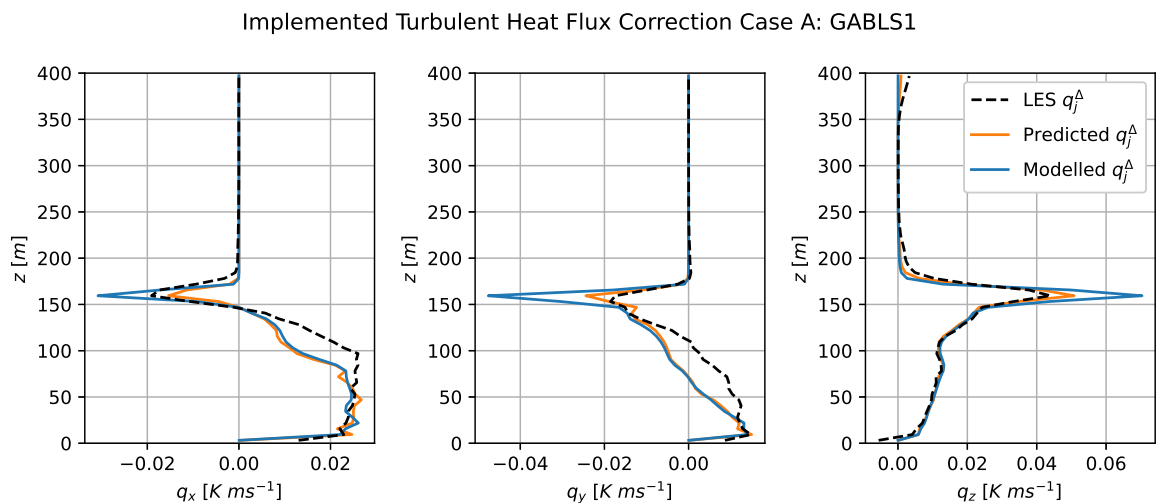


Figure 6.7: Planar-averaged profiles of the modelled THF correction compared against the optimal, frozen correction term and the predicted correction term for Case A: GABLS1.

Figure 6.7 shows a larger discrepancy between the predicted and modelled values of the correction term than the other two corrections. Especially the peaks in the capping inversion are exacerbated by the implemented model. This could be explained by the snow-ball effect of larger gradients, causing large values in the models, leading to even larger gradients, causing over-estimations of the peaks. The target value of the z -component is matched quite well by the model, while the other two components are not matched as well. However, in Subsection 6.2.1 it became clear that the z -component is the only important component.

6.2.4.2. Influence Correction Term Modelling Errors on TKE Production

In the previous paragraph it is shown that all correction models show some deviations from the optimal, frozen values, especially certain components of b_{ij}^Δ and q_j^Δ . To get a sense on how these deviations influence the simulations the planar-averaged profiles of the different TKE production terms are displayed in Figure 6.8. This figure compares the TKE production terms from the simulation with implemented models (solid lines) to the terms from the k-corrective frozen RANS simulation (dashed lines).

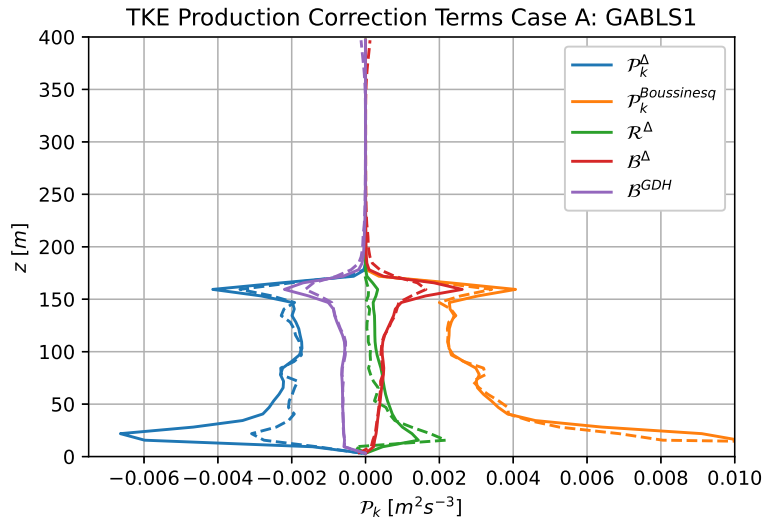


Figure 6.8: Planar-averaged profiles of the different TKE production terms in the simulation with implemented models (solid lines) and in the k-corrective frozen RANS simulation (dashed lines) for Case A: GABLS1

First of all, it is clear that the TKE production due to b_{ij}^Δ shows the largest deviation from the k-corrective frozen RANS simulation. Especially, throughout the lower portion of the ABL the difference is quite pronounced. This was to be expected due to the mismatch between model and target for certain components of this correction term. Furthermore, it deviates close to the wall as the velocity gradient at the wall shows a slight mismatch between the RANS simulation and LES data. The velocity gradients heavily influence the correction models, leading to the significant deviation.

The TKE production correction term shows some slight deviations from the reference value, but nowhere near as pronounced as for the turbulence anisotropy correction. Lastly, the TKE production due to the THF correction shows the same exacerbation of the peak in the capping inversion also seen in the THF correction itself. However, this deviation is much smaller than for the turbulence anisotropy correction and is also partly remedied by the exacerbation of the negative peak in the TKE production due to the gradient-diffusion hypothesis.

6.2.4.3. Influence Correction Term Modelling Errors on Simulation

In Figure 6.8 it is seen that the mismatch of the turbulence anisotropy correction, b_{ij}^Δ , has the largest influence on the TKE production terms in the simulation with implemented models. Therefore, Figure 6.9 shows the planar-averaged profiles of simulations which only model one correction term, while keeping the other correction terms at their optimal, frozen values. This is done in order to get a sense of how the correction term modelling errors influence the overall simulation.

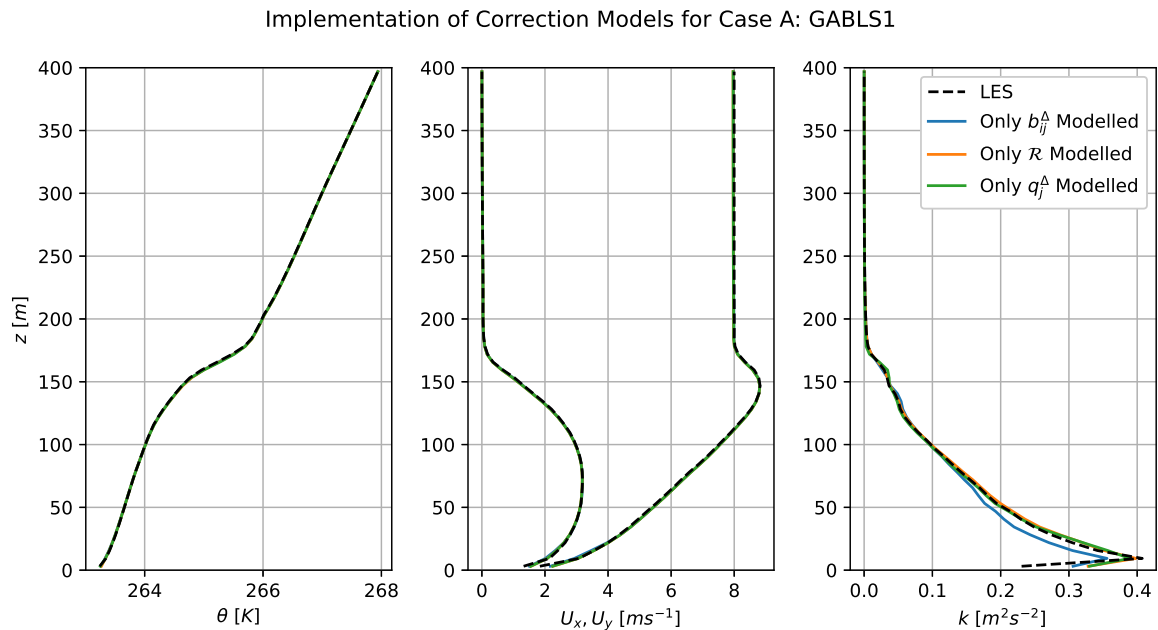


Figure 6.9: Planar-averaged profiles of the temperature, velocity and TKE for Case A: GABLS1 simulations with one correction term modelled, and the others frozen.

From Figure 6.9 it is clear that almost the entire deviation of the TKE in the simulation with implemented models seen in Figure 6.4 is due to the mismatch between the modelled b_{ij}^A and the optimal value. As the TKE profile with only b_{ij}^A modelled is the only TKE profile significantly deviating from the LES data. As seen before, the mismatch between the modelled and optimal turbulence anisotropy correction is due to the inability of the model to match the LES data. This could indicate that additions to the regression library are needed in order to better model the phenomena present in the turbulence anisotropy correction.

6.3. Results Case B: Kokee SBL with Implemented Models

The same analysis of the results of RANS simulations with implemented models for Case B is performed as was done for Case A in the previous section. This means that the influence of the THF correction is investigated, as well as the model selection. The results are compared against a baseline simulations and the performance of the different correction models is investigated. However, started is with an investigation of how the nonphysical turbulence model constants used by Kokee (2021) in the k-corrective frozen approach influences the simulations.

6.3.1. Influence of Nonphysical Turbulence Model Constants

As discussed in Chapter 4, Kokee (2021) used an unrealistic value for C_μ . This parameter influences the simulation through the computation of the turbulent viscosity, ν_t , and is also used in the respective wall models. The much too high value for C_μ used by Kokee (2021) means that for the same k and ϵ the turbulent viscosity is computed to be much higher. For the simulation this directly influences the velocity through the momentum equation and also the computation of k and ϵ themselves. Furthermore, the temperature equation is also influenced as the turbulent diffusivity is computed by dividing the turbulent viscosity by the (constant) turbulent Prandtl number. To get a sense of how the simulation is influenced by C_μ , the results of baseline RANS simulation using the values for $C_\mu = 1.17$ and $C_{\epsilon 1} = 1.81$ from Kokee (2021) is compared to the same simulation but using values for ABLs according to Sogachev et al. (2012): $C_\mu = 0.03$ and $C_{\epsilon 1} = 1.52$. Figure 6.10 displays the TKE-profiles for the respective simulations.

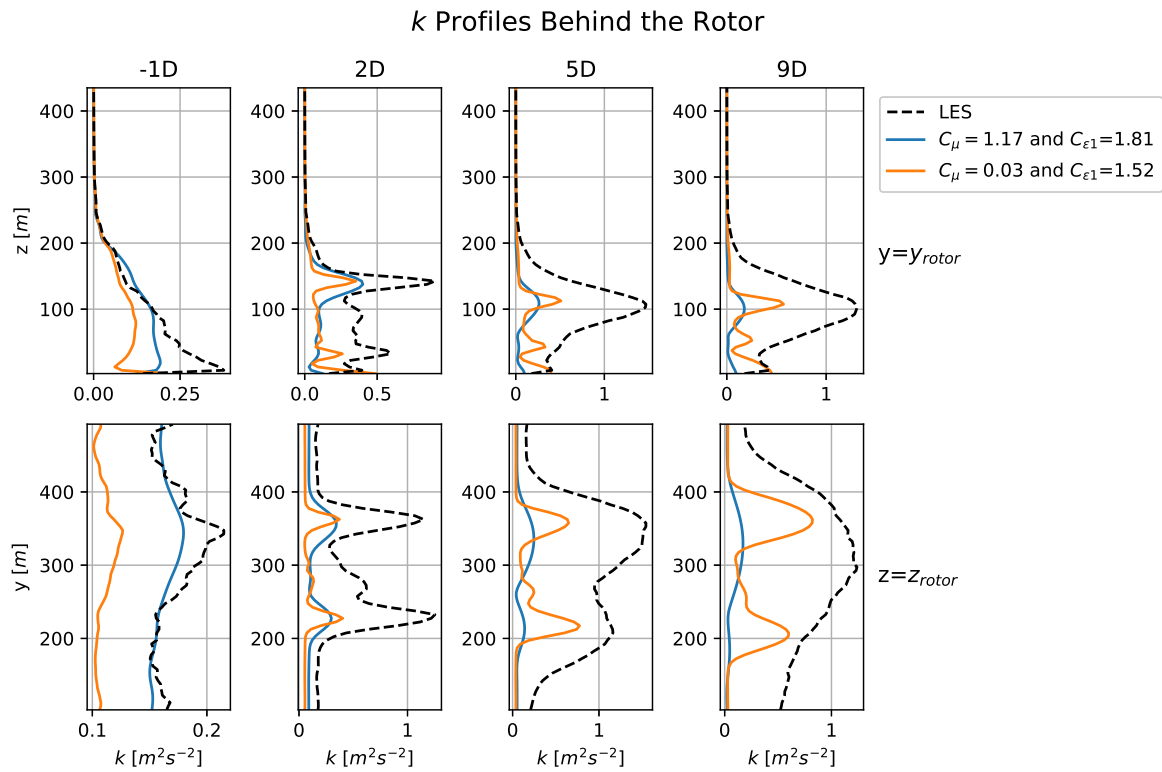


Figure 6.10: Comparison of TKE profiles for baseline RANS simulations of Case B: Kokee SBL with different values for C_μ and C_{ϵ_1} .

Considering Figure 6.10, it can be concluded that closer to the rotor the values from Kokee (2021) yields results closer to the LES reference results, while further away from the rotor the values from Sogachev et al. (2012) yields more accurate results. Another main effect from using the parameter values of Kokee (2021) seems to be that peaks in the profiles are smoothed out. Especially towards the rear of the domain, while the parameter values of Sogachev et al. (2012) do not smooth the peaks enough when comparing to the LES reference data. Aside from that, a surprising observation is that for both sets of parameter values, the turbulence kinetic energy is generally under-estimated with respect to the LES reference data. This is surprising as Steiner et al. (2022) and Goderie (2020) both reported overestimation of the turbulence kinetic energy by the baseline model. A possible explanation for this difference is the fact that this is a stably stratified case, as opposed to the neutral cases of Steiner et al. (2022) and Goderie (2020). It was seen in Chapter 3 that even though there is a very large vertical temperature gradient, the vertical component of the turbulent heat flux in the LES data is relatively small. This means that the gradient-diffusion hypothesis in the baseline model vastly overestimates the vertical component of the turbulent heat flux, leading to an over-estimation of the buoyant destruction of TKE and under-estimation of the TKE.

To see how these differences in TKE computation influence the overall simulation, the stream-wise velocity profiles are displayed in Figure 6.11. The profiles in Figure 6.11 show the same trend as in Figure 6.10: the set of parameter values from Kokee (2021) smoothens the profiles far to much, while the opposite is true for the simulation implementing the reference parameter values from Sogachev et al. (2012). This would suggest that the value for C_μ from Sogachev et al. (2012) is too small. Aside from this effect the accuracy level in simulating the velocity seems quite similar for both sets of parameter values.

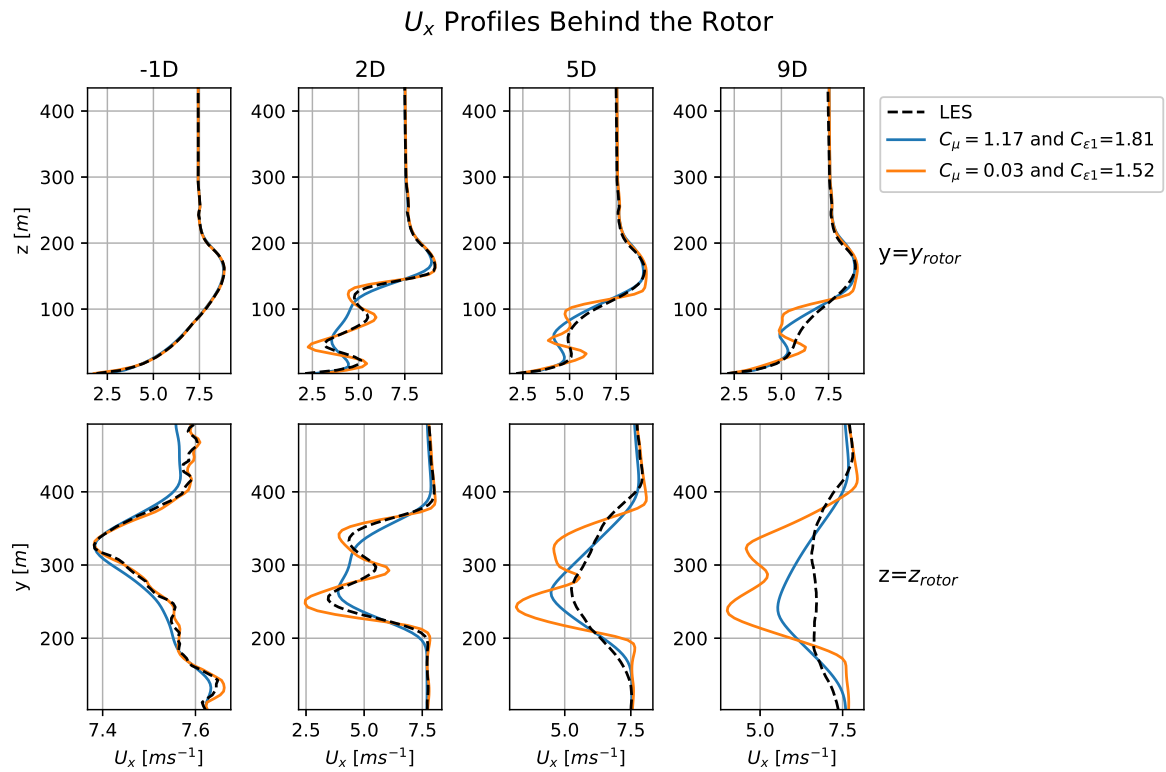


Figure 6.11: Comparison of stream-wise velocity profiles for baseline RANS simulations of Case B: Kokee SBL with different values for C_μ and $C_{\epsilon 1}$.

Lastly, the temperature profiles included in [Figure C.1](#) show that the effect of these parameters on the temperature equation is very limited. This means that the C_μ mainly influences the turbulence computation and the momentum balance. For the correction terms, the use of the unrealistic value for C_μ by [Kokee \(2021\)](#) means that they have to supply additional smoothing of the TKE and velocity profiles. In the remainder of this work, the baseline simulation refers to the simulation using the parameter values from [Kokee \(2021\)](#) as the correction terms are computed based on this value for C_μ .

6.3.2. Influence of the THF Correction

In [Subsection 6.2.1](#) it is concluded that for Case A: GABLS1 the THF correction, q_j^A , only influenced the simulation through added buoyant production of TKE and not through the temperature equation. For Case B: Kokee SBL, the same three simulations are performed: one with implemented optimal, frozen values for the corrections, one with only the z-component of the THF correction and one without the THF correction. [Figure 6.12](#) displays profiles of the vertical component of the turbulent heat flux behind the rotor, with the profiles of the horizontal components being included in [Figure C.2](#) and [Figure C.3](#).

It is clear that the simulations with both the full and with only the z-component of the THF correction almost perfectly match the LES data of the vertical component of the turbulent heat flux. However, the profiles of the horizontal components of the turbulent heat flux in [Appendix C](#) show a much better match between the simulations with only the z-component and without the THF correction. To see how these differences in the simulation of the turbulent heat flux influence the temperature, temperature profiles are displayed in [Figure 6.13](#).

The temperature profiles in [Figure 6.13](#) show some small deviations between the different simulations, especially the simulation without any THF correction shows the most deviation in the horizontal profiles. However, these deviations are mainly shown due to the very small scales of the figures and it can be concluded that these differences are not significant (in the order of 0.01 K). This confirms the notion from [Subsection 6.2.1](#) that the THF correction has a negligible effect on the temperature equation.

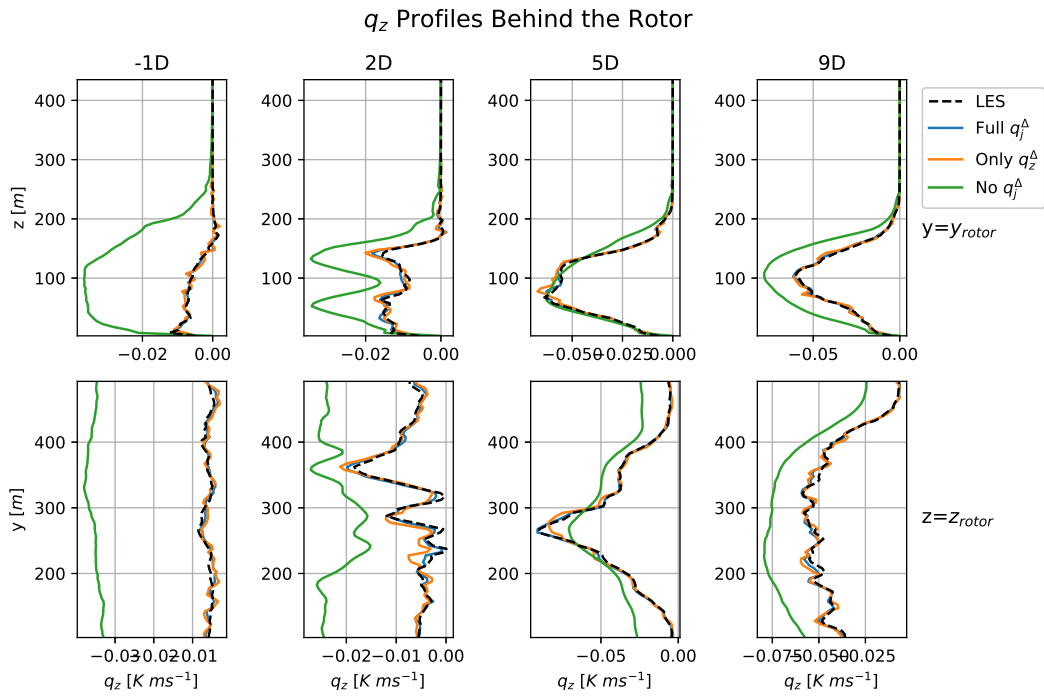


Figure 6.12: Profiles of the z-component of the turbulent heat flux behind the rotor for RANS simulations of Case B: Kokee SBL, with full THF correction implemented (blue), only z-component of THF correction (orange) and without THF correction (green). All simulations implemented the optimal, frozen turbulence anisotropy and TKE production corrections.

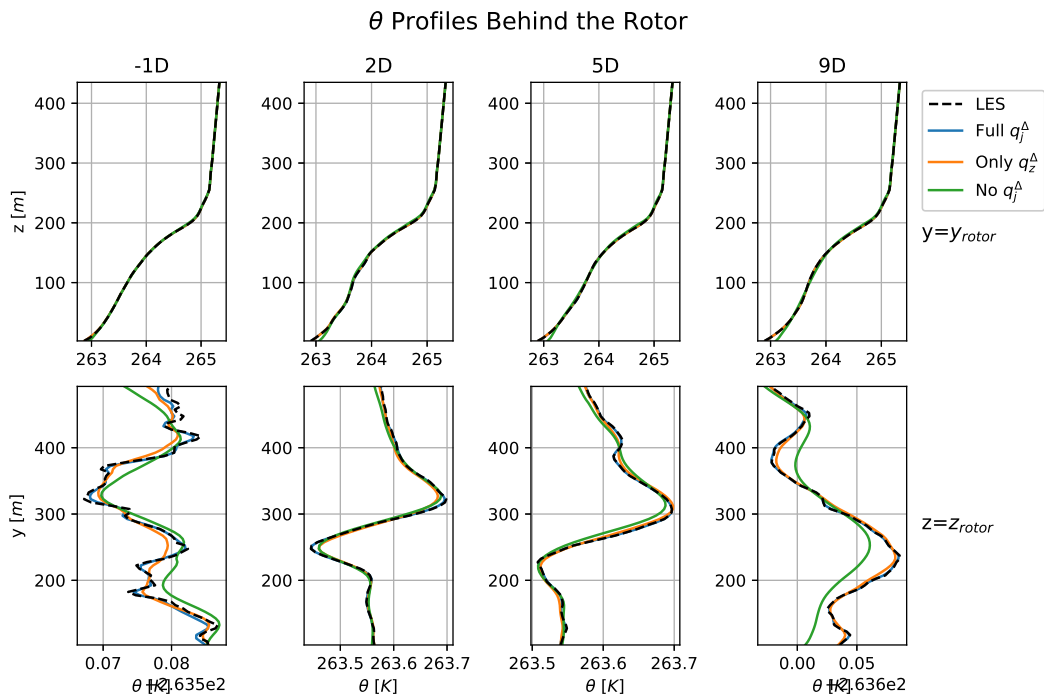


Figure 6.13: Profiles of the temperature behind the rotor for RANS simulations of Case B: Kokee SBL, with full THF correction implemented (blue), only z-component of THF correction (orange) and without THF correction (green). All simulations implemented the optimal, frozen turbulence anisotropy and TKE production corrections.

This only leaves the influence of the THF correction through the buoyant production of TKE. Therefore, the TKE profiles for the different simulations are included in [Figure 6.14](#).

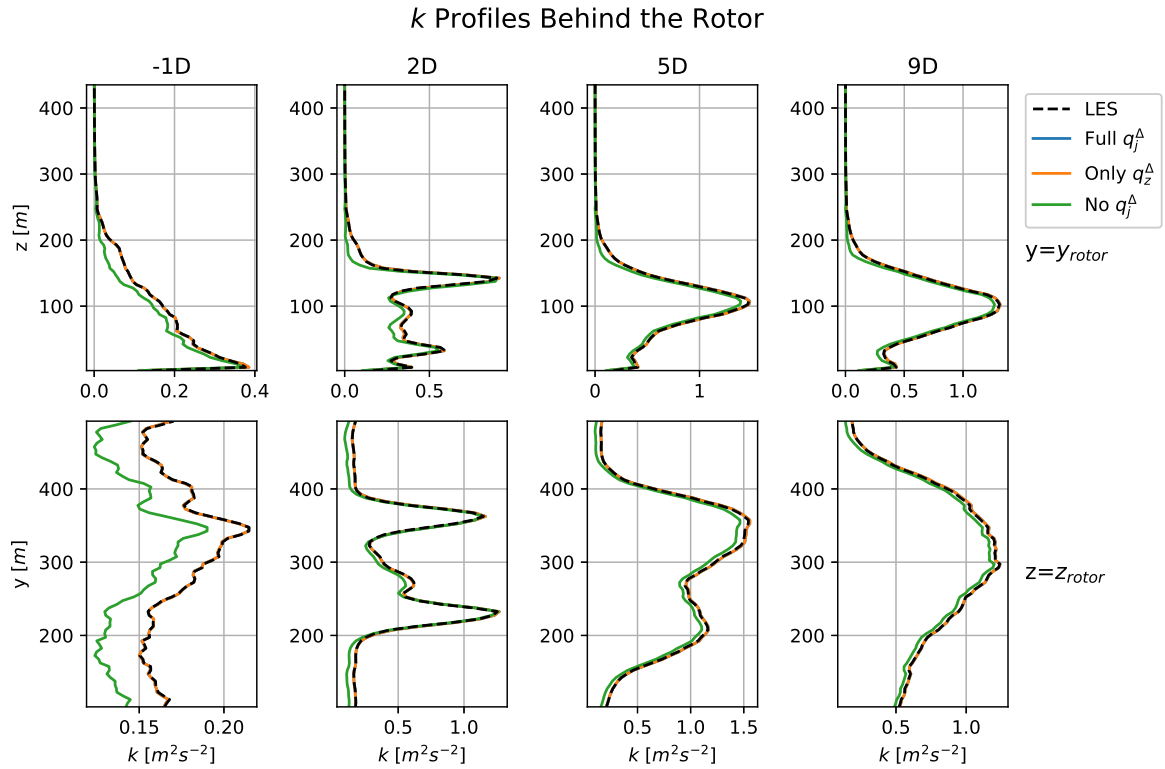


Figure 6.14: Profiles of the turbulence kinetic energy behind the rotor for RANS simulations of Case B: Kokee SBL, with full THF correction implemented (blue), only z-component of THF correction (orange) and without THF correction (green). All simulations implemented the optimal, frozen turbulence anisotropy and TKE production corrections.

The TKE-profiles of the simulations with the z-component and the full THF correction almost perfectly match the LES reference data, while the simulation without the THF correction shows a slight under-prediction of the TKE. This is due to the missing added buoyant production of TKE due to the z-component of the THF correction. This effect is also visible in the horizontal velocity profiles included in Figure C.4. The buoyant production of TKE due to the THF correction could also be incorporated in the overall TKE production correction, rendering the THF correction unnecessary. This is different from the conclusion drawn by Kokee (2021), who argued a scalar correction of the turbulent heat flux is necessary.

Lastly, as the data available is generated incorporating the THF correction, this correction is retained throughout this work (Kokee, 2021).

6.3.3. Model Selection

For each of the three correction terms, multiple models are implemented in order to find out which model selection criteria yield the best models.

6.3.3.1. Model Selection for the Turbulence Anisotropy Correction.

In order to discover the best model for the anisotropy correction, all chosen models from Subsubsection 5.3.2.1 are implemented in RANS simulations of Case B: Kokee SBL. This means that models $[b_{ij}^A]_{4167}^B$, $[b_{ij}^A]_{4159}^B$ and $[b_{ij}^A]_{4371}^B$ are implemented. For the correction terms for the TKE production and turbulent heat flux, the models with the lowest mse after the regression are implemented, which are models $[\mathcal{R}]_{10}^B$ and $[q_j^A]_9^B$. The simulated production of TKE due to the anisotropy correction behind the rotor is displayed in Figure 6.15.

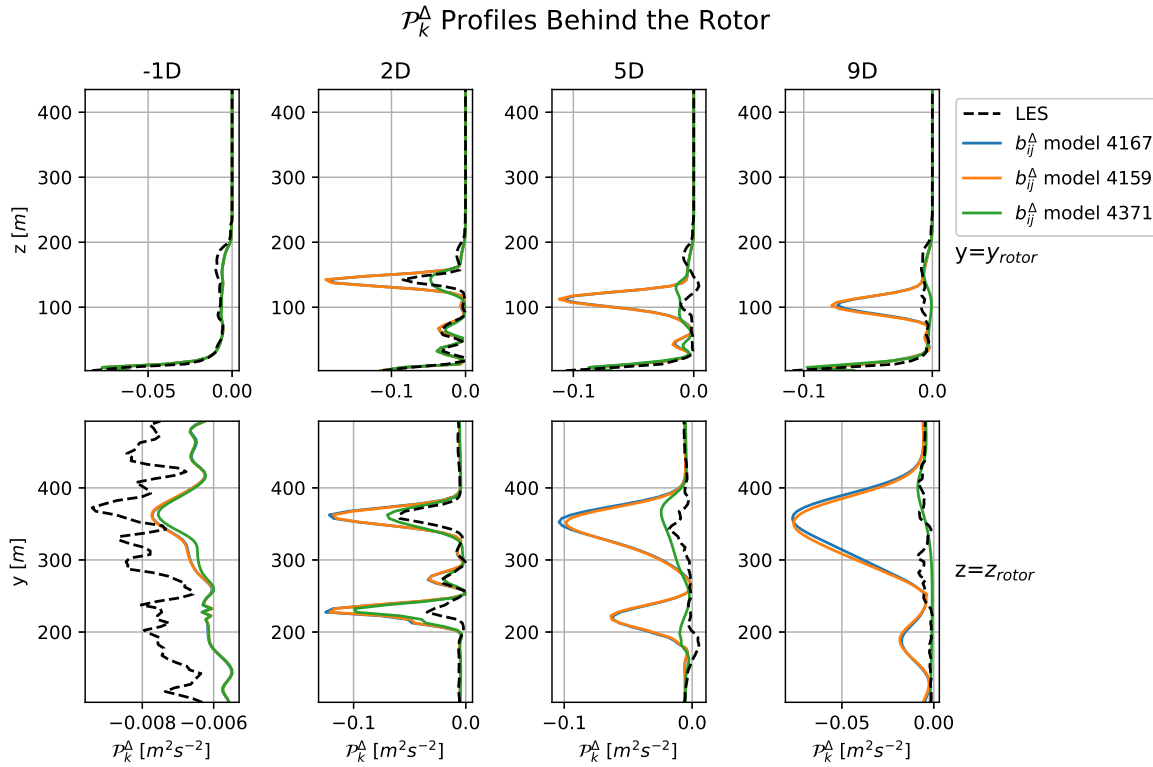


Figure 6.15: Profiles of the production of turbulence kinetic energy due to the anisotropy correction b_{ij}^A behind the rotor for RANS simulations of Case B: Koike SBL. Different simulations implemented different models for the anisotropy correction b_{ij}^A .

This figure shows that the simulation with model 4371, which is the model with the lowest max squared error after the regression, computes the TKE production due to the anisotropy correction closest to the LES data. Especially further downstream the effect becomes very pronounced. Where the simulation with model 4371 stays fairly close to the reference, the peaks in the other two simulation become very exaggerated, even more exaggerated than predicted. To see how this difference influences the main simulation parameters, profiles of the horizontal velocity behind the rotor are included in [Figure 6.16](#) and the same profiles for the temperature and the turbulence kinetic energy are included in [Figure C.5](#).

[Figure 6.16](#) shows that the model which most accurately modelled the TKE correction also simulated the horizontal velocity closest to the LES reference data. Models 4167 and 4159 overestimate the TKE destruction in the shear layers of the wake due to the large gradients present in these layers. This causes the wake to be more pronounced moving downstream as there is less turbulent mixing between the wake and the outside flow. An effect clearly seen in both the horizontal and vertical profiles furthest downstream from the rotor. Therefore, it can be concluded that model $[b_{ij}^A]_{4371}^B$ performs the best of the three chosen models, which means this model is used in all subsequent simulations.

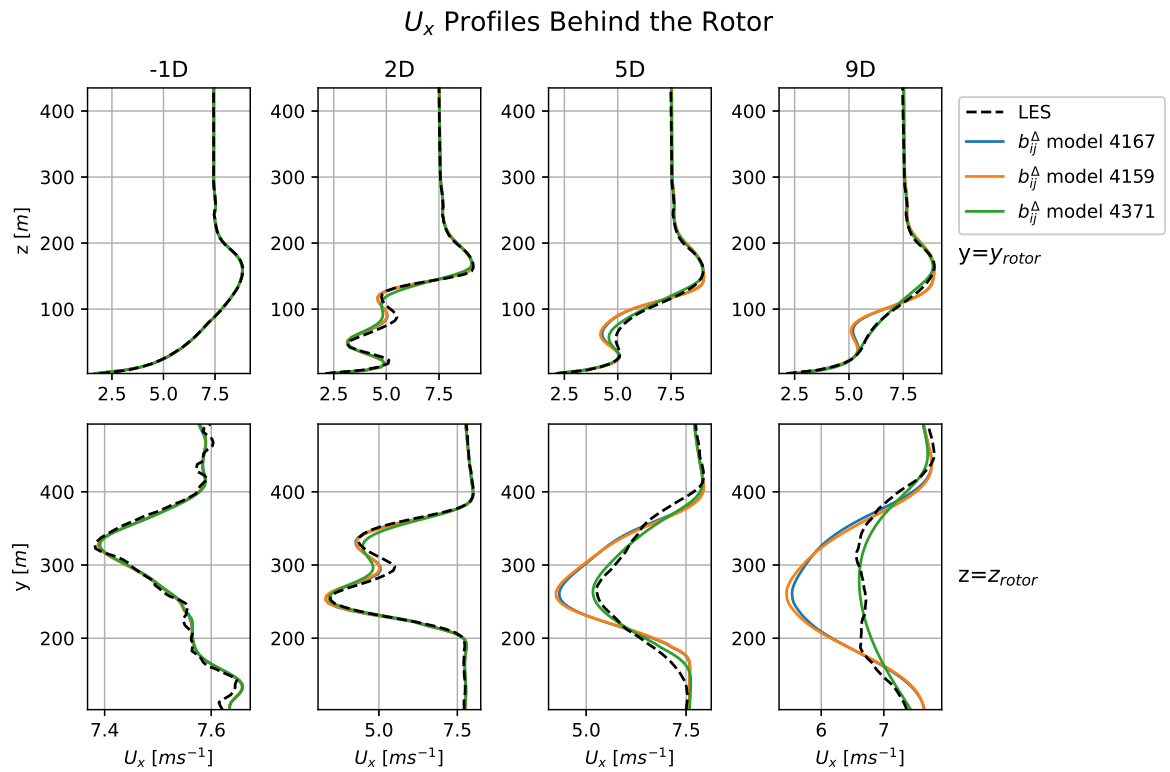


Figure 6.16: Profiles of the horizontal velocity behind the rotor for RANS simulations of Case B: Kokee SBL. Different simulations implemented different models for the anisotropy correction b_{ij}^A .

6.3.3.2. Model Selection for the TKE Production Correction

Just as for the anisotropy correction, all the chosen models for the TKE production correction are implemented in RANS simulations for Case B: Kokee SBL. This means that models $[\mathcal{R}]_{10}^B$, $[\mathcal{R}]_{12}^B$ and $[\mathcal{R}]_7^B$ are implemented. For the anisotropy correction model $[b_{ij}^A]_{4371}^B$ is used as it is found to perform the best in the previous section and for the THF correction model $[q_j^A]_9^B$ is used as it has the lowest mse after the regression.

Sample profiles of the simulated TKE production correction for the simulations with the different TKE production correction models implemented are displayed in Figure 6.17.

Figure 6.17 shows that the vertical profiles are best matched by model 7, especially more downstream. However, the peaks in the horizontal profiles of the TKE production correction close to the rotor are better matched by model 12. It is actually quite surprising that there are such significant differences between the models as the predictions of all models in Figure 5.16 are very close together. The fact that the simulation of models 10 and 12 differ significantly also shows that the term containing the first basis tensor in model 10 does have a significant effect on the simulation. Lastly, the fact that model 7 seems to be outperforming the others is also surprising as it is a very simple model of only one term. To see how the differences in Figure 6.17 influence the overall simulation, sample profiles for the TKE are displayed in Figure 6.18 with the same profiles for the temperature and horizontal velocity being included in Figure C.7 and Figure C.8

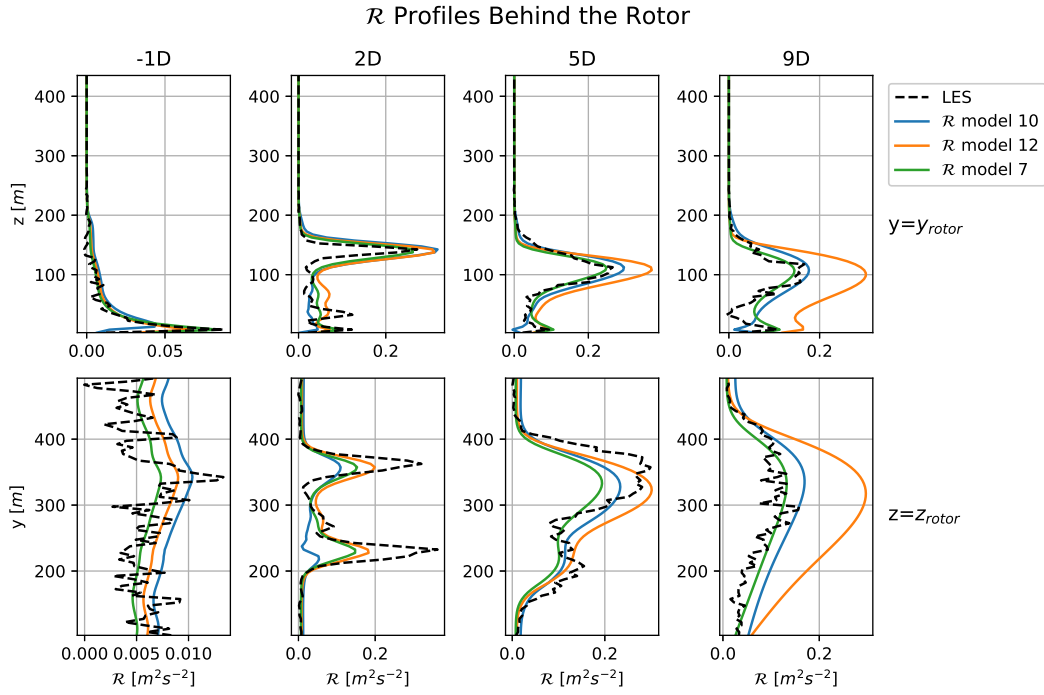


Figure 6.17: Profiles of the production of TKE correction \mathcal{R} behind the rotor for RANS simulations of Case B: Kokee SBL. Different simulations implemented different models for the TKE production correction \mathcal{R} .

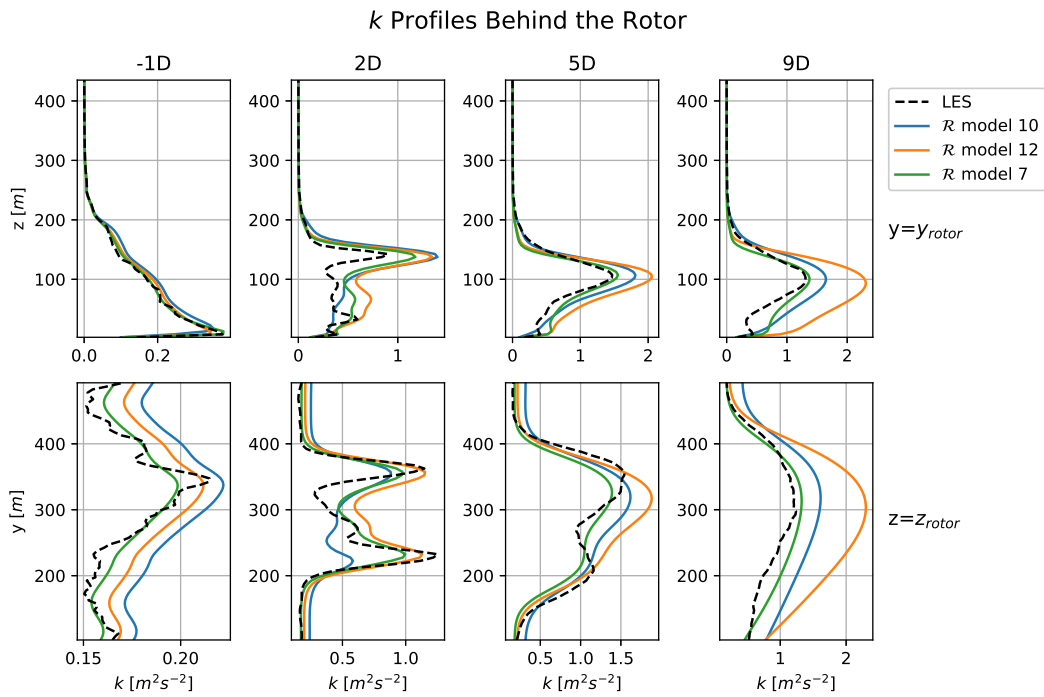


Figure 6.18: Profiles of the production of TKE correction behind the rotor for RANS simulations of Case B: Kokee SBL. Different simulations implemented different models for the TKE production correction \mathcal{R} .

In [Figure 6.18](#) it is clear that model 7 provides the best simulation of the TKE, especially more downstream of the rotor. This is as expected as this model also performed the best in terms of the TKE production correction itself. Therefore, model $[\mathcal{R}]_7^{\beta}$ is chosen as TKE production correction model for all subsequent simulations.

6.3.3.3. Model Selection for the THF Correction

Lastly, the chosen models for the THF correction are implemented. This means that models $[q_j^A]_9^B$ and $[q_j^A]_7^B$ are implemented. For the turbulence anisotropy correction and TKE production correction models $[b_{ij}^A]_{4371}^B$ and $[\mathcal{R}]_7^B$ are used as they were found to be the best performing models in the previous sections.

The vertical component of the THF correction for the two simulations is displayed in [Figure 6.19](#). Very similar to the prediction after the regression, the two models perform about equally with only some deviations here and there. However, one model does not clearly outperform the other. This is not the case for the horizontal components of the THF correction, the figures of which are included in [Figure C.9](#) and [Figure C.10](#), where model 9 performs much better than model 7. However, as seen in [Subsection 6.3.2](#), the horizontal components of the THF correction are of negligible importance.

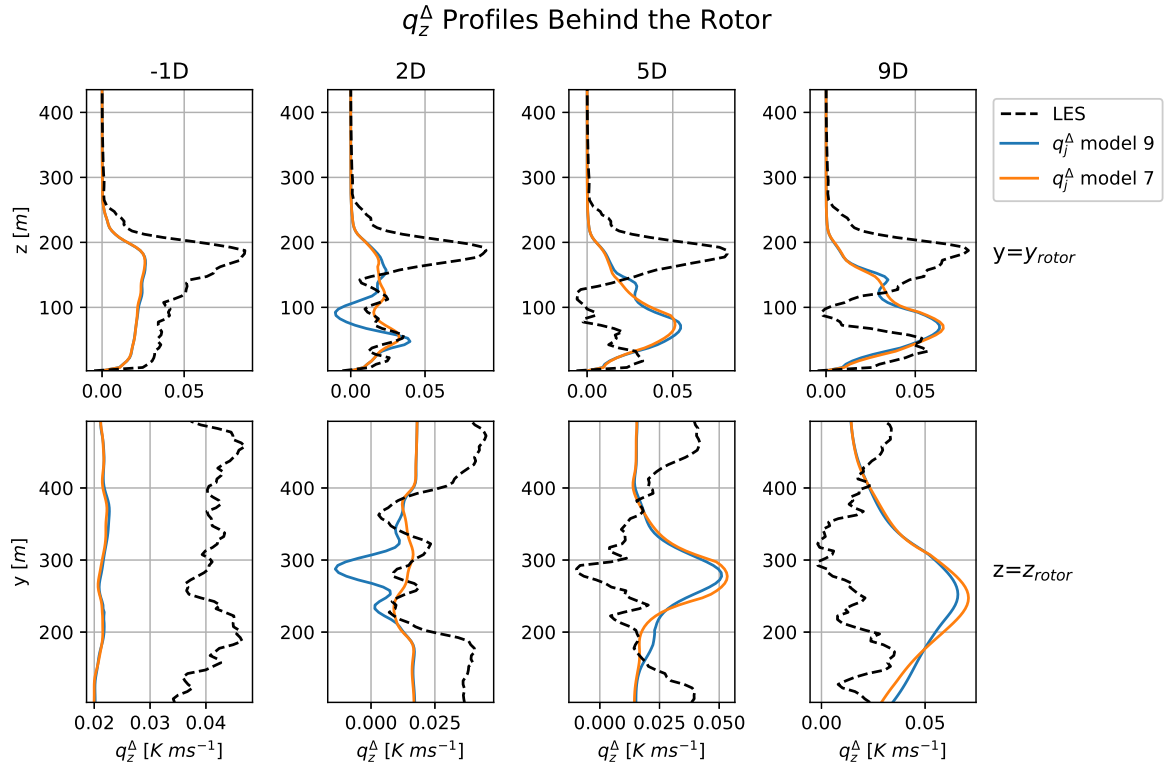


Figure 6.19: Profiles of the z-component of the THF correction q_z^A behind the rotor for RANS simulations of Case B: Kokee SBL. Different simulations implemented different models for the THF correction q_j^A .

Despite the differences in the computation of the THF correction between the models, the effect on the overall simulation is very minimal. As can be seen in the profiles for the horizontal velocity in [Figure 6.20](#) and for the temperature and TKE in [Figure C.11](#) and [Figure C.12](#). This can be explained by the relatively small effect the vertical component of the THF correction has on the overall simulation through the buoyant production of TKE, while the horizontal components have no influence at all, as discussed in [Subsection 6.3.2](#).

Seeing that both models perform very similarly, the simplest model is chosen. This means that model $[q_j^A]_7^B$ is chosen to model the THF correction.

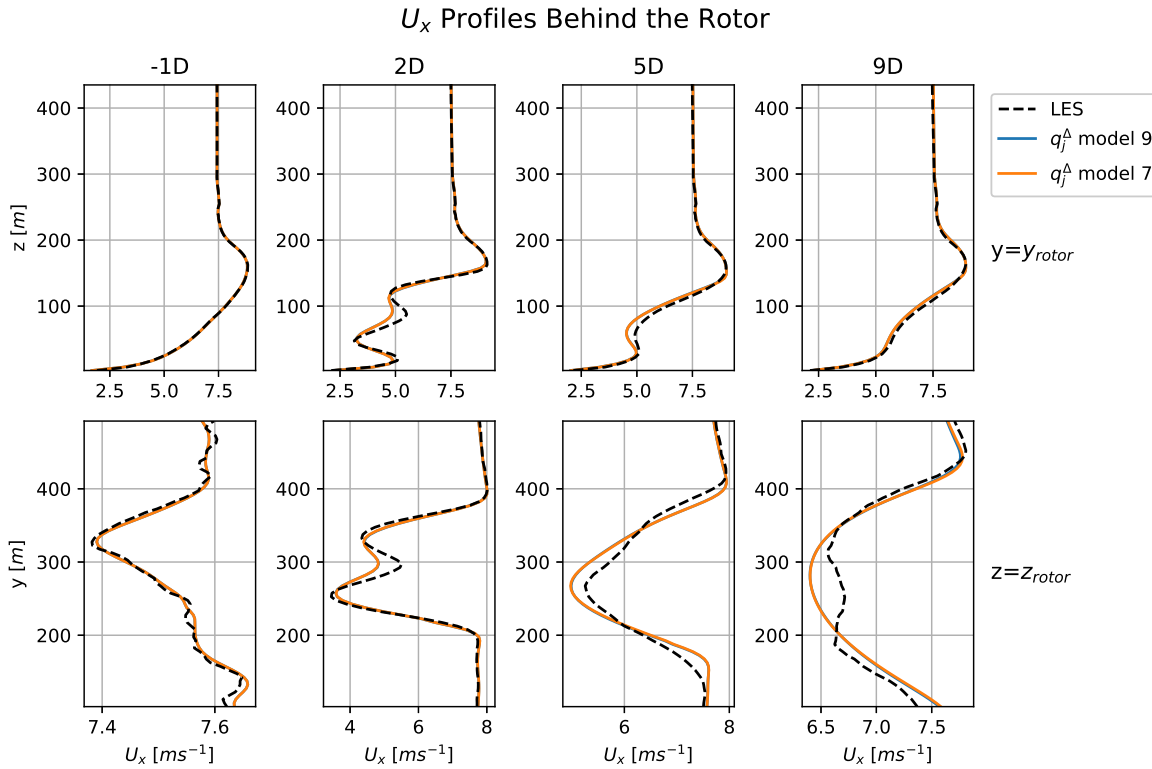


Figure 6.20: Profiles of the horizontal velocity behind the rotor for RANS simulations of Case B: Kokee SBL. Different simulations implemented different models for the THF correction q_j^A .

6.3.3.4. Discussion of Model Selection

After considering the performance of the different chosen models, it is clear that there is still no one clear a priori selection criterion to choose the best models. For the anisotropy correction, the model with the lowest maxse performed the best, while for the TKE production correction the simplest model outperformed the more complex models with lower maxse and mse after the regression. Moreover, the simplest model for the THF correction performed just as good as the more complex model with lower mse and maxse.

6.3.4. Comparison to Baseline

Next, the RANS simulation of Case B: Kokee SBL with the best models implemented is compared against the baseline simulation. The simulation with implemented models implements the best models $[b_{ij}^A]_{14371}^B$, $[\mathcal{R}]_7^B$ and $[q_j^A]_7^B$. Profiles of the turbulence kinetic energy behind the rotor are compared in Figure 6.21 for the LES data, the baseline simulation and corrected simulations.

Figure 6.21 shows that the baseline massively underestimates the turbulence kinetic energy compared to the LES data. Something which is much improved by the simulation with implemented models. A trend which is also visible in the contour plots displayed in Figure 6.22. There, it is also visible that the maximum of turbulence kinetic energy is very close to the edges of the rotor for the baseline, while the location of the maximum is much further downstream for the LES data and simulation with implemented models. This is also visible in the horizontal slices of TKE included in Figure C.13. This phenomenon could indicate that the most important source of TKE for the baseline simulation are the tip vortices introduced at the edge of the rotor. While in the LES and RANS simulation with implemented models the most turbulence is created in the shear layer between the wake and the outside flow. This TKE production in the shear layer only decays further downstream as the shear layer becomes wider due to the turbulent mixing. The disparity in turbulence creation between the baseline and the LES data is corrected for by the implemented models. Referring back to the contour plots of the TKE production due to the different correction terms from Section 4.2 and the TKE breakdown in Figure C.17, it seems like b_{ij}^A mainly removes the TKE very close to the rotor from the baseline, while \mathcal{R} introduces the addi-

tional TKE in the shear layer. Meanwhile, the THF correction mainly removes the buoyant destruction of TKE due to the gradient-diffusion hypothesis in the wake.

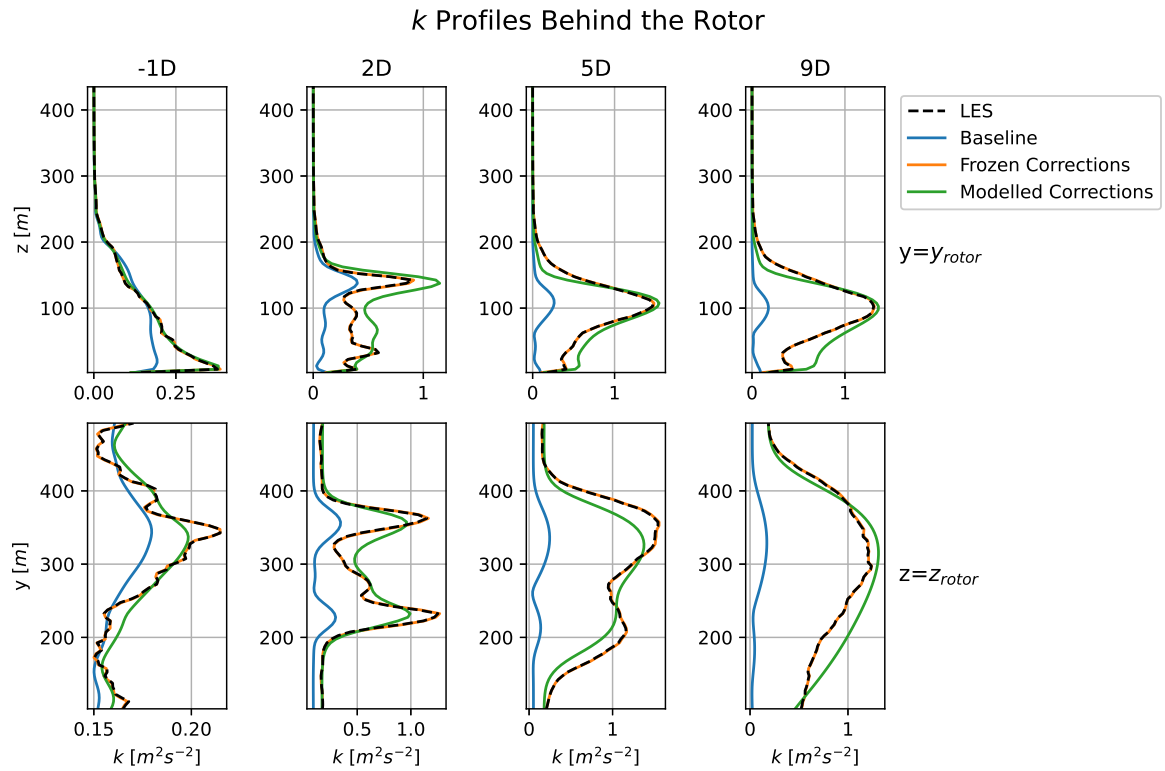


Figure 6.21: Comparison of TKE profiles behind the rotor between the LES data, the baseline simulation, the simulation with optimal, frozen corrections and the simulation with implemented models for Case B: Kokee SBL.

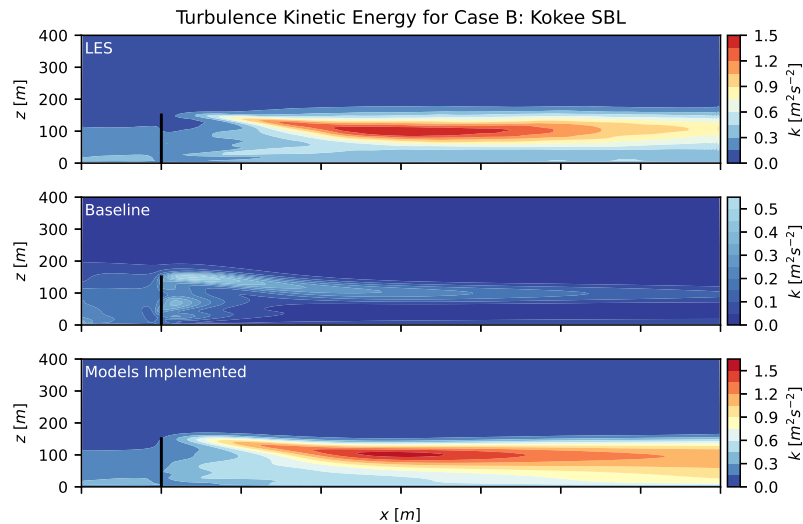


Figure 6.22: Comparison of vertical slices of TKE at the location of the rotor between the LES data, the baseline simulation and the simulation with implemented models for Case B: Kokee SBL. The rotor is represented by the black line and all slices are plotted with the same colour scale for better comparison.

The difference in turbulence creation between the baseline simulation and LES data also influences the stream-wise velocity profiles included in Figure 6.23. The omission of the most important mechanism of turbulence creation in the baseline simulation leads to much reduced mixing of the wake and outside flow. This leads to an over-estimation of the wake further down-stream of the rotor in the baseline simulation. The simulation with implemented models corrects for this effect and show much better agreement with the LES data.

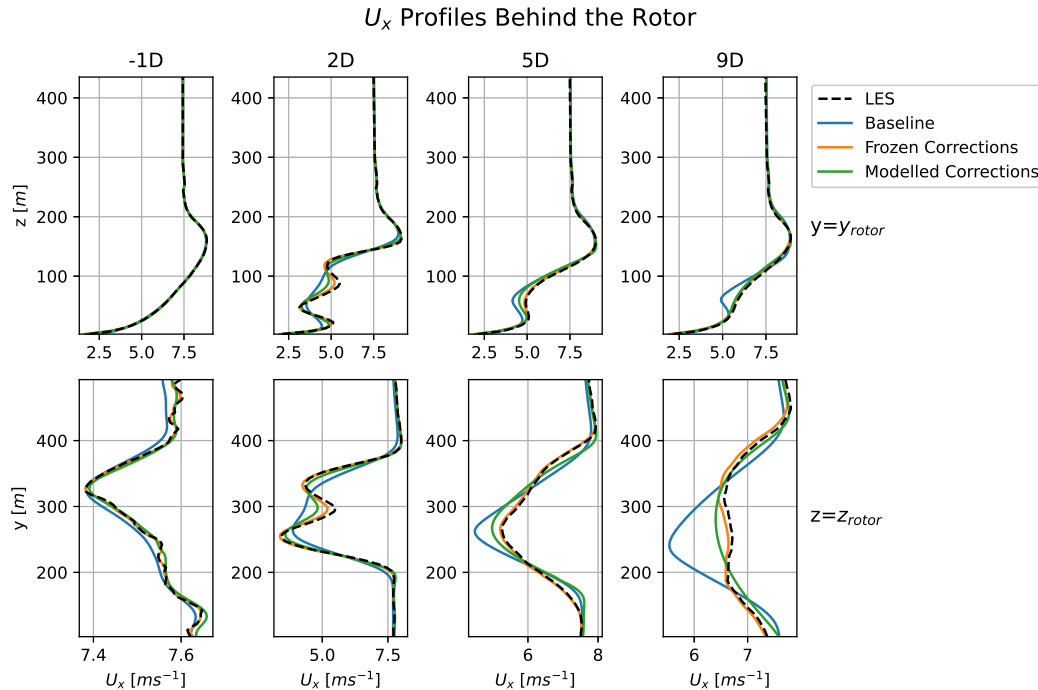


Figure 6.23: Comparison of stream-wise velocity profiles behind the rotor between the LES data, the baseline simulation, the simulation with optimal, frozen corrections and the simulation with implemented models for Case B: Kokee SBL.

The contour plots of the stream-wise velocity in Figure 6.24 tell the same story. The wake is decaying less rapidly for the baseline simulation than for the LES data. Particularly visible is how the shear-layer rapidly widens for the LES data and simulation with implemented models, while the shear-layer stays much more narrow in the baseline simulation. Something which is also visible, to a lesser extent as the shear-layer mixes with the capping inversion, in the vertical slices of stream-wise velocity included in Figure C.14.

Lastly, the temperature profiles included in Figure C.19 show no significant differences between the baseline and the simulation with implemented models. This confirms the assertion that the models do not significantly influence the temperature equation.

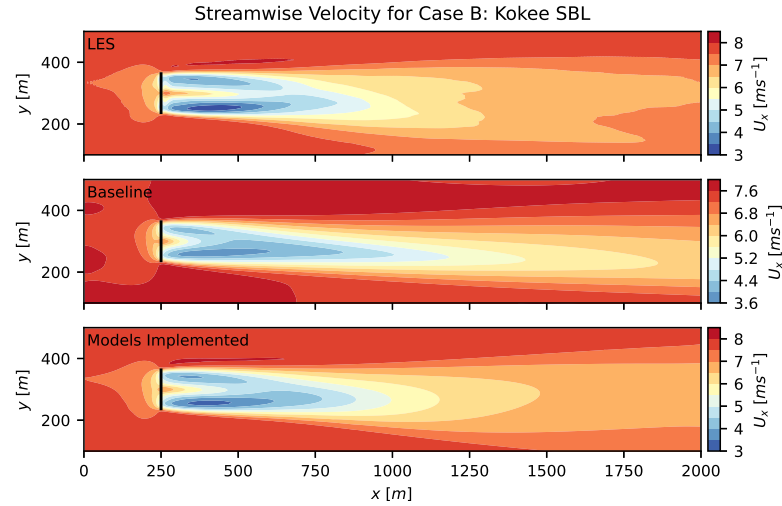


Figure 6.24: Comparison of horizontal slices of stream-wise velocity at hub-height between the LES data, the baseline simulation and the simulation with implemented models for Case B: Kokee SBL. The rotor is represented by the black line and all slices are plotted with the same colour scale for better comparison.

6.3.5. Model Performance

Lastly, the performance of the different correction models implemented for Case B: Kokee SBL is investigated to get a sense of how the modelling errors influence the simulation.

6.3.5.1. Errors in Modelled Correction Terms

First, the simulated correction terms are compared to their optimal, frozen values and their expected values based on the selected model and the data from the k-corrective frozen simulation. This comparison for the TKE production due to the turbulence anisotropy correction is displayed in Figure 6.25, where it is visible that the predicted and simulated profiles are quite close together. The most visible effect is a smoothing of the simulated profiles more downstream of the rotor.

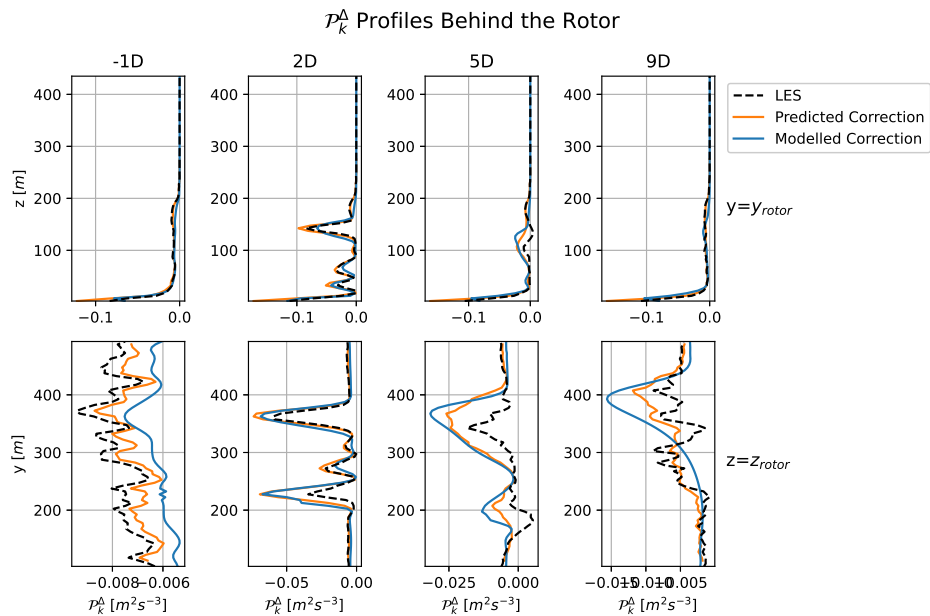


Figure 6.25: Comparison of the TKE production due to the turbulence anisotropy correction, P_{ij}^A , for the optimal, predicted and modelled correction term for Case B: Kokee SBL.

Looking at the TKE production correction in Figure 6.26, some more apparent differences are visible between the expected and simulated correction. Especially the peaks in shear layers between the wake and the outside flow are visibly smoothed.

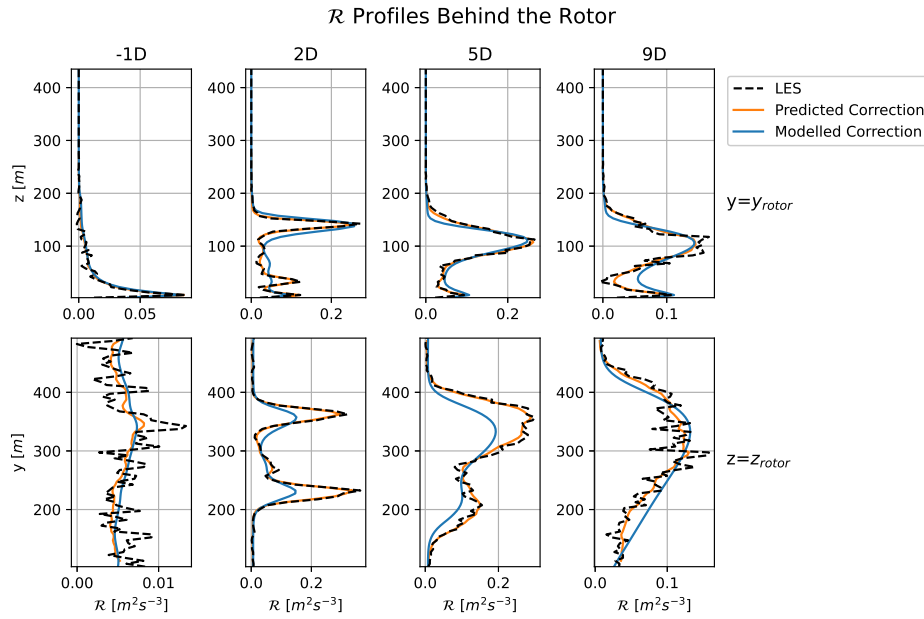


Figure 6.26: Comparison of the TKE production correction, \mathcal{R} , for the optimal, predicted and modelled correction term for Case B: Kokee SBL.

Lastly, the comparison of profiles for the z-component of the THF correction is displayed in Figure 6.27. These profiles show the largest difference between the predicted and simulated values of all the correction term. Especially the peak in the capping inversion is not present at all in the simulated model. However, as seen in Subsection 6.3.2, the effect of the THF correction is quite limited.

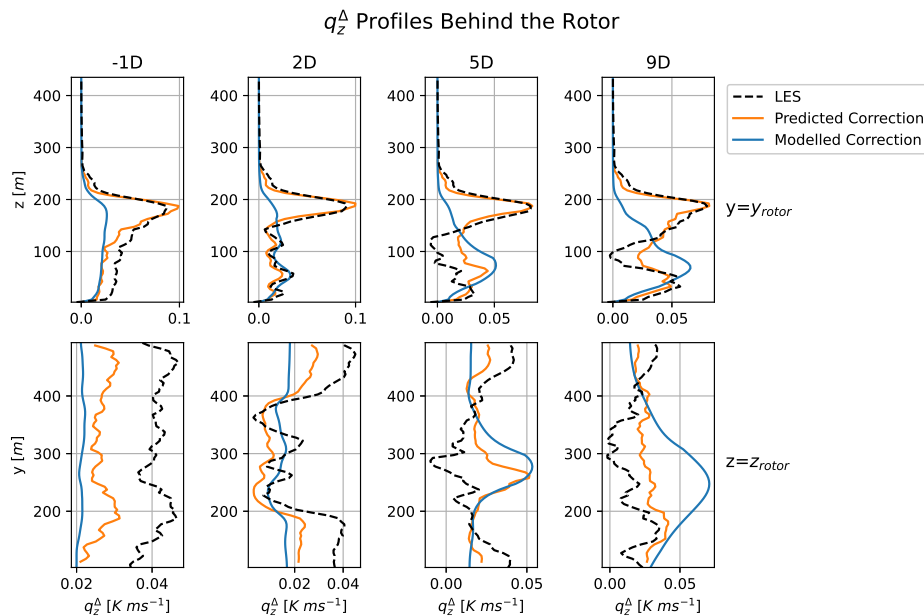


Figure 6.27: Comparison of the THF correction, \mathcal{R} , for the optimal, predicted and modelled correction term for Case B: Kokee SBL.

6.3.5.2. Influence Correction Term Modelling Errors on TKE production

To see how the differences in simulated correction terms influence the production of turbulence kinetic energy, profiles of the different TKE production terms are displayed in Figure 6.28. There, it is visible that the buoyant production of TKE is negligible behind the rotor. Furthermore, similar to Case A, b_{ij}^Δ seems to mainly work against the Boussinesq production of TKE. Also visible is the fact that the peaks in the values of \mathcal{R} in the shear-layers are smoothed in the simulation with implemented models compared to the optimal values of the correction term. The other two correction terms show better agreement with the optimal values.

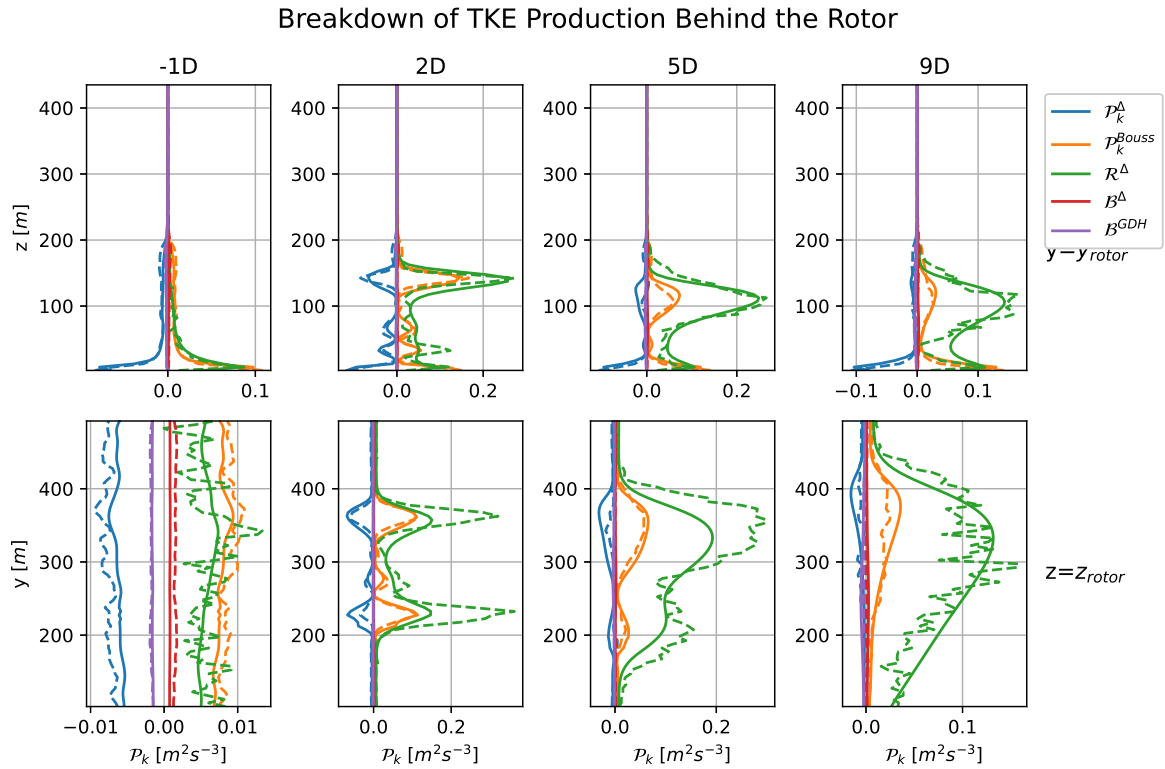


Figure 6.28: Profiles of different TKE production terms from a RANS simulation with implemented models (solid) and from the LES data (dashed) for Case B: Kokee SBL.

6.3.5.3. Influence Correction Term Modelling Errors on Simulation

In Figure 6.28 it is shown that the modelling of the different correction terms has a significant effect on especially the TKE production correction. To get a grasp of how the modelling of the different correction terms influences the final results, three simulations are performed with different configurations as to which correction terms are modelled and which are kept constant at their optimal, frozen values. The resulting profiles for the TKE are displayed in Figure 6.29.

In Figure 6.29 it is visible that the modelling of the TKE production correction introduces a significant error at the bottom of the domain, further downstream of the rotor. Previously it was shown that the prediction of the model struggled at this location, so this result is expected. However, that is not the only significant source of error. The modelling of the anisotropy correction also introduces a significant error closely behind the rotor, which is also where the correction is the most active. Looking at the velocity profiles in Figure C.21, it is also this correction which introduces the largest error in the stream-wise velocity field. This conclusion is different from Case A, where modelling errors of the anisotropy correction are responsible for virtually all of the difference between the LES data and the simulation with implemented models.

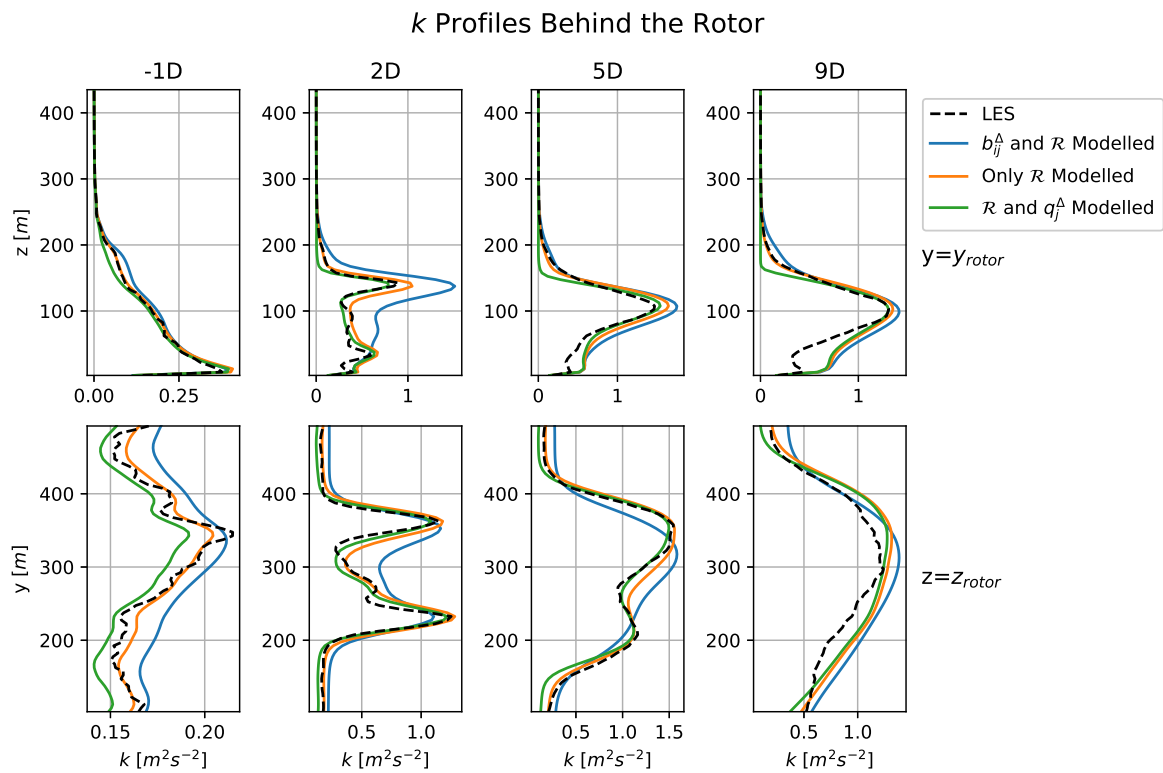


Figure 6.29: TKE profiles for simulations of Case B: Kooke SBL with different configurations of correction terms modelled, all the other correction terms are kept constant at their optimal, frozen values.

Conclusions and Recommendations

The main objective of this thesis was to reduce the $k - \epsilon$ turbulence model and gradient-diffusion hypothesis scalar-flux model uncertainties in stably-stratified wind turbine wake applications by extending the SpaRTA methodology to include the effects of stable stratification. The main addition to extend the SpaRTA methodology towards stable stratification is an additive correction to the turbulent heat flux. This additive correction corrects the gradient-diffusion hypothesis model, most commonly used for turbulent scalar flux modelling. Aside from that, a new feature is introduced to the regression library based on the magnitude of the gradient-diffusion hypothesis version of the turbulent heat flux and the library includes invariants which are temperature gradient-based instead of pressure-based.

The performance of this extended SpaRTA methodology was tested by applying it to two cases. Case A is based on the GABLS1 inter-comparison study and concerns a stably-stratified parcel of air above land without any turbines while Case B concerns a turbine in the same environmental conditions as Case A. The LES ground-truth data and optimal correction fields for Case B could be obtained from [Kokee \(2021\)](#), while all simulations for Case A were performed by the author.

The optimal correction fields for both cases were used to train simple algebraic correction models, which were then implemented in corrected RANS simulations using OpenFOAM. The results were compared against baseline data, based in which conclusions are drawn in [Section 7.1](#).

7.1. Conclusions

In order to answer the main research question of this thesis, first the answers to the sub-questions are discussed.

SQ1. How does the extension of the SpaRTA methodology to also include a model form correction of the turbulent heat flux influence the corrected simulations?

In the LES data of both cases it is clearly visible that the gradient-diffusion hypothesis is not suitable for modelling the turbulent heat flux. This is visible as the turbulent heat flux has a direction approximately perpendicular to the mean temperature gradient for both cases. The vertical component is dominant in the mean temperature gradient, while this component is the smallest in the turbulent heat flux. Therefore, an additive correction of the turbulent heat flux seemed like the appropriate addition to the SpaRTA methodology to include stable stratification.

However, the fact that the temperature profiles for both cases show no significant differences whether the THF correction (q_f^A) is implemented or not indicates that this correction has a negligible effect on the temperature equation. This notion is further confirmed by the velocity and TKE profiles for both cases perfectly coinciding when the full and only the z-component of the THF correction is implemented. This means that the only way this correction influences the simulations for these cases is through the buoyant production term in the k -equation which only includes the z-component of the turbulent heat flux. It seems to mainly counter-act the buoyant destruction of TKE due to the gradient-diffusion hypothesis version of the turbulent heat flux, especially in the wake of Case B. This conclusion was also drawn by [Kokee \(2021\)](#). However, this work further argues that the effect of the THF correction on the k -equation can be absorbed in the TKE production correction (\mathcal{R}) and the THF correction is not necessary as long as accurate simulation of the turbulent heat flux is not a requirement.

SQ2. How do the original model form corrections of the SpaRTA methodology influence the performance of the corrected simulations?

Contrary to the THF correction (q_f^A), the TKE production correction (\mathcal{R}) can only influence the simulations through production or destruction of TKE. The turbulence anisotropy correction (b_{ij}^A) also mainly influences the simulation through production or destruction of TKE. However, this correction also influences the velocity equation through the Reynolds stress.

For Case A, the turbulence anisotropy correction (b_{ij}^A) mainly removes TKE in places where the Boussinesq production of TKE is large. This means throughout the ABL and especially in the capping inversion and towards the bottom of the domain. The effect of the TKE production correction (\mathcal{R}) is smaller, approximately as large as the TKE production due to the THF correction (q_f^A). The TKE production correction adds TKE throughout the ABL and is mainly active towards the bottom of the domain. Together, the corrections correct for the slight over-prediction of the TKE in the ABL by the baseline turbulence model. The effect of this improvement on the velocity profiles is not visible due to the small domain size and simple nature of the case.

Similar to Case A, in Case B the turbulence anisotropy correction (b_{ij}^A) mainly removes TKE from the simulation, while the TKE production correction (\mathcal{R}) mainly adds TKE. However, this time the TKE production correction is the dominant term, while the buoyant production terms of TKE are much smaller. Again, the turbulence anisotropy correction mainly removes TKE in regions where the Boussinesq production is large. This means regions close behind the rotor. Meanwhile, the TKE production correction is mainly active in the shear layer between the wake and the outside flow where the baseline severely under-estimates the production of TKE. Together, the corrections cause the TKE to be much higher in the shear-layer for the corrected simulations than for the baseline. This causes more turbulent mixing between the wake and the outside flow and a faster dissipation of the wake, correcting for the over-prediction of the wake in the velocity profiles of the baseline simulation.

SQ3. What is the best selection criterion for selecting correction models after regression: mean squared error, max squared error or complexity?

Based on the implementation of different selected models for the two cases, it is clear that there is not an a priori selection criterion which is best for selecting correction models.

For Case A different model combinations with low, medium or high complexity were implemented and tested against each other. The models with higher complexity all had lower or equal max squared error (maxse) and mean squared error (mse) when compared to the target data after the regression than models with lower complexity. The surprising result was that the models with medium complexity performed the best of all combinations when implemented in the simulations. This indicates that there are other important factors influencing the performance of models in terms of accuracy, such as terms present or combinations of terms.

The same was visible for Case B, where for each correction term the model selection was done separate. For the anisotropy correction, the model with the lowest maxse with the target data performed the best, while for the TKE production correction the simplest model outperformed the more complex models with lower maxse and mse after the regression. Lastly, the simplest model for the THF correction performed just as good as the more complex models with lower mse and maxse.

SQ4. What are the main factors holding back the performance of the corrected simulations of the extended SpaRTA methodology?

In order to judge the performance of the different correction models, different configurations of constant, optimal and coupled, modelled correction terms were implemented.

For Case A virtually all deviation of the TKE profile can be ascribed to the modelling of the turbulence anisotropy correction b_{ij}^A . Seeing that the modelled turbulence anisotropy correction matches very well with the predicted modelled anisotropy correction based on the LES data, the problem is mainly in the model itself. This would indicate that either more complex models are needed to capture all phenomena present in the anisotropy correction, or the regression library needs to be extended with other terms to more properly capture said phenomena. As the regression library is already quite extensive, the latter seems unlikely.

The modelling of the anisotropy correction also adds deviations from the LES data in the TKE profiles of Case B. These deviations are mainly visible in the TKE profiles close to the rotor, but propagate in the velocity profiles more downstream. However, again the predicted correction term is quite close to the

modelled correction term indicating a need for more complex turbulence anisotropy correction models. Aside from the turbulence anisotropy correction, the TKE production correction also adds a significant error in the corrected simulation. This is mainly visible in the lower TKE profiles further downstream of the rotor. However, for this correction the modelled correction term shows significant deviations from the predicted correction term in the affected regions.

To what extent can the SpaRTA methodology extended to include stratification effects improve RANS simulations of wind farms in stable atmospheric boundary layer conditions?

As all sub-questions have been answered, the main question can be discussed. It is clear that the extended SpaRTA methodology provides significant improvement over the baseline models. However, as stated in the discussion of SQ1, this improvement could probably have been achieved by the original SpaRTA methodology. Contrary to this, the additional THF-based feature introduced in this work is present in some of the best correction models and proves a valuable addition to the SpaRTA methodology.

For Case A the improvement is mainly visible in the TKE field. The temperature and velocity fields are unaffected as they are prescribed at the inflow boundary and the domain is not large enough to see significant differences. However, the corrected simulations do succeed in correcting the slight over-prediction of the TKE in the ABL by the baseline model.

The improvements over the baseline model are more pronounced for Case B. In this case the method manages to correct for a clear under-prediction of the TKE in the turbine wake, especially in the shear layer between the wake and the outside flow. This has a knock-on effect in the velocity field where the corrected simulation corrects for the over-prediction of the wake due to the under-estimation of turbulent mixing in the baseline simulation.

7.2. Recommendations for Future Work

Based on the work performed in this thesis, there are a number of areas where the work can be improved or expanded. These are summarised in the following recommendations for future work.

Ground-Truth Data

The first limitation imposed on the work performed in this thesis is the quality of the ground-truth data available. Both cases suffered from oscillations and transient effects. Better ground-truth data would improve the training data and lead to more accurate correction models as the models are not trained to correct for nonphysical oscillations. However, seeing that stably-stratified cases are inherently unsteady, getting fully steady ground-truth data will not be possible. But the transient effects should be as limited as possible. Another solution could be to try and implement the SpaRTA methodology in unsteady RANS simulations. Furthermore, it is visible that the wall models influence the corrections, so ideally data would be available which has a low enough resolution at the wall as to not require them.

Aside from the quality of the ground-truth data, the volume of data could also be improved. This thesis included two very simple cases, however, for further improvement more complex turbine configurations are necessary in order to train the correction models for turbine-wake and wake-wake interactions. Furthermore, other configurations in terms of Reynolds number, turbulence intensity and stability could also be viable for future research. If enough data is available, more general models could be trained leading to lasting improvements of wind farm simulation.

Turbulent Heat Flux Correction

As stated before, the turbulent heat flux was probably not necessary for these cases as the only influence was through the buoyant production of TKE. It is surmised that this effect can also be absorbed by the TKE production correction, however it is not checked if the performance would be just as high. Aside from that, this conclusion is drawn only for these cases. It could be that for more severely stable ABLs the THF correction does have a significant influence on the temperature equation. Furthermore, this hypothesis also needs to be tested for convective cases.

Correction Models

In this work the largest limiting factor of the performance of the corrected simulation was the modelling of the anisotropy correction. Therefore, a possible improvement could be to implement more complex models or research other possible features to add to the library in order to better model this correction.

Another possible improvement could be to train the models for Case B with the optimal correction fields generated with the proper value for C_μ . Currently, the models are partially correcting for additional errors due to the nonphysical value used in this work.

Aside from that, the model selection overall is still mostly based on trial and error. A vast improvement to the SpaRTA method would be a systematic approach which would consistently select the best models for implementation.

Lastly, the application of the SpaRTA framework for the cases in this thesis could possibly be improved by implementing a limiter which distinguishes between the wake and the free-stream such as in [Steiner et al. \(2021\)](#). As seen in this work, the corrections and correction models are very different for the two.

Bibliography

- K. Abe and K. Suga. Towards the development of a reynolds-averaged algebraic turbulent scalar-flux model. *International Journal of Heat Fluid Flow*, 22(1):19–29, 2001.
- M. Abkar and F. Porté-Agel. Influence of atmospheric stability on wind-turbine wakes: A large-eddy simulation study. *Physics of Fluids*, 27(3):035104, 2015.
- M. Abkar, A. Sharifi, and F. Porté-Agel. Wake flow in a wind farm during a diurnal cycle. *Journal of Turbulence*, 17(4):420–441, 2016.
- D. Allaerts. *Large-eddy Simulation of Wind Farms in Conventionally Neutral and Stable Atmospheric Boundary Layers*. PhD Thesis. KU leuven, 2016.
- B. Baldwin and T. Barth. A one-equation turbulence transport model for high reynolds number wall-bounded flows. In *29th Aerospace Sciences Meeting*, page 610, 1991.
- B. Baldwin and H. Lomax. Thin-layer approximation and algebraic model for separated turbulentflows. In *16th aerospace sciences meeting*, page 257, 1978.
- S. Banerjee, R. Krahl, F. Durst, and C. Zenger. Presentation of anisotropy properties of turbulence, invariants versus eigenvalue approaches. *Journal of Turbulence*, 8(32), 2007.
- R.J. Barthelmie, S.T. Frandsen, M.N. Nielsen, S.C. Pryor, P.-E. Rethore, and H.E. Jørgensen. Modelling and measurements of power losses and turbulence intensity in wind turbine wakes at middelgrunden offshore wind farm. *Journal of Wind Energy: An International Journal for Progress and Applications in Wind Power Conversion Technology*, 10(6):517–528, 2007.
- G.K. Batchelor. Diffusion in a field of homogeneous turbulence. i. eulerian analysis. *Australian Journal of Chemistry*, 2(4):437, 1949.
- R.J. Beare, M.K. Macvean, A.A.M. Holtslag, J. Cuxart, I. Esau, J.-C. Golaz, M.A. Jimenez, M. Khairoutdinov, B. Kosovic, and D. Lewellen. An intercomparison of large-eddy simulations of the stable boundary layer. *Boundary-Layer Meteorology*, 118(2):247–272, 2006.
- A.K. Blackadar. The vertical distribution of wind and turbulent exchange in a neutral atmosphere. *Journal of Geophysical Research*, 67(8):3095–3102, 1962.
- J. Boussinesq. Théorie de l'écoulement tourbillant (theories of swirling flow). *Académie des Sciences de l'Institut de France*, 23:46–50, 1877.
- G. Brethouwer, P. Billiant, E. Lindborg, and J.-M. Chomza. Scaling analysis and simulation of strongly stratified turbulent flows. *Journal of Fluid Mechanics*, 585(01):343–368, 2007.
- R.A. Brost and J.C. Wyngaard. A model study of the stably stratified planetary boundary layer. *Journal of the Atmospheric Sciences*, 35(8):1427–1440, 1978.
- T. Burton, D. Sharpe, N. Jenkins, and E. Bossanyi. *Wind energy handbook*. Wiley, Chichester, West Sussex, 2nd edition, 2011.
- J.A. Businger, J.C. Wyngaard, Y. Izumi, and E.F. Bradley. Flux-profile relationships in the atmospheric surface layer. *Journal of the atmospheric Sciences*, 28(2):181–189, 1971.
- D. Cabezón, E. Migoya, and A. Crespo. Comparison of turbulence models for the computational fluid dynamics simulation of wind turbine wakes in the atmospheric boundary layer. *Wind Energy*, 14(7): 909–921, 2011.

- S.H. Cheung, T.A. Oliver, E.E. Prudencio, S. Prudhomme, and R.D. Moser. Bayesian uncertainty analysis with applications to turbulence modeling. *Reliability Engineering: System Safety*, 96(9): 1137–1149, 2011.
- M.J. Churchfield, S. Lee, J. Michalakes, and P.J. Moriarty. A numerical study of the effects of atmospheric and wake turbulence on wind turbine dynamics. *Journal of turbulence*, 13, 2012a.
- M.J. Churchfield, S. Lee, and P. Moriarty. Overview of the simulator for wind farm application (sowfa). *National Renewable Energy Laboratory*, 2012b.
- D. P. Combest, P. A. Ramachandran, and M. P. Dudukovic. On the gradient diffusion hypothesis and passive scalar transport in turbulent flows. *Industrial and Engineering Chemistry Research*, 50(15): 8817–8823, 2011.
- J. Crank and P. Nicolson. A practical method for numerical evaluation of solutions of partial differential equations of the heat-conduction type. *Mathematical Proceedings of the Cambridge Philosophical Society*, 43(1):50–67, 1947.
- B.J. Daly and F.H. Harlow. Transport equations in turbulence. *The Physics of Fluids*, 13(11):2634–2649, 1970.
- J.W. Deardorff. Stratocumulus-capped mixed layers derived from a three-dimensional model. *Boundary-Layer Meteorology*, 18(4):495–527, 1980.
- M. Dörenkämper, B. Witha, G. Steinfeld, D. Heinemann, and M. Kühn. The impact of stable atmospheric boundary layers on wind-turbine wakes within offshore wind farms. *Journal of Wind Engineering & Industrial Aerodynamics*, 144:146–153, 2015.
- E. Duque, C. Van Dam, and S. Hughes. Navier-stokes simulations of the nrel combined experiment phase ii rotor. In *37th Aerospace Sciences Meeting and Exhibit*, page 37, 1999.
- K. Duraisamy, G. Iaccarino, and H. Xiao. Turbulence modeling in the age of data. *Annual Review of Fluid Mechanics*, 51(1):357–377, 2019.
- P.G. Duynkerke. Application of the $e-\epsilon$ turbulence closure model to the neutral and stable atmospheric boundary layer. *Journal of the atmospheric sciences*, 45(5):865–880, 1988.
- A. El Kasmi and C. Masson. An extended $k-\epsilon$ model for turbulent flow through horizontal-axis wind turbines. *Journal of Wind Engineering and Industrial Aerodynamics*, 96(1):103–122, 2008.
- M. Emory and G. Iaccarino. Visualizing turbulence anisotropy in the spatial domain with componentality contours. *Center for Turbulence Research Annual Research Briefs*, pages 123–138, 2014.
- T. Foken. 50 years of the monin-obukhov similarity theory. *Boundary-Layer Meteorology*, 119(3):431–447, 2006.
- R.O. Fox. *Computational models for turbulent reacting flows*. Cambridge University Press, Cambridge, U.K., 1 edition, 2003.
- M.M. Gibson and B.E. Launder. Ground effects on pressure fluctuations in the atmospheric boundary layer. *Journal of Fluid Mechanics*, 86(3):491–511, 1978.
- M.W. Goderie. Enhancement of data-driven turbulence models for wind turbine wake applications [msc thesis]. *TU Delft*, 2020.
- S.-E. Gryning, E. Batchvarova, B. Brümmner, H.E. Jørgensen, and S. Larsen. On the extension of the wind profile over homogeneous terrain beyond the surface boundary layer. *Boundary-Layer Meteorology : An International Journal of Physical, Chemical and Biological Processes in the Atmospheric Boundary Layer*, 124(2):251–268, 2007.
- GWEC. *Global Wind Report*. Global Wind Energy Council, 2019.

- K.S. Hansen, R.J. Barthelmie, L.E. Jensen, and A. Sommer. The impact of turbulence intensity and atmospheric stability on power deficits due to wind turbine wakes at horns rev wind farm. *Journal of Wind Energy*, 15(1):183–196, 2012.
- Z. Hao and C. Gorié. Pressure scrambling effects and the quantification of turbulent scalar flux model uncertainties. *Physical Review Fluids arXiv preprint arXiv:06782*, 2020.
- G.D. Hess and J.R. Garratt. Evaluating models of the neutral, barotropic planetary boundary layer using integral measures: Part i. overview. *Boundary-layer meteorology*, 104(3):333–358, 2002a.
- G.D. Hess and J.R. Garratt. Evaluating models of the neutral, barotropic planetary boundary layer using integral measures: Part ii. modelling observed conditions. *Boundary-layer meteorology*, 104(3):359–369, 2002b.
- R.J.A. Howard and J.C.F. Pereira. A study of wind turbine power generation and turbine/tower interaction using large eddy simulation. *Wind Structures*, 9(2):95–108, 2006.
- A. Huser, P.J. Nilsen, and H. Skåtun. Application of $k-\epsilon$ model to the stable abl: Pollution in complex terrain. *Journal of wind engineering and industrial aerodynamics*, 67:425–436, 1997.
- R. Johnstone and G.N. Coleman. The turbulent ekman boundary layer over an infinite wind-turbine array. *Journal of Wind Engineering & Industrial Aerodynamics*, 100(1):46–57, 2012.
- W.P. Jones and B.E. Launder. The prediction of laminarization with a two-equation model of turbulence. *International journal of heat mass transfer*, 15(2):301–314, 1972.
- J. Jonkman, S. Butterfield, W. Musial, and G. Scott. Definition of a 5-mw reference wind turbine for offshore system development. Technical report, National Renewable Energy Lab.(NREL), Golden, CO (United States), 2009.
- M.L.A. Kaandorp and R.P. Dwight. Data-driven modelling of the reynolds stress tensor using random forests with invariance. *Computers & Fluids*, 202:104497, 2020.
- S. Khani and M.L. Waite. Buoyancy scale effects in large-eddy simulations of stratified turbulence. *Journal of Fluid Mechanics*, 754:75–97, 2014.
- J. Kim and C. Lee. Prediction of turbulent heat transfer using convolutional neural networks. *Journal of Fluid Mechanics*, 882, 2020.
- T. Koblitz. *CFD Modeling of Non-Neutral Atmospheric Boundary Layer Conditions*, volume 0019(EN) of *DTU Wind Energy PhD*. DTU Wind Energy, 2013.
- L.M. Kokee. Frozen-rans turbulence model corrections for wind turbine wakes in stable, neutral and unstable atmospheric boundary layers [msc thesis]. *TU Delft*, 2021.
- B. Kosović and J.A. Curry. A large eddy simulation study of a quasi-steady, stably stratified atmospheric boundary layer. *Journal of the atmospheric sciences*, 57(8):1052–1068, 2000.
- B.E. Launder, G. Reece Jr, and W. Rodi. Progress in the development of a reynolds-stress turbulence closure. *Journal of fluid mechanics*, 68(3):537–566, 1975.
- S. Lee, M.J. Churchfield, and P. Fleming. Simulator for wind farm applications (sowfa). Technical report, National Renewable Energy Lab (NREL), 2016.
- H.H. Lettau. Theoretical wind spirals in the boundary layer of a barotropic atmosphere. *J Beitr. Phys. Atmos.*, 35:195–212, 1962.
- E. Lindborg. The energy cascade in a strongly stratified fluid. *Journal of Fluid Mechanics*, 550(1): 207–242, 2006.
- J. Ling and J. Templeton. Evaluation of machine learning algorithms for prediction of regions of high reynolds averaged navier stokes uncertainty. *Physics of Fluids*, 27(8), 2015.

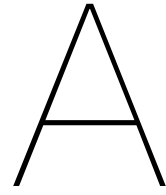
- J. Ling, R. Jones, and J. Templeton. Machine learning strategies for systems with invariance properties. *Journal of Computational Physics*, 318:22–35, 2016a.
- J. Ling, K.J. Ryan, J. Bodart, and J.K. Eaton. Analysis of turbulent scalar flux models for a discrete hole film cooling flow. *Journal of Turbomachinery*, 138(1):011006, 2016b.
- J. Ling, J. Templeton, and A. Kurzawski. Reynolds averaged turbulence modelling using deep neural networks with embedded invariance. *Journal of Fluid Mechanics*, 807:155–166, 2016c.
- H. Lu and F. Porté-Agel. Large-eddy simulation of a very large wind farm in a stable atmospheric boundary layer. *Physics of Fluids*, 23(6):065101, 2011.
- H. Lu and F. Porté-Agel. A modulated gradient model for scalar transport in large-eddy simulation of the atmospheric boundary layer. *Physics of Fluids*, 25(1):015110, 2013.
- H. Lu and F. Porté-Agel. On the impact of wind farms on a convective atmospheric boundary layer. *Boundary-Layer Meteorology : An International Journal of Physical, Chemical and Biological Processes in the Atmospheric Boundary Layer*, 157(1):81–96, 2015.
- J.L. Lumley. The spectrum of nearly inertial turbulence in a stably stratified fluid. *Journal of the Atmospheric Sciences*, 21(1):99–102, 1964.
- J.L. Lumley. *Computational modeling of turbulent flows*, volume 18, pages 123–176. Elsevier, 1979.
- J.L. Lumley and G.R. Newman. The return to isotropy of homogeneous turbulence. *Journal of Fluid Mechanics*, 82(1):161–178, 1977.
- E. Machefaux, G.C. Larsen, T. Koblitz, N. Troldborg, M.C. Kelly, A. Chougule, K.S. Hansen, and J.S. Rodrigo. An experimental and numerical study of the atmospheric stability impact on wind turbine wakes. *Wind Energy*, 19(10):1785–1805, 2016.
- F. Menter. Zonal two equation kw turbulence models for aerodynamic flows. In *23rd fluid dynamics, plasmadynamics, and lasers conference*, page 2906, 1993.
- F. Menter. Two-equation eddy-viscosity turbulence models for engineering applications. *AIAA journal*, 32(8):1598–1605, 1994.
- R. Mikkelsen. *Actuator disc methods applied to wind turbines*. PhD thesis, PhD thesis, Technical University of Denmark, 2003.
- P.M. Milani, J. Ling, G. Saez-Mischlich, J. Bodart, and J.K. Eaton. A machine learning approach for determining the turbulent diffusivity in film cooling flows. *J. Turbomach*, 140(2):021006, 2018.
- P.M. Milani, J. Ling, and J.K. Eaton. Physical interpretation of machine learning models applied to film cooling flows. *J. Turbomach*, 141(1), 2019.
- P.M. Milani, J.K. Eaton, and J. Ling. Turbulent scalar flux in inclined jets in crossflow: counter gradient transport and deep learning modelling. *Journal of Fluid Mechanics*, 906:A27, 2020a.
- P.M. Milani, J. Ling, and J.K. Eaton. Generalization of machine-learned turbulent heat flux models applied to film cooling flows. *J. Turbomach*, 142(1):011007, 2020b.
- C.H. Moeng. A large-eddy-simulation model for the study of planetary boundary-layer turbulence. *Journal of the Atmospheric Sciences*, 41(13):2052–2062, 1984.
- A.S. Monin and A.M. Obukhov. Basic laws of turbulent mixing in the surface layer of the atmosphere. *J Contrib. Geophys. Inst. Acad. Sci. USSR*, 151(163):e187, 1954.
- Y.I. Moon, B. Rajagopalan, and U. Lall. Estimation of mutual information using kernel density estimators. *Physical Review E*, 52(3):2318–2321, 1995.
- A.M. Obukhov. Turbulence in thermally inhomogeneous atmosphere. *J Trudy Inst. Teor. Geofiz. Akad. Nauk SSSR*, 1:95–115, 1946.

- T.A. Oliver and R.D. Moser. Bayesian uncertainty quantification applied to rans turbulence models. Technical Report 1742-6588, IOP Publishing, 2011.
- R.V. Ozmidov. On the turbulent exchange in a stably stratified ocean. *Bull. Acad. Sci. U.S.S.R. Atmos. Oceanic Phys.*, 1:493–497, 1965.
- A. Peña, S.-E. Gryning, and J. Mann. On the length-scale of the wind profile. *Quarterly Journal of the Royal Meteorological Society*, 136(653):2119–2131, 2010.
- S.B. Pope. A more general effective-viscosity hypothesis. *Journal of Fluid Mechanics*, 72(02):331, 1975.
- S.B. Pope. *Turbulent flows*. Cambridge University Press, Cambridge, 2nd edition, 2000.
- F. Porté-Agel, H. Lu, and Y.T. Wu. A large-eddy simulation framework for wind energy applications. In *The fifth international symposium on computational wind engineering*, volume 23, 2010.
- L. Prandtl and K. Wieghardt. Über ein neues formelsystem für die ausgebildete turbulenz. *Nachrichten von der Königlichen Gesellschaft der Wissenschaften zu Göttingen*, pages 6–19, 1945.
- W. Rodi. Examples of calculation methods for flow and mixing in stratified fluids. *Journal of Geophysical Research: Oceans*, 92(C5):5305–5328, 1987.
- J.S. Rodrigo, D. Cabezón, I. Martí, P. Patilla, and J. van Beeck. Numerical cfd modelling of non-neutral atmospheric boundary layers for offshore wind resource assessment based on monin-obukhov theory. In *European Wind Energy Conference and Exhibition*, 2008.
- P.E. Réthoré. *Wind turbine wake in atmospheric turbulence*. PhD Thesis. Risø National Laboratory for Sustainable Energy, 2009.
- R.D. Sandberg, R. Tan, J. Weatheritt, A. Ooi, A. Haghiri, V. Michelassi, and G. Laskowski. Applying machine learnt explicit algebraic stress and scalar flux models to a fundamental trailing edge slot. *Journal of Turbomachinery*, 140(10):101008, 2018.
- B. Sanderse, S.P. Pijl, and B. Koren. Review of computational fluid dynamics for wind turbine wake aerodynamics. *Wind Energy*, 14(7):799–819, 2011.
- M. Schmelzer, R.P. Dwight, and P. Cinnella. Discovery of algebraic reynolds-stress models using sparse symbolic regression. *Flow, Turbulence and Combustion*, 104(2-3):579–603, 2020.
- F.G. Schmitt. About boussinesq’s turbulent viscosity hypothesis: historical remarks and a direct evaluation of its validity. *Comptes rendus - Mécanique*, 335(9):617–627, 2007.
- U. Schumann. Subgrid scale model for finite difference simulations of turbulent flows in plane channels and annuli. *Journal of Computational Physics*, 18(4):376–404, 1975.
- U. Schumann. Realizability of reynolds stress turbulence models. *The Physics of Fluids*, 20(5):721–725, 1977.
- S. Shalev-Shwartz and S. Ben-David. *Understanding machine learning: From theory to algorithms*. Cambridge university press, 2014.
- W.Z. Shen, J.H. Zhang, and J.N. Sørensen. The actuator surface model: A new navier–stokes based model for rotor computations. *J. Sol. Energy Eng*, 131(1), 2009.
- T.H. Shih, W.W. Liou, A. Shabbir, Z. Yang, and J. Zhu. A new $k-\epsilon$ eddy viscosity model for high reynolds number turbulent flows. *Computers & FLuids*, 24(3):227–238, 1995.
- A.M. Smith and T. Cebeci. Numerical solution of the turbulent-boundary-layer equations. Technical report, DOUGLAS AIRCRAFT CO LONG BEACH CA AIRCRAFT DIV, 1967.
- A. Sogachev, M. Kelly, and M.Y. Leclerc. Consistent two-equation closure modelling for atmospheric research: Buoyancy and vegetation implementations. *Boundary-Layer Meteorology*, 145(2):307–327, 2012.

- C. Sotgiu, B. Weigand, and K. Semmler. A turbulent heat flux prediction framework based on tensor representation theory and machine learning. *International Communications in Heat Mass Transfer*, 95:74–79, 2018.
- C. Sotgiu, B. Weigand, K. Semmler, and P. Wellinger. Towards a general data-driven explicit algebraic reynolds stress prediction framework. *International Journal of Heat and Fluid Flow*, 79, 2019.
- P. Spalart and S. Allmaras. A one-equation turbulence model for aerodynamic flows. In *30th aerospace sciences meeting and exhibit*, page 439, 1992.
- C.G. Speziale, S. Sarkar, and T.B. Gatski. Modelling the pressure–strain correlation of turbulence: an invariant dynamical systems approach. *Journal of Fluid Mechanics*, 227:245–272, 1991.
- E.A. Spiegel and G. Veronis. On the boussinesq approximation for a compressible fluid. *The Astrophysical Journal*, 131:442, 1960.
- J. Steiner, R.P. Dwight, and A.C. Viré. Data-driven turbulence modeling for wind turbine wakes under neutral conditions. *Journal of Physics: Conference Series*, 1618(6), 2020.
- J. Steiner, R.P. Dwight, and A.C. Viré. Classifying regions of high model error within a data-driven rans closure: Application to wind turbine wakes. *arXiv preprint arXiv:2106.15593*, 2021.
- J. Steiner, R.P. Dwight, and A.C. Viré. Data-driven rans closures for wind turbine wakes under neutral conditions. *Computers & Fluids*, 233:105213, 2022.
- B. Stevens, C.H. Moeng, and P.P. Sullivan. Entrainment and subgrid lengthscales in large-eddy simulations of atmospheric boundary-layer flows. In *IUTAM Symposium on Developments in Geophysical Turbulence*, pages 253–269. Springer, 2000.
- R. Stoll and F. Porté-Agel. Dynamic subgrid-scale models for momentum and scalar fluxes in large-eddy simulations of neutrally stratified atmospheric boundary layers over heterogeneous terrain. *Water Resources Research*, 42(1), 2006.
- J. Sun, C.J. Nappo, L. Mahrt, D. Belušić, B. Grisogono, D.R. Stauffer, M. Pulido, C. Staquet, Q. Jiang, A. Pouquet, C. Yagüe, B. Galperin, R.B. Smith, J.J. Finnigan, S.D. Mayor, G. Svensson, A.A. Grachev, and W.D. Neff. Review of wave-turbulence interactions in the stable atmospheric boundary layer. *Reviews of Geophysics*, 53(3):956–993, 2015.
- J.N. Sørensen and M. Hansen. Rotor performance predictions using a navier-stokes method. In *1998 ASME Wind Energy Symposium*, page 25, 1998.
- J.N. Sørensen and W.Z. Shen. Numerical modeling of wind turbine wakes. *J. Fluids Eng*, 124(2): 393–399, 2002.
- N.N. Sørensen. *General purpose flow solver applied to flow over hills*. PhD thesis, Technical University of Denmark, 1995.
- J. Thé and H. Yu. A critical review on the simulations of wind turbine aerodynamics focusing on hybrid rans-les methods. *Energy*, 138:257–289, 2017.
- B. Tracey, K. Duraisamy, and J. Alonso. Application of supervised learning to quantify uncertainties in turbulence and combustion modeling. In *51st AIAA aerospace sciences meeting*, page 259, 2013.
- B.D. Tracey, K. Duraisamy, and J.J. Alonso. A machine learning strategy to assist turbulence model development. In *53rd AIAA aerospace sciences meeting*, page 1287, 2015.
- N. Troldborg, J.N. Sørensen, and R. Mikkelsen. Actuator line simulation of wake of wind turbine operating in turbulent inflow. *Journal of Physics: Conference Series*, 75(1), 2007.
- I. Van der Hoven. Power spectrum of horizontal wind speed in the frequency range from 0.0007 to 900 cycles per hour. *Journal of meteorology*, 14(2):160–164, 1957.

- M.P. van der Laan, N.N. Sørensen, P.E. Réthoré, J. Mann, M.C. Kelly, and J.G. Schepers. Nonlinear eddy viscosity models applied to wind turbine wakes. In *International Conference on aerodynamics of Offshore Wind Energy Systems and wakes (ICOWES 2013)*, pages 514–525. Technical University of Denmark, 2013.
- M.P. van der Laan, K.S. Hansen, N.N. Sørensen, and P.E. Réthoré. Predicting wind farm wake interaction with rans: an investigation of the coriolis force. *Journal of Physics: Conference Series*, 625(1), 2015a.
- M.P. van der Laan, N.N. Sørensen, P.E. Réthoré, J. Mann, M.C. Kelly, N. Troldborg, J.G. Schepers, and E. Macheaux. An improved $k-\epsilon$ model applied to a wind turbine wake in atmospheric turbulence. *Journal of Wind Energy*, 18(5):889–907, 2015b.
- M.P. van der Laan, N.N. Sørensen, P.E. Réthoré, J. Mann, M.C. Kelly, and N. Troldborg. The $k-\epsilon$ -fp model applied to double wind turbine wakes using different actuator disk force methods. *Journal of Wind Energy*, 18(12):2223–2240, 2015c.
- M.P. van der Laan, N.N. Sørensen, P.E. Réthoré, J. Mann, M.C. Kelly, N. Troldborg, K.S. Hansen, and J.P. Murcia. The $k-\epsilon$ -fp model applied to wind farms. *Journal of Wind Energy*, 18(12):2065–2084, 2015d.
- F. Vendel, G. Lamaison, L. Soulhac, P. Volta, L. Donnat, O. Duclaux, and C. Puel. Modelling diabatic atmospheric boundary layer using a rans cfd code with a k -epsilon turbulence closure. In *13th Conference on Harmonisation within Atmospheric Dispersion Modelling for Regulatory Purposes*, 2010.
- G. Ver Steeg. Non-parametric entropy estimation toolbox (npeet). Technical report, University of Southern California, 2000.
- G. Ver Steeg and A. Galstyan. Information-theoretic measures of influence based on content dynamics. In *Proceedings of the sixth ACM international conference on Web search and data mining*, page 3–12. Association for Computing Machinery, 2013.
- L.J. Vermeer, J.N. Sørensen, and A. Crespo. Wind turbine wake aerodynamics. *Progress in Aerospace Sciences*, 39(6):467–510, 2003.
- M.L. Waite and P. Bartello. Stratified turbulence dominated by vortical motion. *Journal of Fluid Mechanics*, 517(1):281–308, 2004.
- J. Walters-Williams and Y. Li. *Estimation of Mutual Information: A Survey*, pages 389–396. Lecture Notes in Computer Science : Lecture Notes in Artificial Intelligence 1611-3349. Berlin, Heidelberg : Springer Berlin Heidelberg : Springer, 2009.
- J.X. Wang, J.L. Wu, and H. Xiao. Physics-informed machine learning approach for reconstructing reynolds stress modeling discrepancies based on dns data. *Physical Review Fluids*, 2(3), 2017.
- J. Weatheritt and R.D. Sandberg. A novel evolutionary algorithm applied to algebraic modifications of the rans stress-strain relationship. *Journal of Computational Physics*, 325:22–37, 2016.
- J. Weatheritt and R.D. Sandberg. The development of algebraic stress models using a novel evolutionary algorithm. *International Journal of Heat and Fluid Flow*, 68:298–318, 2017.
- J. Weatheritt, Y. Zhao, R.D. Sandberg, S. Mizukami, and K. Tanimoto. Data-driven scalar-flux model development with application to jet in cross flow. *International Journal of Heat and Mass Transfer*, 147:118931, 2019.
- S. Wharton and J.K. Lundquist. Atmospheric stability affects wind turbine power collection. *Environmental Research Letters*, 7(1):014005, 2012.
- E. Wiebes. Letter to parliament: Offshore wind energy roadmap 2030. *Ministry of Economic Affairs and Climate Policy*, 2018.
- D.C. Wilcox. Reassessment of the scale-determining equation for advanced turbulence models. *AIAA Journal*, 26(11):1299–1310, 1988.

- D.C. Wilcox. *Turbulence modeling for CFD*. DCW Industries, La Canada, 3rd edition, 2006.
- B. Witha, G. Steinfeld, M. Dörenkämper, and D. Heinemann. Large-eddy simulation of multiple wakes in offshore wind farms. *Journal of Physics: Conference Series*, 555(1), 2014.
- J.L. Wu, H. Xiao, and E. Paterson. Physics-informed machine learning approach for augmenting turbulence models: A comprehensive framework. *Physical Review Fluids*, 3(7), 2018.
- J.L. Wu, R. Sun, S. Laizet, and H. Xiao. Representation of stress tensor perturbations with application in machine-learning-assisted turbulence modeling. *Computer Methods in Applied Mechanics and Engineering*, 346:707–726, 2019.
- Y.T. Wu and F. Porté-Agel. Large-eddy simulation of wind-turbine wakes: evaluation of turbine parametrisations. *Boundary-layer meteorology*, 138(3):345–366, 2011.
- J.C. Wyngaard. Modeling the planetary boundary layer—extension to the stable case. *Boundary-Layer Meteorology*, 9(4):441–460, 1975.
- J.C. Wyngaard. *Turbulence in the atmosphere*. Cambridge University Press, Cambridge, UK, 1st edition, 2010.
- G. Xu and L. Sankar. Effects of transition, turbulence and yaw on the performance of horizontal axis wind turbines. In *2000 ASME Wind Energy Symposium*, page 48, 2000.
- B.A. Younis, C.G. Speziale, and T.T. Clark. A rational model for the turbulent scalar fluxes. *Proceedings: Mathematical, Physical and Engineering Sciences*, 461(2054):575–594, 2005.
- Q.-S. Zheng. Theory of representations for tensor functions—a unified invariant approach to constitutive equations. *Applied Mechanics Reviews*, 47(11):545–587, 1994.
- S.S. Zilitinkevich, T. Elperin, N. Kleorin, I. Rogachevskii, and I. Esau. A hierarchy of energy- and flux-budget (efb) turbulence closure models for stably-stratified geophysical flows. *Boundary-Layer Meteorology : An International Journal of Physical, Chemical and Biological Processes in the Atmospheric Boundary Layer*, 146(3):341–373, 2013.
- L. Łobocki. Analysis of vertical turbulent heat flux limit in stable conditions with a local equilibrium, turbulence closure model. *Boundary-layer meteorology*, 148(3):541–555, 2013.



Mutual Information of Features in Library

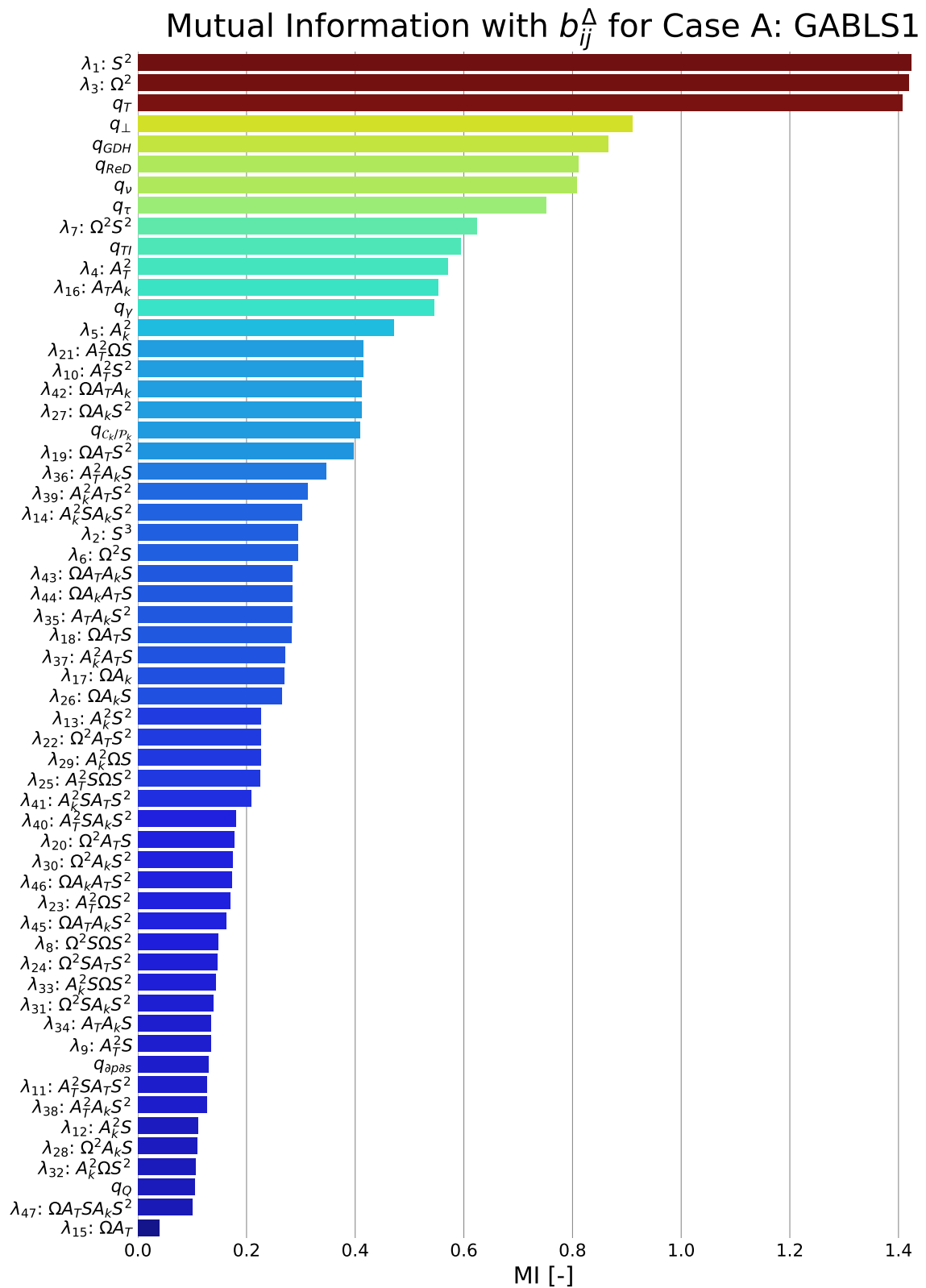


Figure A.1: Mutual Information between second invariant of anisotropy correction and invariants for Case A: GABLS1

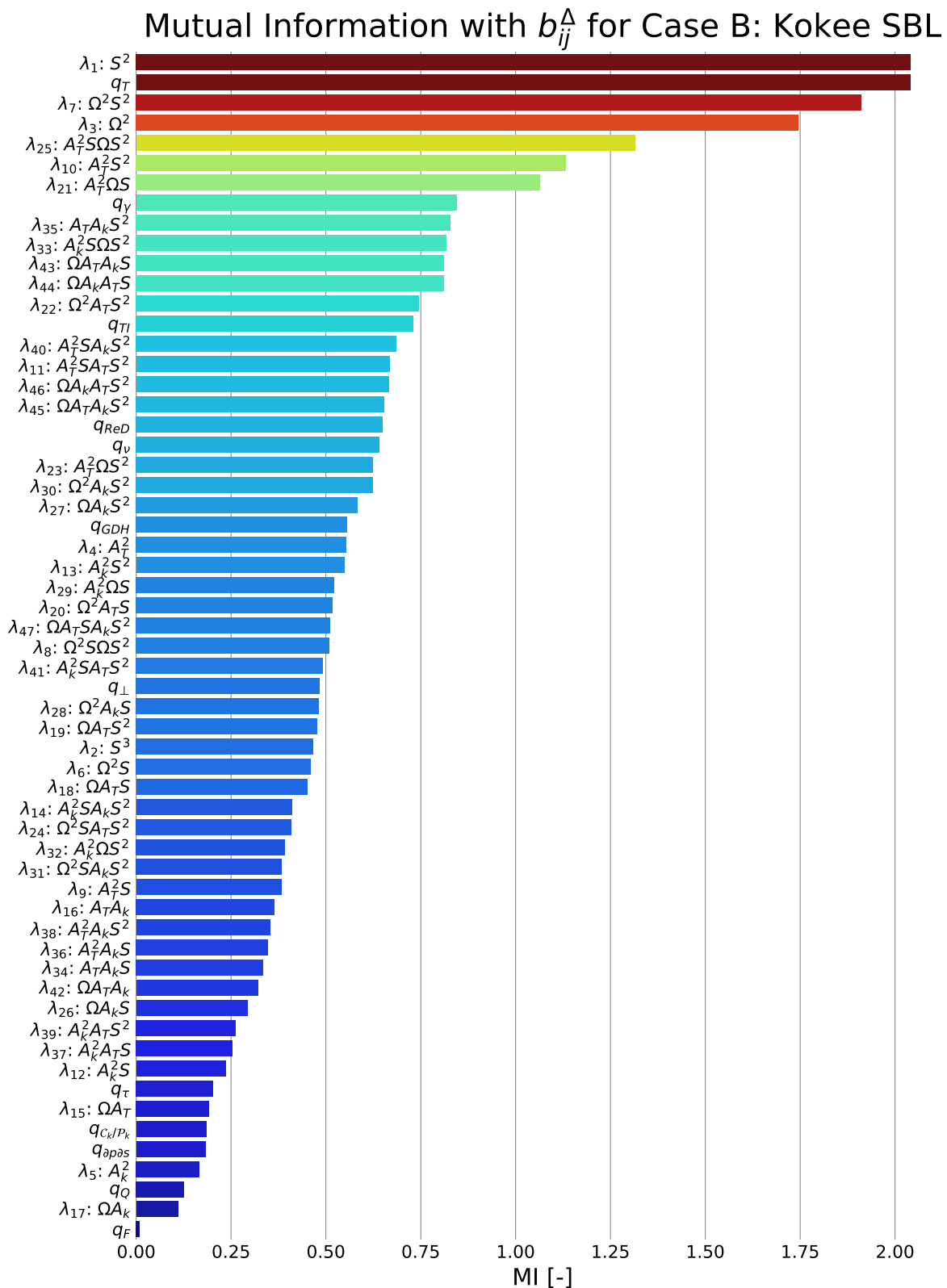


Figure A.2: Mutual Information between second invariant of anisotropy correction and invariants for Case B: Kokee SBL

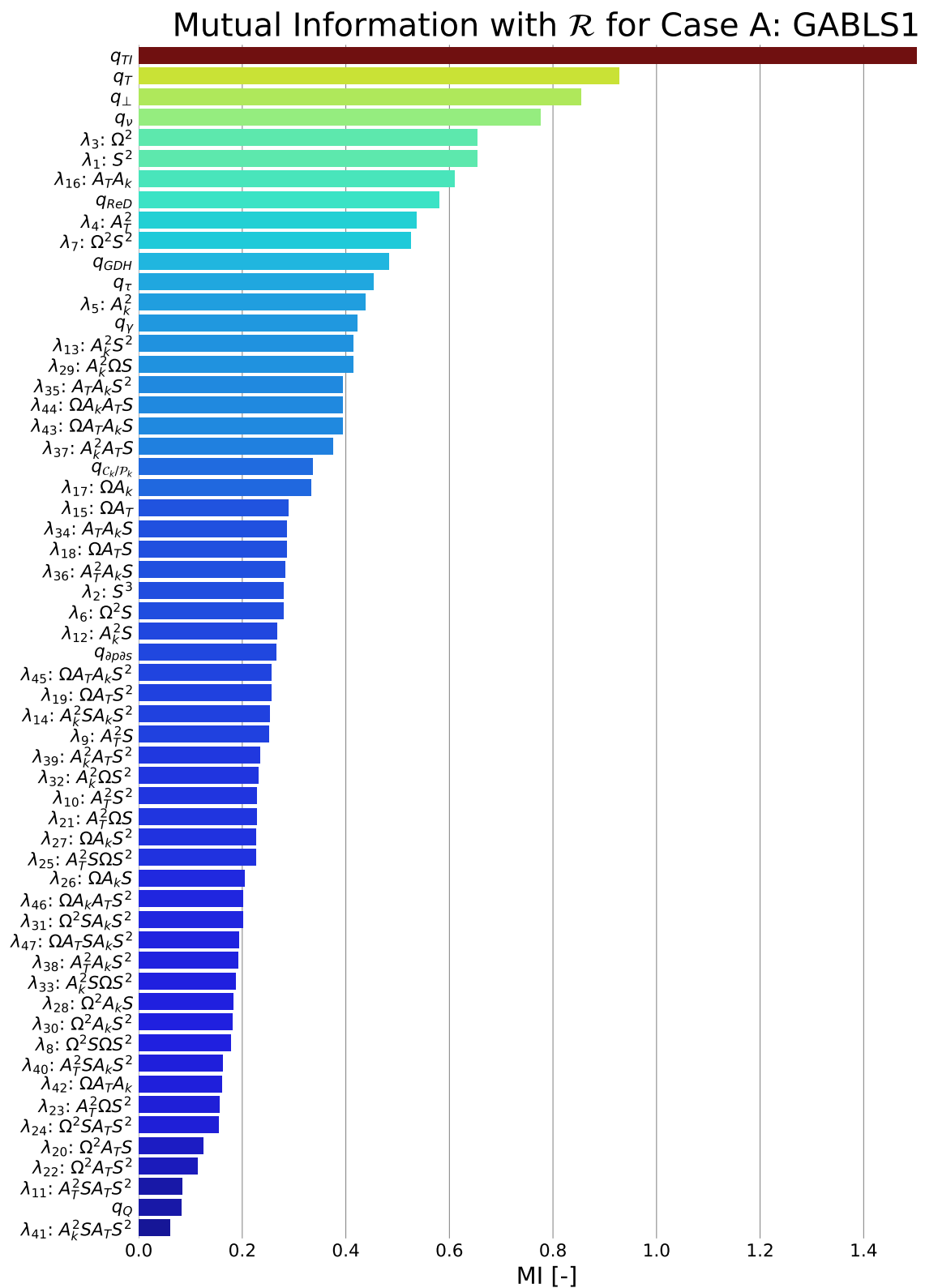


Figure A.3: Mutual Information between TKE production correction and invariants for Case A: GABLS1

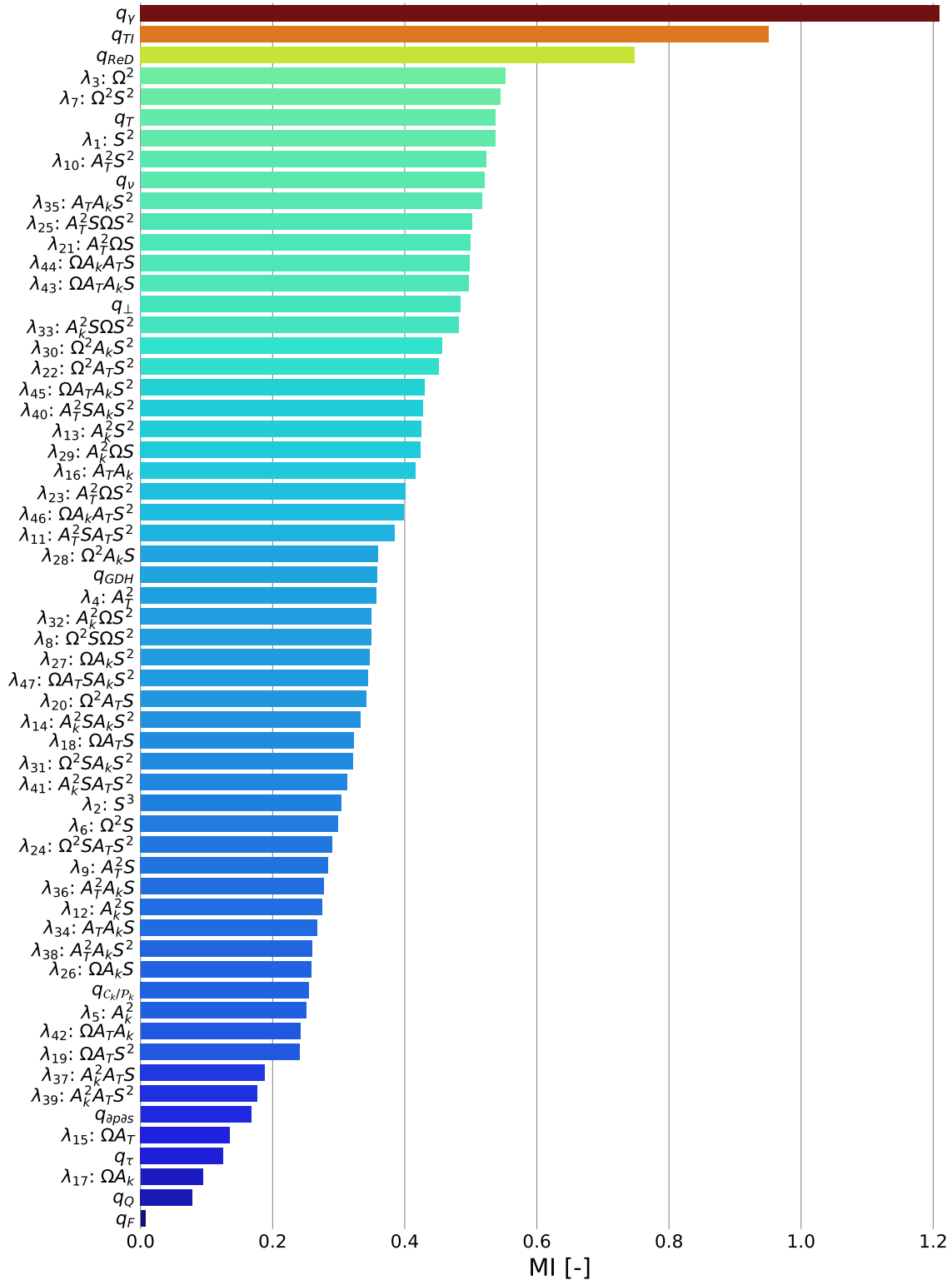
Mutual Information with \mathcal{R} for Case B: Kokee SBL

Figure A.4: Mutual Information between TKE production correction and invariants for Case B: Kokee SBL

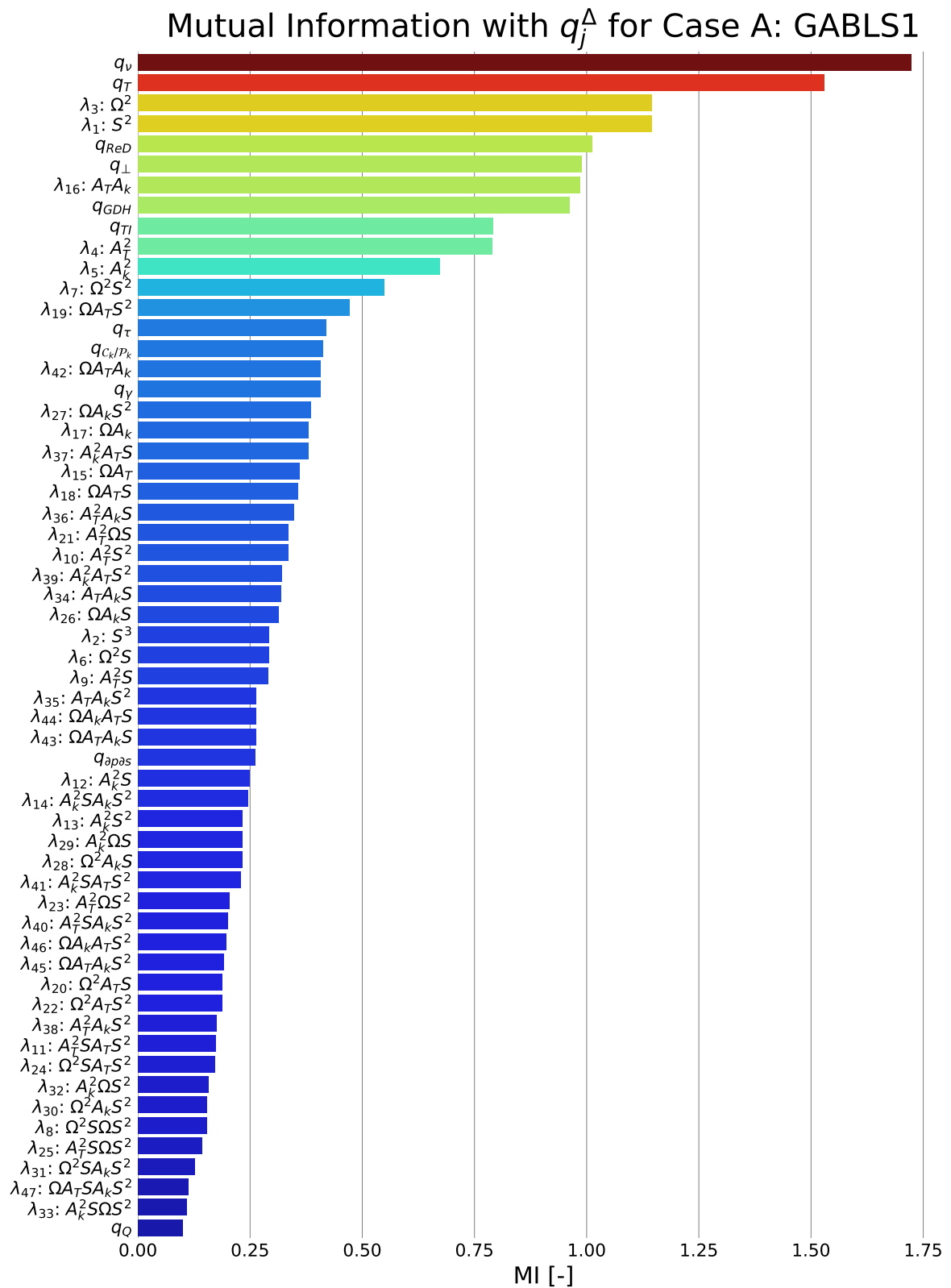


Figure A.5: Mutual Information between z-component of turbulent heat flux correction and invariants for Case A: GABLS1

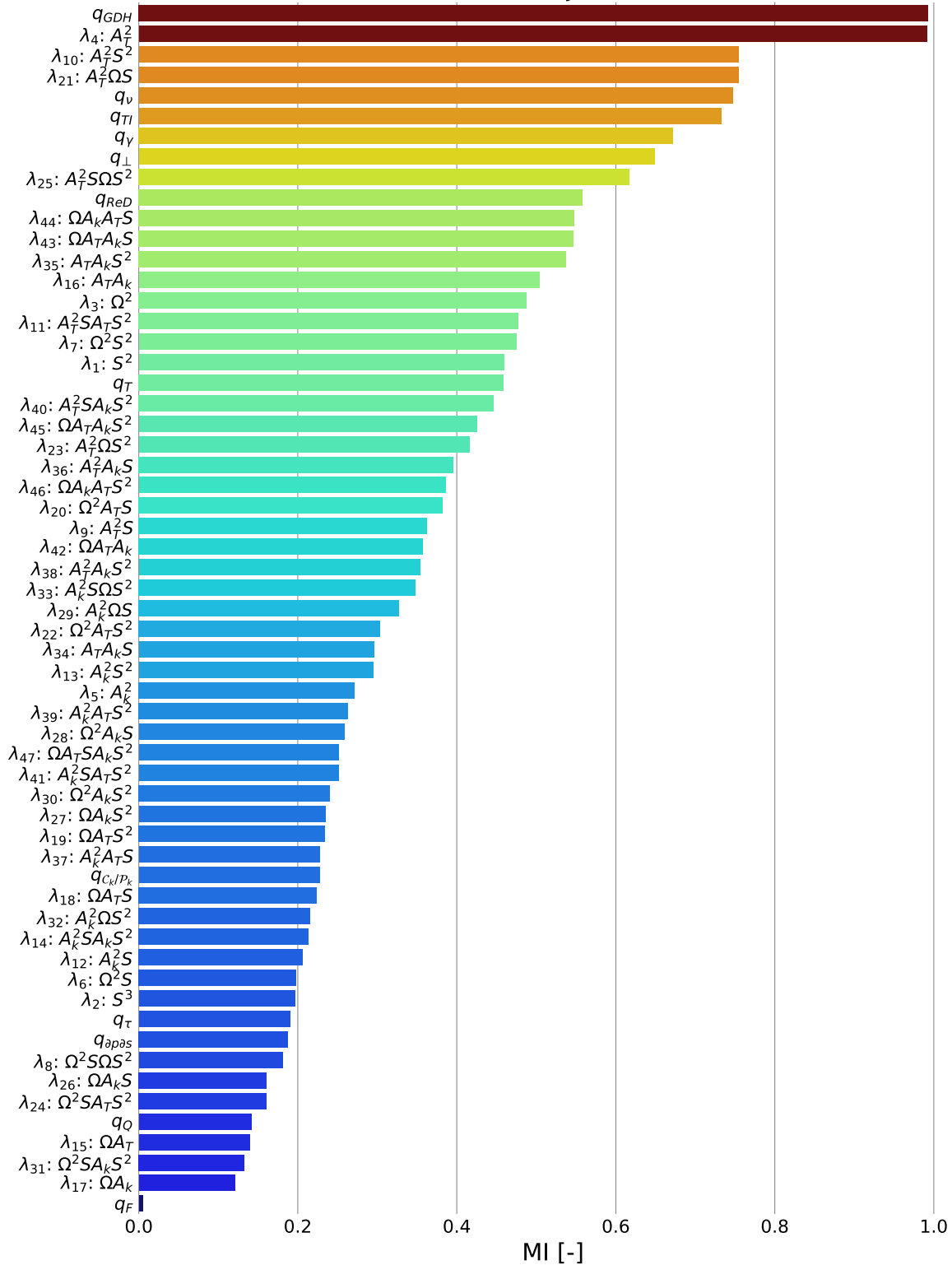
Mutual Information with q_j^Δ for Case B: Kokee SBL

Figure A.6: Mutual Information between z-component of turbulent heat flux correction and invariants for Case B: Kokee SBL

B

Generated Models After Regression

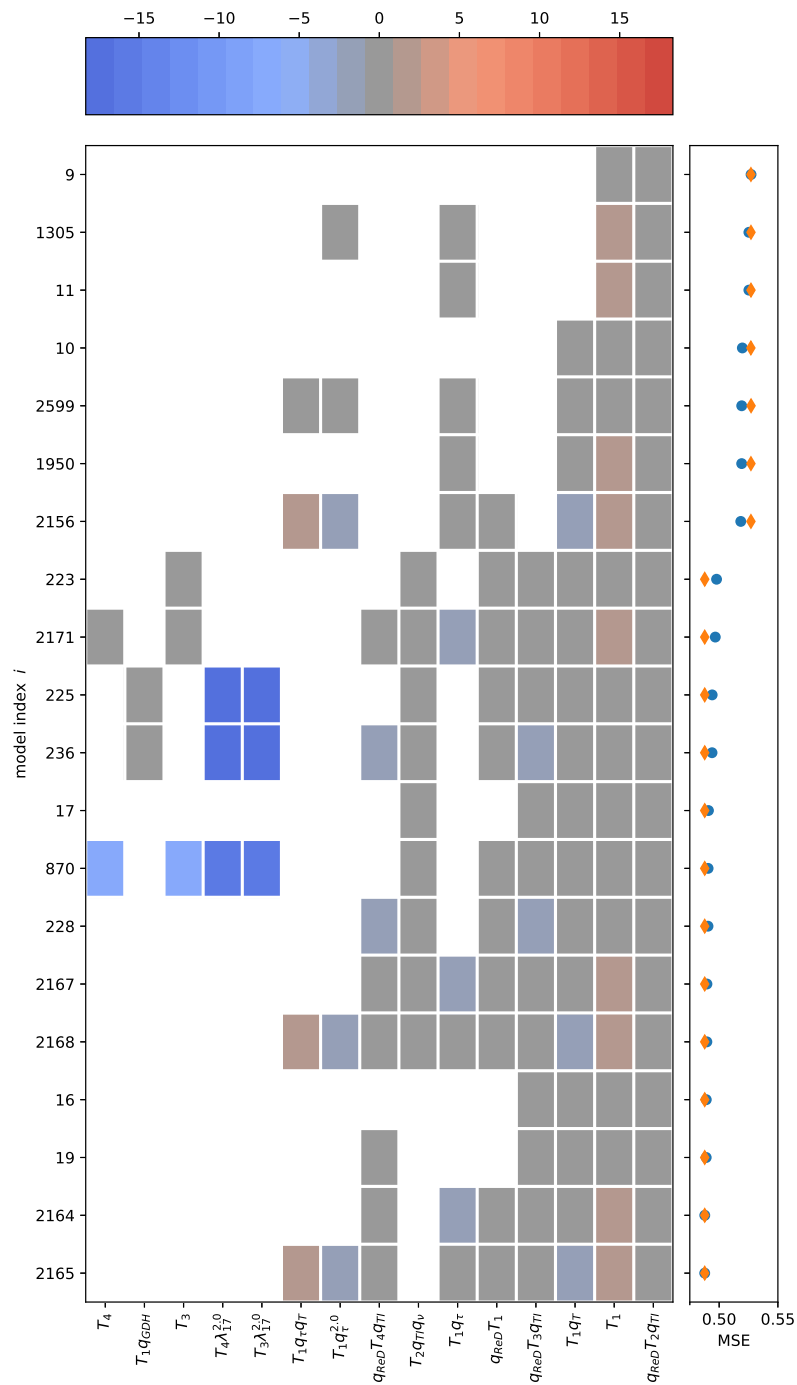


Figure B.1: Terms in the generated correction models for the anisotropy correction b_{ij}^A for Case A: GABLS1. The colours of the squares indicate the relative size of the coefficients, the blue dots indicate the mean-squared error and the yellow diamonds the maximum squared error.

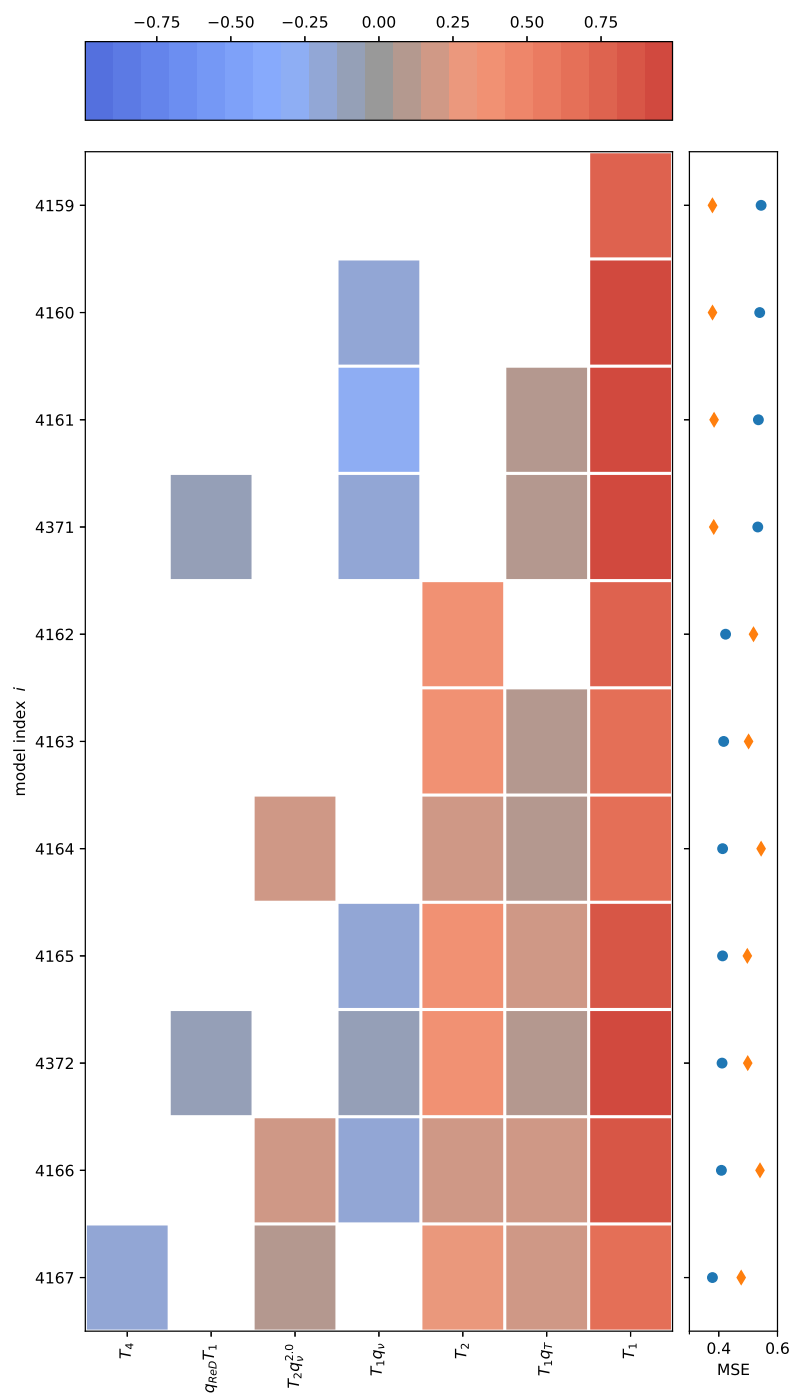


Figure B.2: Terms in the generated correction models for the anisotropy correction b_{ij}^A for Case B: Kokee SBL. The colours of the squares indicate the relative size of the coefficients, the blue dots indicate the mean-squared error and the yellow diamonds the maximum squared error.

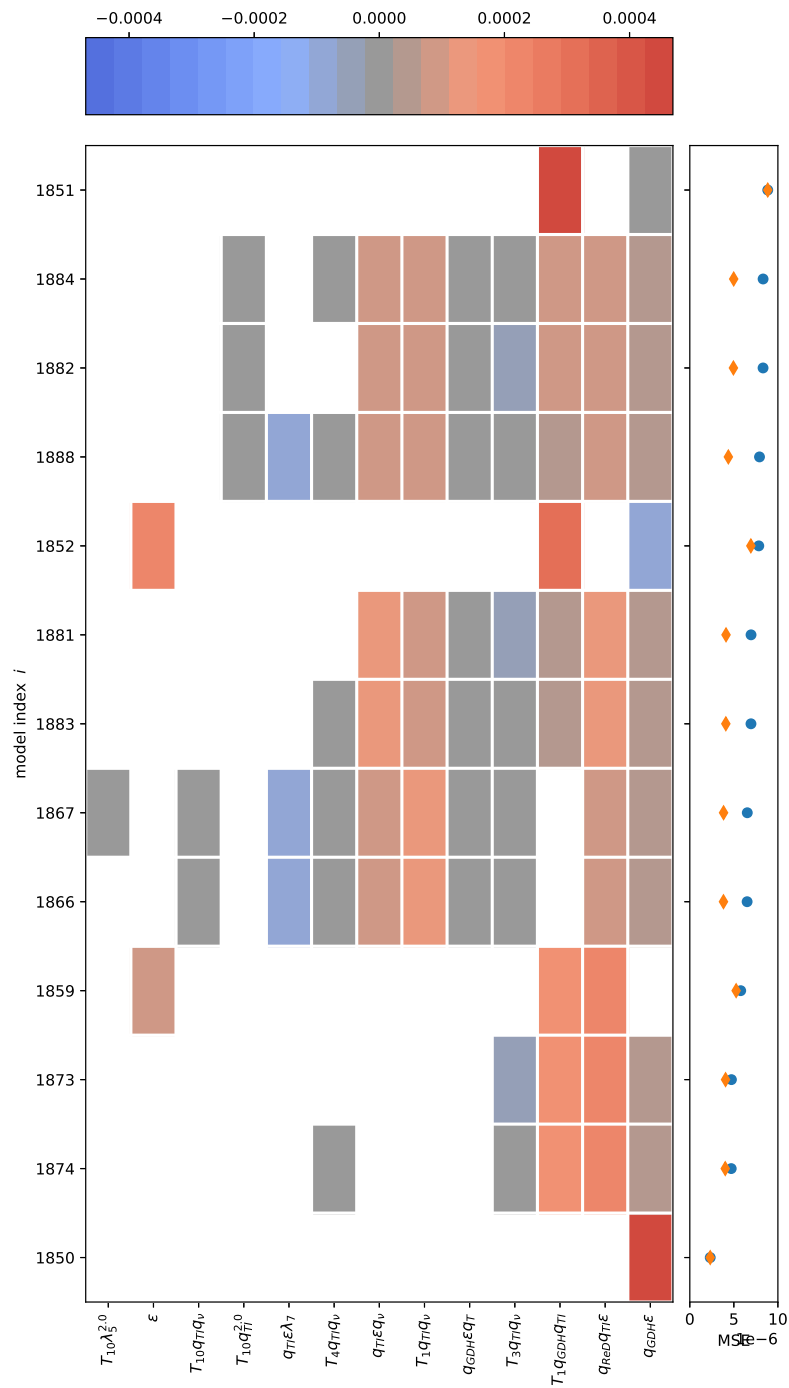


Figure B.3: Terms in the generated correction models for the TKE production correction \mathcal{R} for Case A: GABLS1. The colours of the squares indicate the relative size of the coefficients, the blue dots indicate the mean-squared error and the yellow diamonds the maximum squared error.

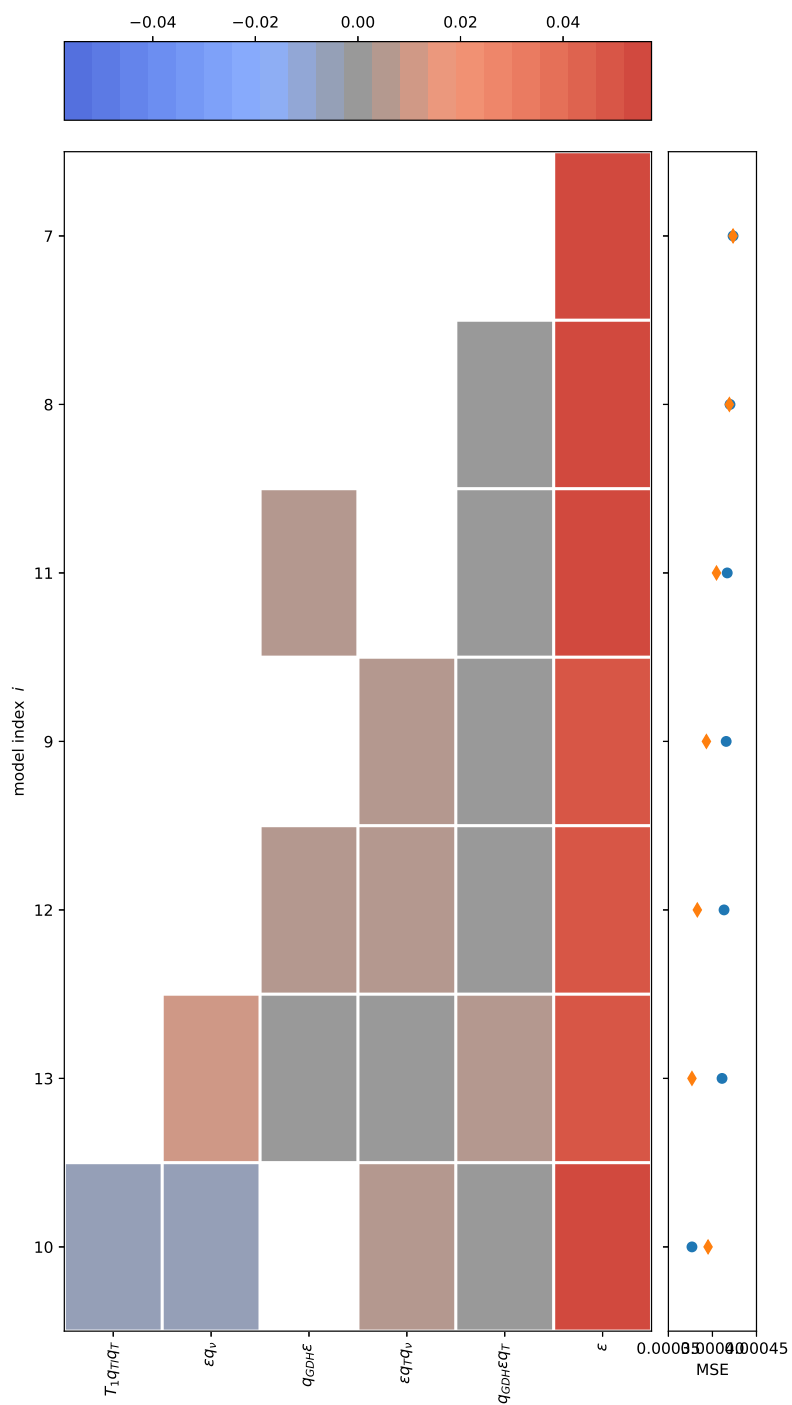


Figure B.4: Terms in the generated correction models for the TKE production correction \mathcal{R} for Case B: Kokee SBL. The colours of the squares indicate the relative size of the coefficients, the blue dots indicate the mean-squared error and the yellow diamonds the maximum squared error.

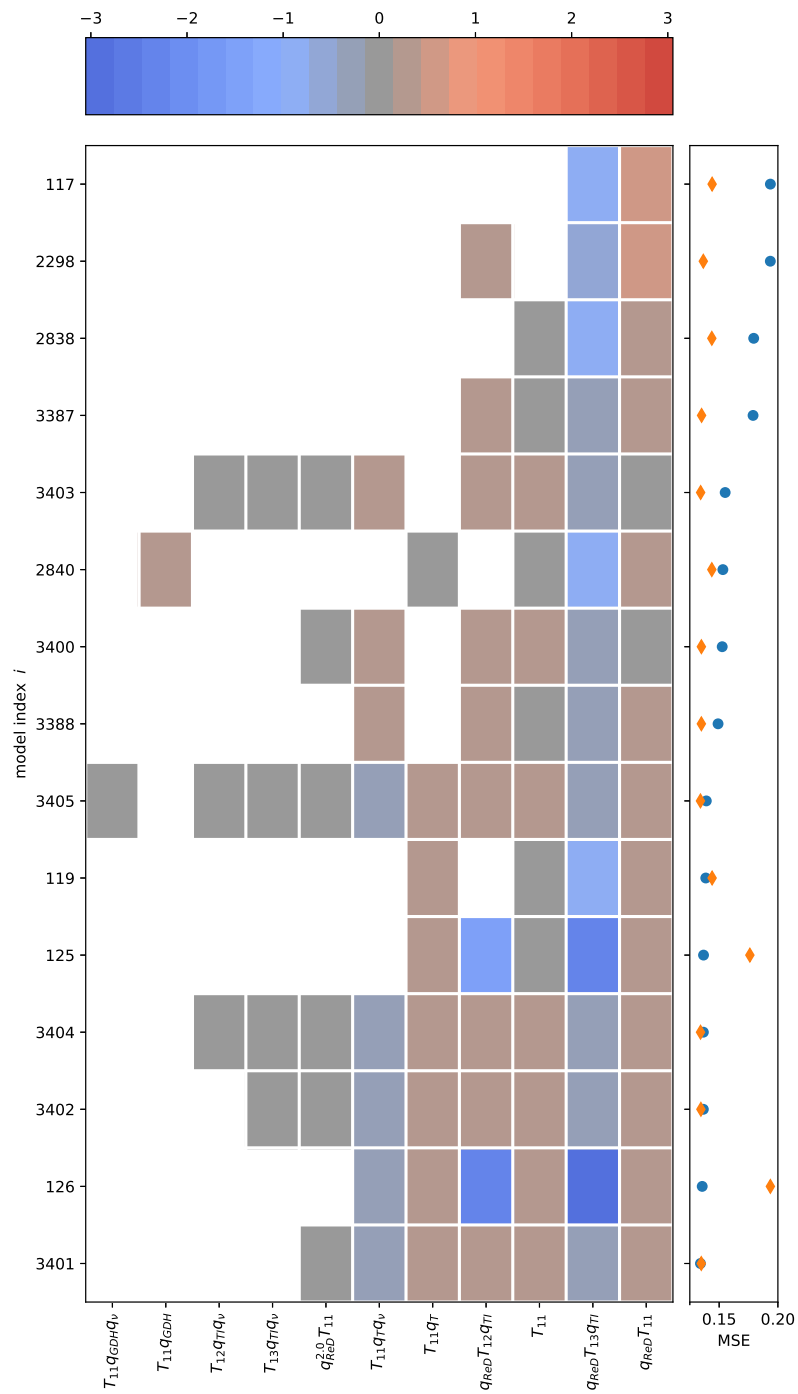


Figure B.5: Terms in the generated correction models for the THF correction q_j^A for Case A: GABLS1. The colours of the squares indicate the relative size of the coefficients, the blue dots indicate the mean-squared error and the yellow diamonds the maximum squared error.

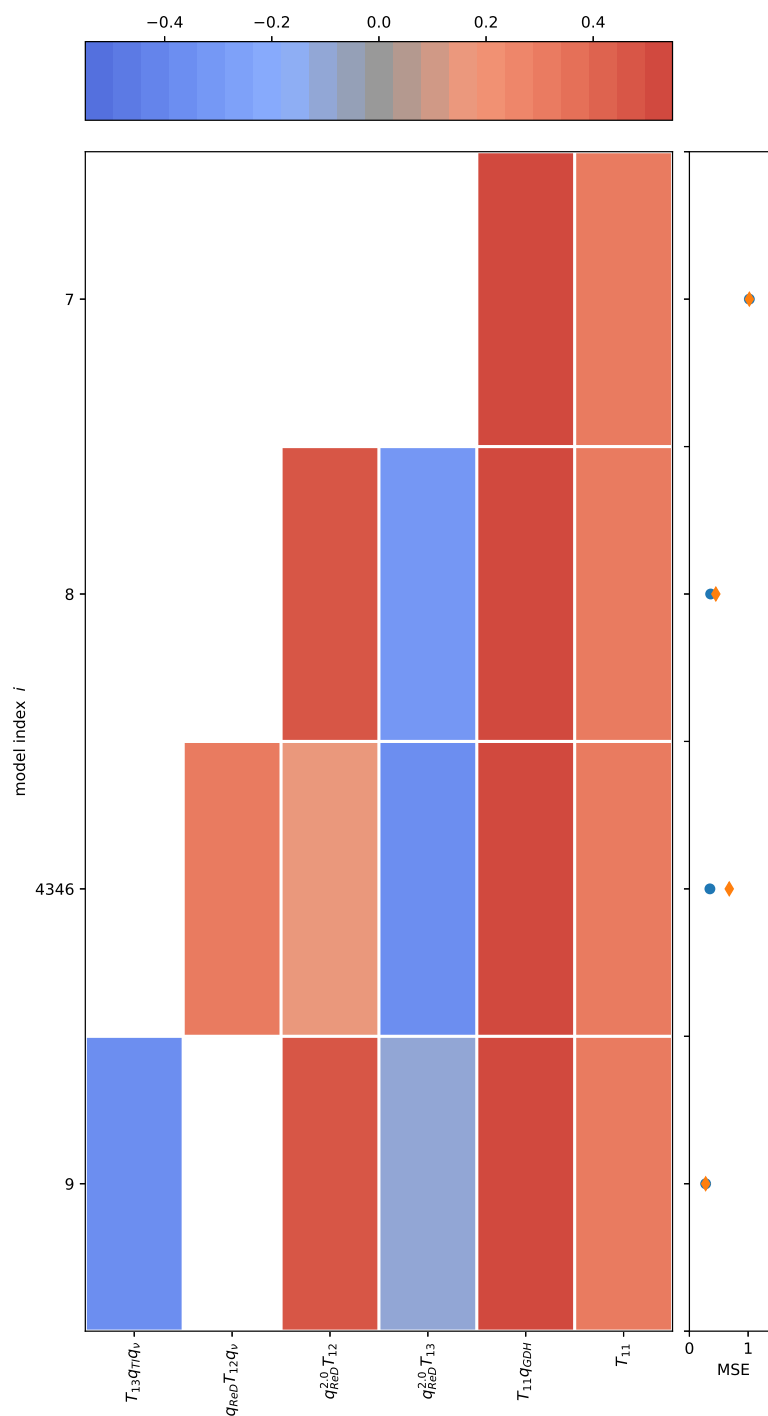
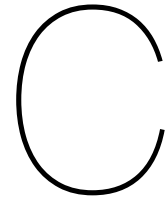


Figure B.6: Terms in the generated correction models for the THF correction q_j^A for Case B: Kokee SBL. The colours of the squares indicate the relative size of the coefficients, the blue dots indicate the mean-squared error and the yellow diamonds the maximum squared error.



Additional Results of Case B: Kokee SBL with Implemented Models

C.1. Influence of Non-physical Turbulence Model Constants

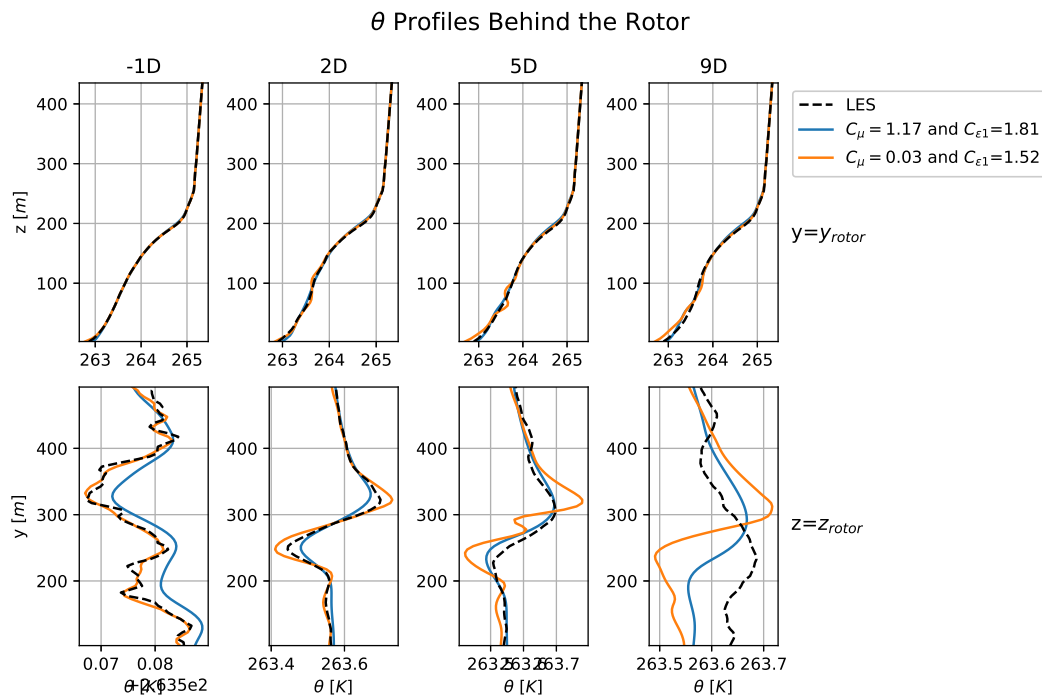


Figure C.1: Comparison of temperature profiles for baseline RANS simulations of Case B: Kokee SBL with different values for C_μ and C_{ϵ_1} .

C.2. Influence of the THF Correction

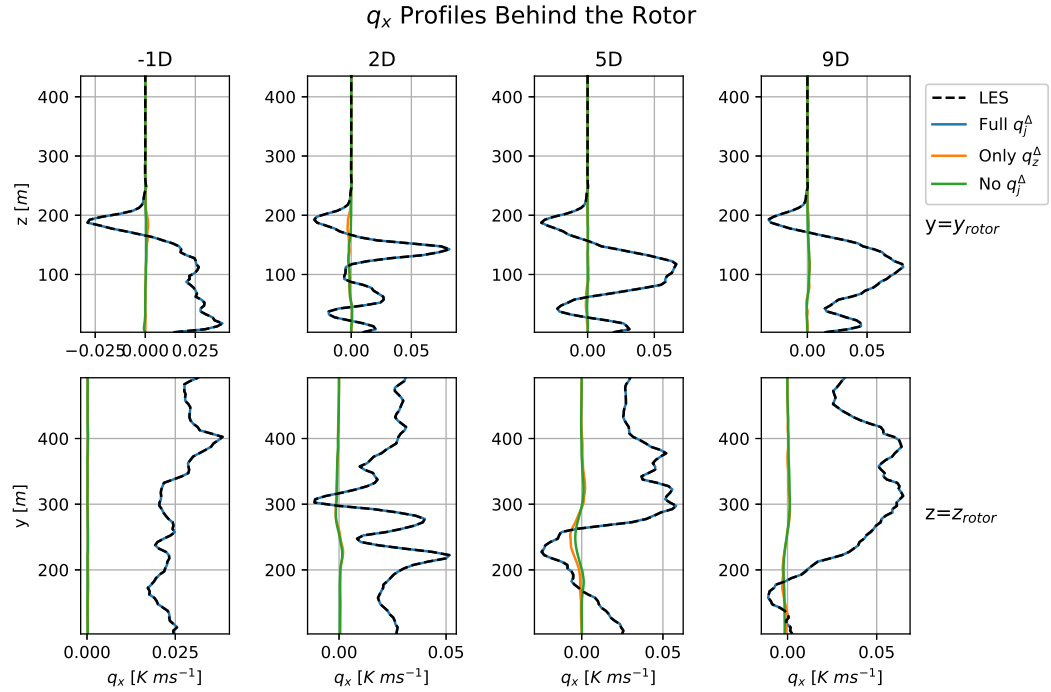


Figure C.2: Profiles of the z-component of the turbulent heat flux behind the rotor for RANS simulations of Case B: Kokee SBL, with full THF correction implemented (blue), only z-component of THF correction (orange) and without THF correction (green). All simulations implemented the optimal, frozen turbulence anisotropy and TKE production corrections.

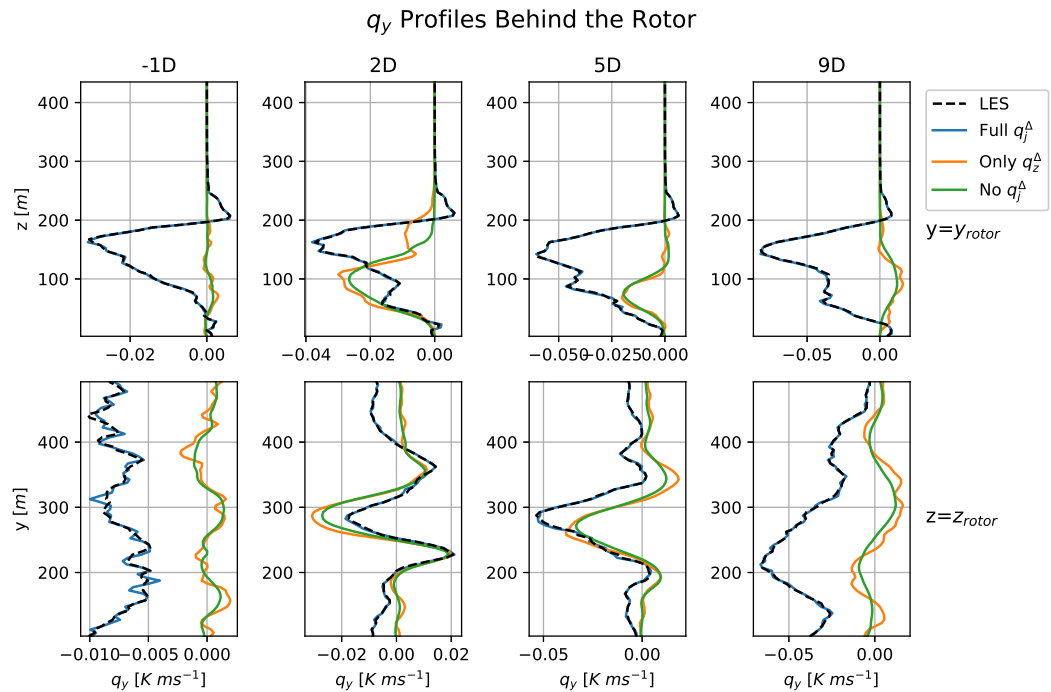


Figure C.3: Profiles of the z-component of the turbulent heat flux behind the rotor for RANS simulations of Case B: Kokee SBL, with full THF correction implemented (blue), only z-component of THF correction (orange) and without THF correction (green). All simulations implemented the optimal, frozen turbulence anisotropy and TKE production corrections.

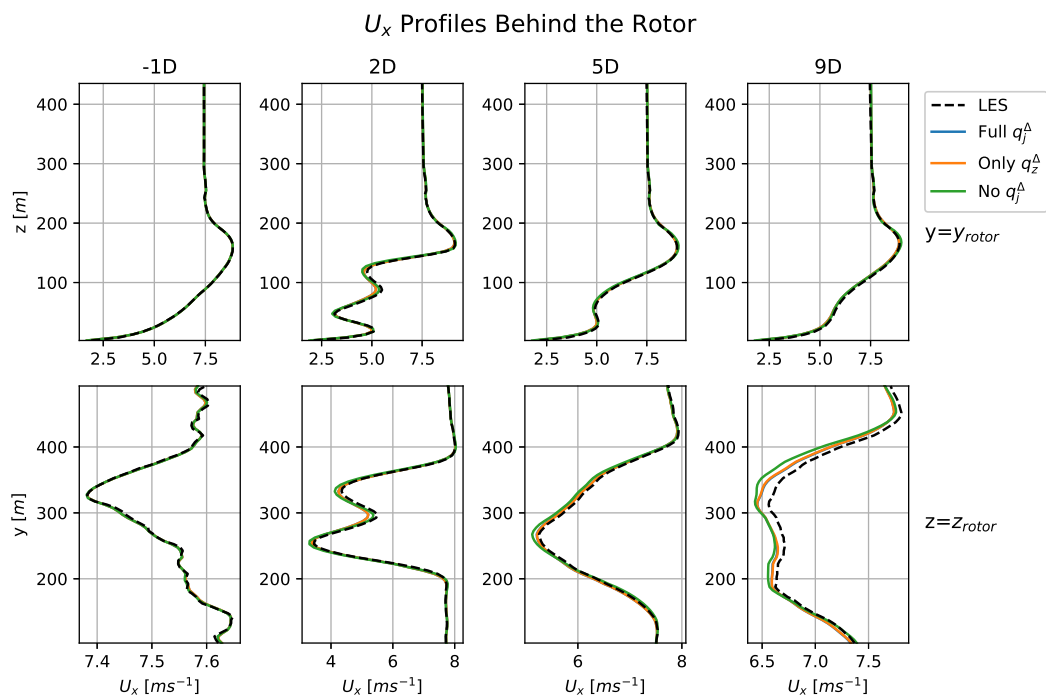


Figure C.4: Profiles of the horizontal velocity behind the rotor for RANS simulations of Case B: Kokee SBL, with full THF correction implemented (blue), only z-component of THF correction (orange) and without THF correction (green). All simulations implemented the optimal, frozen turbulence anisotropy and TKE production corrections.

C.3. Selection of Models for the Turbulence Anisotropy Correction

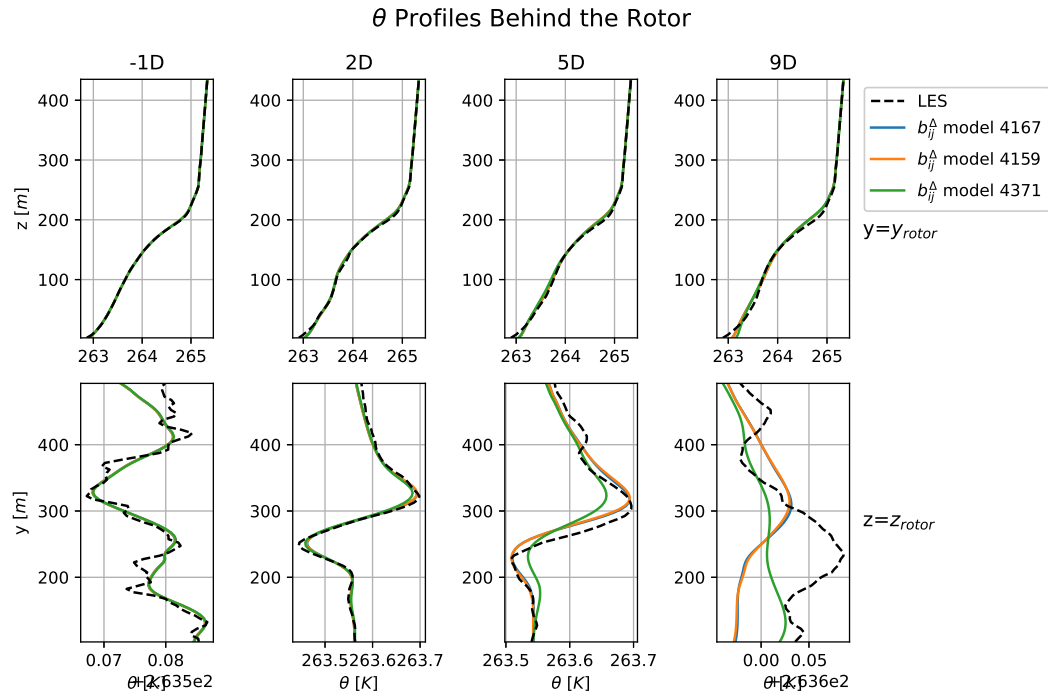


Figure C.5: Profiles of the temperature behind the rotor for RANS simulations of Case B: Kokee SBL. Different simulations implemented different models for the anisotropy correction b_{ij}^A .

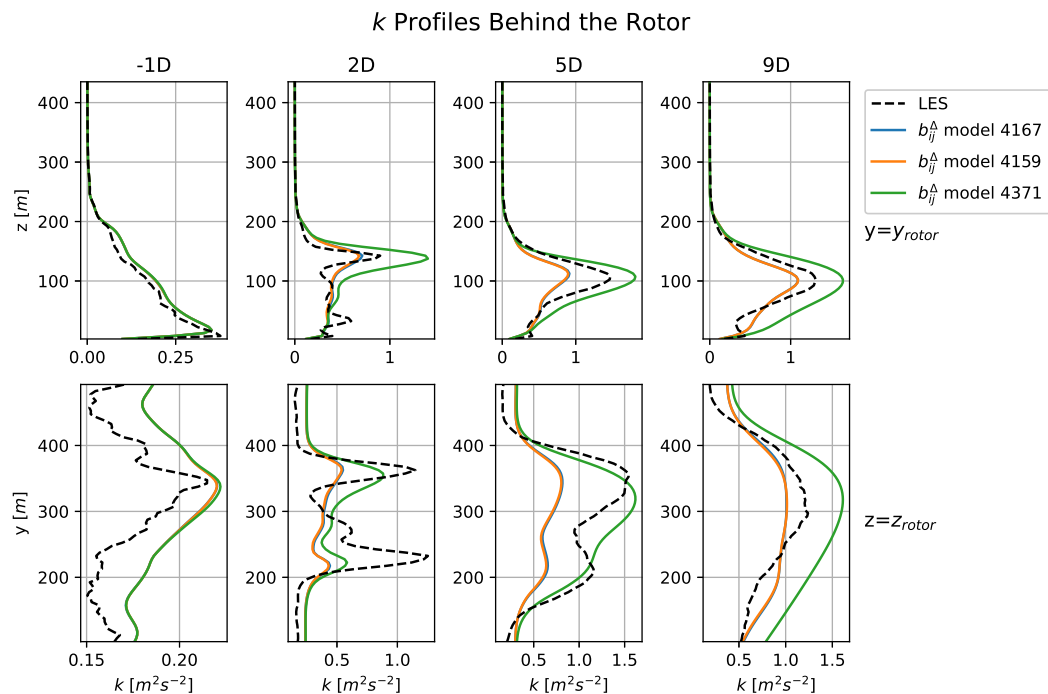


Figure C.6: Profiles of the turbulence kinetic energy behind the rotor for RANS simulations of Case B: Kokee SBL. Different simulations implemented different models for the anisotropy correction b_{ij}^A .

C.4. Selection of Models for the TKE Production Correction

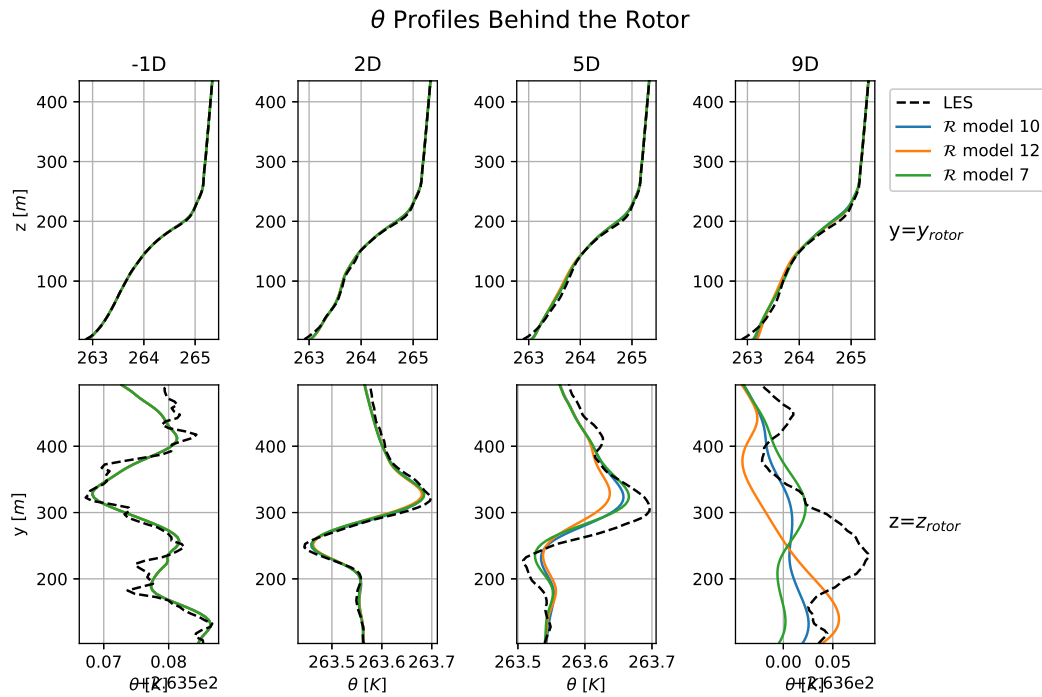


Figure C.7: Profiles of the temperature behind the rotor for RANS simulations of Case B: Kokee SBL. Different simulations implemented different models for the TKE Production correction \mathcal{R} .

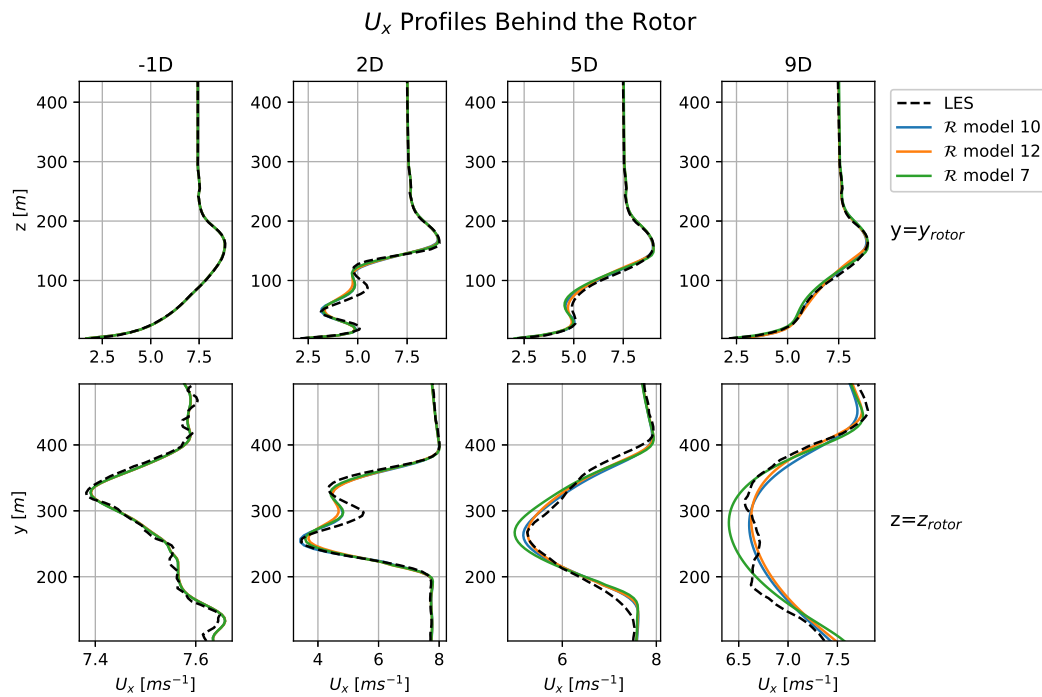


Figure C.8: Profiles of the streamwise velocity behind the rotor for RANS simulations of Case B: Kokee SBL. Different simulations implemented different models for the TKE Production correction \mathcal{R} .

C.5. Selection of Models for the THF Correction

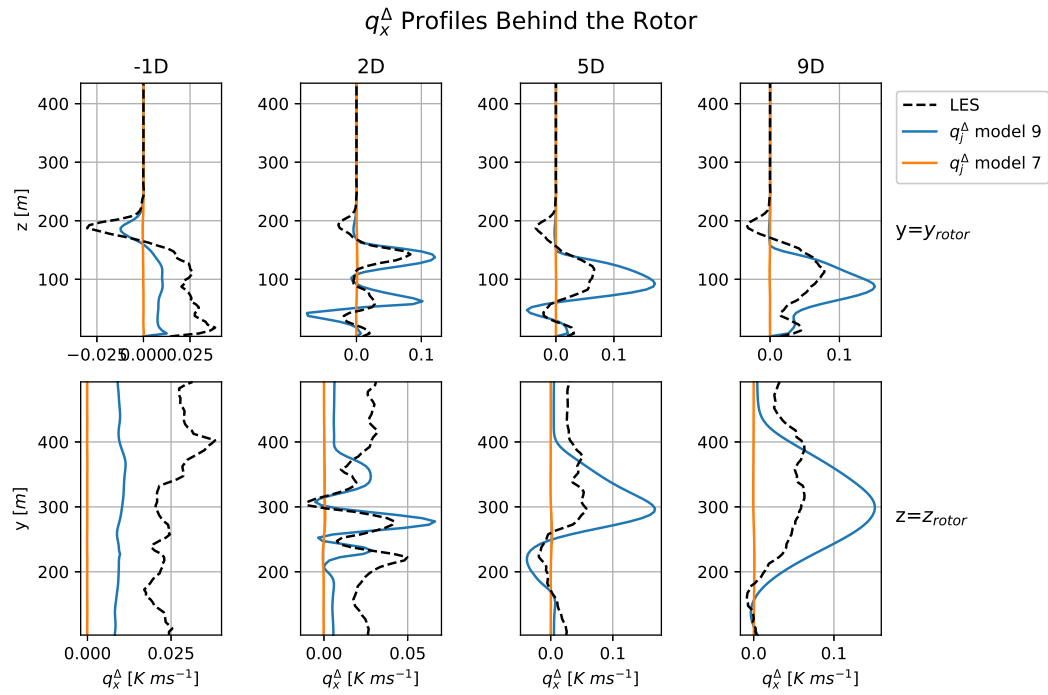


Figure C.9: Profiles of the x-component of the THF correction q_x^Δ behind the rotor for RANS simulations of Case B: Kokee SBL. Different simulations implemented different models for the THF correction q_f^Δ .

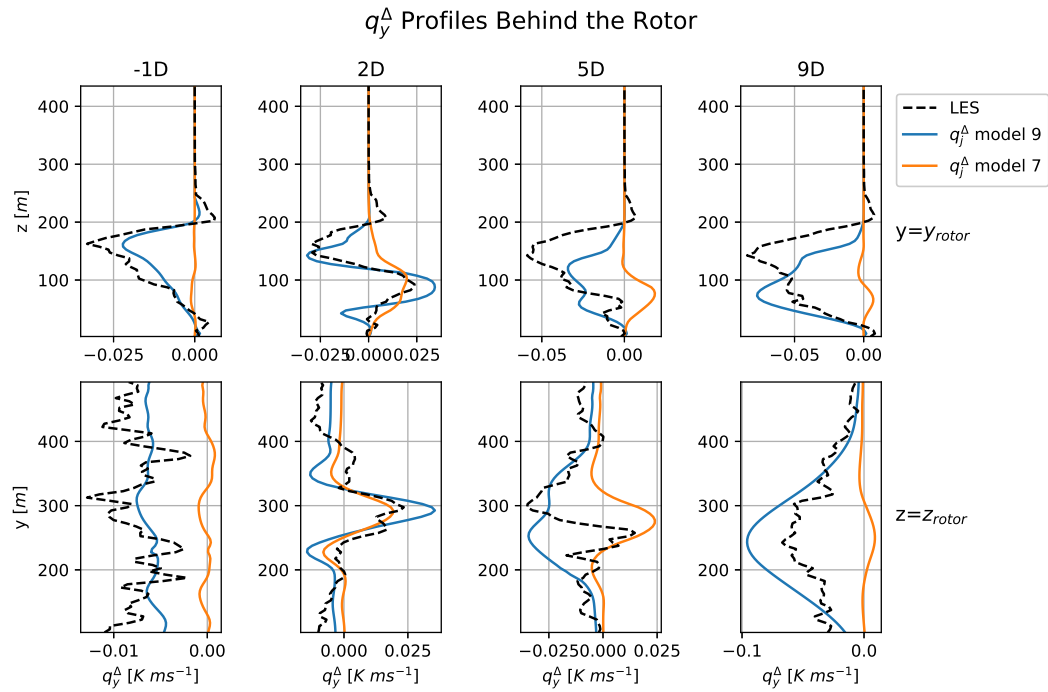


Figure C.10: Profiles of the y-component of the THF correction q_y^Δ behind the rotor for RANS simulations of Case B: Kokee SBL. Different simulations implemented different models for the THF correction q_f^Δ .

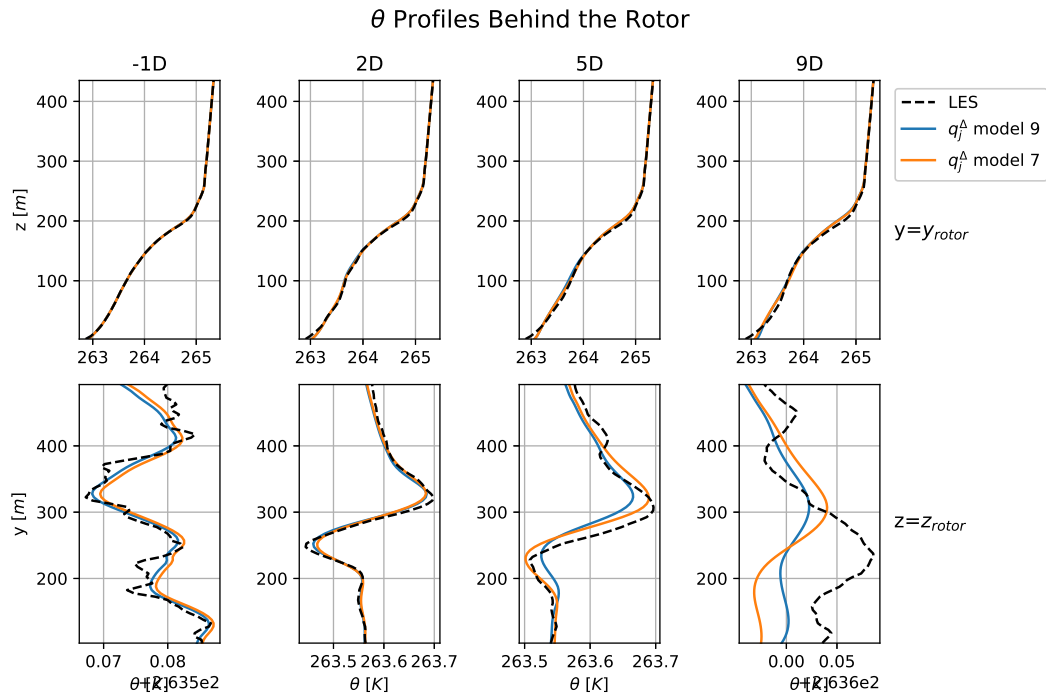


Figure C.11: Profiles of the temperature behind the rotor for RANS simulations of Case B: Kokee SBL. Different simulations implemented different models for the THF correction q_f^A .

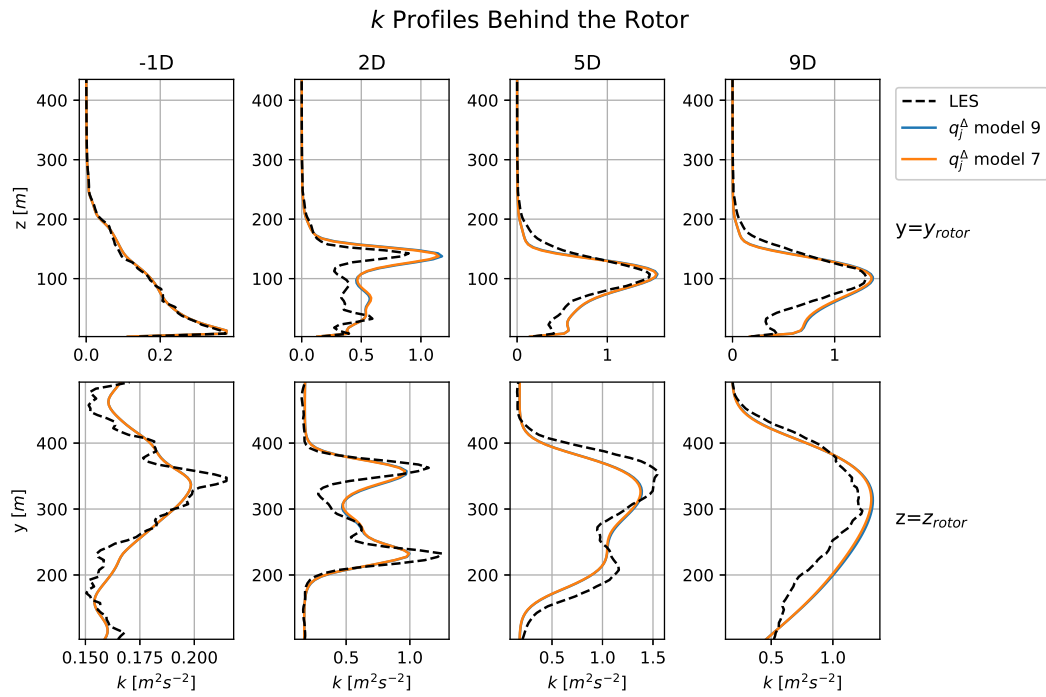


Figure C.12: Profiles of the TKE behind the rotor for RANS simulations of Case B: Kokee SBL. Different simulations implemented different models for the THF correction q_f^A .

C.6. Comparison with Baseline

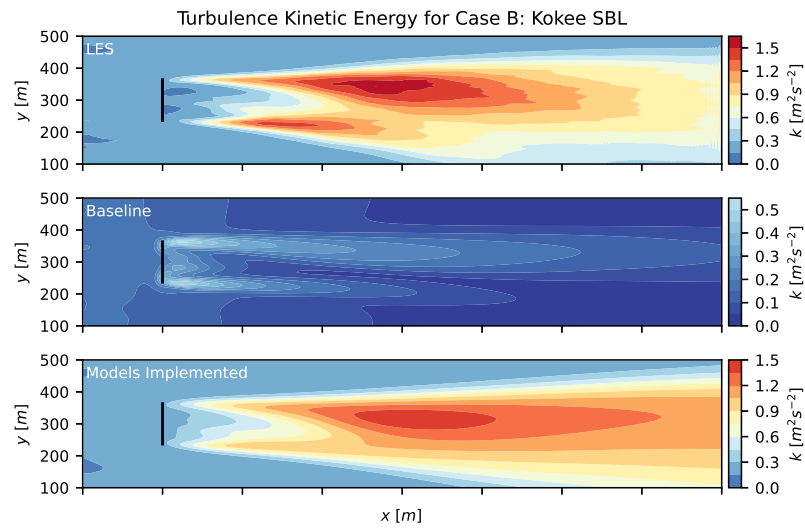


Figure C.13: Comparison of horizontal slices of TKE at hub-height between the LES data, the baseline simulation and the simulation with implemented models for Case B: Kokee SBL. The rotor is represented by the black line and all slices are plotted with the same colour scale for better comparison.

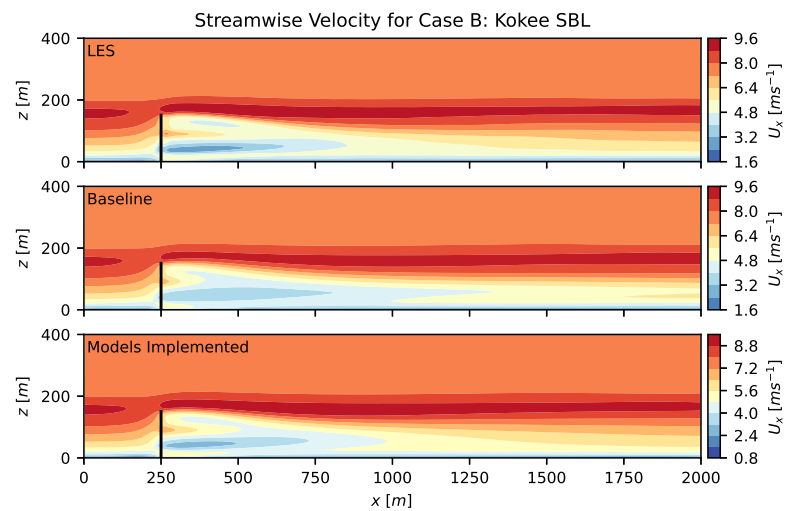


Figure C.14: Comparison of vertical slices of stream-wise velocity at the location of the rotor between the LES data, the baseline simulation and the simulation with implemented models for Case B: Kokee SBL. The rotor is represented by the black line and all slices are plotted with the same colour scale for better comparison.

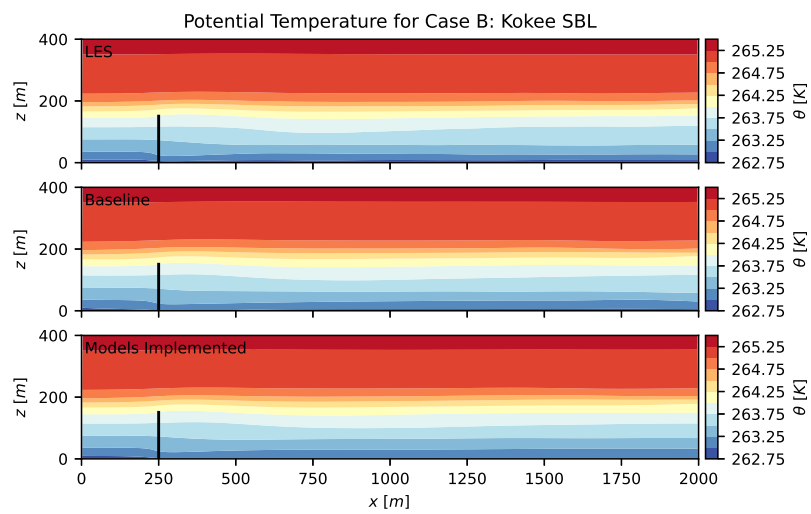


Figure C.15: Comparison of vertical temperature slices at the location of the rotor between the LES data, the baseline simulation and the simulation with implemented models for Case B: Kokee SBL. The rotor is represented by the black line and all slices are plotted with the same colour scale for better comparison.

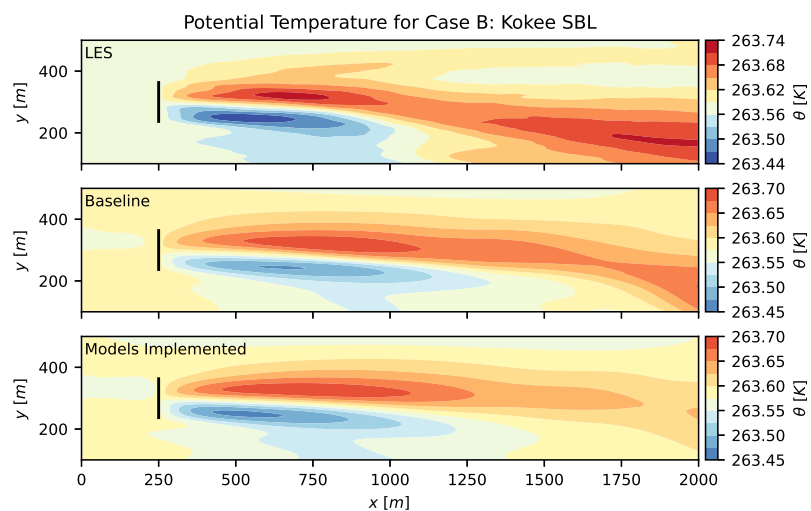


Figure C.16: Comparison of horizontal temperature slices at hub-height between the LES data, the baseline simulation and the simulation with implemented models for Case B: Kokee SBL. The rotor is represented by the black line and all slices are plotted with the same colour scale for better comparison.

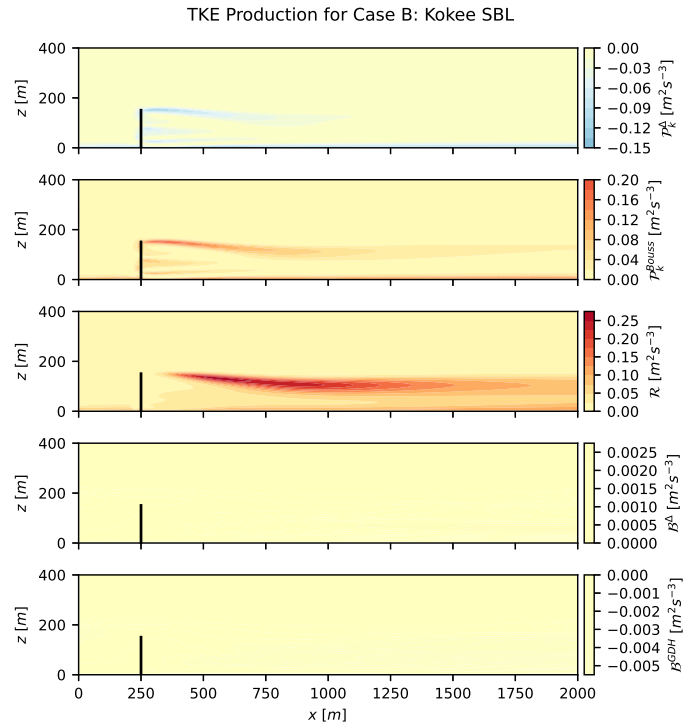


Figure C.17: Breakdown of TKE production in the simulation with implemented models for Case B: Kokee SBL. Colour scales are scaled for better comparison.

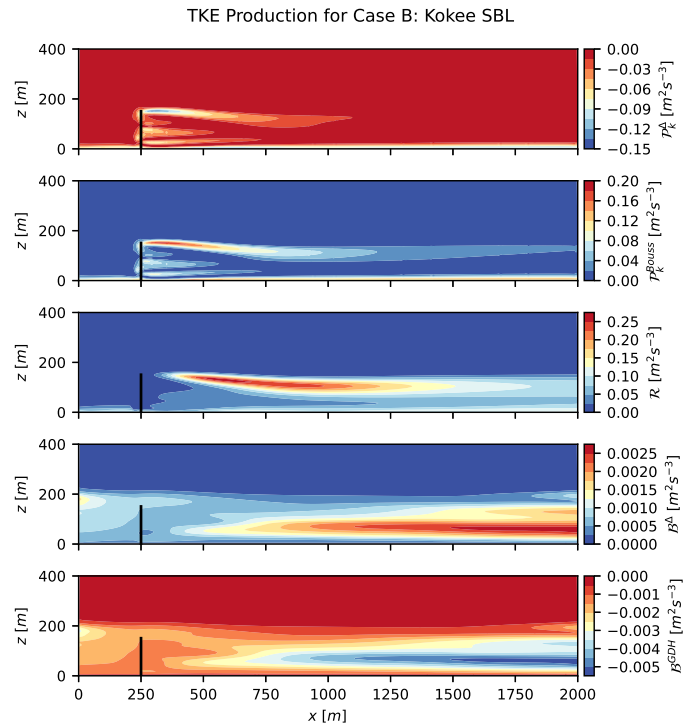


Figure C.18: Breakdown of TKE production in the simulation with implemented models for Case B: Kokee SBL. Colour scales are not scaled

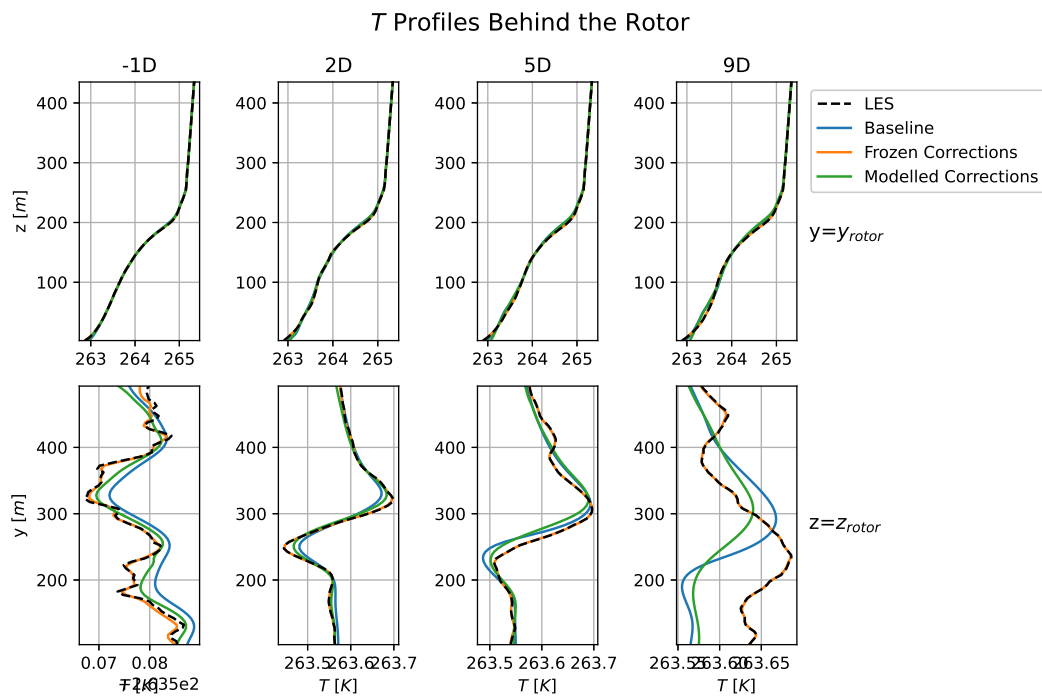


Figure C.19: Comparison of temperature profiles behind the rotor between the LES data, the baseline simulation, the simulation with optimal, frozen corrections and the simulation with implemented models for Case B: Kokee SBL.

C.7. Model Performance

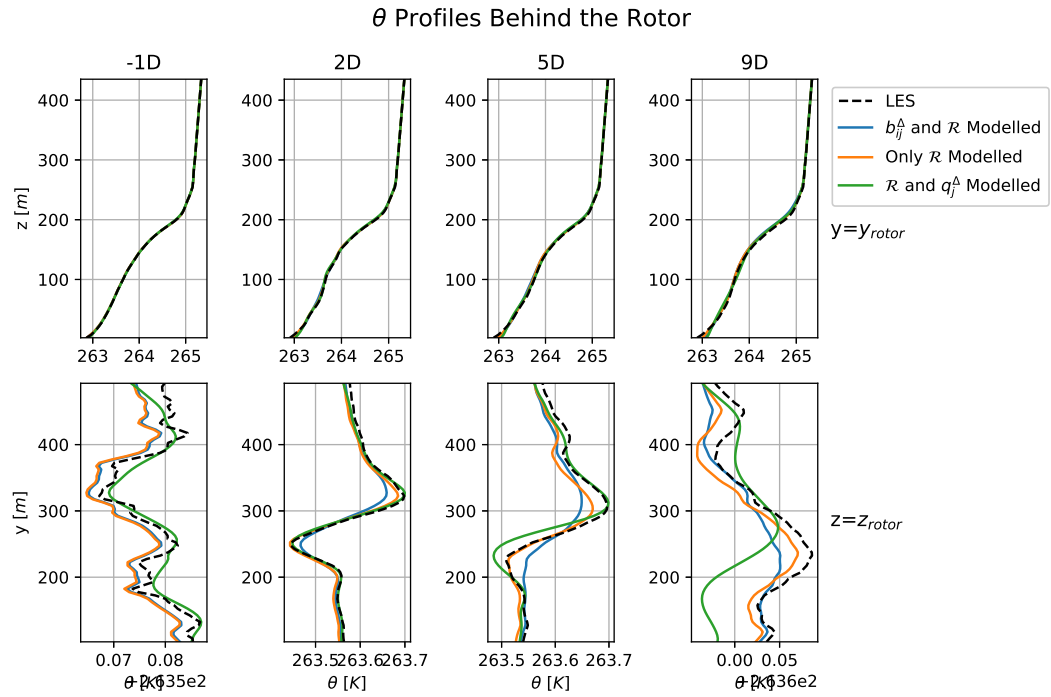


Figure C.20: Temperature profiles for simulations of Case B: Kokee SBL with different configurations of correction terms modelled, all the other correction terms are kept constant at their optimal, frozen values.

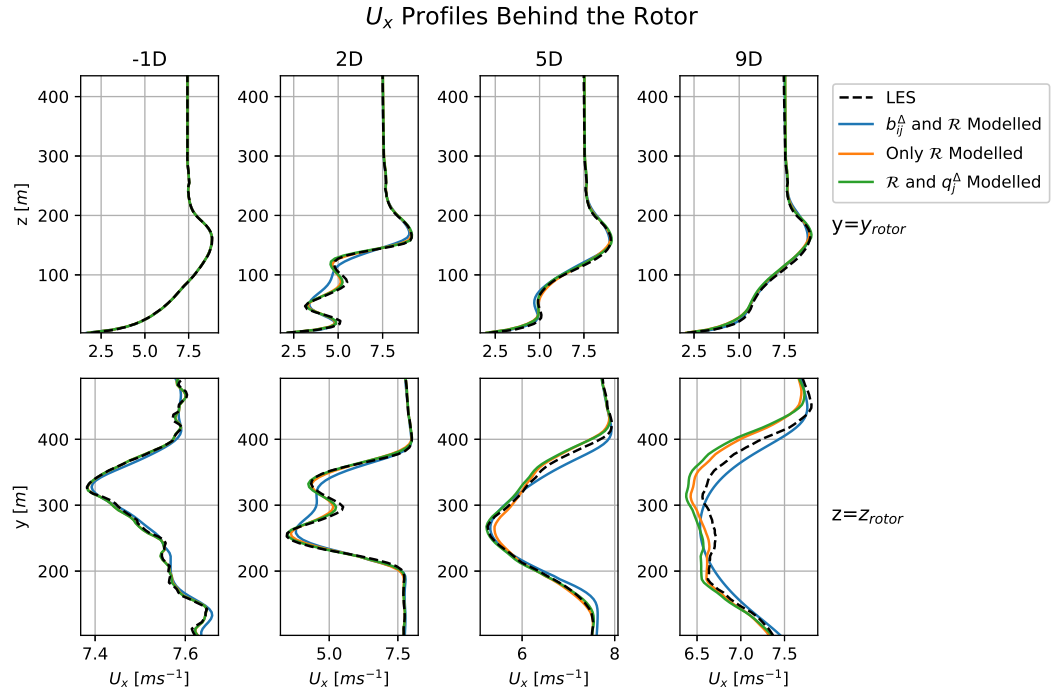


Figure C.21: Stream-wise velocity profiles for simulations of Case B: Kokee SBL with different configurations of correction terms modelled, all the other correction terms are kept constant at their optimal, frozen values.